

**APPLICATION OF TWO-DIMENSIONAL CORRELATION ANALYSIS TO EXPLOSIVES DETECTION AND POLYMER CRYSTALLIZATION**

THESIS BY

Diana Sergeievna Smirnova

In Partial Fulfillment of the Requirements for the

Degree of

Doctor of Philosophy

CALIFORNIA INSTITUTE OF TECHNOLOGY

Pasadena, California

2010

(Defended September 3, 2009)

© 2010

Diana Sergeievna Smirnova

All Rights Reserved

## ACKNOWLEDGEMENTS

I am very fortunate because I have the pleasure to acknowledge a large number of people, many of whom I can thank for a variety of different things.

First, I must thank my thesis committee: Prof. Julie Kornfield, Prof. Rick Flagan, Prof. Dave Tirrell, and Prof. Bob Grubbs, for taking the time to read my thesis and evaluate my work.

As my advisor, Julie's contribution to my scientific work cannot be overstated. Through her creativity, generosity, and enthusiasm for science, Julie has had an enormous impact on both my professional and personal growth. In addition to providing lessons on melt dynamics, she shared invaluable lessons on writing, presenting, and networking. She has inspired creative thinking and risk taking. I no longer fear public speaking because of the many conferences I have attended at her encouragement. She pushed me to spend three months living in France which was an experience so spectacular that words are not sufficient to describe it. And she encouraged me to take advantage of the interview opportunity with ExxonMobil and is the reason I have a place to go from here.

I have had the opportunity to have mentors in others as well. Prof. Flagan's door was always open for questions regarding atmospheric chemistry, scientific writing, or mechanical engineering. Lucia Fernandez Ballester has been instrumental in my getting to this point. She taught me a great deal when I first started and still does. She was a great teacher, colleague, and friend. Lucia introducing me to the synchrotron experience allowed to meet Tim Gough with whom I have had some of my most enlightening and en-

joyable conversations. The majority of the x-ray data presented in the following pages was obtained with their invaluable help. There are few people that one can spend a week's worth of sleepless, stress-filled nights with and still want to talk to at the end of the experience; even fewer that could make that week enjoyable. I was very fortunate to have many beamtimes with Tim and Lucia. I will always remember coke, blue pop, musica (Radiohead, Muse, Arctic Monkeys just to name a few), TextTwist, Chili's, Kinder Bueno and many other memories that still make me smile.

My trip to France allowed me to broaden my perspective both personally and professionally. Along with Julie, Wim Bras's generosity made the trip possible, as well as my travels to other facilities in Europe. While at DUBBLE, Lucia and Giuseppe Portale taught me proper x-ray data analysis techniques and Didier Grandjean was very patient in helping me through many software setbacks during my analysis. Other members of the DUBBLE staff were very welcoming and greatly contributed to my experience: Sergey Nikitenko, Guy Luijckx, Dirk Detollenaere, Kristina Kvashnina, Lian Apostol, and Valerie Clement.

I have had the pleasure to be part of a number of collaborative efforts. The polyethylene studies have been done with the support of David Lohse's team at ExxonMobil, specifically Manika Varma-Nair and Cindy Mitchell. The IED detection project came to us through Ravi Verma and Andrew Pepino from Tanner Labs. Andrew has spent more than a few hours sharing his insights on lasers and optics. David Boyd has brought insights on Raman spectroscopy and SERS to the project. Additionally, while at Caltech, I have had the pleasure of working with and learning from a number of visiting scientists.

Specifically, Manabu Kato, a Japanese visitor, greatly improved our instrument software during his stay. Additionally, a significant portion of the DSC data and some x-ray data presented in this thesis is the work of Dr. Soo-Young Park.

There are a number of current and former members of the Kornfield group that I have come to for scientific answers, advice, or just some stress-relief. Lucia was always willing to answer my multitude of questions, even when she had no time to spare. Neal Scruggs either had the answer or knew where to find it, he is a very handy human thesaurus, and was a great office mate. Rafael Verduzco, Michael Mackel, and Matthew Mattson were always willing to share their wisdom and time. I was fortunate to have Zuleikha Kurji accompany me to one of my beamtimes at Berkeley and assist me in data collection. In my last year, post-doc Bradley Olsen provided inspiration and great advice. Other members of the Kornfield group that I got to share my research experience with are Joyce Huynh, Ryan Turner, Ameri David, Bahar Bignol, Zachary Williams, Yan Xia, Jeremy Wei, Iman Hajimorad, and Rohan Hule.

Many members of the Caltech staff probably do not always get all the credit they deserve. Mike Roy and Steve Olsen from the machine shop and Rick Gerhart from the glass shop are talented and necessary to the success of mine and many other theses. Cory and Moses always gave me reason to smile in addition to providing the right tools and accessories. Kathy Bubash is invaluable in ushering students into and out of their time at Caltech and, along with the other department secretaries, she ensures that the time in between flows fairly smoothly also. Finally, we might all regress back to the dark ages without Suresh's computer assistance.

A unique feature of Caltech is that its small size fosters personal connections with people. Enough credit cannot be given to Anne Hormann and Marcy Fowler, who assisted with both administrative matters and sanity maintenance. Liz Muira Boyd was a great help with Raman spectroscopy and inspired recreational goals. John Doyle and alum Jorge Palamara inspired my triathlon hobby that was a great part of my Caltech experience.

My Caltech experience has been greatly enriched by the people I met here. I found a great friend in Mary Louie by spending hours on the roads trying to outrun our research hiccups. Jeff Hanna and other members of the Caltech tri club encouraged my crazy antics to blow off steam. Yvonne Chen and Havaala Pye were always up for ladies' night. And I must also thank my friend Emma Gregory who has managed to provide in-calculable support while going through her own thesis experience on the other side of the country. My support network is vast and grounded in my family. My parents and sister have always been there for my smallest and biggest moments, and I owe to them all of the good things that I have in my life. My father has read almost every word of this thesis and some of them were incomprehensible before his feedback. Thank you for your time and great patience. And finally, at the end of the day, whether it was the best day or the worst day, I had the joy of coming home to a husband whose patience, understanding, and support have reached levels above and beyond the call of duty—especially in these last few months. This would not have been possible without you, Oliver.

## ABSTRACT

This thesis presents two novel applications of two-dimensional (2D) correlation analysis: (1) long standoff detection of explosives using Raman spectroscopy and (2) examination of morphology development in semicrystalline materials. The power of 2D correlation analysis is its ability to expose and quantify the relationship between changes in distinct observables characterizing a system as it evolves in response to a perturbation. Most frequently, the observables are spectroscopic (intensity  $I(v_i)$ ) at distinct values of the spectral variable,  $v_i$ ), so the method is often called “2D correlation spectroscopy.” Diverse perturbations, such as mechanical stress, change in thermodynamic conditions (e.g., temperature or pressure), and extent of reaction, have been applied to reveal desired information that is obscured in the absence of the perturbation. Even small, subtle changes in response to the perturbation become readily resolved with 2D correlation analysis, which effectively excludes static observables and greatly enhances correlated changes relative to random variations.

Improvised explosive devices (IEDs) are currently the number one killer of both troops and civilians in Iraq and Afghanistan. Effective detection of explosives at standoff distances is important to ensure human safety. Implementation of 2D correlation spectroscopy can increase detection success due to the following advantages of the analysis: (1) simplification of complex spectra by separation of overlapped peaks, (2) enhancement of spectral resolution and enhancement of signal to noise ratio (SNR) through the spreading of peaks over a second dimension, (3) probing specific sequential order of spectral intensity changes, and primarily (4) exclusion of stable compounds and selective exclusion of unsta-

ble explosives. By taking advantage of the unstable nature of explosive compounds through the imposition of thermal degradation, it is possible to further separate spectral features corresponding to explosives both from a noisy background and any contaminants based on their rate of response to heating.

A temperature ramp is used to probe Raman features of explosives and their mixtures with choice contaminants. Implementation of 2D correlation analysis results in significant enhancement of explosive signal relative to background. Effective separation of explosive features is demonstrated for two biogenic contaminants: saliva, which represents proteins, lipids and saccharides, and diesel soot, which contains heteroaromatic species. We discovered that correlation analysis can further provide information on the physical state of the unstable compounds, distinguishing crystalline from amorphous states. The well-established spectral shifts of organic crystals with increasing temperature provide strong 2D spectral features, which could be utilized for further sample identification. Several aspects of the 2D correlation analysis are examined to optimize effectiveness of detection. Use of the time-averaged spectrum as the reference for calculating dynamic spectra yields the best performance. Normalization schemes are found to be of limited utility: some of them enhance specific features, but their application also can result in false positives. The only data pretreatment recommended for the application of long standoff detection in arbitrary environments is the removal of data offset by the subtraction of the minimum value from each spectrum.

The ultimate physical properties of semicrystalline materials, such as strength, toughness, and transparency, are directly related to their morphology through their molecu-

lar characteristics and processing conditions. Morphology is examined using small-angle and wide-angle x-ray scattering (SAXS and WAXS, respectively), for which 2D correlation analysis is well suited due to its simplification of complex scattering curves through the de-convolution of overlapping features, the determination of sequential order of intensity changes, and the enhancement of spectral resolution by spreading data over a second dimension. The effects of different molecular characteristics on crystallization of semi-crystalline polymers are examined by conventional techniques and 2D correlation analysis of x-ray scattering data.

Model short-chain branched (SCB) polyethylenes are found to crystallize in three regimes during quiescent temperature ramps. “Primary-irreversible” crystallization occurs at the highest temperatures and is marked by large changes in the morphological parameters (crystallinity, long period, and overall scattering power) as primary lamellae propagate relatively rapidly through unconstrained melt. Once the majority of unconstrained melt is consumed, secondary lamellar growth occurs in the largest non-crystalline regions between primary lamellae marks slower “secondary-irreversible” crystallization that occurs at intermediate temperatures. At low temperatures, the values of the morphological parameters are equal during cooling and subsequent heating marking the slow formation of fringed microelles that occurs in the “reversible” crystallization regime. While irreversible and reversible crystallization have been observed previously in SCB materials, this is the first time that a physical justification is presented for the separation of the irreversible crystallization into primary- and secondary-irreversible regimes.

Each regime is identified by unique features in the 2D correlation plots. Specifically, 2D heterospectral analysis of SAXS/WAXS data reveals identical qualitative behavior between a series of branched hydrogenated polybutadienes in each regime: the primary-irreversible regime is characterized by the intensity redistribution (sign change) only in SAXS, the secondary-irreversible regime is characterized by the intensity redistribution only in WAXS, while the reversible regime is characterized by the intensity redistribution in both SAXS and WAXS. Additionally, two-dimensional correlation analysis provides a unique approach to gain insight into subtle changes during morphology development, such as the development of density heterogeneities in the non-crystalline regions.

The presence of short-chain branches is found to have a profound, diminishing effect on the formation of oriented structures in response to flow-induced crystallization. Crystallization of SCB materials is examined in the presence of high density polyethylene (HDPE) in order to expose the effectiveness of the branched materials to propagate oriented morphology. HDPE is found to serve as an effective clarifying and nucleating agent for a metallocene copolymer with complex concentration dependence. The SCB material is found to be incapable of propagating oriented growth on large length scales. Evidence presented suggests that this behavior is the result of a buildup of chain defects at the growth front which results in a transition from oriented to isotropic crystallization. Hence, it is proposed that size of crystal structures can be controlled by dictating the amount of copolymer incorporated during oriented structure formation via the crystallization temperature, allowing for the fine-tuning of ultimate material properties. Ultimately, it is found that both quiescent and flow-induced crystallization is dominated by short-chain branching.

Two-dimensional correlation analysis in conjunction with thermal decomposition is demonstrated as an effective means to increase the success of detection of energetic compounds using Raman spectroscopy. This combination of analysis and a perturbation that elicits a unique response in the compound can be applied to variety of other detection systems. Additionally, 2D correlation analysis is demonstrated to provide unique insight into the morphology evolution during crystallization of semicrystalline materials, which can be used to control their material properties. The ideas presented here can be easily applied to study phase transitions in other systems, such as block copolymers.

## TABLE OF CONTENTS

Acknowledgements.....	iii
Abstract.....	vii
Table of Contents.....	xii
List of Figure and Tables .....	xviii
Nomenclature.....	xxii
<b>1. Introduction .....</b>	<b>I-1</b>
1.1 TWO-DIMENSIONAL CORRELATION SPECTROSCOPY .....	I-2
1.2 EXPLOSIVES DETECTION .....	I-10
1.3 SEMICRYSTALLINE MATERIALS.....	I-12
1.4 REFERENCES .....	I-15
<b>2. Two-Dimensional Correlation Analysis for Explosive Detection.....</b>	<b>II-1</b>
2.1 INTRODUCTION .....	II-2
2.2 EXPERIMENTAL METHODS .....	II-6
2.2.1 Materials .....	II-6
2.2.2 Raman Microspectroscopy .....	II-8
2.2.2.1 Contamination Studies.....	II-8
2.2.2.3 Long Standoff Raman Spectroscopy .....	II-9
2.2.2.4 Computation .....	II-10
2.3 RESULTS .....	II-14
2.3.1 Raman Microspectroscopy of Pure Compounds .....	II-14
2.3.1.1 One-Dimensional Raman Spectra .....	II-14
2.3.1.2 Clean Two-Dimensional Correlation Spectra.....	II-15
2.3.1.3 Effect of Background in Two-Dimensional Correlation Spectra .....	II-19
2.3.1.4 Data Pretreatment .....	II-22
2.3.1.5 Reference Spectrum.....	II-23
2.3.2 Raman Microspectroscopy: Contamination Studies.....	II-24
2.3.2.1 Traditional: RDX and Saliva on Sand .....	II-25

2.3.2.2 Multi-Point: RDX, Soot, Sand, Polybutadiene.....	II-27
2.3.2.3 Multi-Sample: PETN, Soot, Polybutadiene.....	II-29
2.3.3 Long Standoff Detection.....	II-32
2.4 DISCUSSION.....	II-34
2.4.1 Application of 2D Correlation Analysis.....	II-34
2.4.1.1 Synchronous Spectra .....	II-36
2.4.1.2 Asynchronous Spectra .....	II-37
2.4.1.3 Data Pretreatments.....	II-39
2.4.2 Fluorescence .....	II-40
2.4.3 Raman Signal Enhancement.....	II-41
2.5 CONCLUSION.....	II-42
2.6 ACKNOWLEDGEMENTS .....	II-44
2.7 REFERENCES .....	II-43

<b>3. Interplay between Short-Chain and Long-Chain Branches.....</b>	<b>III-1</b>
3.1 INTRODUCTION .....	III-2
3.2 EXPERIMENTAL METHODS .....	III-6
3.2.1 Materials .....	III-6
3.2.2 Differential Scanning Calorimetry .....	III-8
3.2.3 X-ray Scattering.....	III-9
3.3 RESULTS .....	III-11
3.3.1 Differential Scanning Calorimetry .....	III-11
3.3.1.1 Temperature Ramps.....	III-11
3.3.1.2 Isothermal Crystallization .....	III-12
3.3.2 X-ray Scattering.....	III-16
3.3.2.1 WAXS: Temperature Ramps.....	III-16
3.3.2.2 SAXS: Temperature Ramps .....	III-19
3.3.2.3 SAXS: Temperature Ramps with Isothermal Step .....	III-23
3.4 DISCUSSION.....	III-26
3.4.1 Morphology Evolution during Cooling and Heating.....	III-26

3.4.1.1 Primary-Irreversible Crystallization .....	III-27
3.4.1.2 Secondary-Irreversible Crystallization .....	III-29
3.4.1.3 Reversible Crystallization at Low Temperatures .....	III-31
3.4.1.4 Transition Temperatures .....	III-33
3.4.2 DSC Double Melting .....	III-34
3.4.3 Effects of Molecular Characteristics .....	III-36
3.4.3.1 Crystallinity .....	III-37
3.4.3.2 Long Period .....	III-38
3.4.3.3 DSC Crystallization Kinetics .....	III-39
3.4.4 Implications for Flow-Induced Crystallization .....	III-40
3.5 CONCLUSION .....	III-41
3.6 APPENDIX—Crystalline and Amorphous Layer Thickness .....	III-44
3.7 ACKNOWLEDGEMENTS .....	III-45
3.8 REFERENCES .....	III-47

<b>4. Morphology Development in Model Polyethylenes via Two-Dimensional Correlation Analysis.....</b>	<b>IV-1</b>
4.1 INTRODUCTION .....	IV-2
4.2 EXPERIMENTAL METHODS .....	IV-6
4.2.1 Materials .....	IV-6
4.2.2 X-ray Scattering .....	IV-6
4.2.3 Computation .....	IV-7
4.2.3.1 Conventional 2D Correlation Analysis.....	IV-7
4.2.3.2 Two-Dimensional Moving Window Analysis.....	IV-8
4.2.3.3 Hetero-Spectral Correlation Analysis.....	IV-9
4.3 RESULTS AND DISCUSSION.....	IV-11
4.3.1 WAXS .....	IV-12
4.3.1.1 Polyethylene WAXS Features .....	IV-12
4.3.1.2 Crystallization of Homopolymers .....	IV-14
4.3.1.3 Crystallization of Random Copolymers .....	IV-19

4.3.1.4 Searching for a Semi-Ordered Phase.....	IV-28
4.3.2 SAXS .....	IV-30
4.3.2.1 Crystallization of Random Copolymers .....	IV-30
4.3.3 SAXS/WAXS Hetero-Spectral Correlation Analysis.....	IV-38
4.3.3.1 Crystallization of Random Copolymers .....	IV-38
4.3.3.2 Scattering at the Onset of Crystallization.....	IV-43
4.3.4 Material Comparisons.....	IV-45
4.4 CONCLUSION .....	IV-45
4.5 ACKNOWLEDGEMENTS.....	IV-49
4.6 REFERENCES .....	IV-50

<b>5. Morphology Development in HDPE/Copolymer Blends: Quiescent and Flow-Induced Crystallization .....</b>	<b>V-1</b>
5.1 INTRODUCTION .....	V-2
5.2 EXPERIMENTAL METHODS .....	V-4
5.2.1 Materials .....	V-4
5.2.2 Differential Scanning Calorimetry .....	V-5
5.2.3 Flow-Induced Crystallization .....	V-6
5.2.4 Optical Characterization .....	V-8
5.2.5 X-ray Scattering.....	V-9
5.2.6 Scanning Transmission Electron Microscopy .....	V-11
5.3 RESULTS .....	V-12
5.3.1 Quiescent Crystallization.....	V-12
5.3.1.1 DSC Nucleation Studies .....	V-12
5.3.1.2 Optical Characterization.....	V-13
5.3.1.3 X-ray Characterization .....	V-19
5.3.1.4 STEM Images .....	V-21
5.3.2 Flow-Induced Crystallization .....	V-22
5.3.2.1 Optical Characterization .....	V-22
5.3.2.2 X-ray Characterization .....	V-25

5.4 DISCUSSION.....	V-26
5.4.1 Quiescent Crystallization.....	V-26
5.4.1.1 Nucleation Effects .....	V-26
5.4.1.2 Morphology Evolution .....	V-28
5.4.2 Flow-Induced Crystallization .....	V-32
5.5 CONCLUSION.....	V-38
5.6 ACKNOWLEDGEMENTS.....	V-40
5.7 REFERENCES .....	V-41

## **APPENDIX A—MATLAB Code for X-ray Data and 2D Correlation**

<b>Analysis .....</b>	<b>A-1</b>
A.1 Save Experimental Parameters.....	A-2
A.2 Open Image Files.....	A-2
A.3 Extract $I(q)$ vs. $q$ .....	A-4
A.4 Lorentz Correction.....	A-5
A.5 Long Period .....	A-6
A.6 SAXS Integrated Intensity .....	A-7
A.7 Conventional 2D Correlation Analysis.....	A-8
A.8 Hilbert-Noda Matrix .....	A-12
A.9 2D Hetero-Spectral Analysis .....	A-12
A.10 2D Moving Window Analysis .....	A-14
A.11 ACKNOWLEDGEMENTS .....	A-15
A.8 REFERENCES .....	A-16

## **APPENDIX B—Flow-Induced Crystallization of Model Systems .....****B-1**

B.1 INTRODUCTION .....	B-2
B.2 EXPERIMENTAL METHODS .....	B-4
B.2.1 Materials.....	B-4
B.2.1.2 Overlap Concentration .....	B-5
B.2.2 Shear-Induced Crystallization.....	B-6

B.3 RESULTS.....	B-6
B.4 DISCUSSION .....	B-7
B.5 CONCLUSION .....	B-10
B.6 ACKNOWLEDGEMENTS .....	B-10
B.7 REFERENCES .....	B-12

## LIST OF FIGURES AND TABLES

### *Chapter 1*

<b>Figure 1.1</b> Simulated dataset for 2D correlation analysis .....	I-6
<b>Figure 1.2</b> Example of 2D correlation analysis .....	I-7
<b>Figure 1.2</b> Schematic representation of branched polymer .....	I-13
 <b>Table 1.1</b> Noda's rules for sequential order .....	I-8

### *Chapter 2*

<b>Figure 2.1</b> Molecular structure of military grade explosives.....	II-7
<b>Figure 2.2</b> Raman spectra of explosive residues.....	II-15
<b>Figure 2.3</b> 2D correlation spectra during heating ramps for RDX and HMX .....	II-17
<b>Figure 2.4</b> Histogram plots of intensity values for 1D and 2D synchronous spectra. ....	II-18
<b>Figure 2.5</b> Raman spectra of PETN collected at select temperatures .....	II-19
<b>Figure 2.6</b> 2D correlation spectra during heating ramps of PETN: normalization comparison .....	II-20
<b>Figure 2.7</b> 2D correlation spectra obtained from floored spectra of RDX, saliva and sand .....	II-26
<b>Figure 2.8</b> Comparison between 1D averaged and autocorrelation spectra following different data pre-treatment.....	II-27
<b>Figure 2.9</b> 2D correlation spectra of multi-point experiment of RDX, diesel soot and PB on sand .....	II-29
<b>Figure 2.10</b> Individual spectra at room temperature of PETN, soot, and bulk PB used for multi-sample experiment .....	II-30
<b>Figure 2.11</b> 2D correlation spectra multi-sample experiment .....	II-31
<b>Figure 2.12</b> Comparison between averaged 1D and autocorrelation spectra of multi- point experiment.....	II-32
<b>Figure 2.13</b> 2D correlation spectra of long standoff RDX excitation .....	II-33

<b>Table 2.1</b> Pre-treatments and normalizations .....	II-11
<b>Table 2.2</b> Perfomance parameter .....	II-18
<b>Table 2.3</b> Comparison of performance parameter based on different normalizations .....	II-22

*Chapter 3*

<b>Figure 3.1</b> Synthesis of hydrogenated polybutadiene via anionic polymerization ...	III-3
<b>Figure 3.2</b> Schematic representation of model polyethylenes .....	III-7
<b>Figure 3.3</b> DSC during temperature ramps .....	III-12
<b>Figure 3.4</b> DSC crystallization kinetics.....	III-13
<b>Figure 3.5</b> DSC melting traces following isothermal crystallization .....	III-14
<b>Figure 3.6</b> Peak melting temperature following isothermal crystallization .....	III-15
<b>Figure 3.7</b> WAXS crystallinity during cooling and heating.....	III-17
<b>Figure 3.8</b> WAXS parameters for HPBDs examined.....	III-18
<b>Figure 3.9</b> Evolution of SAXS intensity during cooling .....	III-19
<b>Figure 3.10</b> Long period during cooling and heating .....	III-20
<b>Figure 3.11</b> SAXS parameters for HPBDs examined.....	III-21
<b>Figure 3.12</b> SAXS integrated intensity during cooling and heating.....	III-22
<b>Figure 3.13</b> Long period during ‘ramp-iso’ protocol.....	III-23
<b>Figure 3.14</b> Long period during isothermal crystallization .....	III-24
<b>Figure 3.15</b> Evolution of SAXS intensity during isothermal crystallization .....	III-25
<b>Figure 3.16</b> Schematic representation of three crystallization regimes of HPBDs	III-28
<b>Figure 3.17</b> Schematic representation of fringed micelle versus lamellae.....	III-32
<b>Figure 3.18</b> Lamellar layer thickness during cooling and heating .....	III-45

<b>Table 3.1</b> Molecular characteristics of model polyethylenes .....	III-7
<b>Table 3.2</b> Peak transition temperatures .....	III-12
<b>Table 3.3</b> Values of high melting peak and its variation .....	III-15

*Chapter 4*

<b>Figure 4.1</b> Schematic representation of 2D correlation moving window analysis ...	IV-9
<b>Figure 4.2</b> WAXS intensity of homopolymer and copolymer .....	IV-12
<b>Figure 4.3</b> 2D correlation analysis of WAXS for homopolymer .....	IV-16
<b>Figure 4.4</b> 2D correlation analysis of WAXS for copolymer.....	IV-21
<b>Figure 4.5</b> Select WAXS intensity curves for copolymer .....	IV-26
<b>Figure 4.6</b> Schematic representation of crystallization.....	IV-30
<b>Figure 4.7</b> Evolution of Lorentz-corrected SAXS for homopolymer .....	IV-31
<b>Figure 4.8</b> 2D correlation analysis of SAXS for copolymer .....	IV-33
<b>Figure 4.9</b> 2D correlation analysis of normalized SAXS for copolymer.....	IV-37
<b>Figure 4.10</b> 2D hetero-spectral analysis of SAXS/WAXS for copolymer .....	IV-39
<b>Figure 4.11</b> 2D hetero-spectral in conjunction of moving window analysis for onset of crystallization of copolymer .....	IV-43

<b>Table 4.1</b> Molecular characteristics of model polyethylenes .....	IV-6
<b>Table 4.2</b> Summary of crystallization behavior of HPBD materials.....	IV-46

*Chapter 5*

<b>Figure 5.1</b> Schematic representation of orientation of chains by flow.....	V-3
<b>Figure 5.2</b> Experimental short-term shear protocol .....	V-7
<b>Figure 5.3</b> Coordinate axes of experimental setup.....	V-9
<b>Figure 5.4</b> Results from DSC nucleation studies .....	V-13
<b>Figure 5.5</b> Transmittance of blends during quiescent crystallization.....	V-14
<b>Figure 5.6</b> Example $H_v$ SALS patterns of blends during quiescent crystallization .	V-15
<b>Figure 5.7</b> Transmittance of 0.5 wt % HDPE blend during quiescent crystallization .....	V-16
<b>Figure 5.8</b> $H_v$ SALS patterns as a function of time during quiescent crystallization of the 0.5 wt % HDPE blend.....	V-17
<b>Figure 5.9</b> Azimuthal dependence of $H_v$ SALS patterns during quiescent crystalli- zation of the 0.5 wt % HDPE blend.....	V-18

<b>Figure 5.10</b> Polarized light optical images for HDPE/EH50 blends .....	V-18
<b>Figure 5.11</b> $H_v$ SALS pattern of 1 wt % HDPE at the onset of crystallization.....	V-19
<b>Figure 5.12</b> WAXS intensity of 1 wt % HDPE blend at 98 °C .....	V-19
<b>Figure 5.13</b> Evolution of SAXS during quiescent crystallization of blends .....	V-21
<b>Figure 5.14</b> STEM images of blends following quiescent crystallization .....	V-22
<b>Figure 5.15</b> Transmittance and apparent birefringence during flow-induced crystal- lization .....	V-23
<b>Figure 5.16</b> $H_v$ SALS patterns subsequent to flow of two blends.....	V-25
<b>Figure 5.17</b> Crystallinity and degree of orientation subsequent to flow .....	V-25
<b>Figure 5.18</b> Schematic representation of quiescent crystallization of blends with two HDPE concentrations.....	V-30
<b>Figure 5.19</b> Schematic representation of orientation of lamellar discs by flow .....	V-34
<b>Figure 5.20</b> Schematic representation of varying extent of oriented growth.....	V-36
<b>Figure 5.21</b> Shish-kebab structure observed in a previous study .....	V-36
<b>Figure 5.22</b> Evolution of degree of orientation following flow at different temperatures .....	V-37

<b>Table 5.1</b> Molecular characteristics of materials used in flow studies .....	V-4
<b>Table 5.2</b> Autocorrelation intensities of (110) reflection during crystallization.....	V-20

*Appendix B*

<b>Figure B.1</b> Schematic representation of overlap concentration.....	B-3
<b>Figure B.2</b> Molecular structure of bimodal blend components .....	B-4
<b>Figure B.3</b> Rheo-optical results of sheared PE blends .....	B-7
<b>Figure B.4</b> Rheo-optical results of sheared iPP blends.....	B-8

<b>Table B.1</b> Molecular characteristics of bimodal blend components .....	B-5
--	-----

## NOMENCLATURE

$a$	unit cell parameter
$A(q)$	autocorrelation intensity
$\hat{A}$	amplitude of response to perturbation
$b$	unit cell parameter
$c^*$	overlap concentration
$d$	sample thickness
DSC	Differential Scanning Calorimetry
FIC	Flow-Induced Crystallization
$G$	relaxation modulus
$G_N^0$	plateau modulus
HDPE	high density polyethylene
HPBD	hydrogenated polybutadiene
$I(q)$	scattering intensity
$I_{\text{perp}}, I_{\text{para}}$	light intensity transmitted through crossed and parallel polarizers, respectively
Im	imaginary part of complex number
$J(q)$	Lorentz-corrected scattering intensity
$L_p$	long period
LCB	long chain branch
$m$	total number of discrete spectra
$M_e$	molecular weight of entanglements
$M_n$	number-average molecular weight
$M_w, M_{w,\text{tot}}$	total weight-average molecular weight
$M_{w,a}$	weight-average molecular weight of long chain branch ('arm')
$M_{w,b}$	weight-average molecular weight of chain backbone
$N_a$	Avogadro's number
$\Delta n$	birefringence
$P$	performance parameter

PDI	polydispersity
PE	polyethylene
$q$	scattering wavevector
$Q$	total SAXS scattering power
$R_g$	radius of gyration
$\text{Re}\{\}$	real part of complex number
SALS	Small Angle Light Scattering
SAXS	Small Angle X-ray Scattering
SCB	short chain branch
$t$	perturbation variable
$t_c$	isothermal crystallization time
$T_c$	experimental isothermal crystallization temperature
$t_{\text{hold}}$	hold-time at elevated temperatures
$T_{\text{hold}}$	elevated temperature used in nucleation studies
$T_m$	peak melting temperature as determined by DSC
$t_{\text{max}}$	peak crystallization time
$T_{\text{min}}, T_{\text{max}}$	limits of perturbation variable
$t_s$	shearing time
$T_x$	peak crystallization temperature as determined by DSC
$\Delta T$	apparent subcooling
$\mathbf{v}$	velocity vector
WAXS	Wide Angle X-ray Scattering
Wi	Wiessenberg number
$X_c$	WAXS crystallinity index
$y_i$	discrete Raman spectrum
$\tilde{y}$	dynamic spectrum
$\tilde{z}$	orthogonal spectrum
$\delta$	sample retardance

$\theta$	azimuthal angle
$t$	time
$\lambda$	wavelength
$\mu$	viscosity
$v$	spectral variable
$\rho$	density
$\sigma_w$	wall shear stress
$\tau_r$	terminal relaxation time
$\phi$	cospectrum
$\Phi$	2D synchronous spectrum
$\psi$	quad-spectrum
$\Psi$	2D asynchronous spectrum
$\omega$	frequency

## **Chapter 1**

### **Introduction**

<b>1.1 TWO-DIMENSIONAL CORRELATION SPECTROSCOPY.....</b>	<b>I-2</b>
<b>1.2 EXPLOSIVES DETECTION .....</b>	<b>I-10</b>
<b>1.3 SEMI-CRYSTALLINE MATERIALS.....</b>	<b>I-12</b>
<b>1.4 REFERENCES.....</b>	<b>I-15</b>

The present thesis explores two applications of two-dimensional correlation analysis: 1) detection of explosive compounds in the presence of dynamic background signals, and 2) categorizing and understanding transient structure development in semi-crystalline materials. Two-dimensional (2D) correlation analysis is a powerful technique that can be used to both visualize the relationship between intensity changes at different spectral points as a result of a perturbation and also elucidate the underlying physical phenomena causing the spectral response. It is applied to a set of one-dimensional (1D) data representing the response of a sample to a specific perturbation. Many scientific experiments result in these types of datasets, yet application of 2D correlation analysis is still mostly limited to the fields of optical and NMR spectroscopy, and furthermore applied predominately in a laboratory setting.

## 1.1 TWO-DIMENSIONAL CORRELATION SPECTROSCOPY

With roots in the field of nuclear magnetic resonance (NMR), two-dimensional (2D) correlation analysis (usually termed 2D correlation spectroscopy because of its frequent use in vibrational spectroscopy) allows one to examine the relationship between changes in spectral intensity at two different spectral variables in response to an external perturbation. Its application to vibrational spectroscopy was introduced by Isao Noda through the study of infrared (IR) spectral response to a sinusoidal perturbation,<sup>1-3</sup> and subsequently generalized to allow the use of a perturbation with arbitrary fluctuations.<sup>4</sup> Furthermore, in 2000, Noda introduced mathematical formulations based on the Hilbert-Noda transformation matrix that greatly simplified the analysis, allowing rapid processing of discrete datasets. These developments resulted in a significant increase in the popularity of 2D correlation spectroscopy.<sup>5, 6</sup>

Generalized two-dimensional correlation spectroscopy is based on the quantitative examination of spectral intensity changes as a function of the external perturbation,  $t$ , observed at two different spectral variables,  $\nu_1$  and  $\nu_2$  (for example, Raman shift as examined in Chapter 2 and scattering vector as examined in Chapter 4). Most commonly, analysis is conducted on a dynamic spectrum, which is defined for each value of the perturbation variable on its interval between  $T_{\min}$  and  $T_{\max}$  with respect to some reference spectrum,  $y_{ref}$ :

$$\tilde{y}(\nu, t) = \begin{cases} y(\nu, t) - y_{ref}(\nu) & \text{for } T_{\min} \leq t \leq T_{\max} \\ 0 & \text{otherwise} \end{cases} \quad (1.1)$$

A diversity of perturbation variables have been examined in literature, including strain, temperature, applied electric/magnetic field, irradiation, and time (see review by Noda<sup>6</sup>). The intensity at distinct spectral variables  $\nu_1$  and  $\nu_2$  tend to vary synchronously when they originate from the same molecular species or underlying physical process. Therefore, analysis of the synchronous two-dimensional correlation is a useful tool for identifying spectral changes that are intimately related. The intensity changes at distinct spectral variables tend to lag (lead) one another when, for example, formation of a given species is a prerequisite for a subsequent reaction to occur. Therefore, it is useful to characterize asynchronous two-dimensional correlations to identify spectral changes that occur sequentially.

The analysis may be readily understood for the simple case of a sinusoidal perturbation in the regime of linear response. A perturbation of the form  $t = \text{Re}\{T' e^{i\omega\theta}\}$  having amplitude  $T'$  would elicit a response at each  $\nu_i$  that would oscillate at the same frequency,  $\omega$ :

$$\tilde{y}(\nu_i, t) = \operatorname{Re} \left\{ A(\nu_i) e^{i(\omega\theta + \beta(\nu_i))} \right\} = \operatorname{Re} \left\{ \hat{A}(\nu_i) e^{i\omega\theta} \right\}, \quad (1.2)$$

with amplitude  $A(\nu_i)$  and phase  $\beta(\nu_i)$ . For distinct values of the spectral variable  $\nu_1$  and  $\nu_2$ , the extent to which variation of intensity occurs simultaneously is captured by the “co-spectrum,”

$$\phi_\omega(\nu_1, \nu_2) \equiv \operatorname{Re} \left\{ \hat{A}(\nu_1) \cdot \hat{A}^*(\nu_2) \right\}, \quad (1.3)$$

and the extent which their variations lag (lead) one another is captured by the “quad-spectrum,”

$$\psi_\omega(\nu_1, \nu_2) \equiv \operatorname{Im} \left\{ \hat{A}(\nu_1) \cdot \hat{A}^*(\nu_2) \right\}, \quad (1.4)$$

where  $\hat{A}^*(\nu_i)$  is the complex conjugate of  $\hat{A}(\nu_i)$ .

For a more complicated perturbation and spectral response composed of multiple sinusoids, the synchronous 2D correlation spectrum,  $\Phi(\nu_1, \nu_2)$ , is defined in terms of the cospectra as

$$\Phi(\nu_1, \nu_2) = \frac{1}{\pi} \int_0^\infty \phi_\omega(\nu_1, \nu_2) d\omega, \quad (1.5)$$

and the asynchronous 2D correlation spectrum,  $\Psi(\nu_1, \nu_2)$ , is defined in terms of the quad-spectra as

$$\Psi(\nu_1, \nu_2) = \frac{1}{\pi} \int_0^\infty \psi_\omega(\nu_1, \nu_2) d\omega. \quad (1.6)$$

Noda further generalized this analysis to arbitrary functional forms of the perturbation,  $t$ , and spectral response,  $\tilde{y}(\nu_1, t) \equiv \tilde{y}_1(t)$ , by first decomposing the signal into sinusoids and representing it in the frequency domain with the application of the Fourier transform with respect to the perturbation,  $t$ :

$$\tilde{Y}(\nu_1, \omega) = \int_{-\infty}^{\infty} \tilde{y}(\nu_1, t) e^{-i\omega t} dt. \quad (1.7)$$

In this case of an arbitrary perturbation defined on the interval between  $T_{\min}$  and  $T_{\max}$ , the 2D correlation spectrum is given by

$$\Phi(\nu_1, \nu_2) + i\Psi(\nu_1, \nu_2) = \frac{1}{\pi(T_{\max} - T_{\min})} \int_0^{\infty} \tilde{Y}_1(\omega) \cdot \tilde{Y}_2^*(\omega) d\omega. \quad (1.8)$$

To circumvent the complexity and required computing power for the Fourier transform calculations, Noda used the well-known Wiener-Khintchine theorem to derive the 2D synchronous spectrum from the cross-correlation function<sup>4, 7</sup> such that

$$\Phi(\nu_1, \nu_2) = \frac{1}{T_{\max} - T_{\min}} \int_{T_{\min}}^{T_{\max}} \tilde{y}(\nu_1, t) \cdot \tilde{y}(\nu_2, t) dt. \quad (1.9)$$

For a rigorous mathematical development, see Appendix 2.1 of reference<sup>5</sup>.

The asynchronous spectrum can be computed from the cross-correlation of the dynamic spectrum,  $\tilde{y}(\nu, t)$ , and its orthogonal spectrum,  $\tilde{z}(\nu, t)$ :

$$\Psi(\nu_1, \nu_2) = \frac{1}{T_{\max} - T_{\min}} \int_{T_{\min}}^{T_{\max}} \tilde{y}(\nu_1, t) \cdot \tilde{z}(\nu_2, t) dt. \quad (1.10)$$

To calculate the orthogonal spectrum, Noda utilized the Hilbert transform, which has the effect of applying a phase shift of  $\pi/2$  to each Fourier component of the dynamic spectrum, such that

$$\tilde{z}(\nu, t) \equiv \frac{1}{\pi} \int_{P\nu-\infty}^{\infty} \frac{\tilde{y}(\nu, t')}{t'-t} dt', \quad (1.11)$$

where  $\int_{P\nu}$  represents the implementation of the Cauchy principal value such that the singularity at  $t = t'$  is excluded from the integration. Hilbert transform pairs, here  $\tilde{y}(\nu, t)$

and  $\tilde{z}(\nu, t)$ , are orthogonal. Hence, through the application of a phase shift in Fourier space, the asynchronous spectrum allows for the examination of temporal separation between intensity changes in real space.

To examine some of the advantages of 2D correlation analysis, let us consider a simulated dataset,  $I(\nu, t)$  for  $T_{\min} \leq t \leq T_{\max}$ , containing three peaks (Figure 1.1a). The first peak increases quadratically in response to the perturbation, the second peak remains unchanged, and the third peak decreases linearly in the perturbation variable (Figure 1.1b).

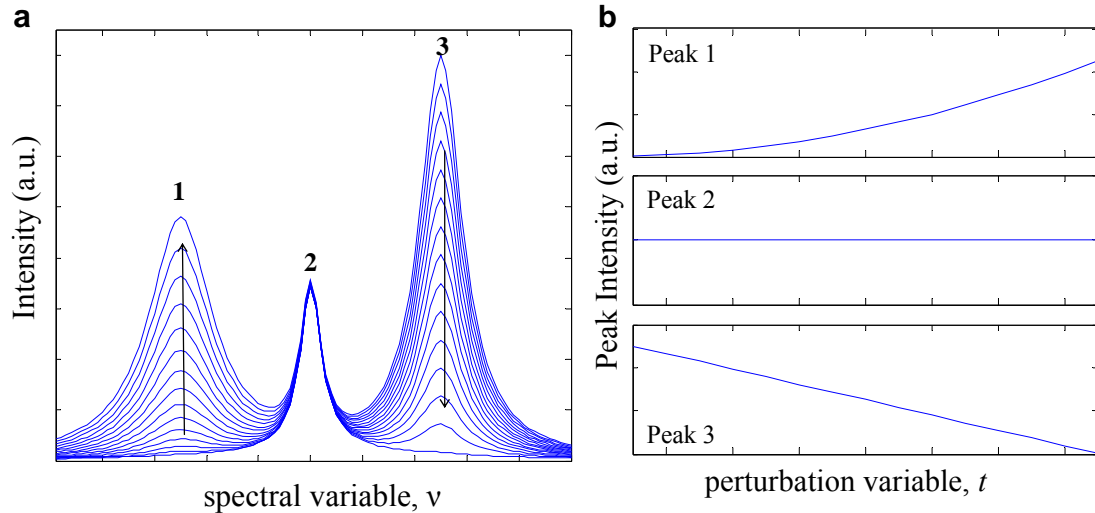


**Figure 1.1** **a)** Simulated dataset. **b)** Evolution of peak intensities with perturbation of peaks in **a**.

The synchronous spectrum,  $\Phi(\nu_1, \nu_2)$ , is symmetric with respect to the diagonal ( $\nu_1 = \nu_2$ ) and reveals simultaneous or coincident changes at two different spectral variables as the result of the perturbation. Consequently, in Figure 1.2, one observes two autopeaks along the diagonal corresponding to the intensity changes of peaks 1 and 3. The autocorrelation intensity along the diagonal is always positive and represents the total amplitude of the intensity variation in response to the perturbation.

In the off-diagonal position corresponding to peaks 1 and 3, one observes cross peaks indicating that the change in these two peaks occurs simultaneously. The negative sign of these features is consistent with the increase of peak 1 and a simultaneous decrease in peak 3 in response to the perturbation. The cross peaks are positive when intensity changes occur in the same direction.

The synchronous plot contains no features corresponding to peak 2 since there is no change in its intensity in response to the perturbation. This aspect of the 2D correlation analysis allows one to filter out static features, making it suitable for selective detection of compounds, as is discussed in Chapter 2.

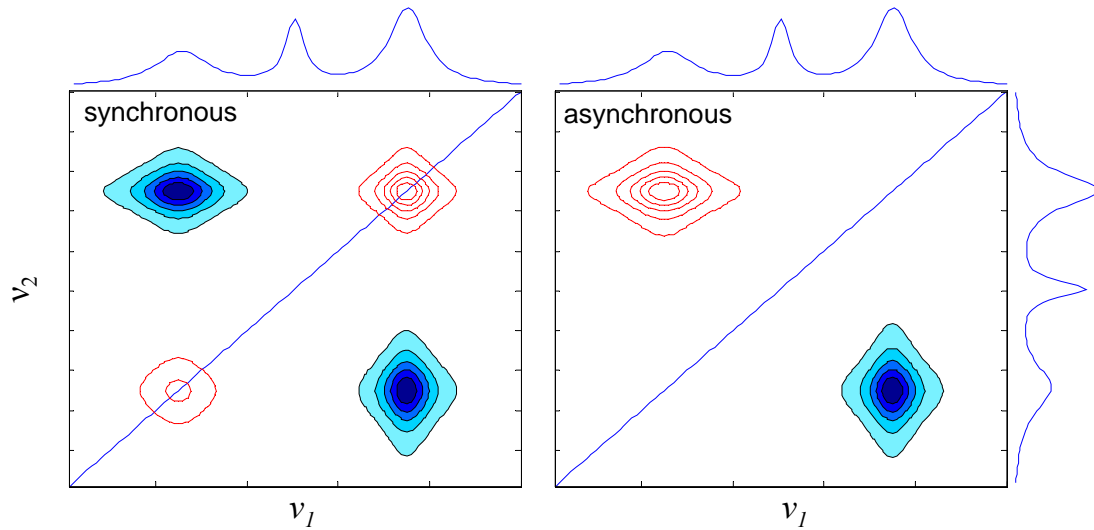


**Figure 1.2** Synchronous (left) and asynchronous (right) spectra corresponding to simulated dataset in Figure 1.1. Shaded-in contours are negative, while non-shaded contours are positive. The average 1D spectra are plotted on the sides.

The 2D asynchronous spectrum,  $\Psi(v_1, v_2)$ , reveals the extent to which intensity changes at two spectral variables lead or lag one another during a perturbation. By its nature, it is antisymmetric and contains no autopeaks. In Figure 1.2, one observes features corresponding to peaks 1 and 3, indicating that there is temporal separation between these intensity changes.

The sign of the cross peaks reveals the sequential order of peak variations based on Noda's rules.<sup>3, 5</sup> Since the 2D asynchronous spectrum is anti-symmetric, it suffices to consider the region where  $\nu_1 > \nu_2$  (below the diagonal). Interpretation of the sign of a cross peak at  $(\nu_1, \nu_2)$  when  $\nu_1 > \nu_2$  in the asynchronous spectrum,  $\Psi(\nu_1, \nu_2)$ , depends on the sign of the intensity of the synchronous spectrum at  $(\nu_1, \nu_2)$ : if  $\Phi(\nu_1, \nu_2)$  is positive, then a positive asynchronous cross peak below the diagonal indicates that the response at  $\nu_1$  precedes that at  $\nu_2$ ; if  $\Phi(\nu_1, \nu_2)$  is negative, then that positive cross peak indicates that the response at  $\nu_1$  lags that at  $\nu_2$  (Table 1.1). In the present case, negative features corresponding to peaks 1 and 3 are observed both in the synchronous and asynchronous plots. Therefore, the change in peak 3 precedes that in peak 1. This temporal separation can be interpreted in a more practical manner as a difference in half intensity and half time of peak evolution.<sup>8</sup> From Figure 1.1b, it is apparent that peak 3 has greater intensity half-way through the perturbation (half intensity) and achieves half of the total intensity change earlier along the perturbation (half time) than peak 1, resulting in changes in peak 3 preceding those in peak 1.

**Table 1.1 Noda's Rules for sequential order when  $\nu_1 > \nu_2$ .**

$\Phi(\nu_1, \nu_2)$	$\Psi(\nu_1, \nu_2)$	Interpretation
+	+	$\nu_1$ precedes $\nu_2$
+	-	$\nu_1$ lags $\nu_2$
-	+	$\nu_1$ lags $\nu_2$
-	-	$\nu_1$ precedes $\nu_2$

In reality, the analysis of 2D spectra can be quite complex, especially in the case of the asynchronous spectrum. The introduction of noise can often lead to artificial peaks in the asynchronous spectrum.<sup>9, 10</sup> Additionally, variations in the peaks themselves (i.e., position, shape, height, and width) can lead to patterns with multiple interpretations.<sup>11-13</sup>

These peak effects have been studied through simulated spectra revealing patterns in both the synchronous and asynchronous spectra that correspond to some commonly observed behaviors.<sup>5, 11, 12</sup> For example, a “four-leaf clover” pattern in the synchronous spectrum can indicate either two overlapping peaks whose intensities vary in opposite directions or a peak that steadily shifts in position. The explanation for the pattern can be discerned by evaluating the asynchronous spectrum. A four-leaf clover can be assigned to overlapping peaks exhibiting opposite changes in intensity if the asynchronous pattern contains either no peaks (if changes are simultaneous) or one pair of complimentary peaks (above and below the diagonal if the intensity changes are temporally separated). On the other hand, a four-leaf clover in the synchronous spectrum can be assigned to a peak shifting in position if the asynchronous spectrum contains a distinct “butterfly” pattern. The importance of such patterns is apparent in Chapter 4.

Two-dimensional correlation analysis has gathered momentum due to the numerous advantages it provides. It allows for the simplification of complex spectra containing overlapped peaks. Additionally, one obtains enhancement in spectral resolution due to the spreading of data over a second dimension. It is possible to establish unambiguous assignments through correlation of bands, as well as determine specific sequential order of intensity changes. Furthermore, Noda’s efforts have resulted in nearly universal applicability of the technique, which is now regularly applied across different disciplines to examine ‘spectral’ responses to a variety of perturbation types. While the application of 2D correlation spectroscopy is still predominantly to optical spectra, approximately 1 in 6 published experiments have used other analytical probes,<sup>6</sup> including x-rays, as is the case in Chapters 3 through 5. Although temperature, the most commonly employed perturba-

tion, is used in the following chapters, composition, chemical reactions, and physical processes can also be employed.<sup>6</sup>

Furthermore, the abundant application of 2D correlation spectroscopy has allowed for its further evolution. A summary of this was formulated by Noda in 2008;<sup>6</sup> developments of note are moving window and hetero-correlation analyses. Moving window 2D correlation analysis (MW2D) is designed to probe complicated spectral responses by analyzing smaller subsets of data that are shifted incrementally along the perturbation axis to cover the full set. This analysis allows one to gauge the spectral response at specific points along the perturbation variable rather than the overall response to the full range. Further detail and an example of this technique are presented in Chapter 4. Hetero-correlation analysis is applied to two independent measurements of perturbation-induced dynamic spectra. Most frequently, hetero-spectral correlation is applied to a sample's response to a perturbation probed by two different spectral probes. An example of SAXS-WAXS hetero-spectral correlation analysis is presented in Chapter 4.

## 1.2 EXPLOSIVES DETECTION

Improvised Explosive Devices (IEDs) continue to be the most effective weapon employed against coalition forces in Iraq and Afghanistan. The Joint Improvised Explosive Device Defeat Organization (JIEDDO) is currently implementing over 300 initiatives to tackle this problem.<sup>14</sup> In this era of persistent conflict and global terrorism, the ability to detect explosives in both war zones and high-security installations can save human lives.

The vast challenge in the detection of explosives is in part due to their nature (e.g., small quantities and low vapor pressure) and in part due to concealment in the field and

interference from contaminants. Common explosives are known to have very low vapor pressures,<sup>15, 16</sup> making vapor-based detection, such as infrared spectroscopy, particularly challenging. Furthermore, military grade explosives are often found in solid solutions, such as RDX in plastic composition C4 (C4) explosive, which further limits their vapor pressures.<sup>17</sup> Detection of solid-state explosives is usually based on identifying trace amounts which requires extreme sensitivity. To compound these intrinsic challenges, explosives are often found concealed in a large variety of dynamic environments.

In a laboratory, when they have been separated from any contaminants, explosives can be detected by many reliable techniques, such as mass spectrometry, ion mobility spectrometry, and fluorescence quenching of polymers.<sup>15, 16</sup> However, few of these techniques can be applied at an airport to screen passengers and even fewer still can be implemented in the desert environments of Iraq to detect hidden IEDs.

Furthermore, in the case of IEDs, it is desirable to accomplish detection at a distance, in order to ensure human safety. Standoff detection systems are being developed based on photodissociation laser-induced fluorescence,<sup>18-20</sup> laser-induced breakdown spectroscopy,<sup>21</sup> terahertz time domain spectroscopy,<sup>22</sup> and Raman spectroscopy.<sup>23-29</sup> In most of these cases, the focus is on improvement of hardware. While this approach has resulted in good progress toward effective long standoff detection, further advancement can be achieved through data analysis algorithms, such as spectral pattern recognition and chemometric-based techniques.<sup>15, 30</sup>

Two-dimensional correlation analysis is well suited for detection applications because of its simplification of complex spectra and enhancement of spectral resolution. Additionally, the unstable nature of explosive compounds lends them to respond strongly

to a thermal perturbation, especially when compared to contaminants, such as humic substances. The possibility of using 2D correlation analysis in conjunction with a thermal modulation is examined in Chapter 2.

### 1.3 SEMI-CRYSTALLINE MATERIALS

More than two-thirds of the annual commercial production of synthetic polymers is comprised of semi-crystalline materials. The many advantages of these materials, such as light weight, flexibility, chemical resistance and toughness, are the reason they are so abundant in today's society, finding applications in the medical market, electronics, construction, textiles and packaging.<sup>31</sup> Specifically, polyethylene (PE) and polypropylene (PP) dominate the semi-crystalline polymer market with demand for PE and PP in North America just below 40 billion pounds and 21 billion pounds, respectively, in 2006.<sup>32</sup> Demand is expected to grow because low cost and expanding versatility make these polymers prime candidates to substitute for less desirable materials. For example, PE can be used to replace steel in automotive fuel tanks and PP can be used to replace aluminum honeycombs as an impact energy absorber.<sup>33</sup>

PP and PE, like other semi-crystalline materials, spontaneously form a nanocomposite structure that confers strength from its crystalline domains and toughness from the non-crystalline material in between. As such, ultimate physical properties of these materials are directly related to their morphology (the distribution of crystalline and non-crystalline regions). The morphology is primarily a function of molecular characteristics (molecular weight, molecular architecture, etc.) and processing conditions (thermal and flow history).

Fabrication processes with PP and PE include injection molding, film blowing, and fiber spinning, and involve non-isothermal conditions, as well as very strong and complex flow fields (shear, elongational, or mixed). Different processing conditions can alter the spatial organization and alignment of the crystallites, affecting properties such as strength, hardness, and surface texture. For example, the elastic modulus of highly-oriented PE fibers is 100 times that of quiescently crystallized PE.<sup>34</sup>

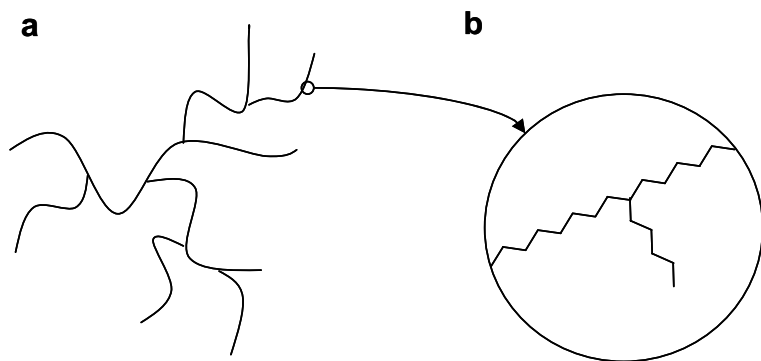


**Figure 1.3** Schematic diagram of a polymer containing both long-chain branches evident in **a** and short-chain branches evident in **b**.

In addition, a polymer's molecular characteristics can affect its response to processing conditions. Long-chain branches (LCB) alter melt dynamics affecting the melt's response to a flow field and hence its subsequent morphology. Short-chain branches (SCB) can act as crystal defects decreasing melting temperature and crystallinity.<sup>35</sup> Polymers containing SCB and LCB (Figure 1.3) are of particular interest because of their rich material properties and are examined in Chapter 3. With advances in synthesis, it is now possible to create varying branched polymers on the commercial scale. Low Density PE (LDPE), an LCB and SCB material, and Linear Low Density PE (LLPDE), an SCB material, comprise over half of the current PE market and are used to make films.<sup>36</sup> Therefore, it is of imperative technological relevance to understand the crystallization

process of such linear and branched semi-crystalline materials in order to control their physical properties. Crystallization of SCB materials under flow is examined in Chapter 5. By understanding the behavior of these materials, we can greatly expand the property envelope of semi-crystalline materials, particularly polyolefins.

Polymer crystallization studies employ many probes in order to gain insight into the hierarchy of structures that are formed by semi-crystalline materials. Wide angle x-ray scattering (WAXS) provides insight into the crystal unit cell (i.e., type, dimensions, coherence) that is on the order of angstroms. Small angle x-ray scattering (SAXS) provides insight on the organization of these unit cells into nanoscopic ( $\sim 10 - 100$  nm) structures and distribution of these nanoscopic structures in the non-crystalline regions (e.g., chain-folded lamellar stacks which are on the order of nanometers). Small angle light scattering provides information on the microscopic structure organization, such as spherulites that are on the order of microns. SAXS and WAXS, which are utilized in Chapters 3 through 5, rely heavily upon the analysis of a series of one-dimensional (1D) scattering curves (intensity versus scattering vector). Scattering curves are usually collected as a function of temperature during ramp cooling/heating (crystallization/melting) or time in the case of isothermal crystallization. These experiments result in large datasets with transient behaviors that are well suited for 2D correlation analysis. Its sensitivity to changes in spectral features makes 2D correlation analysis a powerful tool in evaluating morphology development in semi-crystalline systems, as illustrated in Chapter 4 for quiescent crystallization.

## 1.4 REFERENCES

1. Noda, I., Two-Dimensional Infrared (2D IR) Spectroscopy. *Bulletin of the American Physical Society* **1986**, 31, 520.
2. Noda, I., Two-Dimensional Infrared-Spectroscopy. *Journal of the American Chemical Society* **1989**, 111, (21), 8116-8118.
3. Noda, I., 2-Dimensional Infrared (2d Ir) Spectroscopy - Theory and Applications. *Applied Spectroscopy* **1990**, 44, (4), 550-561.
4. Noda, I., Generalized Two-Dimensional Correlation Method Applicable to Infrared, Raman, and Other Types of Spectroscopy. *Applied Spectroscopy* **1993**, 47, (9), 1329-1336.
5. Noda, I.; Ozaki, Y., *Two-Dimensional Correlation Spectroscopy*. John Wiley & Sons Ltd.: West Sussex 2004.
6. Noda, I. In *Recent advancement in the field of two-dimensional correlation spectroscopy*, 2008; Elsevier Science Bv: 2008; pp 2-26.
7. Noda, I., Determination of Two-Dimensional Correlation Spectra Using the Hilbert Transform. *Applied Spectroscopy* **2000**, 54, (7), 994-999.
8. Jia, Q.; Wang, N. N.; Yu, Z. W., An Insight into Sequential Order in Two-Dimensional Correlation Spectroscopy. *Applied Spectroscopy* **2009**, 63, (3), 344-353.
9. Czarnecki, M. A., Interpretation of two-dimensional correlation spectra: Science or art? *Applied Spectroscopy* **1998**, 52, (12), 1583-1590.
10. Hu, Y.; Li, B. Y.; Sato, H.; Noda, I.; Ozaki, Y., Noise perturbation in functional principal component analysis filtering for two-dimensional correlation spectroscopy: Its

theory and application to infrared spectra of a poly(3-hydroxybutyrate) thin film. *Journal of Physical Chemistry A* **2006**, 110, (39), 11279-11290.

11. McNavage, W.; Dai, H. L., Two-dimensional cross-spectral correlation analysis and its application to time-resolved Fourier transform emission spectra of transient radicals. *Journal of Chemical Physics* **2005**, 123, (18), 12.

12. Gericke, A.; Gadaleta, S. J.; Brauner, J. W.; Mendelsohn, R., Characterization of biological samples by two-dimensional infrared spectroscopy: Simulation of frequency, bandwidth, and intensity changes. *Biospectroscopy* **1996**, 2, (6), 341-351.

13. Morita, S.; Miura, Y. F.; Sugi, M.; Ozaki, Y., New correlation indices invariant to band shifts in generalized two-dimensional correlation infrared spectroscopy. *Chemical Physics Letters* **2005**, 402, (1-3), 251-257.

14. Joint Improvised Explosive Device Defeat Organization. [www.jieddo.dod.mil](http://www.jieddo.dod.mil)

15. Steinfeld, J. I.; Wormhoudt, J., Explosives detection: A challenge for physical chemistry. *Annual Review of Physical Chemistry* **1998**, 49, 203-232.

16. Moore, D. S., Instrumentation for trace detection of high explosives. *Review of Scientific Instruments* **2004**, 75, (8), 2499-2512.

17. *Proceedings of the First International Symposium on Explosive Detection Technology* U.S. Department of Transportation: Atlantic City, NJ, May 1992, p 988.

18. Arusi-Parpar, T.; Heflinger, D.; Lavi, R., Photodissociation followed by laser-induced fluorescence at atmospheric pressure and 24 degrees C: a unique scheme for remote detection of explosives. *Applied Optics* **2001**, 40, (36), 6677-6681.

19. Wynn, C. M.; Palmacci, S.; Kunz, R. R.; Clow, K.; Rothschild, M. In *Detection of condensed-phase explosives via laser-induced vaporization, photodissociation, and resonant excitation*, 2008; Optical Soc Amer: 2008; pp 5767-5776.
20. Wynn, C. M.; Palmacci, S.; Kunz, R. R.; Rothschild, M., A Novel Method for Remotely Detecting Trace Explosives. *Lincoln Laboratory Journal* **2008**, 17, (2), 27-39.
21. Czarnecki, M. A., Two-dimensional correlation spectroscopy: Effect of normalization of the dynamic spectra. *Applied Spectroscopy* **1999**, 53, (11), 1392-1397.
22. Hua, Z.; Redo, A.; Yunqing, C.; Xi-Cheng, Z., THz wave standoff detection of explosive materials. *Proceedings of the SPIE - The International Society for Optical Engineering* **2006**, 6212, 62120L-1-62120L-62120L-8.
23. Carter, J. C.; Angel, S. M.; Lawrence-Snyder, M.; Scaffidi, J.; Whipple, R. E.; Reynolds, J. G., Standoff Detection of High Explosive Materials at 50 Meters in Ambient Light Conditions Using a Small Raman Instrument. *Applied Spectroscopy* **2005**, 59, (6), 769-775.
24. Carter, J. C.; Scaffidi, J.; Burnett, S.; Vasser, B.; Sharma, S. K.; Angel, S. M., Standoff Raman detection using dispersive and tunable filter based systems. *Spectrochimica Acta Part A* **2005**, 61, 2288-2298.
25. Comanescu, G.; Manka, C. K.; Grun, J.; Nikitin, S.; Zabetakis, D., Identification of explosives with two-dimensional ultraviolet resonance Raman spectroscopy. *Applied Spectroscopy* **2008**, 62, (8), 833-839.
26. Eckenrode, B. A.; Bartick, E. G.; Harvey, S. D.; Vucelick, M. E.; Wright, B. W.; Huff, R. A., Portable Raman Spectroscopy Systems for Field Analysis. *Forensic Science Communications* **2001**, 3, (4).

27. Grasso, R. J.; Russo, L. P.; Barrett, J. L.; Odhner, J. E.; Egbert, P. I., An accurate modeling, simulation, and analysis tool for predicting and estimating Raman LIDAR system performance. *Proceedings of the SPIE - The International Society for Optical Engineering* **2007**, 6681, (1), 66810D-1-66810D-66810D-18.

28. Hayward, I. P.; Kirkbride, T. E.; Batchelder, D. N.; Lacey, R. J., Use of a Fiber Optic Probe for the Detection and Identification of Explosive Materials by Raman-Spectroscopy. *Journal of Forensic Sciences* **1995**, 40, (5), 883-884.

29. Sharma, S. P.; Lahiri, S. C., Absorption spectroscopic and FTIR studies on EDA complexes between TNT (2,4,6-trinitrotoluene) with amines in DMSO and determination of the vertical electron affinity of TNT. *Spectrochimica Acta Part a-Molecular and Biomolecular Spectroscopy* **2008**, 70, (1), 144-153.

30. Brown, S. D.; Barker, T. Q.; Larivee, R. J.; Monfre, S. L.; Wilk, H. R., Chemometrics. *Analytical Chemistry* **1988**, 60, (12), R252-R273.

31. *Modern Plastics World Encyclopedia*. The McGraw-Hill Companies, Inc.: New York, NY, 2000.

32. Plastics News. [www.plasticsnews.com](http://www.plasticsnews.com)

33. *Modern Plastics Encyclopedia*. The McGraw-Hill Companies, Inc: New York, NY, 1999.

34. Ehrenstein, G. W., *Polymeric Materials: Structure, Properties, Applications*. Hanover Gardner Publications, Inc.: Cincinnati, Ohio, 2001.

35. Bustos, F.; Cassagnau, P.; Fulchiron, R., Effect of molecular architecture on quiescent and shear-induced crystallization of polyethylene. *Journal of Polymer Science Part B - Polymer Physics* **2006**, 44, (11), 1597-1607.

36. Lal, S.; Grady, N. K.; Kundu, J.; Levin, C. S.; Lassiter, J. B.; Halas, N. J., Tailoring plasmonic substrates for surface enhanced spectroscopies. *Chemical Society Reviews* **2008**, 37, 898-911.

## Chapter 2

### Two-Dimensional Correlation Analysis for Explosive Detection

<b>2.1</b>	<b>INTRODUCTION.....</b>	<b>II-2</b>
<b>2.2</b>	<b>EXPERIMENTAL METHODS .....</b>	<b>II-6</b>
<b>2.2.1</b>	<b>Materials .....</b>	<b>II-6</b>
<b>2.2.2</b>	<b>Raman Microspectroscopy.....</b>	<b>II-8</b>
2.2.2.1	Contamination Studies .....	II-8
<b>2.2.3</b>	<b>Long Standoff Raman Spectroscopy.....</b>	<b>II-9</b>
<b>2.2.4</b>	<b>Computation.....</b>	<b>II-10</b>
<b>2.3</b>	<b>RESULTS .....</b>	<b>II-14</b>
<b>2.3.1</b>	<b>Raman Microspectroscopy of Pure Compounds .....</b>	<b>II-14</b>
2.3.1.1	One-Dimensional Raman Spectra.....	II-14
2.3.1.2	Clean Two-Dimensional Correlation Spectra .....	II-15
2.3.1.3	Effect of Background in Two-Dimensional Correlation Spectra.....	II-19
2.3.1.4	Data Pretreatment.....	II-22
2.3.1.5	Reference Spectrum .....	II-23
<b>2.3.2</b>	<b>Raman Microspectroscopy: Contamination Studies .....</b>	<b>II-24</b>
2.3.2.1	Traditional: RDX and Saliva on Sand .....	II-25
2.3.2.2	Multi-Point: RDX, Soot, Sand, Polybutadiene .....	II-27
2.3.2.3	Multi-Sample: PETN, Soot, Polybutadiene .....	II-29
<b>2.3.3</b>	<b>Long Standoff Detection.....</b>	<b>II-32</b>
<b>2.4</b>	<b>DISCUSSION .....</b>	<b>II-34</b>
<b>2.4.1</b>	<b>Application of 2D Correlation Analysis.....</b>	<b>II-34</b>
2.4.1.1	Synchronous Spectra.....	II-36
2.4.1.2	Asynchronous Spectra.....	II-37
2.4.1.3	Data Pretreatments .....	II-39
<b>2.4.2</b>	<b>Fluorescence .....</b>	<b>II-40</b>
<b>2.4.3</b>	<b>Raman Signal Enhancement.....</b>	<b>II-41</b>
<b>2.5</b>	<b>CONCLUSION .....</b>	<b>II-42</b>
<b>2.6</b>	<b>ACKNOWLEDGEMENTS .....</b>	<b>II-43</b>
<b>2.7</b>	<b>REFERENCES.....</b>	<b>II-45</b>

## 2.1 INTRODUCTION

Improvised Explosive Devices (IEDs) are currently the number one killer of both troops and civilians in Iraq and Afghanistan.<sup>1</sup> Furthermore, world-wide IED events outside Iraq and Afghanistan number over 300 per month.<sup>1</sup> The ability to detect explosives prior to detonation would save lives; hence many laboratory techniques have been explored for explosive detection and classification (see reviews by Moore, 2004<sup>2</sup> or Steinfeld and Wormhoudt, 1998<sup>3</sup>). With the exception of the human eye and canine units, the most successful detection schemes are based on ion-mobility spectrometry, gas-chromatography/mass spectrometry, and fluorescence quenching of polymers. These all share the serious drawback of proximal sampling, which is extremely hazardous. An ideal system should quickly and accurately identify the presence of a variety of explosive traces in different environments with dynamic backgrounds at a safe standoff distance.

A possible solution to this complex problem is an optical-based scheme.<sup>2,3</sup> Attempts have been made to utilize infrared (IR) spectroscopy,<sup>4</sup> photodissociation laser-induced fluorescence (PD-LIF),<sup>5-7</sup> laser-induced breakdown spectroscopy (LIBS),<sup>8</sup> and terahertz time domain spectroscopy (THz-TDS).<sup>9</sup> While well-suited for standoff detection, not all of these techniques meet the additional challenges of low vapor pressure of explosives and small sample size, as well as both optical and chemical interference – while requiring no sample preparation. However, even those techniques that are able to meet the challenges presented above suffer other serious drawbacks (for example, safety of implementation).<sup>2-4, 10-12</sup> This study focuses on a detection scheme based on long standoff Raman spectroscopy.<sup>13-19</sup>

Raman spectra provide direct information about molecular structure that can be used for identification. It is a non-invasive technique capable of analyzing both organic and inorganic compounds in any state (solid, liquid, gas), in most environments and without specific sample preparation requirements. The Raman Effect is the result of inelastic scattering of light from molecules that is shifted in frequency due to specific molecular vibrations. When an incident photon induces a dipole moment within a molecule, the result is a transfer of energy. If the molecule absorbs energy, the result is a photon scattered with less energy than the incident photon, or Stokes scattering. If, on the other hand, the molecule loses energy, the scattered photon will have greater energy and will be part of Anti-Stokes scattering. Stokes lines have greater intensity than Anti-Stokes lines at room temperature and are the focus of the current work.

The unique Raman signatures of many explosive materials are well known.<sup>15, 20-29</sup> The challenge is in obtaining these spectra from a distance of a few to hundreds of meters. Standoff systems often utilize a powerful, pulsed laser as the excitation source and a large optic to collect scattered photons that are sent to a dispersive spectrograph. Recent advances in optical-based standoff detection schemes have stemmed primarily from developments in the instrumentation of the detection system.<sup>7, 11, 13, 14, 17-19, 30</sup> However, long standoff detection of trace explosives presents a number of difficult challenges associated with rapid detection of a weak signal in a noisy and dynamic environment. Additional attempts have been made to enhance detection of explosives by exploiting their unique predisposition to decompose during heating.<sup>21, 31-36</sup> Another possible approach to increase the success of long standoff detection (based on any scheme) is through the analysis of spectra after collection, although this has received little attention.<sup>12, 37, 38</sup>

The system envisioned by Dr. Ravi Verma and Dr. Andrew Pipino at Tanner Research Inc. (Monrovia, CA) combines these three factors (hardware, material characteristics, and data analysis) to meet the challenges of long standoff Raman detection. Instrument design and assembly have been conducted by Dr. Andrew Pipino and includes a gated mechanism to minimize the amount of ambient light and luminescence that reaches the detector.<sup>13, 30, 39</sup> Once complete, the system would exploit the instability of explosives during incremental heating, which can be induced from a long standoff distance using a carbon dioxide (CO<sub>2</sub>) laser. The enhancement in detection achieved by employing two-dimensional correlation spectroscopy is examined as part of this thesis. It was hypothesized that peaks characteristic of specific explosives would decrease as the explosive underwent thermal degradation while peaks corresponding to the decomposition products would increase. Furthermore, many of the potential interfering compounds in the operating environment have sufficient thermal stability that they would not be affected by the degree of heating used to induce thermal decomposition of energetic materials. The compounds that change due to heating would be selectively retained in the two-dimensional correlation spectra and the unchanged background would not contribute.

Two-dimensional (2D) correlation spectroscopy is a robust and versatile technique used to study molecular behavior as a function of a perturbation variable (e.g., temperature). Since its generalization by Noda,<sup>40</sup> the analysis has been applied to a variety of measurements across different fields.<sup>41-49</sup> Specifically, this analysis allows for separation of spectral features corresponding to explosives both from a noisy background and from any contaminants based on their rate of response to heating. Advantages of 2D correlation spectroscopy pertinent to detection include (1) simplification of complex

spectra by separation of overlapped peaks, (2) enhancement of spectral resolution and enhancement of signal to noise ratio (SNR) through the spreading of peaks over a second dimension, and (3) probing specific sequential order of spectral intensity changes.<sup>50</sup> In the current application, 2D correlation analysis should allow for rapid discrimination between unstable explosive traces and more stable contaminants, as the nature of the 2D approach is to eliminate static spectral features.

In this work, the concept of thermal decomposition in conjunction with 2D correlation spectroscopy for the detection of trace explosives was initially examined using a Raman microscope and a heating stage. Further investigations evaluated the two aspects of the analysis that can be used to further enhance detection: data pre-treatment and selection of the reference spectrum.

Data-pretreatments, such as smoothing, averaging, or normalization, can greatly enhance spectral features. In long standoff detection, a noisy background poses a significant challenge. This background can negatively affect SNR of synchronous spectra and sometimes produce artificial peaks in the asynchronous spectra.<sup>51</sup> Proper background subtraction is unrealistic due to the time-sensitive nature of the desired detection scheme, so alternatives must be considered. The effect of background scattering can be minimized through the use of first<sup>52</sup> and second<sup>51</sup> derivatives of the spectra. Alternatively, spectral normalization can also be utilized to enhance spectral features. In many cases, normalization schemes have little effect on qualitative results of 2D correlation analysis.<sup>53, 54</sup> However, in some studies, implementation of a normalization scheme has resulted in artificial peaks, especially in the asynchronous spectrum.<sup>55-57</sup> Given that the pre-treatment is dependent on and applied to each individual one dimensional (1D) spectrum, the following

correlation analysis may result in a significantly different SNR of the 2D spectra.

Since the ultimate goal is to identify explosives while minimizing the probability of false negatives and false alarms, both derivatives and a variety of normalization techniques were examined for greatest enhancement of explosive features in the 2D synchronous plot while minimizing the appearance of artificial peaks.

An additional variable in the 2D analysis that can be adjusted for better results is the reference spectrum selected for calculating the dynamic spectra. The selection of this reference spectrum is rather arbitrary;<sup>50, 58</sup> a simple option is to use an individual spectrum from the dataset.<sup>47, 50, 58</sup> Most commonly, the time-averaged (i.e., perturbation-averaged) spectrum is used, resulting in mean-centered dynamic spectra being analyzed.<sup>40, 44, 59, 60</sup> Each of these options was tested for the current application to determine which provided the best enhancement of explosive spectral features in the 2D synchronous plot, similar to the normalization schemes.

While noise is considered the greatest challenge of standoff detection, the ability to identify explosives in the presence of contaminants is not trivial. Therefore, additional studies were conducted to test the detection scheme in the presence of common interfering compounds. Finally, identification of trace explosive based on fine-tuned 2D correlation spectroscopy was demonstrated using the long standoff system at Tanner Research.

## 2.2 EXPERIMENTAL METHODS

### 2.2.1 Materials

For Raman Microspectroscopy experiments, cyclotrimethylenetrinitramine (RDX), pentaerythritol tetranitrate (PETN), 1,3,5,7-tetranitro-1,3,5,7-tetrazocane (HMX),

and trinitrotoluene (TNT) were purchased from Cerilliant at concentrations of 1000  $\mu\text{g/mL}$  in acetonitrile (Figure 2.1). Neat residues of explosives were created by placing several drops of each solution onto glass slides and allowing the acetonitrile to evaporate under ambient conditions. For contamination studies, explosive solution was placed on glass slides in the presence of sand, saliva, urine, diesel soot and ester-terminated telechelic polybutadiene (PB; obtained from Materia) and allowed to dry.

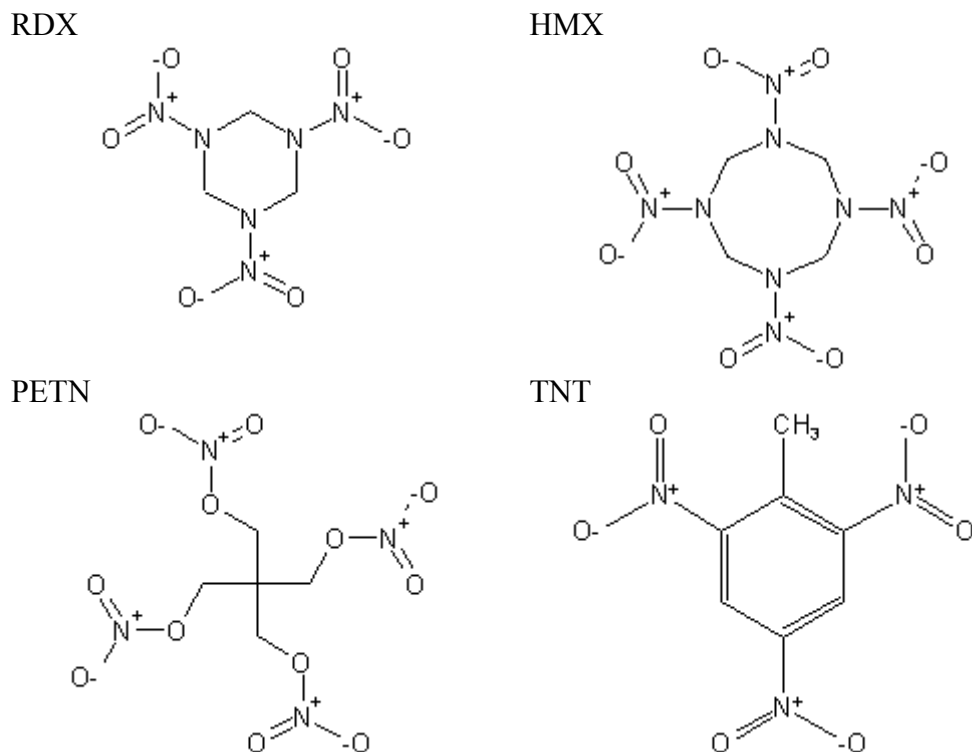


**Figure 2.1** Molecular structure of the four military grade explosives examined.

For long standoff Raman experiments, 8 wt % RDX in a dry silica matrix (the most common constituent of sand) was purchased as a Non-Explosive Security Training and Testing (NESTT) product from XM division of Van Aken International. Approximately 10 grams of material as received was placed in a Petri dish at an approximate angle of  $45^\circ$  to the excitation beam.

## 2.2.2 Raman Microspectroscopy

Raman Microspectroscopy studies were conducted using a Renishaw MicroRaman Spectrometer in Professor George Rossman's laboratory in Caltech's Geological and Planetary Sciences Division with a continuous excitation wavelength of 514 nm and a grating size of 1800 lines/mm. The maximum power output from the excitation laser was 25 mW resulting in approximately 5 mW at the sample with a spot size of 30  $\mu\text{m}$ . To simulate a thermal perturbation, a Linkam hot stage was used to heat samples at 10  $^{\circ}\text{C}/\text{min}$  while static spectra in the range of interest for each compound were acquired with acquisition times of 1.5 s. Maximum temperatures, which ranged from 150 to 200  $^{\circ}\text{C}$  were selected to achieve full conversion (i.e., disappearance of Raman signatures) of the explosive residues in order to obtain maximum features in the 2D correlation spectra, which measure the degree of change in a system. At the end of the heating ramp, 200 to 450 spectra were available for analysis.

### 2.2.2.1 Contamination Studies

Contamination studies proved difficult due to the small spot size of the Raman microscope excitation laser. Given the intrinsic heterogeneities in the sample and the 30  $\mu\text{m}$  irradiated spot size, it was unfeasible to probe a representative average in the beam. As an alternative, detection of explosives in the presence of contaminants was evaluated by examining both multiple points on the same sample and multiple individual samples.

In the first scheme ('multi-point' experiment), a sample containing RDX, diesel soot, sand, and polybutadiene deposited from toluene solution was placed on a glass slide in a Linkam hot stage. Five points on the sample were selected based on visual inspection

through the microscope in an effort to obtain spectra of each material on the slide. A total of eight spectra were collected for each point as a function of temperature from room temperature up to 200 °C at discrete intervals of 25 °C. Temperature changes were conducted at 30 °C/min. One of the five points was excluded from the analysis due to large fluorescence, likely due to contamination at that point on the slide. The remaining four spectra were summed for each temperature to obtain a total spectrum representative of the whole sample at a particular temperature.

In the second scheme ('multi-sample' experiment), temperature-dependent spectra for individual materials collected during different experiments were summed and analyzed. Specifically, spectra for PETN, diesel soot, and bulk PB were collected during temperature ramps as described in Section 2.2.2. This procedure neglects any interaction that could occur between materials upon heating. However, this consequence does not appear to affect identification of explosive residue, which can be based on the disappearance of the energetic compound.

### **2.2.3 Long Standoff Raman Spectroscopy**

Long standoff experiments were conducted by Dr. Andrew Pipino at Tanner Research, in Monrovia, California. The system, built by Dr. Pipino, utilized a frequency-doubled Nd:Yag laser (532 nm, 10 Hz) for sample excitation. A projection telescope was used to focus the excitation beam to a 2–3 mm spot on the sample approximately 9 m away. Excitation source power was approximately 0.1 watts at the sample. Data was collected using a Spectra Pro 2300i spectrometer (Princeton Instruments) set to a 50 ns gate delayed 107 ns from the trigger of the pulsed excitation source. This combination of gate

width and delay was experimentally optimized to maximize the scattering signal and exclude fluorescence based on the disparity in lifetimes between Raman scattering ( $10^{-13}$ – $10^{-11}$  s) and fluorescence ( $10^{-9}$ – $10^{-7}$  s).<sup>13, 39, 61</sup> Noise was further decreased through multi-spectra averaging: an average of 10 spectra each obtained by an additional 10-pulse detector average (1 spectrum every 10 s) was compared with single-pulse data and no averaging (1 spectrum every 0.1 s). Thermal modulation was accomplished with a carbon dioxide (CO<sub>2</sub>, 10.6 μm) laser whose output was absorbed by the sand substrate. The laser was controlled by a transistor-transistor-logic (TTL) oscillator with a 50% duty cycle and a frequency of 0.1 Hz. CO<sub>2</sub> laser power was approximately 2 watts at the sample.

#### 2.2.4 Computation

Two-dimensional (2D) correlation spectra were calculated using Noda's generalized method<sup>40, 62</sup> from a discrete set of spectra measured at  $m$  equally spaced points during a thermal perturbation:

$$y_i(v) = y(v, T_i) \quad i = 1, 2, 3, \dots, m. \quad (2.1)$$

A variety of data pre-treatments and normalizations (Table 2.1) were tested using a dataset that was affected by noise and light fluorescence (a set of PETN spectra), two of the challenges faced in the operational environment. Derivatives can be applied to highlight rapid changes in the system and allow for the elimination of a dynamic baseline offset.<sup>51, 52</sup> Mean normalization has the effect of assigning an equal distribution of variances to the data, resulting in spectra with equal areas.<sup>59, 63</sup> Modified mean normalization (MMN) accounts for differences in peak area and half width by approximating bands as Lorentzian peaks in order to de-convolute overlapping features.<sup>64</sup> Principal component

analysis (PCA) is a data-reduction technique that can be used to obtain a vector that accounts for the greatest variation in the dataset containing all spectral points called the first principal component,  $PC_1$ . This first principal component is an  $m$ -dimensional column vector ( $PC_1 = [pc_{11}, pc_{12}, \dots, pc_{1m}]^T$ ) with elements composed of linear combinations of the original spectra:  $pc_{1i} = a_{11}y_{i1} + a_{12}y_{i2} + \dots + a_{1n}y_{in}$ , where  $y_{ij}$  is the intensity at the  $j^{\text{th}}$  spectral variable in the  $i^{\text{th}}$  spectrum containing  $n$  total points and the loadings,  $a$ , represent the weights of each original spectral intensity in the calculation of the first principal component.<sup>65</sup> All of these approaches normalize each spectrum by a constant that represents the overall intensity in that spectrum. The simplest means of achieving this is through

**Table 2.1 Summary of pre-treatments and normalizations tested on a noisy PETN dataset for best 1D and 2D synchronous performance parameter.**

pre-treatment/normalization	$y_i(\nu)$
1 <sup>st</sup> derivative with respect to Raman shift	$\frac{\partial y_i}{\partial \nu}$
1 <sup>st</sup> derivative with respect to the perturbation variable <sup>52</sup>	$\frac{\partial y_i}{\partial T_i}$
2 <sup>nd</sup> derivative with respect to Raman shift <sup>51</sup>	$\frac{\partial^2 y_i}{\partial \nu^2}$
2 <sup>nd</sup> derivative with respect to the perturbation variable <sup>51</sup>	$\frac{\partial^2 y_i}{\partial T_i^2}$
Mean normalization <sup>59, 63</sup>	$\frac{y_i}{y_{i,mean}}$ , where $y_{i,mean} = \frac{1}{(\nu_{\text{max}} - \nu_{\text{min}})} \int_{\nu_{\text{min}}}^{\nu_{\text{max}}} y_i(\nu) d\nu$
Modified mean normalization (MMN) <sup>64</sup>	$\frac{y_i}{C_i}$ , where $C_i = \frac{y_{i,mean}^2}{y_{i,\text{max}}}$
Principal component normalization <sup>65</sup>	$\frac{y_i}{pc_{1i}}$ , where $pc_{1i}$ is the $i^{\text{th}}$ loading of the first principal component
Peak value normalization <sup>66</sup>	$\frac{y_i}{y_i(\nu = 1290)}$ , where $1290 \text{ cm}^{-1}$ is the position of the peak of interest for PETN

normalization by a specific peak value of interest.<sup>66</sup> The effectiveness of each treatment was evaluated based on the performance parameter (eq 2.2) of the 1D dynamic and 2D synchronous spectra, as well as a qualitative assessment.

To determine the effectiveness of signal detection, a performance parameter,  $P$ , is defined as the ratio of the variance of the signal to the variance of the background:

$$P = \frac{\sigma_{signal}^2}{\sigma_{bkgr}^2}. \quad (2.2)$$

For each material, well-defined 1D Raman spectra were used to select areas of the background that did not contain any Raman lines. The signal variance was defined for the primary Raman peak at  $877 \text{ cm}^{-1}$  for RDX,  $844 \text{ cm}^{-1}$  for HMX, and  $1290 \text{ cm}^{-1}$  for PETN (see Section 2.3.1.1). The performance parameter was calculated and averaged for 1D dynamic spectra following pretreatment. Comparisons were made with  $P$  values calculated for the corresponding 2D synchronous correlation spectra using the same baseline and signal ranges in two dimensions along the diagonal. The performance parameter is based on the definition of signal to noise ratio (SNR) commonly used in digital signal processing: variance of signal to variance of noise.<sup>67, 68</sup>

The discrete dynamic spectra,  $\tilde{y}$ , were calculated from the normalized data with respect to a reference spectrum,  $y_{ref}$ :

$$\tilde{y}_i(\nu) = y_i(\nu) - y_{ref}(\nu) \quad i = 1, 2, 3, \dots, m. \quad (2.3)$$

Three options for  $y_{ref}$  were examined: (1) 1<sup>st</sup> spectrum of the set ( $y_{ref}(\nu) = y_1(\nu)$ ), (2) last spectrum of the set ( $y_{ref}(\nu) = y_m(\nu)$ ), and (3) time-averaged (or, in this case, temperature-averaged) spectrum:

$$\bar{y}(\nu) = \frac{1}{m} \sum_{i=1}^m y(\nu, T_i). \quad (2.4)$$

The reference spectrum yielding the highest performance parameter for the 2D synchronous spectrum (eq 2.2) was used for the remainder of the analysis.

The synchronous 2D correlation intensity, demonstrating simultaneous or coincidental changes in intensity, is given by

$$\Phi(\nu_1, \nu_2) = \frac{1}{m-1} \sum_{i=1}^m \tilde{y}_i(\nu_1) \cdot \tilde{y}_i(\nu_2). \quad (2.5)$$

The asynchronous 2D correlation spectra, showing decoupled changes in intensity, is given by

$$\Psi(\nu_1, \nu_2) = \frac{1}{m-1} \sum_{i=1}^m \tilde{y}_i(\nu_1) \cdot \tilde{z}_i(\nu_2), \quad (2.6)$$

where  $\tilde{z}_i(\nu_2)$  is the discrete orthogonal spectra resulting from a linear transformation,

$$\tilde{z}_i(\nu_2) = \sum_{j=1}^m N_{ij} \cdot \tilde{y}_j(\nu_2), \quad (2.7)$$

and  $N_{ij}$  is the Hilbert-Noda transformation matrix,

$$N_{ij} = \begin{cases} 0 & \text{if } i = j \\ \frac{1}{\pi(j-i)} & \text{otherwise} \end{cases}. \quad (2.8)$$

All 2D correlation computation and plot generation was conducted using MATLAB R2008a.

## 2.3 RESULTS

### 2.3.1 Raman Microspectroscopy of Pure Compounds

#### 2.3.1.1 One-Dimensional Raman Spectra

The Stokes Raman spectra of the investigated compounds have been described previously.<sup>19, 21, 23, 69</sup> Of particular interest in long standoff detection is the range of 150 to 3500  $\text{cm}^{-1}$  containing a number of unique molecular signatures that can be used to identify RDX, HMX, and PETN (Figure 2.2). For RDX, the cluster of peaks in the range of 1200 to 1500  $\text{cm}^{-1}$  is due to symmetric  $\text{NO}_2$  and N-N stretches. The peaks in the range of 500  $\text{cm}^{-1}$  are the result of ring torsion. The primary peak at 877  $\text{cm}^{-1}$  and the few surrounding it are caused by ring stretch.<sup>21</sup> HMX, being a nitramine explosive like RDX, has many similar features. There are signatures of symmetric  $\text{NO}_2$  and N-N stretches in the region of 1200 to 1500  $\text{cm}^{-1}$ .<sup>19</sup> Although not as prominent, its primary peak at 844  $\text{cm}^{-1}$  is due to ring stretching.<sup>23</sup> HMX has an additional broader peak in the range of 1100 to 1200  $\text{cm}^{-1}$  also attributed to ring stretching.<sup>19</sup> The peak at approximately 1550  $\text{cm}^{-1}$  is due to anti-symmetric stretching of  $\text{NO}_2$  groups.<sup>69</sup> The spectral features of PETN include a relatively broad peak at approximately 1650  $\text{cm}^{-1}$  due to anti-symmetric  $\text{NO}_2$  stretching and a sharp peak at 860  $\text{cm}^{-1}$  attributed to the O-N stretching mode. The strong peak at 1290  $\text{cm}^{-1}$  is due to symmetric stretching of the nitro groups.<sup>23</sup> The strong peaks common to all three explosives at 3000  $\text{cm}^{-1}$  are due to aliphatic CH stretching and overlap with abundant species (organic matter) in the operating environment. Although it is possible to distinguish between different types of explosives (e.g., nitramines like RDX versus nitroaromatics like TNT) through careful evaluation of these bands (relative intensity and band width),<sup>23</sup> the required analysis is too time-consuming for the current application, es-

pecially if mixtures of explosives are used. Unfortunately, due to large fluorescence, distinguishable TNT peaks were not observed.

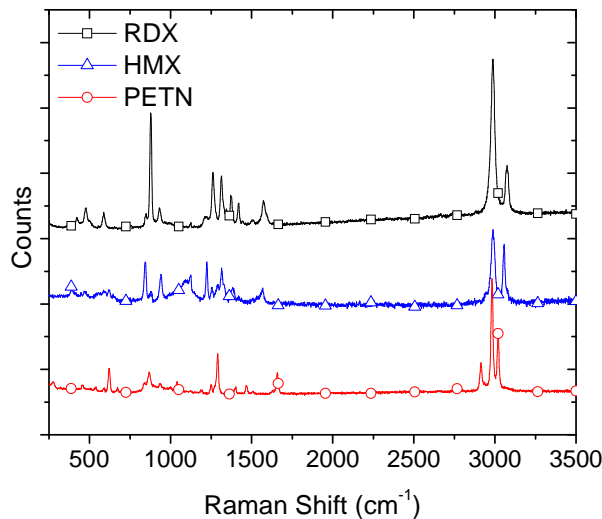


**Figure 2.2** Raman spectra of explosive residues.

For preliminary studies, cropped ranges were selected for each material to achieve rapid detection. These ‘areas of interest’ were selected to include the most intense peaks (excluding the region around  $3000\text{ cm}^{-1}$  as mentioned above) for each material as these would exhibit the greatest change upon full conversion of the explosive. From Figure 2.2, these peaks are at  $877\text{ cm}^{-1}$  for RDX,  $844\text{ cm}^{-1}$  for HMX, and  $1290\text{ cm}^{-1}$  for PETN.

### 2.3.1.2 Clean Two-Dimensional Correlation Spectra

Two dimensional correlation analysis was applied to “clean” (high SNR, flat baseline) sets of RDX and HMX spectra in a narrow range. During the heating ramps, no new Raman peaks appeared in the 1D spectra that could correspond to decomposition products. Rather, all features of the explosive compound decreased and eventually disap-

peared. Corresponding 2D correlation spectra show distinct peaks for both materials that can be used to identify the explosives. In the synchronous spectrum of RDX (Figure 2.3a, left), only one strong autopeak is observed on the diagonal at  $878\text{ cm}^{-1}$ . However, positive cross peaks at  $848$  and  $932\text{ cm}^{-1}$  indicate that there are weaker autopeaks at those Raman shifts which are not much higher than the baseline. All cross peaks are positive, indicating that upon heating, all of the RDX peaks change in the same direction—that is, they decrease. The asynchronous plot shows a tight four-leaf pattern centered at the primary RDX peak (Figure 2.3a, right). The corresponding pairs of peaks are located adjacent to the main peak at (1)  $885$  and  $878\text{ cm}^{-1}$  and at (2)  $870$  and  $878\text{ cm}^{-1}$  and do not correspond to multiple peaks in the 1D spectrum (inset in Figure 2.3a, right). This unexpected pattern can be understood in terms of the crystal structure of the materials as discussed later. The light streaks in the asynchronous plot are due to noise in the background which contributes random fluctuations that are then magnified by the primary RDX peak.<sup>51</sup>

The synchronous spectrum for HMX is slightly more complex containing more auto- and cross peaks (Figure 2.3b, left). The strongest peaks are those forming a correlation square defined by the autopeaks at  $844$  and  $940\text{ cm}^{-1}$ . Similar to RDX, all of the peaks appearing in the synchronous spectrum are positive. The asynchronous spectrum again shows streaking as a result of background noise (Figure 2.3b, right). The increased intensity of streaks at larger Raman shift values indicates that there are larger background fluctuations at those spectral values. Additionally, similar to RDX, concentrated pairs of cross peaks corresponding to the vertices of the correlation square are observed due to the crystalline nature of HMX: (1)  $844$  and  $851\text{ cm}^{-1}$  and (2)  $940$  and  $945\text{ cm}^{-1}$ .

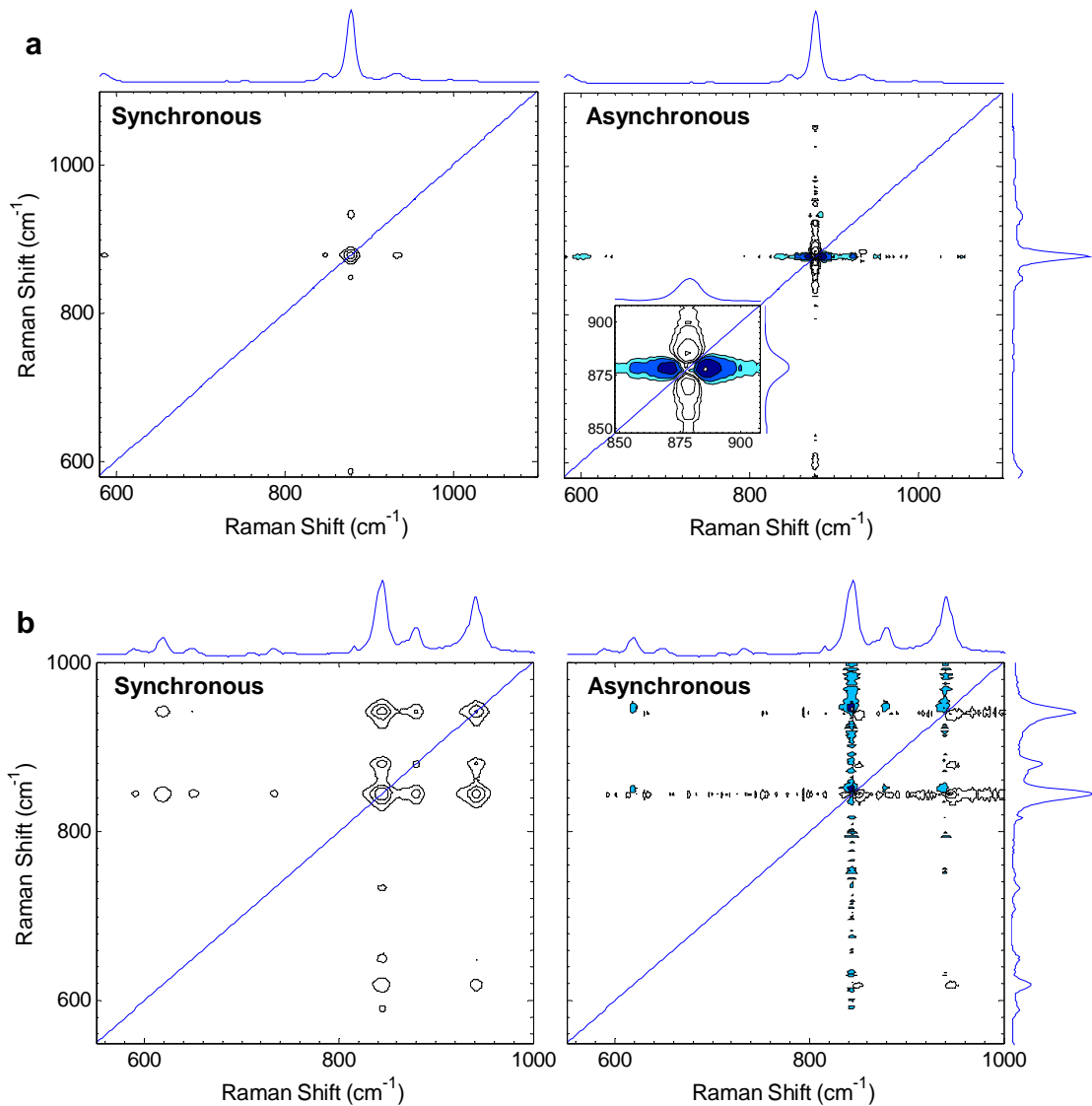


**Figure 2.3** 2D synchronous (left) and asynchronous (right) correlation spectra during heating ramps for **a)** RDX and **b)** HMX. Positive and negative contours are shown as open and filled, respectively. Averaged 1D spectra are shown on the sides.

Application of the 2D correlation analysis results in much greater values for the performance parameter,  $P$  (Table 2.2). In the cases of these well-defined RDX and HMX spectra, improvements in  $P$  are multiple orders of magnitude. Increased values of  $P$  lead to improved discrimination between peak values of interest and baseline scattering as can be seen in histograms of intensity values. As demonstrated in an example of HMX in

Figure 2.4, the 2D nature of the analysis significantly increases peak values (as a result of peak-peak correlation) and minimizes baseline (as a result of weak or absent correlation).

**Table 2.2 Performance parameters and their ratios for RDX<sup>a</sup>, HMX<sup>a</sup>, and PETN<sup>b</sup>.**

Sample	$P_{2D}^c$	$P_{1D}^d$	$P_{2D} / P_{1D}$
RDX	$6.7 \times 10^6$	$2.9 \times 10^2$	$2.4 \times 10^4$
HMX	$1.2 \times 10^5$	$3.2 \times 10^1$	$3.7 \times 10^3$
PETN, no treatment	$3.1 \times 10^2$	$3.4 \times 10^1$	$9.0 \times 10^0$
PETN, floored	$2.7 \times 10^4$	$3.4 \times 10^1$	$8.1 \times 10^2$
PETN, MMN	$1.4 \times 10^5$	$2.5 \times 10^2$	$5.7 \times 10^2$

<sup>a</sup>Figure 2.3

<sup>b</sup>Figure 2.6

<sup>c</sup> $P_{2D}$ : performance parameter for synchronous 2D spectrum

<sup>d</sup> $P_{1D}$ : average performance parameter for 1D dynamic spectra

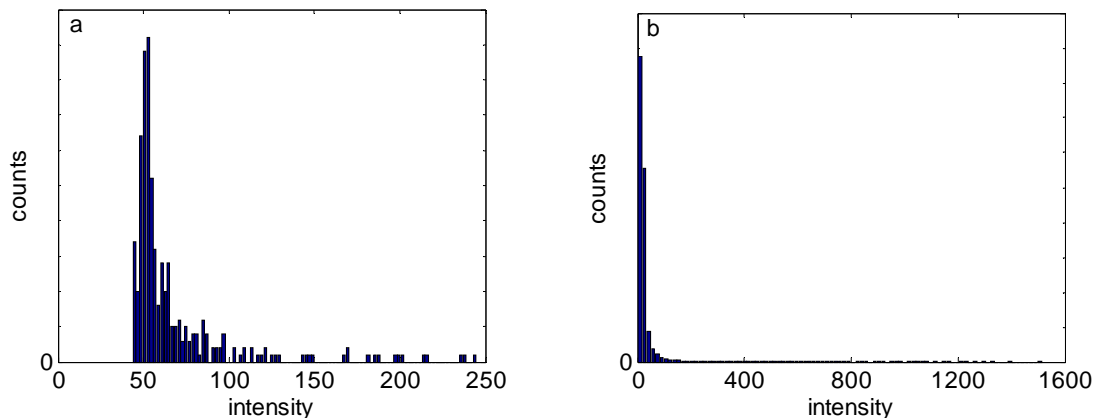


**Figure 2.4** Histogram plots of intensity values for **a)** 1D and **b)** 2D synchronous spectra of HMX corresponding to Figure 2.3b.

### 2.3.1.3 Effect of Background in Two-Dimensional Correlation Spectra

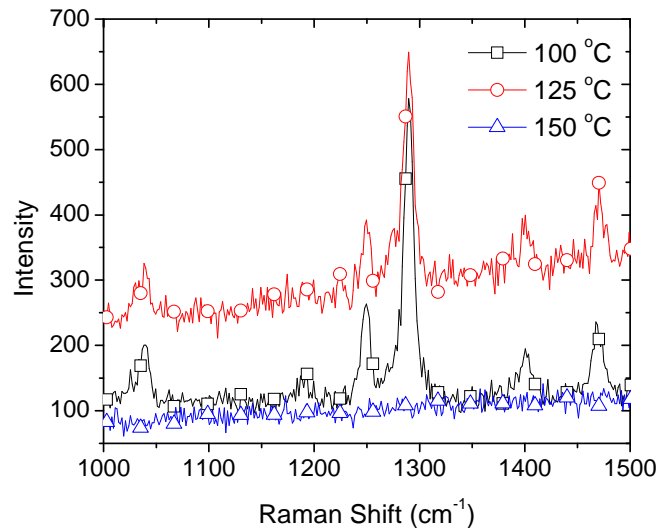


**Figure 2.5** Raman spectra of PETN collected at select temperatures during heating ramp.

In contrast to spectra containing strong peaks and flat baselines (RDX and HMX above), challenges arose when individual spectra,  $y_i(v)$ , exhibited a varying fluorescent background. The development of mild fluorescence was evident in a set of PETN spectra (Figure 2.5), where the background remained stationary at temperatures below 100 °C, grew at higher temperatures as the magnitude of PETN peaks began to decrease, and dropped again near the highest temperatures once PETN peaks disappeared. These observations are consistent with previous studies on time-dependent luminescence following decomposition of PETN.<sup>70</sup>

Fluorescence is characterized by larger intensity at larger Raman shift, which is manifested in the 2D synchronous spectrum as excess background noise and heavy streaks corresponding to the strong PETN features (Figure 2.6a). Since the growth of fluorescence coincided with a change in PETN features but did not follow the same

monotonic trend, the asynchronous spectrum also exhibits heavy streaking. Although the primary PETN peak at  $1290\text{ cm}^{-1}$  is evident in both the synchronous and asynchronous plots, the observed streaks are undesirable since they may mask the presence of weaker peaks of significance. Additionally, from Table 2.1, it is evident that the floating background negatively affects the synchronous performance parameter.

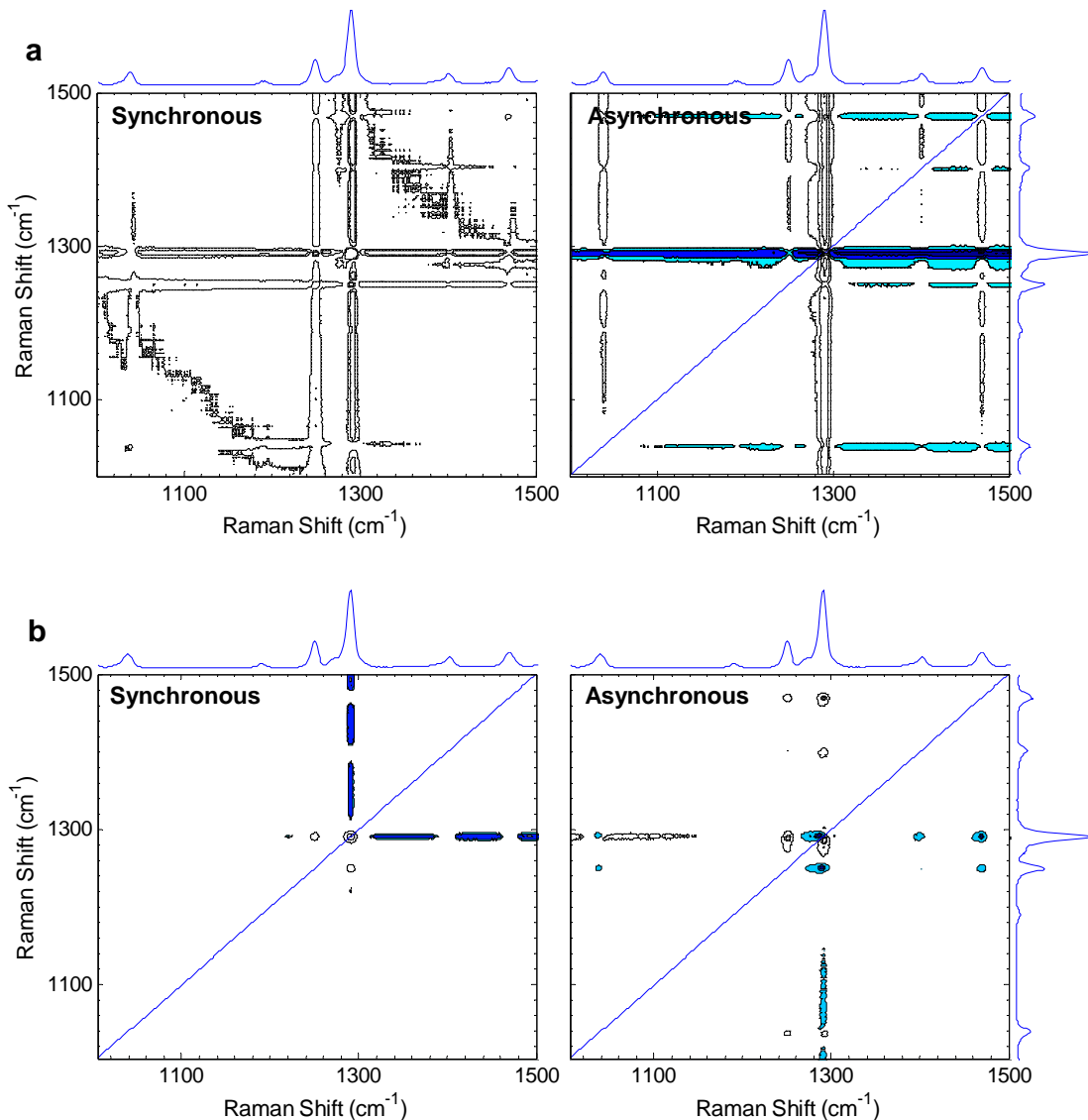


**Figure 2.6** 2D synchronous (left) and asynchronous (right) correlation spectra during heating ramps of PETN: **a)** no data pre-treatment **b)** flooring followed by modified mean normalization applied to each 1D dynamic spectrum. Positive and negative contours are shown as open and filled, respectively. Averaged 1D spectra are shown on the sides.

The initial approach employed to handle the adverse effects of this non-static background was to subtract the minimum value from each spectrum prior to calculating the dynamic spectra.<sup>51</sup> This ‘flooring’ treatment, compensates for the dynamic baseline offset and results in an improvement of two orders of magnitude in  $P_{2D}$  in the current case. However, the tilt in the background remains, as do the streaks in the 2D spectra at higher Raman shift.

Modified mean normalization<sup>64</sup> of each dynamic spectrum results in cleaner corresponding 2D spectra (Figure 2.6b). In the synchronous spectrum, the primary PETN peak is clearly identified, in addition to a number of cross peaks corresponding to other PETN features. The appearance of negative, elongated cross peaks associated with the primary peak (located in line with  $1290\text{ cm}^{-1}$  and extending to larger Raman shift values) are consistent with simultaneous increase of fluorescence and decrease of the Raman peak at  $1290\text{ cm}^{-1}$ . In the asynchronous plot, the streaks are diminished revealing a pair of elongated cross peaks close to the diagonal corresponding to the primary PETN peak at  $1290\text{ cm}^{-1}$ . Furthermore, there are a number of cross peaks in the asynchronous spectrum corresponding to separate PETN features which suggests that the changes in these peaks are not fully synchronized. Care must be exercised in assigning these features: the observation could be an artifact of the normalization or the result of the crystalline nature of PETN and will be discussed later. Finally, mean normalization increases both the 1D and 2D performance parameter by an additional order of magnitude (Table 2.2).

### 2.3.1.4 Data Pretreatment

Encouraged by the increase in  $P$  as the result of normalization (above), a number of common data pretreatments (Table 2.1) were tested for efficacy in minimizing the effects of noise and background on the performance parameter of the synchronous 2D spectra. All data pretreatments examined affected both the 1D and 2D performance parameter. Although one would normally expect  $P_{ID}$  to remain unchanged after normalization by a constant, this is not the case when constants are spectrum-dependant and  $P$  is evaluated for dynamic spectra. When each spectrum is normalized by a unique constant defined by the values in that spectrum, the result is an average spectrum that is no longer linearly related to the average spectrum prior to normalization. Hence, the normalized dynamic spectra will have a different value of  $P$ .

The first four pretreatments are based on differentiation and have sometimes resulted in enhanced spectral features.<sup>51, 52</sup> While differentiation minimizes adverse effects of a tilted baseline, it also increases the effects of noise. In the present case, these pretreatments reduced  $P$  for both the 1D dynamic and 2D synchronous spectra of PETN (Figure 2.6a) and, hence, were excluded from further analysis.

**Table 2.3 Performance parameters and their ratios for floored PETN spectra corresponding to Figure 2.6a treated with different normalizations (Table 2.1).**

	Mean Normalized	Modified Mean (MMN)	Principal Component, PC <sub>1</sub>	Peak Normalized, $y(\nu=1290 \text{ cm}^{-1})$
$P_{2D}^a$	$6.2 \times 10^4$	$1.4 \times 10^5$	$5.0 \times 10^4$	$1.7 \times 10^1$
$P_{ID}^b$	$3.8 \times 10^1$	$2.5 \times 10^2$	$1.9 \times 10^2$	$5.4 \times 10^0$
$P_{2D} / P_{ID}$	$1.7 \times 10^3$	$5.7 \times 10^2$	$2.6 \times 10^2$	$3.2 \times 10^0$

<sup>a</sup> $P_{2D}$ : performance parameter for synchronous 2D spectrum

<sup>b</sup> $P_{ID}$ : average performance parameter for 1D dynamic spectra

Of the remaining four normalization schemes (outlined in Table 2.3), the least effective (lowest  $P$ ) was normalizing the raw data,  $y_i(v)$ , by the intensity value of the primary PETN peak at  $1290\text{ cm}^{-1}$ . This result is not surprising given the nature of PETN disappearance that is at the center of this detection scheme. Normalization by the peak value would be more effective if the peak exhibited only minor intensity changes. However, given that, at the end of the experiment, the intensity at  $1290\text{ cm}^{-1}$  is comparable to the background, the background intensities of these spectra are assigned equal weight by the treatment subsequently resulting in very noisy correlation spectra. Of the normalization methods examined, modified mean normalization (MMN) yielded both the highest  $P_{1D}$  and  $P_{2D}$  by an order of magnitude. While it may seem desirable to apply modified mean normalization to all further analysis, care must be taken as sometimes artifacts appear in the resulting spectra.<sup>57</sup>

### 2.3.1.5 Reference Spectrum

The selection of a reference spectrum can be adjusted in the 2D correlation analysis to yield optimal results.<sup>50, 58</sup> Of the three possibilities examined (Section 2.2.4), the temperature-averaged spectrum (eq 2.4) gives the greatest value for performance parameter for the 2D synchronous spectra for all cases analyzed. Relative to using the first or last spectrum (i.e.,  $y_1(v)$  or  $y_m(v)$ ) as a reference, which both contribute similar noise to that already present in each  $y_i(v)$ , subtracting the average spectrum from each  $y_i(v)$  has the advantage of the reference contributing noise that is reduced by  $m^{-0.5}$ . Although it has been suggested that no reference spectrum can be useful when data are excessively noisy,<sup>51</sup> the use of a reference spectrum is necessary to achieve removal of stationary peaks from 2D

spectra. Hence, the temperature-averaged spectrum was used to calculate the dynamics spectra for all of the results presented.

### **2.3.2 Raman Microspectroscopy: Contamination Studies**

A further challenge for the 2D correlation approach is to identify explosives in the presence of common contaminants. Additionally, it is of interest to understand how explosives behave in the presence of such contaminants under heating and the consequent effects on the 2D spectra. Although several studies have found that the presence of sand or soil does not affect Raman signatures of some military-grade explosives, to our knowledge, temperature effects were not examined in prior literature.<sup>20, 22</sup>

Contamination studies were performed using protocols suitable for the MicroRaman spectrometer used for this work. As noted in prior literature, luminescence can severely interfere with acquisition of Raman spectra.<sup>13, 71</sup> A highly fluorescent yet common contaminant in the operating environment is urine.<sup>72</sup> The spectrometer used for the present thermal oxidation experiments was not equipped with gating, and urine was observed to mask the signal from any other compounds present in the sample. Consequently, detection of explosives in the presence of urine could not be tested using the Renishaw MicroRaman spectrometer. In view of the small size of the irradiated area, which made it difficult to ensure multiple materials in a heterogeneous specimen were adequately sampled in the beam, two alternative methods were used in addition to traditional contamination studies: multi-point and multi-sample experiment. The following three case studies are presented to gauge the effectiveness of 2D correlation analysis for explosive detection in the presence of different contaminants.

### 2.3.2.1 Traditional: RDX and Saliva on Sand

A traditional contamination study, in which multiple specimens were in the beam and undergoing simultaneous thermal treatment, was successful for a sample containing trace RDX and saliva on sand, which is primarily composed of quartz. In the full range examined (Figure 2.7a), both the 1D and the 2D spectra were dwarfed by the quartz peak at  $460\text{ cm}^{-1}$ . The presence of the quartz peak in the 2D spectra is surprising given that this stable substance is not expected to undergo chemical changes at the moderate temperatures employed ( $<200\text{ }^{\circ}\text{C}$ ). However, the crystal nature of quartz results in slight shifting and broadening of the Raman feature with increasing temperatures, which is apparent in the 2D spectra.<sup>73, 74</sup> Further evidence for this explanation is apparent in the asynchronous spectrum which displays a pair of cross peaks near the diagonal corresponding to the quartz Raman feature, which are known to be present in cases of minor peak shifting and broadening.<sup>50, 51</sup> The 2D synchronous plot (Figure 2.7a, left) also exhibits autopeaks belonging to RDX at  $878$ ,  $1264$ , and  $1315\text{ cm}^{-1}$ . The corresponding positive cross peaks are expected since the peaks are all decreasing. The negative cross peaks corresponding to the quartz and RDX autopeaks and are a consequence of the difference in behavior of the spectral features of the corresponding materials. The asynchronous plot shows a cross peak at  $460$  and  $878\text{ cm}^{-1}$ , which indicates that the spectral changes of RDX and quartz are temporally separated (Figure 2.7b, right). Overlapped peaks at large Raman shift are the result of a fluorescent background that grows upon thermal treatment, similar to PETN.

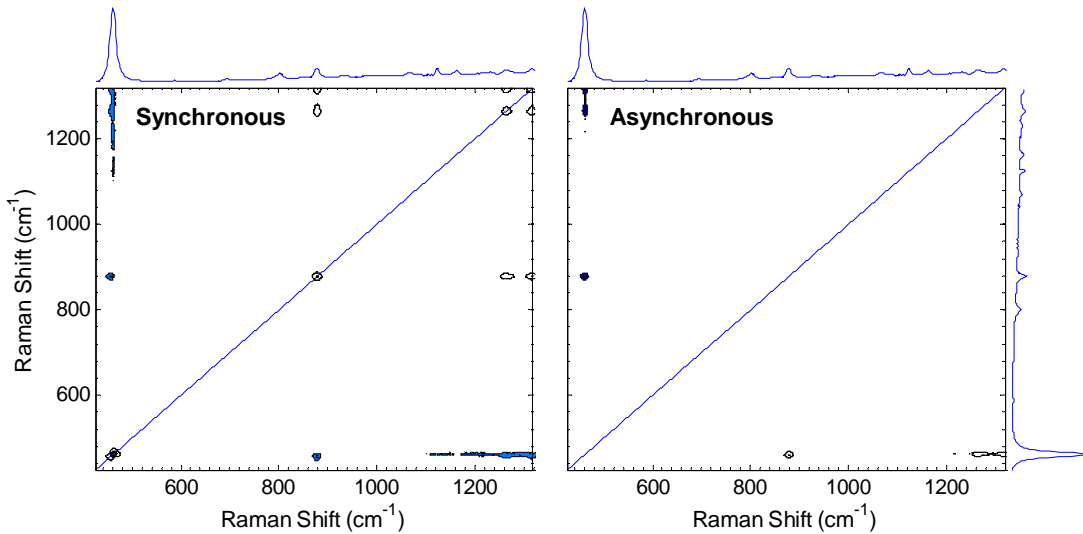


**Figure 2.7** 2D synchronous (left) and asynchronous (right) correlation spectra obtained from floored spectra collected during heating ramp of RDX, saliva and sand in the beam of the excitation laser. Positive and negative contours are shown as open and filled, respectively. Averaged 1D spectra are shown on the sides.

Given the likelihood of observing the non-static quartz peak in an operational environment, it would be desirable to remove it for simplification of analysis. The solitary nature of the peak makes this possible. The average of the resulting 1D spectra clearly show a number of peaks attributed to saliva (Figure 2.8a). This dataset exhibited a fluctuating, sloped background; therefore, this data is useful for re-evaluating normalization schemes in terms of maintaining the integrity of the dataset.

The results of 2D correlation analysis were compared for a dataset pretreated in two different ways: (1) only flooring and (2) flooring followed by modified mean normalization. The differences are evident in the resulting autocorrelation spectra (diagonal of 2D synchronous spectrum) in each case (Figure 2.8b and c, respectively). The three primary RDX peaks at 878, 1264, and  $1315\text{ cm}^{-1}$  are the only features evident when no normalization is used, indicating that the saliva peaks, which do not significantly respond to thermal perturbation in this temperature range ( $<200\text{ }^{\circ}\text{C}$ ), are successfully filtered out

by the 2D correlation analysis. In comparison, small features at 801, 1125, and  $1162\text{ cm}^{-1}$  that correspond to the saliva peaks become apparent with the use of modified mean- and the other normalizations examined (see Table 2.1). The nature of normalization is to assign weight to every point on a spectrum, including the peak values. When a spectrum with an increased background is normalized, intensities at all spectral variables are diminished causing an artificial depression in the peak of interest. Hence, normalization can result in artificially induced changes in otherwise static peaks and can lead to false positives.

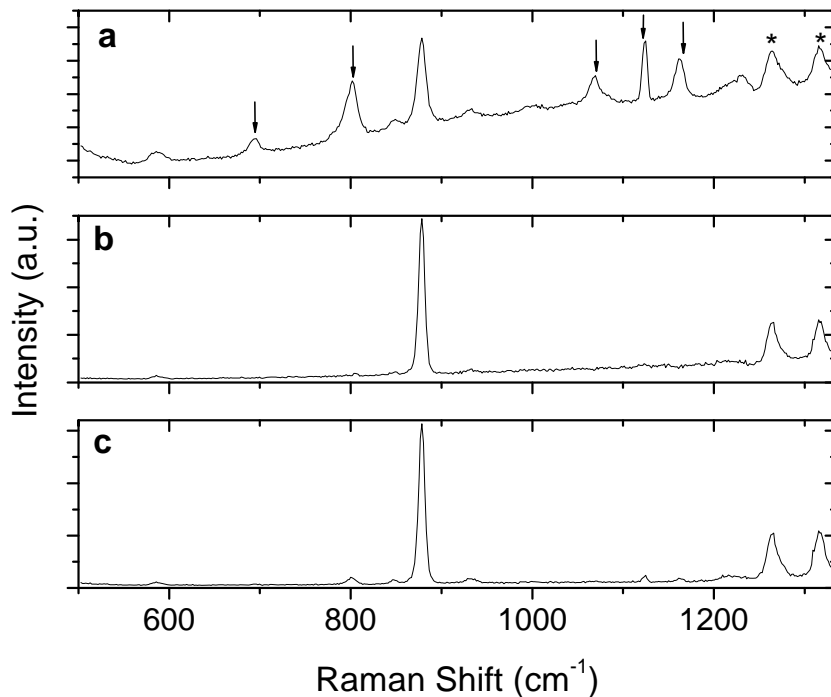


**Figure 2.8** 1D spectra from heating of RDX and saliva on sand: **a)** Temperature-averaged spectrum. **b)** Autocorrelation spectrum for floored spectra. **c)** Autocorrelation spectrum for floored and modified-mean-normalized spectra. Arrows indicate peaks attributed to saliva. Asterisks indicate peaks associate with nitroamine groups.

### 2.3.2.2 Multi-Point: RDX, Soot, Sand, Polybutadiene

The multi-point method was used in the contamination study of RDX in the presence of diesel soot, polybutadiene, and sand; all species were subjected to simultaneous

thermal treatment, while Raman spectra were collected at four different points on the sample at determined temperatures. For each temperature, the four spectra are summed and floored. The resulting 1D spectra at eight temperatures are processed using 2D correlation analysis (Figure 2.9). The spectral range was cropped to remove the quartz peak as discussed previously. The data illustrate some of the challenges anticipated in the field. For example, the primary RDX peak at  $877\text{ cm}^{-1}$  is dwarfed by the broad feature centered at  $1000\text{ cm}^{-1}$ , most likely due to the underlying material (here, glass slide the sample was placed on). Fortunately, the cluster of autopeaks and positive cross peaks between  $1200$  and  $1400\text{ cm}^{-1}$  in the synchronous spectrum allow for the identification of RDX, as well as other nitramine compounds (Figure 2.9, left). As expected, the asynchronous spectrum shows no temporal separation between these features since they are all the result of the same chemical moiety. The sharp feature at  $1122\text{ cm}^{-1}$  was attributed to a residue on a dirty optic. It appears to be lightly correlated with the RDX features but also with significant temporal separation. The slight wave-like behavior of scattering at high Raman shift was unchanged by heating and was the result of two broad soot bands, disorder (D) and graphitic (G), centered at approximately  $1350$  and  $1580\text{ cm}^{-1}$ , respectively.<sup>75, 76</sup>

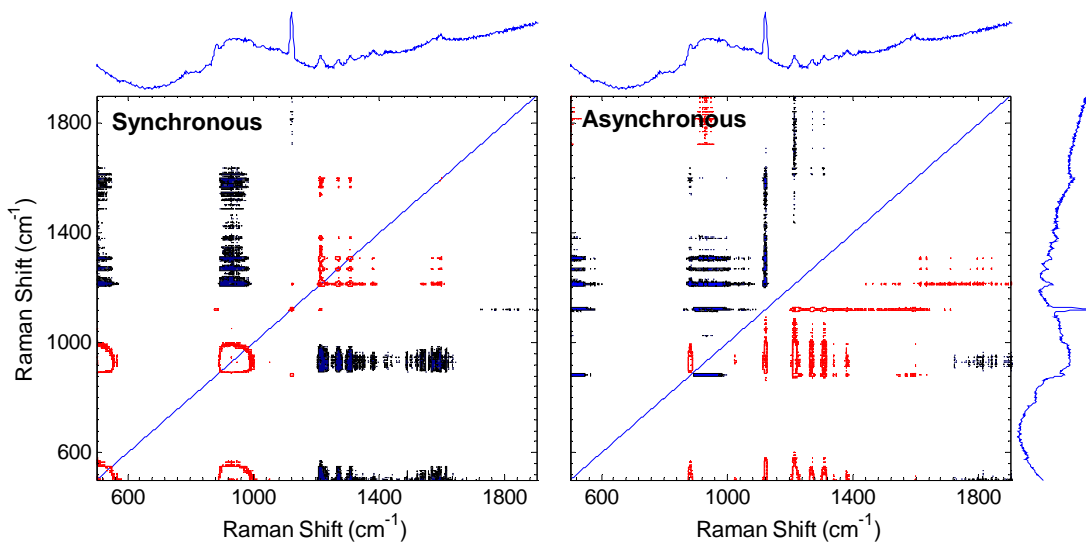


**Figure 2.9** 2D synchronous (left) and asynchronous (right) correlation spectra derived from the sum of spectra collected at 4 spots on a sample of trace RDX, diesel soot and PB on sand during a heating ramp. Positive and negative contours are shown as open grey and filled black, respectively. Averaged 1D spectra are shown on the sides.

### 2.3.2.3 Multi-Sample: PETN, Soot, Polybutadiene

In the multi-sample contamination study, individual datasets collected during separate heating of PETN, diesel soot, and bulk PB (Figure 2.10) were summed and analyzed. Although difficult to see due their large band width and low intensity, soot in this spectral range is characterized by the D and G bands at approximately 1350 and 1580  $\text{cm}^{-1}$ .<sup>75, 76</sup> For PB, the majority of the spectral features in the range of interest are due to deformations of CH groups.<sup>77</sup> To simulate the challenges associated with detecting trace amounts of explosives in the presence of a large background, the PB contribution was scaled to be much stronger than that of PETN, as shown in Figure 2.10.

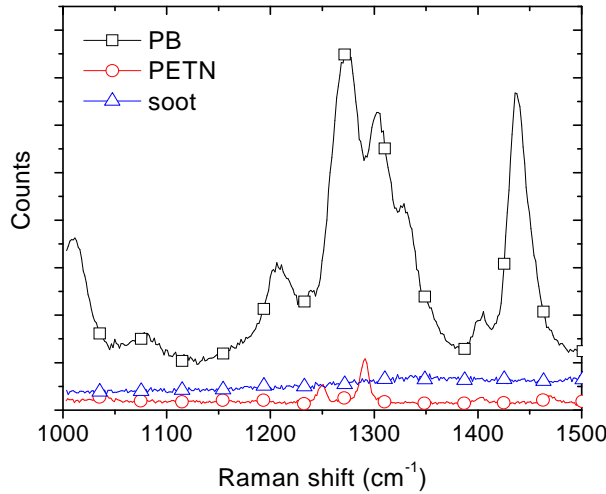


**Figure 2.10** Individual spectra at room temperature of PETN, soot, and bulk PB summed to simulate identification of explosives in the presence of contaminants.

Two-dimensional plots were derived from these 1D spectra after they were summed and then floored (Figure 2.11). As expected, diesel soot was stable under the heating conditions and, as such, its features were filtered out of the 2D spectra. This was also the case if the strong PB signal was excluded (not shown). In contrast, both PB and PETN spectra exhibited changes upon heating as evidenced by the complexity of the 2D spectra (Figure 2.11). Fortunately, the disparity in stability of PB and PETN allows for their discrimination. Although the 1D spectra contain a PETN peak at  $1290\text{ cm}^{-1}$  that is barely noticeable over the strong PB features (Figure 2.12a), the magnitude of the PETN peak in the autocorrelation spectrum is greater than surrounding features by at least a factor of three (Figure 2.12b).

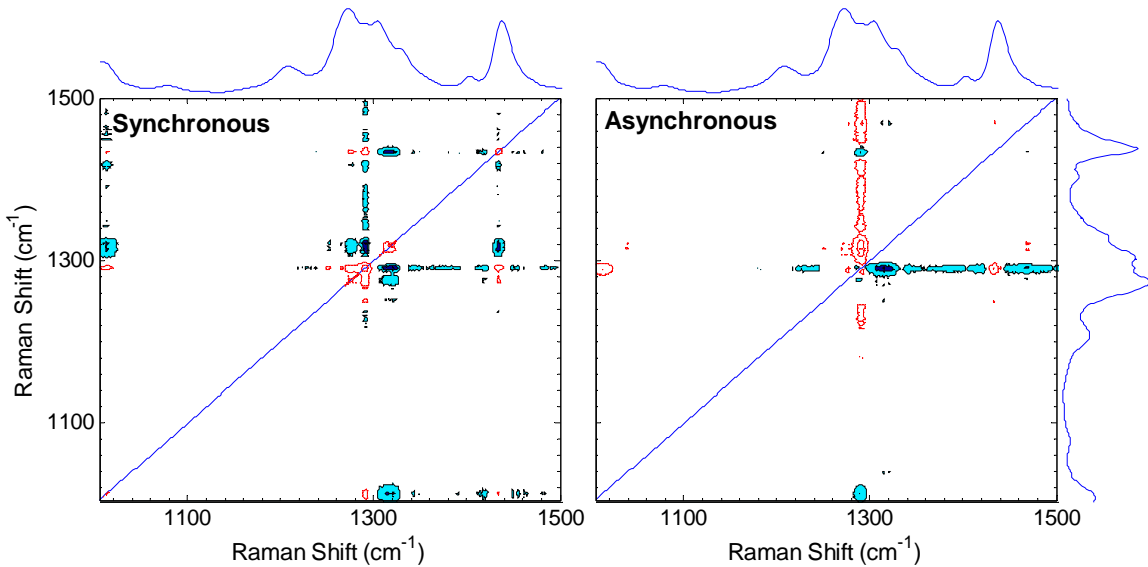


**Figure 2.11** 2D synchronous (left) and asynchronous (right) correlation spectra of summed and floored spectra during individual heating ramps of PETN, diesel soot, and PB. Positive and negative contours are shown open grey and filled black, respectively. Averaged 1D spectra are shown on the sides.

Autopeaks corresponding to the PB at  $1275$ ,  $1329$ , and  $1436\text{ cm}^{-1}$  are observed in the 2D synchronous and the autocorrelation spectra. Unlike previous results presented, positive cross peaks in the synchronous spectrum (Figure 2.11, left) are not solely due to the explosive residue. PB peaks at  $1275$  and  $1436\text{ cm}^{-1}$  also appear to decrease during the heating treatment, although much less so than the PETN peak. The asynchronous spectrum shows that changes in the spectra at large Raman shift are temporally separated from the PETN features. However, as described above, these features can be attributed to the changes in fluorescence that occur during heating of neat PETN (Figure 2.5).

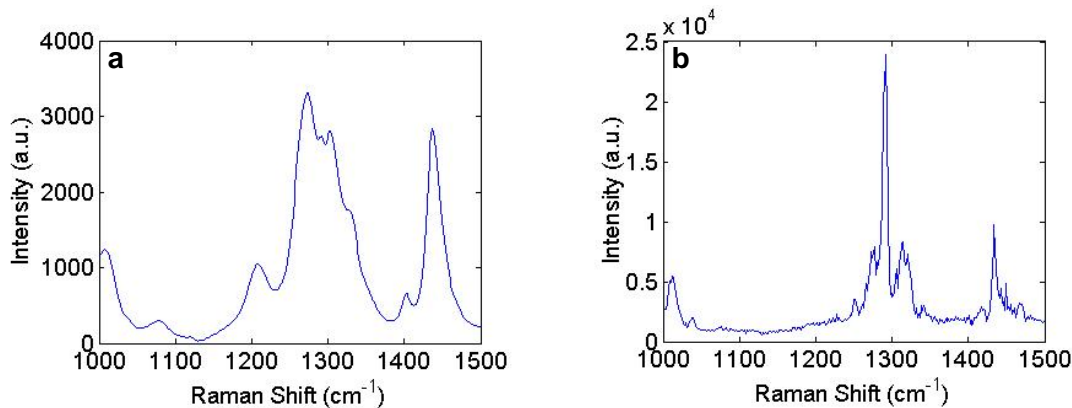


**Figure 2.12** a) Average 1D spectra and b) autocorrelation intensity of summed and floored spectra during individual heating ramps of PETN, diesel soot, and PB.

### 2.3.3 Long Standoff Detection

The experiments using a conventional Raman microscope demonstrated the value of thermal decomposition in conjunction with 2D correlation analysis and highlighted the challenge posed by fluorescence. Additional enhancement in detection can be achieved by utilizing established methods to minimize fluorescence that reaches the detector. Specifically, the near instantaneous character of Raman scattering (in contrast to the relatively prolonged fluorescence emission) can be used to retain the Raman signal and reject most of the fluorescence: only the signal associated with the duration of the excitation pulse (ca. 50 ns) would be acquired. From a substantial distance, thermal modulation would be achieved optically, using successive pulses of infrared light from a CO<sub>2</sub> laser that is absorbed by the sand substrate. Dr. Andrew Pipino at Tanner Research conducted experiments on RDX to test the feasibility of the long standoff system. In agreement with prior studies using a gating scheme,<sup>13, 30, 39</sup> spectral datasets exhibited no signs of fluorescence, which is typically a significant challenge in long standoff Raman. Additionally, the potential to induce thermal oxidation from a standoff distance was demonstrated. The intensity value at 877 cm<sup>-1</sup> was used to monitor conversion of the explosive caused by

heating as a result of CO<sub>2</sub> laser pulses, which are strongly absorbed by the substrate (i.e., silica). In an experiment during which peak intensity dropped by 37.5%, RDX can be unambiguously identified by 2D correlation analysis of averaged spectra (Figure 2.13).

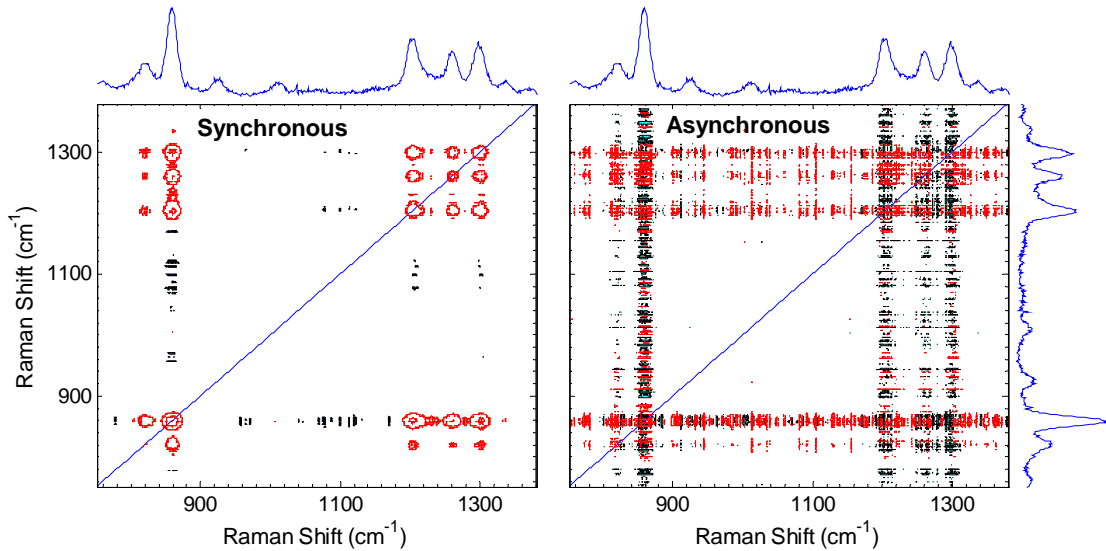


**Figure 2.13** 2D synchronous (left) and asynchronous (right) correlation spectra obtained without mean-normalization from long standoff measurements of RDX with a collection frequency of 1 spectrum every 10 s. Positive and negative contours are shown in open grey and filled black, respectively. Averaged 1D spectra are shown on the sides.

Due to the system averaging, which resulted in 1 spectrum every 10 seconds, direct analysis of the raw data without any pre-treatment resulted in a relatively high value of  $P$ . However, the individual spectra had a stationary, elevated background as the result of the amplifier used to collect the scattering signal. Flooring the dataset led to almost an order of magnitude improvement in  $P$  with resulting values of 690 for 2D synchronous and 65 for 1D dynamic spectra. Due to the standoff distance, the dataset contained significant random noise which is manifested in the asynchronous spectrum. Normalization by the first principal component resulted in another order of magnitude improvement in

$P_{2D}$ . Although the noise levels were decreased by this pre-treatment, the artificial peaks in the asynchronous spectrum remained.<sup>51</sup>

In a separate experiment, more applicable 1-to-1 averaging (1 spectrum every 0.1 second) yielded a spectral dataset with a low average 1D dynamic  $P$  value of 2. The corresponding  $P_{2D}$  was 6. In this case,  $P$  was not affected by flooring the dataset prior to 2D correlation analysis. Normalization of the floored dataset by the first principal component resulted in a 3-fold increase in  $P_{2D}$ . Two factors led to the low  $P$  values of the 2D spectrum in this case. First, noise levels were increased due to lack of spectral averaging. Second, although there were fluctuations of intensity of the RDX peak value, a quantifiable, monotonic decrease characteristic of compound conversion was not observed during the experiment.

## 2.4 DISCUSSION

### 2.4.1 Application of 2D Correlation Analysis

The well-known susceptibility of energetic compounds to mild heating in air was demonstrated to be a valuable means to selectively perturb their spectral features, enabling 2D correlation analysis to enhance their signal in the presence of relatively static background materials. The 2D correlation spectra showed a monotonic decrease and eventual disappearance of features corresponding to explosive residues. These were relatively simple. Complications that might arise due to decomposition of explosives upon heating were not observed. This simplifying behavior can be explained by some combination of vaporization and decomposition.<sup>78, 79</sup> The three explosives examined (RDX, HMX, and PETN) are known to undergo vaporization below their melting points with ac-

tivation energies of 100-150 kJ/mol.<sup>78, 80, 81</sup> The lack of new Raman peaks can also be explained by thermal decomposition of energetic compounds that yields gas-phase products: NO, NO<sub>2</sub>, N<sub>2</sub>O and HCN.<sup>82</sup> Although trace amounts of gas could not be observed due to Raman detection limits, some material condensed on the microscope optic above the heating stage resulting in a Raman peak at 1122 cm<sup>-1</sup>. Chemical reactions during heating of these compounds did produce a mild growth in fluorescence that was particularly noticeable when Raman intensities were relatively low (e.g., PETN<sup>70</sup>). In the case of TNT, this growth in fluorescence upon decomposition was strong enough to mask all of the expected spectral features.<sup>83, 84</sup> The appearance of specific reaction products when energetic compounds undergo thermal decomposition in the presence of ambient compounds cannot be excluded; however it was not observed in the presence of sand, soil, and polybutadiene (sometimes used as a plasticizer) for the military-grade explosives examined here.

The differences in the thermal stability of different energetic compounds may be used to further distinguish between them in a plastic explosive sample like C4. RDX and PETN exhibited similar responses to thermal treatment with full conversion occurring between 150 °C and 200 °C. HMX proved to be slightly less stable with decomposition/vaporization ending just above 100 °C. TNT residues were so unstable that they underwent photodecomposition at room temperature, in agreement with previous literature<sup>14</sup> (possibly due to the formation of electron donor-acceptor, EDA, complexes that shift the absorption maximum closer to the excitation wavelength)<sup>85</sup> or upon heating to only approximately 60 °C.<sup>13</sup> While not addressed here, the sensitivity of TNT to heating highlights the importance of selecting the proper CO<sub>2</sub> laser power in the long standoff system.

Heating must be sufficient to induce some vaporization/decomposition but not so much as to fully convert the energetic species with one pulse.

In the present studies, RDX, PETN, and HMX could be identified by strong autopeaks in the 2D synchronous spectra with peak intensities that were related to the magnitude of the response to the thermal modulation. Data pre-treatments can be used to enhance the discrimination of these peaks from the background. The sign of the cross peaks in the synchronous spectrum can be used to discriminate explosive peaks from features of other compounds that also responded to the thermal treatment. Although not as easily interpreted, the 2D asynchronous spectrum offers an opportunity to extract additional information for identification of peaks corresponding to energetic compounds.

#### **2.4.1.1 Synchronous Spectra**

The diagonal of the 2D synchronous spectrum contains spectral peaks that correspond to compounds that responded to the thermal modulation. The relative intensity of these autopeaks is enhanced compared to the 1D spectra and increases the probability of their detection, as demonstrated by moderate to significant improvement in the performance parameter. This is due to the nature of the 2D spectrum in which multiplication of small background values by small background values and multiplication of large peak values by large peak values results in greater separation of signal from noise. In addition to improvement in  $P$ , this separation allows the possibility of improved success of detection through the application of automated thresholding algorithms or more advanced statistical signal analysis.

In addition to strong autopeaks at the focus of calculations of the performance parameter, cross peaks are present in the synchronous spectrum between spectral features of

the same energetic compound. Unfortunately, as demonstrated by Figure 2.9 and Figure 2.11, positive cross peaks also appear for some contaminants. In this situation, examination of the corresponding asynchronous spectrum can aid in the distinction between explosive and contaminant peaks.

#### 2.4.1.2 Asynchronous Spectra

The individual Raman signatures of a single compound undergoing vaporization/decomposition are expected to decrease and eventually disappear together. In this situation, the asynchronous spectrum should be free of peaks. Hence, it was initially surprising that asynchronous cross peaks were observed both within and between strong, 1D spectral features for all explosives examined. Both observations can be attributed to the crystalline nature of the explosive materials.

The presence of a pair of asynchronous cross peaks within one, strong 1D peak (inset of Figure 2.3) is usually due to temporal separation between overlapping bands but can also be attributed to slight peak shifting.<sup>51</sup> McNesby et al. reported subtle shifting of RDX Raman peaks during heating and attributed the observation to increasing lattice spacing in the crystal.<sup>25</sup> Hence, it is reasonable to attribute this surprising observation to the crystal nature of the compound. The existence of asynchronous peaks between strong, 1D spectral features indicates that these features are temporally separated as a result of different rates of change of those spectral features. McNesby et al. also observed uneven intensity changes between peaks of Raman spectra during heating,<sup>25</sup> which was attributed to the loss of crystal order at elevated temperatures.<sup>28</sup> Hence, the temporal separation observed for peaks of a single compound can again be attributed to the crystalline nature of the material. Since HMX and PETN are also crystalline, similar patterns are expected and

were observed in their asynchronous spectra. While details of the crystalline structure may be used to identify these materials and potentially even trace them in the future, a profound consequence of these observations is that cross peaks evident of temporal separation do not necessarily indicate separate species as originally anticipated.

Furthermore, interpretation of the asynchronous spectrum can be quite complicated, especially in a multi-component sample. In more complex samples, the possibility of overlapping bands and temporal separation between different species can result in similar patterns to those described above. Hence, assignment of asynchronous peak pairs is more ambiguous. Additionally, apparent temporal separation can be an artifact of growing fluorescence (Figure 2.6) or improper normalization (Figure 2.8). Hence, interpretation of the asynchronous spectrum must be done with care.

Nevertheless, as demonstrated in the results section, under certain conditions the asynchronous spectrum can provide an additional level of discrimination of compounds. These desirable conditions include (1) static background scattering, which should be attainable by minimizing fluorescence with the gating employed by the long standoff system and (2) moderate noise levels to mask the crystalline nature of the explosive materials (see PETN spectra in Figure 2.6 for example). The latter condition is based on the fact that the asynchronous peaks attributed to the crystalline nature of the material are the result of subtle changes in the Raman spectra; hence, they are very sensitive to noise. If they are present, it may be possible to exploit this feature in order to discriminate between the two possibilities for their observation: (1) crystalline nature of compound or (2) separate species. By inserting controlled amounts of artificial noise into the acquired 1D

spectra, asynchronous peaks resulting from the crystalline nature of a compound should be readily masked revealing more substantial changes in the spectra.

#### 2.4.1.3 Data Pretreatments

Data pretreatments can be used to improve discrimination of signal relative to background (increase the performance parameter) and, hence, decrease the probability of overlooking a compound that is actually present (false negatives). For the current application data pretreatment should be rapid and data-blind. Standard background subtraction would require time for background collection and is not ideal for the current application. The approximation of a background would require human intervention, which is also undesirable. An alternative approach to minimize background effects is to subtract the minimum intensity value from each spectrum ('flooring'). This was effective in increasing  $P$  in most cases, except when  $P$  is already very low.

A further increase in  $P$  could be obtained through a variety of normalizations (Table 2.1). Modified mean normalization proved to be most effective for a sample displaying mild fluorescence. Ideally, fluorescence would be rejected from the acquired signal by the gating scheme. However, the challenges due to fluorescence, which are manifested as a non-stationary background (i.e., significant background contribution to 2D spectra), could be introduced by other aspects of the operating environment. While normalization minimizes background effects, artifacts are introduced to the 2D spectra (Figure 2.12).<sup>57</sup> Hence, cross peaks observed in synchronous and asynchronous spectra obtained from normalized data cannot be used to discriminate energetic compounds from more stable species.

Alternatively, additional enhancement of peak identification can be achieved through a pretreatment that smoothes the 1D data. The simplest smoothing algorithms should be avoided as they cannot discriminate noise from peaks when  $P$  is low. Possible algorithms might include filters based on noise perturbation in conjunction with PCA.<sup>42</sup> An additional requisite for the final smoothing pretreatment, as for all data manipulations for the current application, is that it require a reasonable amount of computing power.

#### 2.4.2 Fluorescence

The presence of fluorescence affects both the quantitative (performance parameter) and qualitative (artifacts) aspects of 2D correlation spectra. Varying levels of fluorescence can be introduced by decomposition products of energetic compounds or even the products themselves.<sup>70, 86</sup> However, this is minor compared to the luminescence that is encountered from contaminants (e.g., urine, diesel fuel<sup>86</sup>) and ambient species in the operating environment.<sup>13, 30, 71</sup> To cope, the standoff system utilizes a gating scheme to minimize the amount of fluorescence that reaches the detector based on the disparity in lifetimes between Raman scattering ( $10^{-12}$ – $10^{-13}$  s) and fluorescence ( $10^{-7}$ – $10^{-9}$  s).<sup>39, 61</sup> Preliminary studies have demonstrated its effectiveness for a target at a fixed distance for which the delay and gate width were optimized.<sup>13, 30, 71</sup> However, previous studies have observed that gating is not fully effective at rejecting luminescence from some backgrounds.<sup>30, 71</sup> Therefore, additional attempts have been made to overcome fluorescence, which is typically  $10^4$  to  $10^6$  times greater in intensity than Raman scattering with excitation in the visible range,<sup>87</sup> by enhancing the Raman signal.

### 2.4.3 Raman Signal Enhancement

The small cross section for Raman scattering ( $10^{-30}$  to  $10^{-25}$   $\text{cm}^2/\text{molecule}$ )<sup>88</sup> has inspired attempts to enhance the signal through different techniques.<sup>15, 27, 87, 89, 90</sup> The simplest one, as mentioned above, is the use of a shorter excitation wavelength. Since the Raman cross section scales as the inverse of scattering wavelength to the fourth power ( $\lambda^{-4}$ ), using a shorter wavelength will enhance the signal and decrease excitation power requirement. Additionally, the use of ultraviolet (UV) excitation energies close to those of allowed electronic transitions of the material results in resonance and pre-resonance enhancement that can overcome fluorescence.<sup>15, 27, 71, 91</sup> The use of deep UV excitation (<260 nm) provides the additional advantage of a fluorescence-free background since fluorescence typically occurs at longer wavelengths.<sup>30, 87, 91</sup>

An alternative technique to increase the Raman signal is the use of a substrate containing metallic nanostructures. Surface Enhanced Raman Spectroscopy (SERS) may be observed when particular molecules are coupled with the plasmon resonance of the metallic nanostructures of the substrate onto which they are absorbed. Research in the field of SERS is currently very active in attempts to gain full understanding of the effect so as to fully exploit it. Enhancement of signal by factors of  $10^5$  to  $10^9$  has been observed, adequate to overcome fluorescence.<sup>92, 93</sup> A number of attempts have been made to use SERS for detection of explosive residues.<sup>24, 29, 94</sup> We have conducted preliminary experiments on 25 nm gold nanoparticle arrays fabricated by Dr. David Boyd (Caltech), but no evidence of SERS was observed. Currently, there is no practical way to implement SERS for long standoff detection of explosives; however that does not rule out future applications.

## 2.5 CONCLUSION

Two-dimensional correlation spectroscopy in conjunction with thermal modulation was demonstrated to be an effective scheme for the detection of explosive residues via long standoff Raman Spectroscopy. Thermal modulation was found to be an effective means to perturb the Raman features of the energetic compounds. The modulated signal was enhanced through the application of 2D correlation analysis, which resulted in synchronous spectra containing autopeaks with increased explosive peak values. This increase in the ‘performance parameter’ can reduce both the probability of false alarm and false negatives based on automated thresholding algorithms or more advanced statistical signal analysis. In some cases, the sign of the cross peaks (positive for energetic compounds) in the synchronous spectrum can be used to further discriminate between possible energetic compounds and ambient compounds that also respond to thermal treatment. When this distinction is not effective, the asynchronous spectrum, although sometimes difficult to interpret, can provide information about temporal separation of features which can further discriminate explosive compounds.

Several data-blind pre-treatments were examined for improvement in  $P$ . Background fluctuations can be minimized to some degree by flooring data prior to 2D correlation analysis. Peak identification can be further enhanced by normalization of the 1D spectra. Improvement in  $P$  by normalizing long standoff data by the first principal component provides motivation for further testing of this technique. However, the implementation of normalization can produce artifacts when background scattering is not static, like the in the case of fluorescence. Hence, successive 1D spectra should be checked for static backgrounds if normalization is to be used.

The optimum detection range should be between 800 and 1500  $\text{cm}^{-1}$  such that it is as small as possible for rapid detection while including key features of energetic compounds: their strongest peaks (e.g., ring stretch for RDX or HMX) as well as the distinct  $\text{NO}_2/\text{N-N}$  stretches of nitramine explosives. Additionally, two-dimensional correlation spectroscopy is not immune to the challenges presented by fluorescence because fluorescence is not static. Hence, the successful gating scheme implemented to collect the nearly immediate Raman scattering from relatively delayed fluorescence is imperative for the implementation of the proposed scheme.

Further studies of the effectiveness of the proposed scheme should include a range of contaminants and substrates, as well as other explosives. A number of home-made explosives are of particular interest: ammonium nitrate fuel oil (ANFO), urea nitrate (UN), triacetone triperoxide (TATP), and potassium chlorate (KCl). Some of these have the potential to be especially challenging to detect due to their similarity to common fertilizer, native fluorescence,<sup>86</sup> and a lack of  $\text{NO}_2$  or N-N structures typical of military grade explosives.

On a final note, the strategy that is pursued—two-dimensional correlation analysis in conjunction with a thermal perturbation—may be extended to other spectroscopic techniques.

## 2.6 ACKNOWLEDGEMENTS

The idea for this work came from Dr. Ravi Verma and Dr. Andrew Pipino at Tanner Research. (Monrovia, CA). Their financial and intellectual support was invaluable to its progress. Additionally, our collaboration with Dr. David Boyd at Caltech

proved incredibly fruitful. I thank Elizabeth Miura Boyd and Prof. George Rossman from the spectroscopy lab in Geology and Planetary Sciences (Caltech) for support, discussions, and use of the facility. Finally, I would like to acknowledge Oliver Buccicone (Tanner Research., Monrovia, CA) for discussions regarding motivation behind and feasibility of the project. Manuscript preparation was graciously assisted by Prof. Julia Kornfield (Caltech), Oliver Buccicone, Elizabeth Miura Boyd, and Dr. Andrew Pipino.

## 2.7 REFERENCES

1. Joint Improvised Explosive Device Defeat Organization. [www.jieddo.dod.mil](http://www.jieddo.dod.mil).
2. Moore, D. S., Instrumentation for trace detection of high explosives. *Review of Scientific Instruments* **2004**, 75, (8), 2499-2512.
3. Steinfeld, J. I.; Wormhoudt, J., Explosives detection: A challenge for physical chemistry. *Annual Review of Physical Chemistry* **1998**, 49, 203-232.
4. Bauer, C.; Sharma, A. K.; Willer, U.; Burgmeier, J.; Braunschweig, B.; Schade, W.; Blaser, S.; Hvozdara, L.; Muller, A.; Holl, G., Potentials and limits of mid-infrared laser spectroscopy for the detection of explosives. *Applied Physics B-Lasers and Optics* **2008**, 92, (3), 327-333.
5. Arusi-Parpar, T.; Heflinger, D.; Lavi, R., Photodissociation followed by laser-induced fluorescence at atmospheric pressure and 24 degrees C: a unique scheme for remote detection of explosives. *Applied Optics* **2001**, 40, (36), 6677-6681.
6. Wynn, C. M.; Palmacci, S.; Kunz, R. R.; Clow, K.; Rothschild, M. In *Detection of condensed-phase explosives via laser-induced vaporization, photodissociation, and resonant excitation*, 2008; Optical Soc Amer: 2008; pp 5767-5776.
7. Wynn, C. M.; Palmacci, S.; Kunz, R. R.; Rothschild, M., A Novel Method for Remotely Detecting Trace Explosives. *Lincoln Laboratory Journal* **2008**, 17, (2), 27-39.
8. Dikmelik, Y.; Spicer, J. B., Femtosecond laser-induced breakdown spectroscopy of explosives and explosive-related compounds. *Proceedings of the SPIE - The International Society for Optical Engineering* **2005**, 5794, (1), 757-761.

9. Hua, Z.; Redo, A.; Yunqing, C.; Xi-Cheng, Z., THz wave standoff detection of explosive materials. *Proceedings of the SPIE - The International Society for Optical Engineering* **2006**, 6212, 62120L-1-62120L-62120L-8.
10. Wentworth, R. M.; Neiss, J.; Nelson, M. P.; Treado, P. J. In *Standoff Raman hyperspectral imaging detection of explosives*, 2007 IEEE Antennas and Propagation Society International Symposium, Honolulu, HI, USA, 9-15 June, 2008; Ieee: Honolulu, HI, USA, 2008; pp 4925-4928.
11. Committee on the Review of Existing and Potential Standoff Explosives Detection Techniques, N. R. C., *Existing and Potential Standoff Explosives Detection Techniques*. The National Academies Press: Washington D.C., 2004; p 148.
12. Gottfried, J. L.; De Lucia, F. C.; Munson, C. A.; Mizolek, A. W., Strategies for residue explosives detection using laser-induced breakdown spectroscopy. *Journal of Analytical Atomic Spectrometry* **2008**, 23, (2), 205-216.
13. Carter, J. C.; Angel, S. M.; Lawrence-Snyder, M.; Scaffidi, J.; Whipple, R. E.; Reynolds, J. G., Standoff Detection of High Explosive Materials at 50 Meters in Ambient Light Conditions Using a Small Raman Instrument. *Applied Spectroscopy* **2005**, 59, (6), 769-775.
14. Carter, J. C.; Scaffidi, J.; Burnett, S.; Vasser, B.; Sharma, S. K.; Angel, S. M., Standoff Raman detection using dispersive and tunable filter based systems. *Spectrochimica Acta Part A* **2005**, 61, 2288-2298.
15. Comanescu, G.; Manka, C. K.; Grun, J.; Nikitin, S.; Zabetakis, D., Identification of explosives with two-dimensional ultraviolet resonance Raman spectroscopy. *Applied Spectroscopy* **2008**, 62, (8), 833-839.

16. Eckenrode, B. A.; Bartick, E. G.; Harvey, S. D.; Vucelick, M. E.; Wright, B. W.; Huff, R. A., Portable Raman Spectroscopy Systems for Field Analysis. *Forensic Science Communications* **2001**, 3, (4).
17. Grasso, R. J.; Russo, L. P.; Barrett, J. L.; Odhner, J. E.; Egbert, P. I., An accurate modeling, simulation, and analysis tool for predicting and estimating Raman LIDAR system performance. *Proceedings of the SPIE - The International Society for Optical Engineering* **2007**, 6681, (1), 66810D-1-66810D-66810D-18.
18. Hayward, I. P.; Kirkbride, T. E.; Batchelder, D. N.; Lacey, R. J., Use of a Fiber Optic Probe for the Detection and Identification of Explosive Materials by Raman-Spectroscopy. *Journal of Forensic Sciences* **1995**, 40, (5), 883-884.
19. Sharma, S. K.; Misra, A. K.; Sharma, B. In *Portable remote Raman system for monitoring hydrocarbon, gas hydrates and explosives in the environment*, 2005; Pergamon-Elsevier Science Ltd: 2005; pp 2404-2412.
20. Ballesteros, L. M.; Herrera, G. M.; Castro, M. E.; Briano, J.; Mina, N.; Hernandez-Rivera, S. P., Spectroscopic signatures of PETN in contact with sand particles. *Proceedings of the SPIE - The International Society for Optical Engineering* **2005**, 5794, (1), 1254-1262.
21. Fell, N. F.; Vanderhoff, J. A.; Pesce-Rodriguez, R. A.; McNesby, K. L., Characterization of Raman spectral changes in energetic materials and propellants during heating. *Journal of Raman Spectroscopy* **1998**, 29, (3), 165-172.
22. Herrera-Sandoval, G. M.; Ballesteros, L. M.; Mina, N.; Briano, J.; Castro, M. E.; Hernandez-Rivera, S. P., Raman signatures of TNT in contact with sand particles.

*Proceedings of the SPIE - The International Society for Optical Engineering* **2005**, 5794, (1), 1245-1253.

23. Lewis, I. R.; Daniel, N. W.; Griffiths, P. R., Interpretation of Raman spectra of nitro-containing explosive materials. Part I: Group frequency and structural class membership. *Applied Spectroscopy* **1997**, 51, (12), 1854-1867.

24. McHugh, C. J.; Keir, R.; Graham, D.; Smith, W. E., Selective functionalisation of TNT for sensitive detection by SERRS. *Chemical Communications* **2002**, (6), 580-581.

25. McNesby, K. L.; Fell, N. F., Jr.; Vanderhoff, J. A., Detection and characterization of explosives using Raman spectroscopy: identification, laser heating, and impact sensitivity. *Proceedings of the SPIE - The International Society for Optical Engineering* **1997**, 3082, 121-135.

26. Moore, D. S.; Lee, K. Y., Raman spectroscopy as a tool for long-term energetic material stability studies. *Journal of Raman Spectroscopy* **2007**, 38, (9), 1221-1224.

27. Nagli, L.; Gaft, M.; Fleger, Y.; Rosenbluh, M., Absolute Raman cross-sections of some explosives: Trend to UV. *Optical Materials* **2008**, 30, 1747-1754.

28. Reylafon, M.; Trinquec.C; Cavagnat, R.; Forel, M. T., Study on Vibration Spectra of Hexhydro-1,3,5-Trinitro Sym Triazine .1. Analysis of Infrared and Raman Spectra between 3200 and 200 Cm-1. *Journal De Chimie Physique Et De Physico-Chimie Biologique* **1971**, 68, (10), 1533-&.

29. Sylvia, J. M.; Janni, J. A.; Klein, J. D.; Spencer, K. M., Surface-enhanced Raman detection of 1,4-dinitrotoluene impurity vapor as a marker to locate landmines. *Analytical Chemistry* **2000**, 72, (23), 5834-5840.

30. Gaft, M.; Nagi, L. In *UV gated Raman spectroscopy for standoff detection of explosives*, 2008; Elsevier Science Bv: 2008; pp 1739-1746.
31. Wormhoudt, J.; Kebabian, P. L.; Kolb, C. E., Infrared fiber-optic diagnostic observations of solid propellant combustion. *Combustion and Flame* **1997**, 108, (1-2), 43-60.
32. Riris, H.; Carlisle, C. B.; McMillen, D. F.; Cooper, D. E., Explosives detection with a frequency modulation spectrometer. *Applied Optics* **1996**, 35, (24), 4694-4704.
33. Bannister, W. W.; Chen, C.-C.; Curby, W. A.; Chen, E. B.; Damour, P. L.; Morales, A. Thermal analysis for detection and identification of explosives and other controlled substances. 2004.
34. Wormhoudt, J.; Shorter, J. H.; McManus, J. B.; Kebabian, P. L.; Zahniser, M. S.; Davis, W. M.; Cespedes, E. R.; Kolb, C. E. In *Tunable infrared laser detection of pyrolysis products of explosives in soils*, 1996; Optical Soc Amer: 1996; pp 3992-3997.
35. Lemire, G. W.; Simeonsson, J. B.; Sausa, R. C., Monitoring of Vapor-Phase Nitro-Compounds Using 226-Nm Radiation - Fragmentation with Subsequent No Resonance-Enhanced Multiphoton Ionization Detection. *Analytical Chemistry* **1993**, 65, (5), 529-533.
36. Ger, M. D.; Hwu, W. H.; Huang, C. C., A Study on the Thermal-Decomposition of Mixtures Containing an Energetic Binder and a Nitramine. *Thermochimica Acta* **1993**, 224, 127-140.
37. De Lucia, F. C.; Gottfried, J. L.; Munson, C. A.; Mizolek, A. W. In *Multivariate analysis of standoff laser-induced breakdown spectroscopy spectra for classification of explosive-containing residues*, 2008; Optical Soc Amer: 2008; pp G112-G121.

38. Hua, Z.; Cunlin, Z.; Liangliang, Z.; Yuejin, Z.; Xi-Cheng, Z., A phase feature extraction technique for terahertz reflection spectroscopy. *Applied Physics Letters* **2008**, 92, (22), 221106-1-221106-221106-3.

39. Vanduyne, R. P.; Jeanmair.Dl; Shriver, D. F., Mode-Locked Laser Raman-Spectroscopy - New Technique for Rejection of Interfering Background Luminescence Signals. *Analytical Chemistry* **1974**, 46, (2), 213-222.

40. Noda, I., Generalized Two-Dimensional Correlation Method Applicable to Infrared, Raman, and Other Types of Spectroscopy. *Applied Spectroscopy* **1993**, 47, (9), 1329-1336.

41. Gericke, A.; Gadaleta, S. J.; Brauner, J. W.; Mendelsohn, R., Characterization of biological samples by two-dimensional infrared spectroscopy: Simulation of frequency, bandwidth, and intensity changes. *Biospectroscopy* **1996**, 2, (6), 341-351.

42. Hu, Y.; Li, B. Y.; Sato, H.; Noda, I.; Ozaki, Y., Noise perturbation in functional principal component analysis filtering for two-dimensional correlation spectroscopy: Its theory and application to infrared spectra of a poly(3-hydroxybutyrate) thin film. *Journal of Physical Chemistry A* **2006**, 110, (39), 11279-11290.

43. Kim, H. J.; Bin Kim, S.; Kim, J. K.; Jung, Y. M., Two-dimensional heterospectral correlation analysis of wide-angle X-ray scattering and infrared spectroscopy for specific chemical interactions in weakly interacting block copolymers. *Journal of Physical Chemistry B* **2006**, 110, (46), 23123-23129.

44. McNavage, W.; Dai, H. L., Two-dimensional cross-spectral correlation analysis and its application to time-resolved Fourier transform emission spectra of transient radicals. *Journal of Chemical Physics* **2005**, 123, (18), 12.

45. Meng, S.; Sun, B.; Guo, Z.; Zhong, W.; Du, Q.; Wu, P., Two-dimensional correlation ATR-FTIR studies on PEO-PPO-PEO tri-block copolymer and its phosphorylcholine derivate as thermal sensitive hydrogel systems. *Polymer* **2008**, 49, 2738-2744.

46. Murayama, K.; Czarnik-Matusewicz, B.; Wu, Y.; Tsenkova, R.; Ozaki, Y., Comparison between Conventional Spectral Analysis Methods, Chemometrics, and Two-Dimensional Correlation Spectroscopy in the Analysis of Near-Infrared Spectra of Protein. *Applied Spectroscopy* **2000**, 54, (7), 978-985.

47. Nabet, A.; Auger, M.; Pezolet, M., Investigation of the temperature behavior of the bands due to the methylene stretching vibrations of phospholipid acyl chains by two-dimensional infrared correlation spectroscopy. *Applied Spectroscopy* **2000**, 54, (7), 948-955.

48. Noda, I. In *Recent advancement in the field of two-dimensional correlation spectroscopy*, 2008; Elsevier Science Bv: 2008; pp 2-26.

49. Noda, I.; Allen, W. M.; Lindberg, S. E., Two-Dimensional Raman Correlation Spectroscopy Study of an Emulsion Copolymerization Reaction Process. *Applied Spectroscopy* **2009**, 63, (2), 224-232.

50. Noda, I.; Ozaki, Y., *Two-Dimensional Correlation Spectroscopy*. John Wiley & Sons Ltd.: West Sussex 2004.

51. Czarnecki, M. A., Interpretation of two-dimensional correlation spectra: Science or art? *Applied Spectroscopy* **1998**, 52, (12), 1583-1590.

52. Hu, Y.; Zhang, Y.; Li, B. Y.; Ozaki, Y., Application of sample-sample two-dimensional correlation spectroscopy to determine the glass transition temperature of poly(ethylene terephthalate) thin films. *Applied Spectroscopy* **2007**, 61, (1), 60-67.

53. Yu, Z. W.; Noda, I., On the normalization method in two-dimensional correlation spectra when concentration is used as a perturbation parameter. *Applied Spectroscopy* **2003**, 57, (2), 164-167.

54. Czarnecki, M. A., Two-dimensional correlation spectroscopy: Effect of normalization of the dynamic spectra. *Applied Spectroscopy* **1999**, 53, (11), 1392-1397.

55. Noda, I.; Ozaki, Y., Response to "some comments on tine application of two-dimensional correlation spectroscopy and normalization of the dynamic spectra" by Miroslaw A. Czarnecki. *Applied Spectroscopy* **2003**, 57, (1), 110-112.

56. Czarnecki, M. A., Some comments on the application of two-dimensional correlation spectroscopy and normalization of the dynamic spectra. *Applied Spectroscopy* **2003**, 57, (1), 107-109.

57. Diewok, J.; Ayora-Canada, M. J.; Lendl, B., 2D correlation spectroscopy and multivariate curve resolution in analyzing pH-dependent evolving systems monitored by FT-IR spectroscopy, a comparative study. *Analytical Chemistry* **2002**, 74, (19), 4944-4954.

58. Czarnecki, M. A., Two-dimensional correlation spectroscopy: Effect of reference spectrum on noise-free and noisy spectra. *Applied Spectroscopy* **2003**, 57, (8), 991-995.

59. Sasic, S.; Muszynski, A.; Ozaki, Y., A new possibility of the generalized two-dimensional correlation spectroscopy. 1. Sample-sample correlation spectroscopy. *Journal of Physical Chemistry A* **2000**, 104, (27), 6380-6387.

60. Shinzawa, H.; Morita, S.; Noda, I.; Ozaki, Y. In *Effect of the window size in moving-window two-dimensional correlation analysis*, 2006; Elsevier Science Bv: 2006; pp 28-33.

61. Ferraro, J. R.; Nakamoto, K.; Brown, C. W., *Introductory Raman Spectroscopy*. second ed.; Academic Press: Boston, 2003.

62. Noda, I., Determination of Two-Dimensional Correlation Spectra Using the Hilbert Transform. *Applied Spectroscopy* **2000**, 54, (7), 994-999.

63. Sasic, S.; Ozaki, Y., Comparison of principal component analysis and generalized two-dimensional correlation spectroscopy: Spectral analysis of synthetic model system and near-infrared spectra of milk. *Applied Spectroscopy* **2001**, 55, (1), 29-38.

64. Wang, Y. W.; Gao, W. Y.; Noda, I.; Yu, Z. W. In *A modified mean normalization method to reduce the effect of peak overlap in two-dimensional correlation spectroscopy*, 2006; Elsevier Science Bv: 2006; pp 128-133.

65. Wang, Y. W.; Gao, W. Y.; Wang, X. G.; Yu, Z. W. In *A novel normalization method based on principal component analysis to reduce the effect of peak overlaps in two-dimensional correlation spectroscopy*, 2008; Elsevier Science Bv: 2008; pp 66-72.

66. Goormaghtigh, E.; Ruysschaert, J. M.; Raussens, V., Evaluation of the information content in infrared spectra for protein secondary structure determination. *Biophysical Journal* **2006**, 90, (8), 2946-2957.

67. Frank, J., *Three-Dimensional Electron Microscopy of Macromolecular Assemblies*. 2 ed.; Oxford University Press: Oxford, 2006.

68. Shlens, J. *A Tutorial on Principal Component Analysis*; 2005.

69. Iqbal, Z.; Bulusu, S.; Autera, J. R., Vibrational-Spectra of Beta-Cyclotetramethylene Tetranitramine and Some of Its Isotopic Isomers. *Journal of Chemical Physics* **1974**, 60, (1), 221-230.

70. Aduev, B. P.; Belokurov, G. M.; Grechin, S. S.; Tupitsin, E. V., Electron beam induced explosive luminescence of PETN. *Technical Physics Letters* **2004**, 30, (8), 660-662.

71. Nagli, L.; Gaft, M., Raman scattering spectroscopy for explosives identification. *Proceedings of the SPIE - The International Society for Optical Engineering* **2007**, 6552, (1), 65520Z-1-65520Z-65520Z-10.

72. Cherney, D. P.; Ekman, D. R.; Dix, D. J.; Collette, T. W., Raman Spectroscopy-Based Metabolomics for Differentiating Exposures to Triazole Fungicides Using Rat Urine. In 2007; Vol. 79, pp 7324-7332.

73. Ichikawa, S.; Suda, J.; Sato, T.; Suzuki, Y., Lattice dynamics and temperature dependence of the first-order Raman spectra for alpha-SiO<sub>2</sub> crystals. *Journal of Raman Spectroscopy* **2003**, 34, (2), 135-141.

74. Shapiro, S. M.; Oshea, D. C.; Cummins, H. Z., Raman Scattering Study of Alpha-Beta Phase Transition in Quartz. *Physical Review Letters* **1967**, 19, (7), 361-&.

75. Knauer, M.; Carrara, M.; Rothe, D.; Niessner, R.; Ivleva, N. P., Changes in Structure and Reactivity of Soot during Oxidation and Gasification by Oxygen, Studied by Mi-

cro-Raman Spectroscopy and Temperature Programmed Oxidation. *Aerosol Science and Technology* **2009**, 43, (1), 1-8.

76. Brunetto, R.; Pino, T.; Dartois, E.; Cao, A. T.; d'Hendecourt, L.; Strazzulla, G.; Brechignac, P., Comparison of the Raman spectra of ion irradiated soot and collected extraterrestrial carbon. *Icarus* **2009**, 200, (1), 323-337.

77. Cornell, S. W.; Koenig, J. L., Raman Spectra of Polybutadiene Rubbers. *Macromolecules* **1969**, 2, (5), 540-&.

78. Long, G. T.; Vyazovkin, S.; Brems, B. A.; Wight, C. A., Competitive vaporization and decomposition of liquid RDX. *Journal of Physical Chemistry B* **2000**, 104, (11), 2570-2574.

79. Ng, W. L.; Field, J. E.; Hauser, H. M., Thermal, Fracture, and Laser-Induced Decomposition of Pentaerythritol Tetranitrate. *Journal of Applied Physics* **1986**, 59, (12), 3945-3952.

80. Zenin, A. A.; Finjakov, S. V., Characteristics of RDX combustion zones at different pressures and initial temperatures. *Combustion Explosion and Shock Waves* **2006**, 42, (5), 521-533.

81. Pitchimani, R.; Zheng, W.; Simon, S. L.; Hope-Weeks, L. J.; Burnham, A. K.; Weeks, B. L. In *Thermodynamic analysis of pure and impurity doped pentaerythritol tetranitrate crystals grown at room temperature*, 2007; Springer: 2007; pp 475-478.

82. Adams, G. F.; Shaw, R. W., Chemical-Reactions in Energetic Materials. *Annual Review of Physical Chemistry* **1992**, 43, 311-340.

83. Oxley, J. C.; Smith, J. L.; Zhou, Z. L.; McKenney, R. L., Thermal-  
Decomposition Studies on Nto and Nto/Tnt. *Journal of Physical Chemistry* **1995**, *99*,  
(25), 10383-10391.

84. Tanaka, J.; Yoshihara, K., Absorption and Fluorescence Spectra of Anthracene-s-  
Trinitrobenzene Complex Crystal. *Bulletin of the Chemical Society of Japan* **1965**,  
*38*, (5), 739-745.

85. Sharma, S. P.; Lahiri, S. C., Absorption spectroscopic and FTIR studies on EDA  
complexes between TNT (2,4,6-trinitrotoluene) with amines in DMSO and determi-  
nation of the vertical electron affinity of TNT. *Spectrochimica Acta Part a-Molecular  
and Biomolecular Spectroscopy* **2008**, *70*, (1), 144-153.

86. Phifer, C. C.; Schmitt, R. L.; Thorne, L. R.; Jr., P. H.; Parmeter, J. E. *Studies of the  
Laser-Induced Fluorescence of Explosives and Explosive Compositions*; Sandia Na-  
tional Laboratories: October 2006, 2006.

87. Hug, W. F.; Bhartia, R.; Tsapin, A.; Lane, A.; Conrad, P.; Sijapati, K.; Reid, R. D.,  
Water and surface contamination monitoring using deep UV laser induced native  
fluorescence and Raman spectroscopy. *Proceedings of the SPIE - The International  
Society for Optical Engineering* **2006**, *6378*, (1), 63780S-1-63780S-63780S-13.

88. Kneipp, K.; Kneipp, H.; Itzkan, I.; Dasari, R. R.; Feld, M. S., Ultrasensitive chemical  
analysis by Raman spectroscopy. *Chemical Reviews* **1999**, *99*, (10), 2957-+.

89. Lal, S.; Grady, N. K.; Kundu, J.; Levin, C. S.; Lassiter, J. B.; Halas, N. J., Tailoring  
plasmonic substrates for surface enhanced spectroscopies. *Chemical Society Reviews*  
**2008**, *37*, 898-911.

90. Le, F.; Brandl, D. W.; Urzhumov, Y. A.; Wang, H.; Kundu, J.; Halas, N. J.; Aizpurua, J.; Nordlander, P., Metallic Nanoparticle Arrays: A Common Substrate for Both Surface-Enhanced Raman Scattering and Surface-Enhanced Infrared Absorption. *ACS Nano* **2008**, 2, (4), 707-718.

91. Asher, S. A.; Johnson, C. R., Raman-Spectroscopy of a Coal Liquid Shows That Fluorescence Interference Is Minimized with Ultraviolet Excitation. *Science* **1984**, 225, (4659), 311-313.

92. Moskovits, M., Surface-Enhanced Spectroscopy. *Reviews of Modern Physics* **1985**, 57, (3), 783-826.

93. Polavarapu, L.; Xu, Q.-H., Water-Soluble Conjugated Polymer-Induced Self-Assembly of Gold Nanoparticles and Its Application to SERS. *Langmuir* **2008**, 24, 10608-10611.

94. Kneipp, K.; Wang, Y.; Dasari, R. R.; Feld, M. S.; Gilbert, B. D.; Janni, J.; Steinfield, J. I., Near-infrared surface-enhanced Raman scattering of trinitrotoluene on colloidal gold and silver. *Spectrochimica Acta Part a-Molecular and Biomolecular Spectroscopy* **1995**, 51, (12), 2171-2175.

## Chapter 3

### Interplay between Short-Chain and Long-Chain Branches

<b>3.1</b>	<b>INTRODUCTION.....</b>	<b>III-2</b>
<b>3.2</b>	<b>EXPERIMENTAL METHODS .....</b>	<b>III-6</b>
<b>3.2.1</b>	<b>Materials .....</b>	<b>III-6</b>
<b>3.2.2</b>	<b>Differential Scanning Calorimetry .....</b>	<b>III-8</b>
<b>3.2.3</b>	<b>X-ray Scattering.....</b>	<b>III-9</b>
<b>3.3</b>	<b>RESULTS .....</b>	<b>III-11</b>
<b>3.3.1</b>	<b>Differential Scanning Calorimetry .....</b>	<b>III-11</b>
3.3.1.1	Temperature Ramps .....	III-11
3.3.1.2	Isothermal Crystallization.....	III-12
<b>3.3.2</b>	<b>X-ray Scattering.....</b>	<b>III-16</b>
3.3.2.1	WAXS: Temperature Ramps .....	III-16
3.3.2.2	SAXS: Temperature Ramps.....	III-19
3.3.2.3	SAXS: Temperature Ramps with Isothermal Step .....	III-23
<b>3.4</b>	<b>DISCUSSION .....</b>	<b>III-26</b>
<b>3.4.1</b>	<b>Morphology Evolution during Cooling and Heating.....</b>	<b>III-26</b>
3.4.1.1	Primary-Irreversible Crystallization .....	III-27
3.4.1.2	Secondary-Irreversible Crystallization .....	III-29
3.4.1.3	Reversible Crystallization at Low Temperatures.....	III-31
3.4.1.4	Transition Temperatures .....	III-33
<b>3.4.2</b>	<b>DSC Double Melting .....</b>	<b>III-34</b>
<b>3.4.3</b>	<b>Effects of Molecular Characteristics.....</b>	<b>III-36</b>
3.4.3.1	Crystallinity.....	III-37
3.4.3.2	Long Period.....	III-38
3.4.3.3	DSC Crystallization Kinetics .....	III-39
<b>3.4.4</b>	<b>Implications for Flow-Induced Crystallization .....</b>	<b>III-40</b>
<b>3.5</b>	<b>CONCLUSION .....</b>	<b>III-41</b>
<b>3.6</b>	<b>APPENDIX—Crystalline and Amorphous Layer Thickness .....</b>	<b>III-44</b>
<b>3.7</b>	<b>ACKNOWLEDGEMENTS .....</b>	<b>III-45</b>
<b>3.8</b>	<b>REFERENCES.....</b>	<b>III-47</b>

### 3.1 INTRODUCTION

The ultimate physical properties of semicrystalline materials are directly related to their molecular characteristics. For example, a strong, opaque plastic bin and flexible, transparent wrap can be made from materials having identical chemical formulas. However, the molecular architecture of plastic wrap is quite different and is composed of many short-chain and long-chain branches; in comparison, the molecular architecture of the plastic bin is primarily branch-free.

Long-chain branches (LCB) are well known to affect the melt dynamics of a polymer,<sup>1, 2</sup> which becomes exceedingly important when semicrystalline materials are exposed to flow during processing.<sup>3-5</sup> Based on their relaxation rates, molecules in a flow field will be perturbed from their equilibrium configuration by varying degrees, sometimes resulting in the formation of oriented crystal nuclei.<sup>6, 7</sup> These thread-like precursors result in increased nucleation density and serve as a template for the formation of an oriented morphology with increased crystallization kinetics.<sup>8-12</sup> LCB materials provide an ideal system to probe the effects of melt dynamics because they relax through a hierarchy of motions;<sup>13</sup> for example, an H-polymer exhibits two relaxation processes—that of the arms followed by that of the backbone.<sup>14</sup> Systematic variation of melt relaxation times can be achieved through the synthesis of well-defined materials with controlled lengths and amounts of long-chain branching.

On an industrial scale, long-chain branched molecules can be synthesized using metallocene catalyst technology, which allows the incorporation of branches into the chain during polymerization.<sup>5, 15-19</sup> However, the resulting materials are far from mono-disperse ( $M_w/M_n > 2$ ) and the LCB content is not precisely controlled.<sup>2, 20</sup> Additionally,

metallocene materials have been found to contain a small amount of interchain and intrachain heterogeneities, leading to distributions of branches that are not entirely random.<sup>21</sup> In contrast, anionic polymerization followed by hydrogenation allows for the synthesis of fairly monodisperse ( $M_w/M_n < 1.1$ ) polyethylene molecules of well-defined architecture, such as star, H-, pom-pom, and comb polymers, similar to the ones used in this work.<sup>22-26</sup> These model polyethylenes were initially thought to be ideal systems for studies regarding melt dynamics.<sup>3</sup> However, in addition to long-chain branches, short-chain branching (SCB) are also incorporated into the chain; during the polymerization, a minimum 8% of the ethylene addition is 1,2 versus the standard 1,4 addition, resulting in a random distribution of ethyl side groups (Figure 3.1).<sup>27, 28</sup> The resulting molecules are termed hydrogenated polybutadienes (HPBDs) because they are chemically equivalent to random, homogeneous ethylene-co-butene copolymers with a minimum of 7 wt % butene.

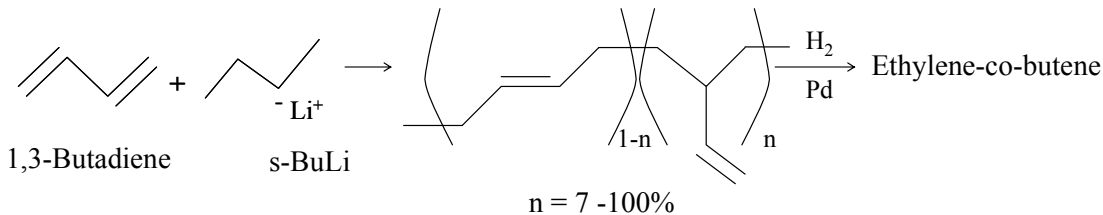


**Figure 3.1** HPBD synthesis via anionic polymerization followed by hydrogenation.

The presence of short-chain branches complicates the application of HPBD materials to probe melt dynamics since LCB effects must be isolated from SCB effects. On the other hand, these model systems allow for well-defined studies of the interplay between long-chain and short-chain branches. These systems can be used to gain further understanding of highly industrially-relevant materials like low density polyethylene (LDPE), which contains many short-chain and long-chain branches and is used abundantly for all-purpose containers, machinable plastic parts, and computer components.

Short-chain branches directly affect crystallinity and have very pronounced effects on the structure and properties of semicrystalline materials,<sup>29-32</sup> spurring investigations of linear, homogenous copolymers. The presence of short-chain branches results in increased flexibility and toughness as a consequence of decreased crystallinity.<sup>29, 30, 33-35</sup> The melting point decreases with increasing SCB content due to decreased crystal size,<sup>4, 36, 37</sup> which leads to a deteriorated morphology.<sup>30, 32, 37, 38</sup> Under quiescent conditions, molecules with increased SCB content form thinner lamellae with decreased lateral dimensions and lose the ability to organize into super-molecular structures, such as spherulites. At sufficiently high concentrations (>8 mol % comonomer<sup>32</sup>), crystallization is limited to neighboring ethylene sequences resulting in bundle-like crystals often termed fringed micelles. All of these observations are the result of the exclusion of short-chain branches from the crystal when the branches are longer than a methyl group (methyl groups are incorporated into the crystal lattice to a substantial degree resulting in distorted unit cells<sup>33, 34, 39-42</sup>). Similar behavior has been observed between HPBD and LCB-free metallocene copolymers, which have been studied containing ethyl, butyl, and octyl branches.<sup>43, 44</sup> Accordingly, in most cases the branch length was found to be irrelevant since their primary role is as defects.<sup>34, 39, 41, 45, 46</sup> Some authors argue that ethyl branches are incorporated into the crystal to a small degree,<sup>47-49</sup> however, this effect must be minor since evidence of this is not always observed. The consequence of the exclusion of chain defects is that crystallization is governed by the ethylene sequence length distribution (ESLD) between these short-chain branches. The ESLD dictates the availability of ethylene units having sufficient length to crystallize at a given temperature and is more important than copolymer composition.<sup>34, 46, 50, 51</sup>

Due to the dependence on ESLD, random copolymers exhibit several behaviors that distinguish them from homopolymers. In contrast to homopolymers, the morphology and thermal properties of copolymers are fairly insensitive to crystallization conditions.<sup>43, 52</sup> Furthermore, this sensitivity decreases with increasing SCB content.<sup>30, 53</sup> As discussed below, in contrast to homopolymers, crystallization kinetics of copolymers appears to be only weakly dependent on melt dynamics. Additionally, there is on-going debate about the evolution of morphology during crystallization due to the unusual observation of dual melting endotherms by Differential Scanning Calorimetry (DSC) following isothermal crystallization.

Initial theories to account for this double melting behavior of copolymers centered on the melting-recrystallization-remelting (mrr) phenomenon that is commonly observed in thin homopolymer crystals.<sup>54</sup> However, careful DSC studies have indicated that the distinct double melting behavior (e.g., Figure 3.5) is not the result of mrr.<sup>21, 34, 43, 45, 55-59</sup> While mrr has been confirmed for copolymers with a small amount of short-chain branching, the phenomenon is manifested as an additional third peak that is much smaller in magnitude and only observed at low heating rates.<sup>60, 61</sup> Presently, double melting is commonly attributed to two crystal populations having different thermal stabilities.

A number of theories have been presented to account for the differences in thermal stability of crystals supposedly formed at the same isothermal temperature ( $T_c$ ). One widespread theory advocates differences in morphology between the two populations: ethylene sequences that are long enough to rapidly chain-fold into lamellae while those that are shorter, but are still capable of crystallization at  $T_c$ , crystallize much slower with nearest-neighbor ethylene sequences into fringed micelles.<sup>43, 45, 52, 55, 61</sup> Another theory is

that the two populations contain equal lamellar thicknesses but a bimodal distribution of density and surface characteristics.<sup>62</sup> An alternative explanation is based on a bimodal lamellar thickness distribution: longer ethylene sequences crystallize rapidly forming thick lamellae while thinner, less thermally stable lamellar crystals form slowly from shorter ethylene sequences.

In the present work, we examine double melting behavior and other aspects of crystallization of HPBDs of different molecular architectures (short linear, long linear, star, and H-polymer). We investigate the effect of long-chain branching on thermal and morphological properties in these model systems. Accounting for previous studies, morphology evolution both during temperature ramps and under isothermal conditions is re-evaluated. Finally, we comment on the implications of our findings on the use of these materials as model systems for studying the effects of melt dynamics on flow-induced crystallization.

## 3.2 EXPERIMENTAL METHODS

### 3.2.1 Materials

The majority of the materials used in these studies are hydrogenated polybutadienes (HPBDs) that were synthesized via anionic polymerization followed by hydrogenation. This method, in conjunction with hydrosillation, allows for the synthesis of molecules that are well-defined in both long-chain branching (LCB) and molecular weight ( $PDI = M_w/M_n < 1.1$ ).<sup>22,27</sup> The resulting materials are analogous to random ethylene-co-butenes with a minimum of 7 wt % butene—in other words, 19 or more ethyl side groups per 1000 backbone carbon atoms. HPBD materials were graciously provided by

ExxonMobil in collaboration with Professor Nikos Hadjichristidis (University of Athens, Athens, Greece) and characterized by Dr. David Lohse and his team (ExxonMobil, Clinton, NJ).

**Table 3.1 Molecular characteristics of polyethylene materials examined. All values provided by ExxonMobil.**

Polymer	Type	$M_{w,tot}$ (kg/mol)	PDI	$M_{w,b}$ (kg/mol)	$M_{w,a}$ (kg/mol)	SCB/ 1000 back- bone C <sup>a</sup>
L53	Linear	53	<1.05	53		19.2
L152	Linear	152	<1.05	152		19.5
S3	3-arm star	141	<1.05		47	18.9
H4	H-polymer	156	<1.05	112	11	26.3
HDPE	Linear	529	3.0	529		0.2

<sup>a</sup> obtained via  $^{13}\text{C}$  NMR

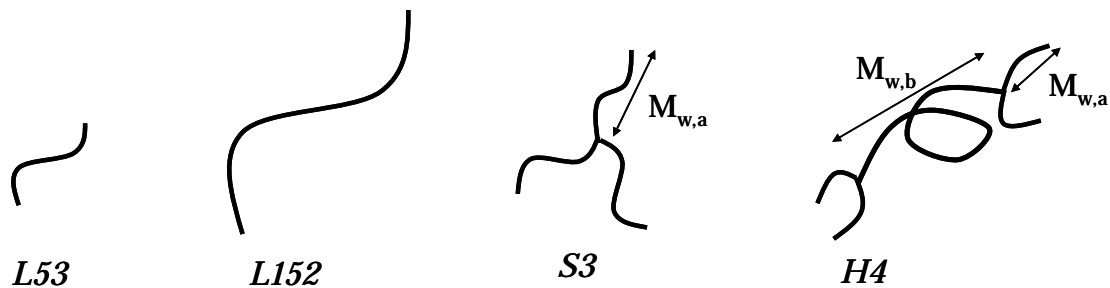


**Figure 3.2** Schematic representation of the four HPBD materials examined: short linear (L53), long linear (L152), 3-arm star (S3), and H-polymer (H4).

Quiescent crystallization was studied on four HPBDs (Table 3.1): two linear chains (L53 and L152) and two molecules containing long-chain branches—a symmetric, three-arm star (S3) with each arm having molecular weight ( $M_{w,a}$ ) of 47 kg/mol and an H-polymer (H4) with a backbone molecular weight ( $M_{w,b}$ ) of 112 kg/mol and two 11 kg/mol arms on each end (Figure 3.2). In this context, ‘linear’ refers to molecules that are free from LCB; as mentioned above, all chains contain short-chain branches (SCB). It is important to note that L53, L152, and S3 all contain approximately 19 branches per

1000 carbon atoms—the minimum SCB content accessible via anionic polymerization. The H4 polymer has higher overall SCB content than the rest, despite having arms with similar SCB content to the previous three samples; the difference originates from the synthetic route to the telechelic backbone, which results in higher SCB content along the backbone. Consequently, the H4 molecule has a homogenous SCB distribution within each long branch but not within each molecule. Additionally, high density polyethylene (HDPE) was included for comparison (no LCB and very few SCB).

Comparison of these molecules enables elucidation of the effects of molecular weight (L53 versus L152) and long-chain branching (L152 versus S3). Effects of short-chain branching are difficult to isolate because the comparison of L152 or S3 to H4 is more complicated due to the combined effects of LCB, overall SCB content, and intramolecular SCB distribution. However, in most cases, SCB effects can be inferred based on prior literature.

### **3.2.2 Differential Scanning Calorimetry**

Differential Scanning Calorimetry (DSC) experiments were conducted by Dr. Soo-Young Park (Kyunpook National University, Daegu, South Korea) to study thermal transitions of each polymer (5-10 mg samples) using a Perkin Elmer 7 DSC system calibrated with an indium standard. Both temperature ramps and isothermal studies were conducted under a nitrogen atmosphere. Peak melting and crystallization temperatures were obtained during cooling and subsequent heating ramps performed at 10 °C/min from 140 to 40 °C. Additional scans at 10 °C/min were conducted by Dr. Manika Varma-Nair (ExxonMobil, Clinton, NJ) in a larger temperature range of 160 to -30 °C.

Isothermal crystallization was conducted at a variety of temperatures for each polymer. After erasing thermal history at an elevated temperature of 130 °C, a 5-10 mg sample was cooled to the desired crystallization temperature,  $T_c$ , at 40 °C/min. The sample was left at this temperature for 30 minutes and then heated at 10 °C/min; heat flow was monitored throughout the experiment. Additional isothermal studies were conducted by Robert Panepinto (ExxonMobil, Clinton, NJ) for independent validation using the same isothermal temperatures but a higher temperature (140 °C) to erase thermal history and a faster cooling rate (~200 °C/min) to  $T_c$ .

### 3.2.3 X-ray Scattering

Morphology development during heating and cooling ramps was followed using wide angle and small angle x-ray scattering (WAXS and SAXS, respectively). An INSTECH STC200 hot stage was used to subject samples to temperature ramps at 10 °C/min in a range of 160 to 0 °C. Samples were placed between Kapton tape into a holder with 0.5 cm diameter and 1.558 mm thickness. Additional SAXS experiments, termed ‘ramp-iso’, included temperature ramps (10 °C/min) with a 30-minute, isothermal step at a temperature approximately 16 °C below  $T_m$  (apparent subcooling,  $\Delta T = T_m - T_c \approx 16$  °C). There isothermal temperatures were  $T_c = 95$  °C for L53,  $T_c = 87$  °C for L152 and S3, and  $T_c = 76$  °C for H4. For comparison, L53 was also subjected to the same ramp with an isothermal step at 102 °C—the highest isothermal DSC temperature at which two melting peaks were observed.

Scattering experiments were carried out at beamline X27C of the National Synchrotron Light Source (NSLS, Brookhaven National Lab, Upton, NY).<sup>63</sup> A MARCCD

detector with 158  $\mu\text{m}$  pixel size was used to record two-dimensional scattering patterns generated with x-rays having a wavelength,  $\lambda$ , of 1.371  $\text{\AA}$ . For WAXS experiments, the detector was placed 11.4 cm from the sample and camera length was calibrated using aluminum oxide ( $\text{Al}_2\text{O}_3$ ). For SAXS, the sample-to-detector distance was 1.9 m, and calibration was conducted using silver behenate. One scattering image was collected every 2  $^{\circ}\text{C}$ .

SAXS data during temperature ramps for H4 were obtained at beamline 7.3.3 of the Advanced Light Source (ALS, Lawrence Berkeley National Lab, Berkeley, CA).<sup>64</sup> Scattering data was collected using an ADSC Quantum 4u CCD detector at a distance of 2.84 m and a source wavelength,  $\lambda$ , of 1.371  $\text{\AA}$ . The sample-to-detector distance was calibrated using silver behenate. A Linkam calorimetry stage was used to subject samples pressed in aluminum pans to temperature ramps at 10  $^{\circ}\text{C}/\text{min}$  from 160 to 0  $^{\circ}\text{C}$  while measuring heat flow. One scattering image was collected every 7  $^{\circ}\text{C}$ . Data collected at both beamlines for L53 and S3 were compared for consistency.

X-ray data pre-treatment included the subtraction of a background and adjustment for incident x-ray beam flux and acquisition time. The integrated intensity was extracted as a function of scattering vector,  $q = 4\pi\sin(\theta)/\lambda$ , where  $\theta$  is the scattering angle. Since the samples were isotropic, a Lorentz correction<sup>65</sup> was applied by multiplying the scattering intensity,  $I(q)$ , by the square of scattering vector,  $q$ :  $J(q) = I(q)q^2$ .

The SAXS long period,  $L_p$ , was determined from the position of the peak in  $J(q)$ ,  $q_{max}$ , as:  $L_p = 2\pi/q_{max}$ . The long period is a measure of the periodicity within the sample resulting from electron density differences and is interpreted as a characteristic spacing of crystalline and non-crystalline domains for a two-phase system. The area under the Lor-

entz-corrected SAXS intensity curve (for isotropic samples) in the full range of  $q$  ( $0 < q < \infty$ ) defines the invariant, which is a measure of the total scattering power of the sample. Given the experimental constraints, we approximate the invariant by the integrated intensity,  $Q$ , in the range available ( $q_{min} < q < q_{max}$ ):

$$Q = \int_{q_{min}}^{q_{max}} q^2 I(q) dq . \quad (3.1)$$

The WAXS crystallinity index,  $X_c$ , was determined as the ratio of the area of the crystalline peaks,  $A_c$ , to the combined area of the amorphous halo,  $A_a$ , and the crystalline peaks:  $X_c = A_c/(A_a+A_c)$ . Areas were obtained after fitting the amorphous halo and the orthorhombic crystal reflections due to the (110)- and (200)-planes with Lorentzian functions using Origin 7.5. X-ray data analysis was conducted using code written in MATLAB R2008b (Thesis Appendix A).

### 3.3 RESULTS

#### 3.3.1 Differential Scanning Calorimetry

##### 3.3.1.1 Temperature Ramps

Heating and cooling traces for each material are shown in Figure 3.3. In agreement with prior literature, the crystallization exotherms for the HPBD materials contain two peaks: the primary peak at higher temperatures ( $T_{x,high}$ ) and a much smaller peak at lower temperatures ( $T_{x,low}$ ; marked by asterisks in Figure 3.3a).<sup>45, 66</sup> The low crystallization peak is least prominent for H4. Upon subsequent heating, only one broad peak is observed. Nearly identical behavior is observed for L152 and S3. As expected, HPBDs exhibit smaller, broader DSC peaks as a consequence of the ethylene sequence length dis-

tribution.<sup>21, 32, 43, 45, 52, 57, 67</sup>

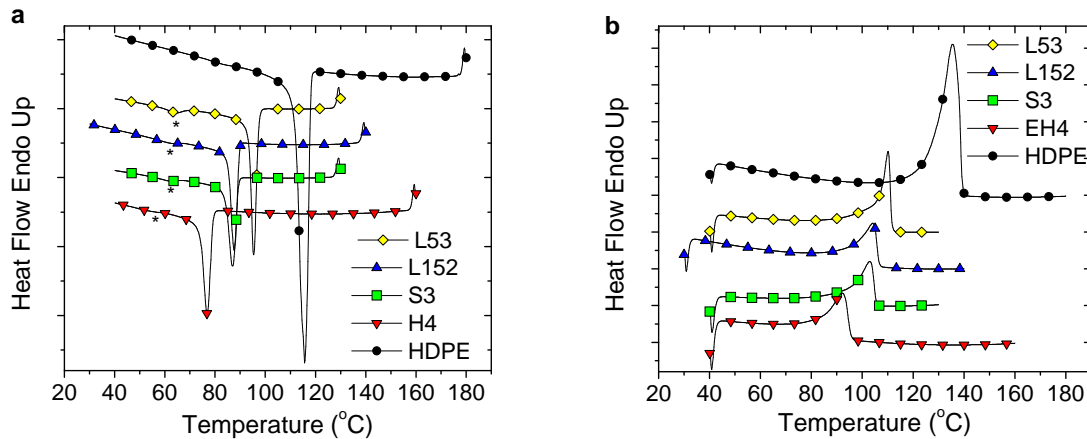


**Figure 3.3** DSC **a)** cooling and **b)** heating traces obtained at 10 °C/min. Asterisks mark  $T_{x,low}$ .

Corresponding peak melting and crystallization temperatures ( $T_m$  and  $T_x$ , respectively) for each material are tabulated in Table 3.2. All three transition temperatures decrease with both increasing molecular weight (L53 vs. L152) and SCB content (L152 vs. H4), as has been observed previously as a consequence of decreased crystal size.<sup>21, 30, 32, 35, 36, 44, 48, 52</sup> Transition temperatures for L152 and S3 are nearly identical.

**Table 3.2 Peak transition temperatures obtained by DSC during heating and cooling ramps at 10 °C/min.**

Polymer	$T_{x,low}$ (°C)	$T_{x,high}$ (°C)	$T_m$ (°C)
L53	64.3	95.3	110.2
L152	61.8	87.6	104.4
S3	61.5	87.0	102.9
H4	56.6	76.8	92.2
HDPE		117.7	135.7

### 3.3.1.2 Isothermal Crystallization

Crystallization kinetics of each material were examined during isothermal crystallization. As done by Haigh et al.,<sup>68</sup> the time necessary to reach 10% of the maximum crystallinity ( $t_{0.1}$ ) at a given temperature was taken as a measure of the crystallization rate.

From Figure 3.4, it is clear that HDPE exhibits the fastest crystallization kinetics, as expected, while H4 exhibits the slowest. In agreement with Haigh et al., L53 has the fastest kinetics out of the HPBDs examined due to its low molecular weight.<sup>35, 68</sup> Differences in crystallization kinetics due to the presence of long-chain branching, expected based on prior literature,<sup>4, 68, 69</sup> were not immediately observed since L152 and S3 exhibited very similar behavior.

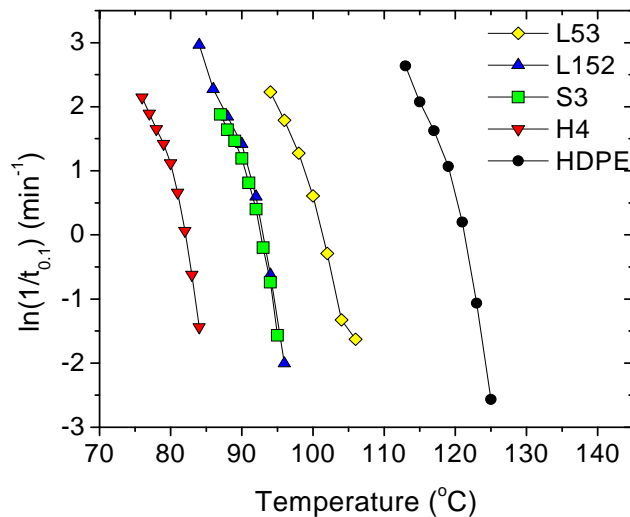


**Figure 3.4** Crystallization kinetics represented as the amount of time necessary to reach 10% maximum crystallinity ( $t_{0.1}$ ) as a function of the isothermal crystallization temperature.

Melting traces following isothermal crystallization of HPBD materials are characterized by two peaks, high-melting ( $T_{m,\text{high}}$ ) and low-melting ( $T_{m,\text{low}}$ ), at all but the highest crystallization temperatures examined.<sup>21, 43, 45, 55, 70</sup> When comparing traces at similar apparent undercoolings,  $\Delta T = T_m - T_c$ , the magnitude of both peaks appears to be only a function of molecular weight and not SCB content or distribution. As an example, melting traces for each sample isothermally crystallized at  $\Delta T = 16$  °C are shown in Figure 3.5. Aside from HDPE, which only exhibits the expected single melting peak, L53 has

the largest high-melting peak. Again L152 and S3 possess nearly identical traces.

The melting trace for H4, although shifted to lower temperatures due to increased SCB content, is very similar to the two HPBDs of similar molecular weight. Closer examination, however, reveals a larger low-melting peak for H4 than for L152 and S3.

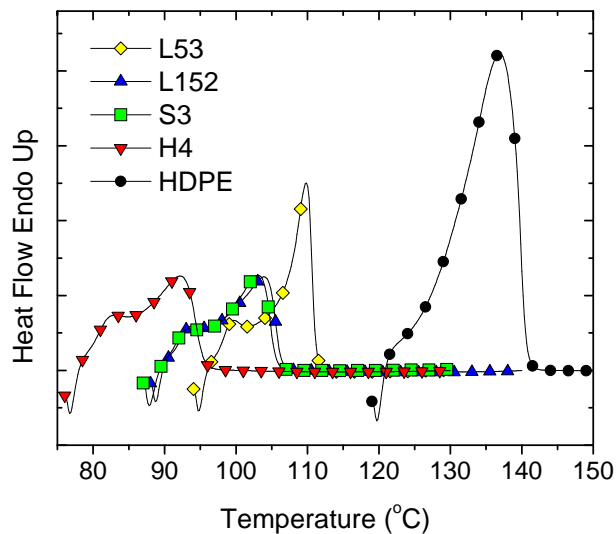


**Figure 3.5** DSC melting traces obtained during heating at 10 °C/min following isothermal crystallization for each material at  $T_c = T_m - 16$  °C.

An examination of the dependence of both melting peak temperatures on the isothermal crystallization temperature reveals interesting behavior typical of copolymers (Figure 3.6). Plotting melting point as a function of the isothermal crystallization temperature (sometimes called a Hoffman-Weeks plot) is often used to determine the equilibrium melting temperature of a semicrystalline polymer. For homopolymers like HDPE, extrapolating  $T_m$  versus  $T_c$  to the melting temperature of a perfect crystal (i.e., the intersection of a linear fit through  $T_m$  versus  $T_c$  with the  $T_m = T_c$  line) reveals the equilibrium melting temperature.<sup>71, 72</sup> However, this procedure fails when applied to either melting peak of copolymers.<sup>43, 44, 73</sup> The high-melting peak appears nearly independent of the iso-

thermal crystallization temperature, while the low-melting peak is parallel to  $T_m = T_c$ .<sup>47, 58, 61, 70</sup>

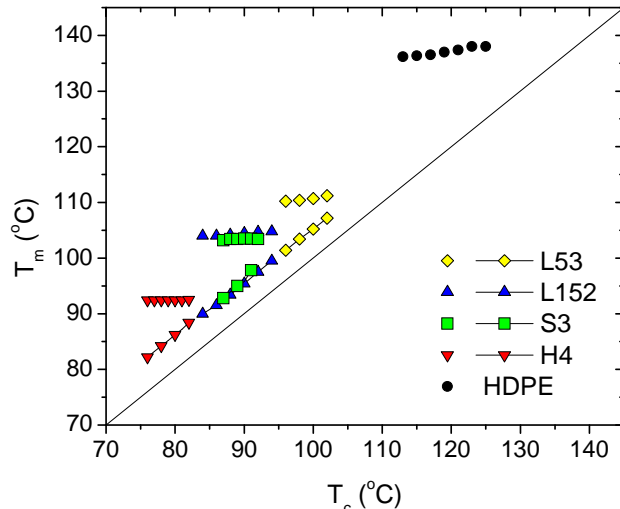


**Figure 3.6** Peak high-melting (symbols) and low-melting (line + symbols) temperatures as a function of isothermal crystallization temperature ( $T_c$ ) obtained during heating in DSC at 10 °C/min.

The average high-melting peak value ( $T_{m,\text{high}}$ ) for each material is insensitive to  $T_c$ , in agreement with past literature,<sup>43, 70</sup> and is very similar to the peak melting temperature obtained during temperature ramps (Table 3.3 versus Table 3.2).<sup>43</sup> The extent to which  $T_{m,\text{high}}$  changes with  $T_c$ , characterized by the approximate slope of  $T_{m,\text{high}}$  versus  $T_c$ ,  $\Delta T_{m,\text{high}}/\Delta T_c$  (Table 3.3), is greatest for the short linear HPBD and least for the H-polymer.

**Table 3.3 Average high-melting peak ( $T_{m,\text{high}}$ ) obtained during heating at 10 °C/min subsequent to isothermal crystallization and its dependence on the change in the isothermal crystallization temperature.**

Sample	$T_{m,\text{high}}$ (°C)	$\Delta T_{m,\text{high}}/\Delta T_c$
L53	$110.5 \pm 0.5$	0.23
L152	$104.4 \pm 0.4$	0.08
S3	$103.4 \pm 0.1$	0.06
H4	$92.4 \pm 0.1$	0.02

The low-melting peak ( $T_{m,low}$ ) appears to be offset from the isothermal crystallization temperature by a constant (Figure 3.6).<sup>43, 55, 59, 60, 74</sup> This constant appears to be independent of not only SCB content and molecular weight, as demonstrated by Alamo et al.,<sup>44</sup> but also long-chain branching.

### 3.3.2 X-ray Scattering

#### 3.3.2.1 WAXS: Temperature Ramps

A comparison of the temperature dependence of the WAXS crystallinity,  $X_c$ , during temperature ramps revealed a strong dependence on SCB content (Figure 3.7).<sup>29, 30, 33-35</sup> Additionally, two types of behavior were observed: (1) the expected hysteresis in crystallinity during cooling and heating at elevated temperatures termed ‘irreversible’ crystallization and melting because crystals formed during cooling required higher temperatures to melt and (2) ‘reversible’ crystallization and melting at lower temperatures where crystallinity values during cooling and subsequent heating overlap. These two regimes are consistent with previous DSC, SAXS, and WAXS studies on polyethylenes containing short-chain branches.<sup>45, 62, 66, 67, 75, 76</sup>

The presence of short-chain branching in L152 results in a decreased transition temperature between reversible and irreversible behavior,  $T_{r,w}$  (defined as the temperature at which crystallinity upon cooling and subsequent heating differs by less than 10%), compared to HDPE (Figure 3.7). A small amount of reversible crystallization of HDPE (~15%), occurring between  $T_{r,w}$  and 0 °C, is attributed to surface crystallization/melting.<sup>75, 77</sup> In contrast, reversible crystallization accounts for a greater percentage of total crystallinity at 0 °C in L152 (~25%). Additionally, irreversible crystallization and

melting of L152 occurs over a larger temperature range than HDPE because it is governed by the ESLD.<sup>50,78</sup> Of added interest is the lull in crystallinity evolution apparent at temperatures immediately above  $T_{r,w}$  in all HPBD materials examined (marked by an asterisks in Figure 3.7). Possible explanations for this observation are detailed in the discussion section.

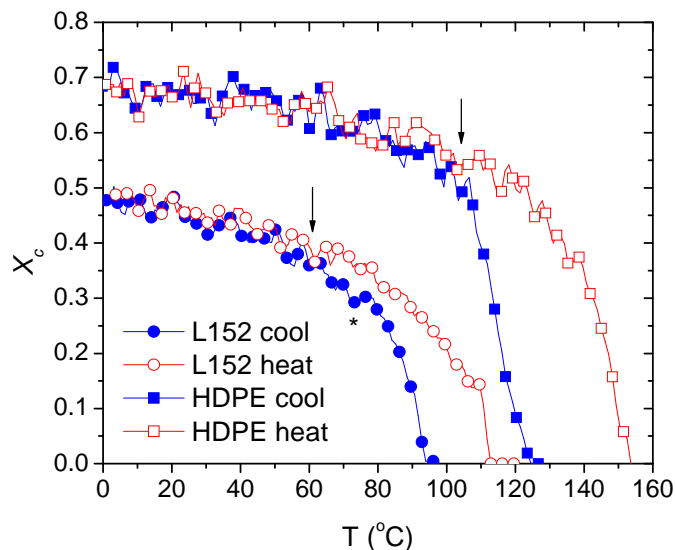


**Figure 3.7** Crystallinity determined by WAXS as a function of temperature during heating and cooling ramps of L152 and HPDE at 10 °C/min. Arrows indicate  $T_{r,w}$ . Asterisk marks lull in crystallinity evolution.

A comparison between the four HPBD materials reveals that  $T_{r,w}$  is greatest for L53 ( $71 \pm 3$  °C) and is within the range of  $62.8 \pm 3.8$  °C for the higher molecular weight HPBDs, with S3 being at the high end of the range (Figure 3.8, open triangles). The similarity of  $T_{r,w}$  between L152 and H4 is inconsistent with previous observations of the transition temperature decreasing with increasing SCB content.<sup>45</sup> The corresponding crystallinity at  $T_{r,w}$ ,  $X_c(T_{r,w})$ , is similar for the three materials of similar SCB content (L53, L152, and S3) at  $39 \pm 4\%$  (Figure 3.8, filled squares). As expected, H4 exhibits lower crystallin-

ity ( $31 \pm 3\%$ ) due to its increased SCB content.<sup>29, 30, 33, 34</sup> A similar trend is observed at  $T = 0^\circ\text{C}$  ( $X_c(0^\circ\text{C})$  in Figure 3.8, filled circles). The slightly elevated crystallinity of S3 compared to L152 at  $0^\circ\text{C}$  can be attributed to the small difference in SCB content between the two materials (18.9 for S3 versus 19.5 for L152; Table 3.1) and further highlights the significance of short-chain branching. The relative amount of reversible crystallization appears to be in the same range for all four materials, with S3 again being at the high end of the range (difference between filled circles and squares in Figure 3.8). This observation is inconsistent with previous works that found that the relative amount of reversible crystallization increases with increasing SCB content.<sup>45, 75, 79</sup>

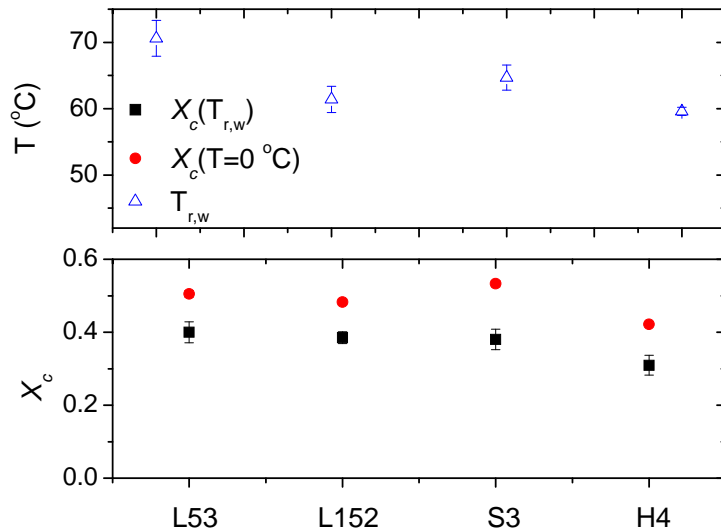


**Figure 3.8** WAXS-determined transition temperature ( $T_{r,w}$ ) to reversible crystallization, the crystallinity at that temperature ( $X_c(T_{r,w})$ ), and the maximum crystallinity obtained ( $X_c(0^\circ\text{C})$ ) for each HPBD material.

### 3.3.2.2 SAXS: Temperature Ramps

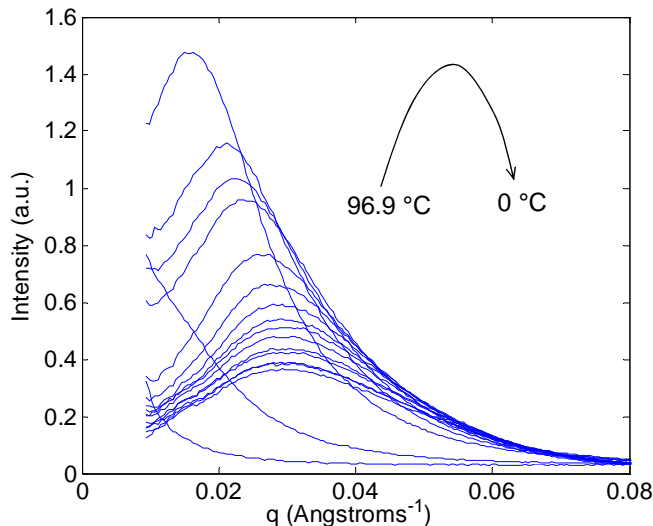


**Figure 3.9** SAXS intensity collected during cooling of L152 at 10 °C/min (1 trace every ~6 °C). Arrow shows general peak movement in temperature range examined.

SAXS scattering curves exhibited significant variation in peak height, width, and position with temperature (e.g., Figure 3.9), as seen in previous investigations of polyethylenes containing short-chain branching.<sup>66, 80-83</sup> An example of the general trend is exhibited by L152 during a cooling ramp. Initially, SAXS intensity,  $I(q)$ , grows at low  $q$ -values, corresponding to zero scattering angle, similar to HDPE,<sup>84, 85</sup> then a peak develops and grows in intensity while its position moves to higher  $q$ -values; eventually, it reaches a maximum and declines while broadening and moving further to higher values of  $q$ . At lower temperatures, the peak position reaches a plateau at  $q \sim 0.033 \text{ \AA}^{-1}$  but continues to broaden at the expense of peak height.

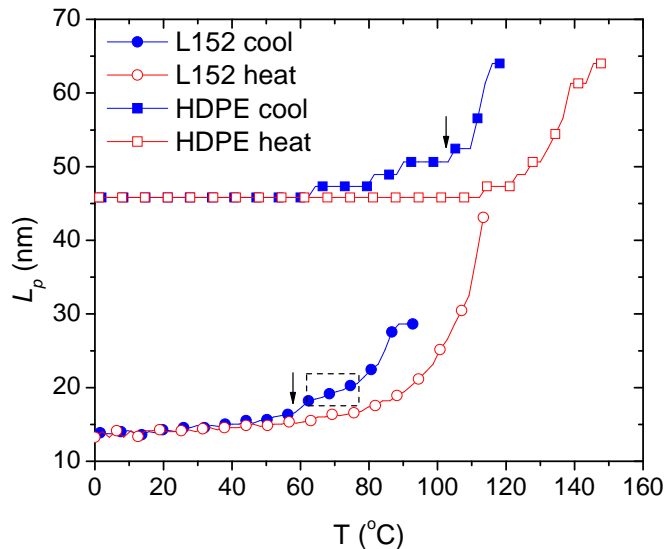


**Figure 3.10** Long period as a function of temperature during heating and cooling ramps of L152 and HPDE at 10 °C/min. Box identifies lull in long period evolution. Arrows mark  $T_{r,s}$ .

The long period,  $L_p$ , determined by SAXS of all materials examined exhibited regions corresponding to reversible and irreversible crystallization (Figure 3.10), similar to crystallinity evolution (Figure 3.7).<sup>67, 80</sup> However, during reversible crystallization, the long period of HDPE remains constant while that of HPBD materials continues to decrease, as has been observed previously.<sup>48, 79, 80, 83, 86-88</sup> Below the transition temperature,  $T_{r,s}$  (defined as the temperature at which the difference in long period during cooling and subsequent heating is less than 10%), the HDPE long period varies less than 2%. In contrast, the long period of L53 decreases by 8%, that of L152 and S3 by 14%, and that of H4 by 23%. The transition temperature itself follows a similar trend: largest for L53, lowest for H4, and of similar intermediate values for L152 and S3 (Figure 3.11, open triangles). Consequently,  $T_{r,s}$  and the amount of change in  $L_p$  during reversible crystallization appear to be a function of molecular weight and SCB content, but not long chain

branching.

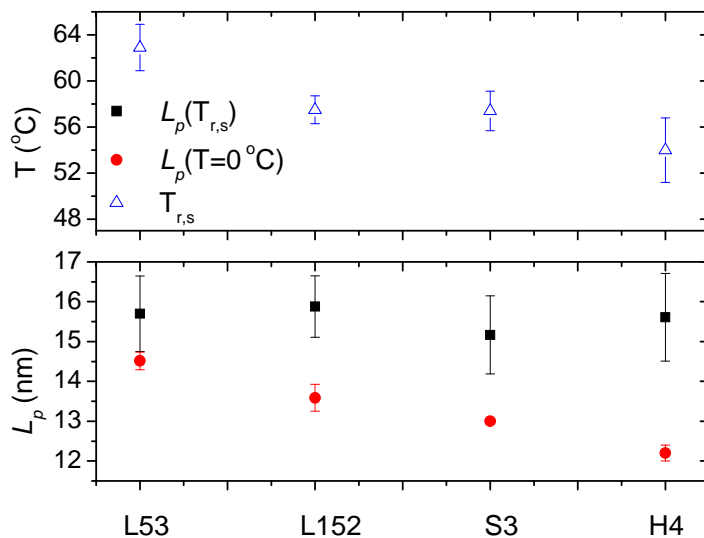


**Figure 3.11** SAXS-determined transition temperature ( $T_{r,s}$ ) to reversible crystallization, the long period at that temperature ( $L_p(T_{r,s})$ ), and the minimum long period obtained ( $L_p(0\text{ }^{\circ}\text{C})$ ) for each HPBD material.

All HPBD materials exhibit a similar long period at  $T_{r,s}$ ,  $L_p(T_{r,s})$ , of  $15.5 \pm 1$  nm (Figure 3.11, filled squares). In contrast, the long period at  $T = 0\text{ }^{\circ}\text{C}$ ,  $L_p(0\text{ }^{\circ}\text{C})$ , appears to be dependent on molecular weight, short-chain and long-chain branching with  $L53 > L152 > S3 > H4$ . The variation among the first 3 materials is inconsistent with the work of Alamo et al. who observed similar room-temperature long periods for samples of similar SCB content but different molecular weight.<sup>44</sup>

All four HPBD materials examined exhibited a lull in the evolution of long period during crystallization, which is highlighted in Figure 3.10. When observed in a previous study, this inflection in  $L_p$  versus  $T$  was attributed to the transition of the system to a homogenous crystallinity distribution.<sup>66</sup> In agreement with this previous study, the increased change in long period at temperatures immediately below this lull is near the low crystal-

lization temperature observed by DSC ( $T_{x,low}$ ; Figure 3.3 and Table 3.2). Furthermore, this inflection point coincides with the maximum in the SAXS integrated intensity (Figure 3.12), which also exhibits reversible and irreversible crystallization/melting.

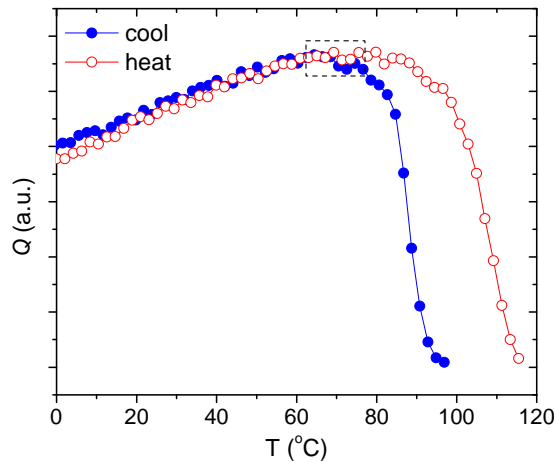


**Figure 3.12** SAXS integrated intensity during cooling and heating of L152 at 10 °C/min. Box identifies region corresponding to lull in long period evolution (Figure 3.10).

A final observation of interest is the difference in transition temperatures between irreversible and reversible behavior as determined by WAXS crystallinity, SAXS integrated intensity, and long period. The transition temperature to reversible integrated intensity behavior is the highest of the three and occurs near the maximum of the scattering power during cooling. The temperature to reversible crystallinity evolution is higher than that of long period evolution indicating that there is a small window upon cooling and heating during which the formation of reversible crystals leads to irreversible changes in long period.

### 3.3.2.3 SAXS: Temperature Ramps with Isothermal Step

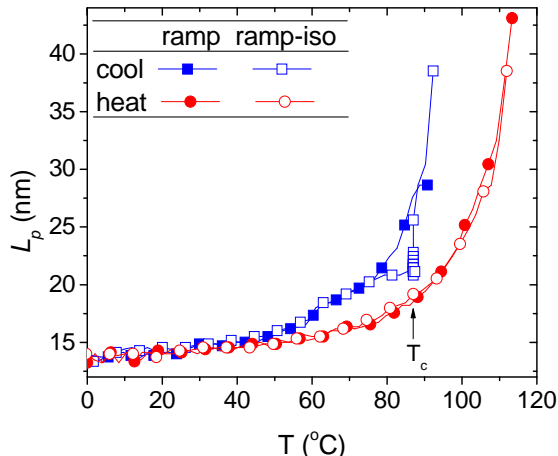


**Figure 3.13** Evolution of SAXS long period for L152 during temperature ramps at 10 °C/min (filled symbols) and the ramp-iso protocol with an isothermal step at  $T_c = 87$  °C during cooling (open symbols).

Further insight into the crystallization behavior of these materials may be gained by inserting an isothermal step during cooling (“ramp-iso” protocol). During the hold at  $T_c$ , the long period decreased to a limiting value (e.g., L152 in Figure 3.13). For L152,  $L_p$  decreased from approximately 26 to 21 nm during the 30 minute hold at 87 °C. Once cooling was resumed, a short induction period was observed before the long period continued to decrease; the evolution of  $L_p$  during further cooling coincided with that observed in a continuous ramp (compare filled and open squares for  $T < 75$  °C in Figure 3.13). Long period evolution during subsequent heating traces was very similar for both protocols (open vs. filled circles in Figure 3.13), in agreement with previous works indicating minimal effects of thermal and mechanical history on random copolymers.<sup>52,62,86,89</sup> A reversible crystallization region was still observed. Similar behavior as depicted above was observed for the other HPBDs.

During the 30-minute isothermal hold at similar apparent subcooling  $\Delta T = T_m - T_c = 16$  °C, L152 unexpectedly developed a long period that was larger by almost 1 nm compared with L53 and S3 (Figure 3.14). The long period obtained for S3 was only slightly smaller than that of L53. Due to its high nominal melting point, L53 was anticipated to develop morphology with the largest characteristic length scale out of the trio.

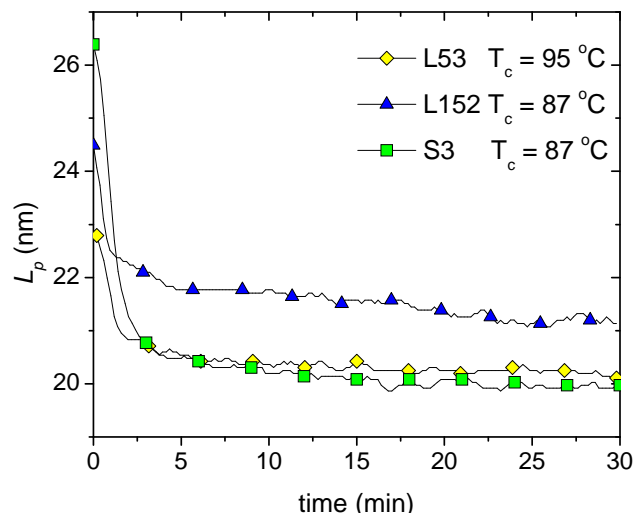


**Figure 3.14** Long period of HPBD materials as a function of time during isothermal crystallization at  $T_c = T_m - 16$  °C inserted into a cooling ramp at 10 °C/min.

Further insight into evolution of morphology can be gained through the examination of scattering patterns corresponding to the first two minutes of the isothermal step (Figure 3.15). No noticeable crystallization occurred during cooling to a lower  $\Delta T$  (L53 at 102 °C, Figure 3.15a); during the first two minutes, SAXS intensity increased while peak position only shifted slightly, consistent with isothermal growth dominated by a single long spacing. Upon reaching  $\Delta T \sim 16$  °C, each material already possessed a well-defined long period (Figure 3.15b, c, and d). For L53 and S3, scattering intensity initially increased at all  $q$ -values. L53 exhibited growth in peak intensity in conjunction with mild

peak position shifting until crystallization slowed significantly (evidenced by highly overlapped scattering curves in Figure 3.15b). In contrast to S3 and L152, L53 did not exhibit any obvious decrease of SAXS intensity during isothermal treatment.

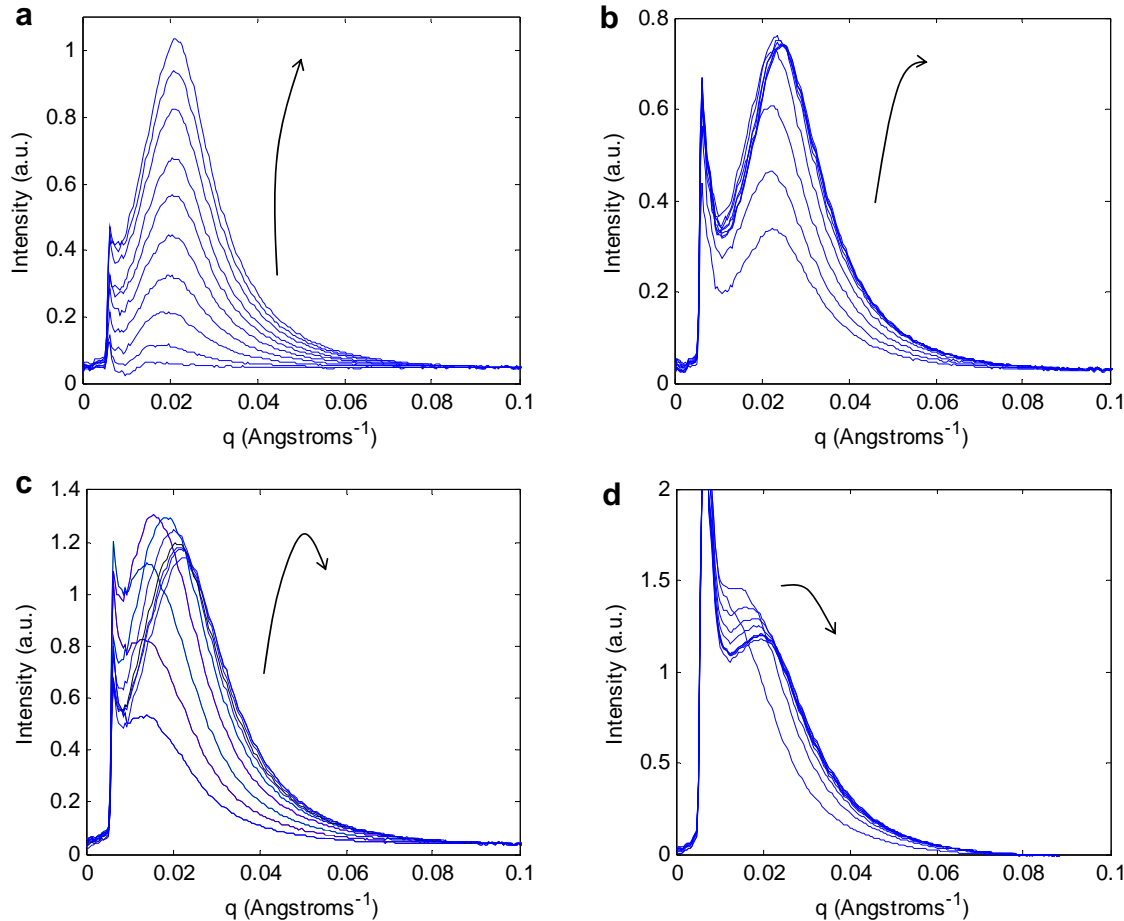


**Figure 3.15** SAXS intensity during the first 120 s of isothermal crystallization (1 trace every 12 s): **a)** L53 at 102 °C, **b)** L53 at 95 °C, **c)** S3 at 87 °C, and **d)** L152 at 87 °C. Arrows indicate trend in peak movement.

S3 exhibits a SAXS peak in Figure 3.15c that initially starts at a smaller  $q$ -value compared to L53 (corresponding to a larger  $L_p$ ). This peak shifts gradually to larger  $q$ -values while intensity first grows and then decreases before the crystallization rate slows. Decreasing SAXS intensity is consistent with the elimination of the corresponding long periods via lamellar insertion. This process is more prevalent for S3 than L53 given that

S3 was crystallized at a lower temperature, providing adequate driving force for crystallization of shorter ethylene sequences.

L152 exhibited strikingly different behavior: scattering intensities at low  $q$ -values decreased after only 12 s of isothermal crystallization. Compared with S3 and L53, L152 underwent little isothermal crystallization, indicating that most of the crystallization occurred during cooling. Hence, the predominant long period was larger due to its formation at higher temperatures—relative to the nominal melting point—compared to S3 and L53.

The pronounced difference in behavior between S3 and L152 is very surprising given the similarity in DSC results. Upon closer inspection, the slight difference in crystallization kinetics at  $T_c = 87$  °C between L152 and S3 (Figure 3.4) corresponds to approximately 10% faster crystallization of L152 compared with S3. This relatively small difference in crystallization kinetics has significant impact on morphology development because of the limited amount of copolymer that is able to crystallize at elevated temperatures. Hence, the faster-crystallizing L152 completes most of its primary lamellar growth before reaching  $T_c = 87$  °C.

## 3.4 DISCUSSION

### 3.4.1 Morphology Evolution during Cooling and Heating

Similar to homopolymers, copolymers require supercooling of the melt to achieve crystallization. Nucleation and growth is responsible for the irreversible behavior observed at higher temperatures both in WAXS crystallinity ( $X_c$ ; Figure 3.7,  $T > T_{r,w}$ ), SAXS long period ( $L_p$ ; Figure 3.10,  $T > T_{r,s}$ ) and SAXS integrated intensity ( $Q$ ; Figure

3.12). The irreversible crystallization/melting region of random copolymers includes two qualitatively distinct subdivisions that can be seen by comparing Figure 3.7, Figure 3.10 and Figure 3.12, as is done in Figure 3.16a. The irreversible regime includes an upper-temperature window in which the three morphological quantities,  $X_c$ ,  $L_p$ , and  $Q$ , show a pronounced hysteresis as well as a lower-temperature window in which hysteresis effects are milder. Based on the dominant morphological features that form in each regime (see below), we term the former ‘primary-irreversible’ crystallization/melting and the latter ‘secondary-irreversible’ crystallization/melting. The lowest temperature range defines the ‘reversible’ crystallization/melting regime, in which the three morphological quantities exhibit distinctly similar values upon cooling and heating.

#### **3.4.1.1 Primary-Irreversible Crystallization**

During cooling, the onset of crystallization in the polymer system is followed by relatively fast crystallization that is associated with the largest changes in morphology. The corresponding formation of the primary DSC exotherm ( $T_{x,\text{high}}$  in Figure 3.3) indicates that a large fraction of the total crystallization occurs by nucleation and growth in this primary-irreversible regime.<sup>67</sup> We envision this occurring by the propagation of primary lamellae through an unconstrained melt (Figure 3.16b), in agreement with previous theories.<sup>45, 55</sup> During cooling through the primary-irreversible regime, lamellae form with continuously decreasing long periods resulting in a shift in the SAXS peak to high wavevectors. This behavior is partially a consequence of kinetic effects but primarily due to the limit on the amount of crystallizable material at each temperature based on the ethylene sequence length distribution (ESLD).

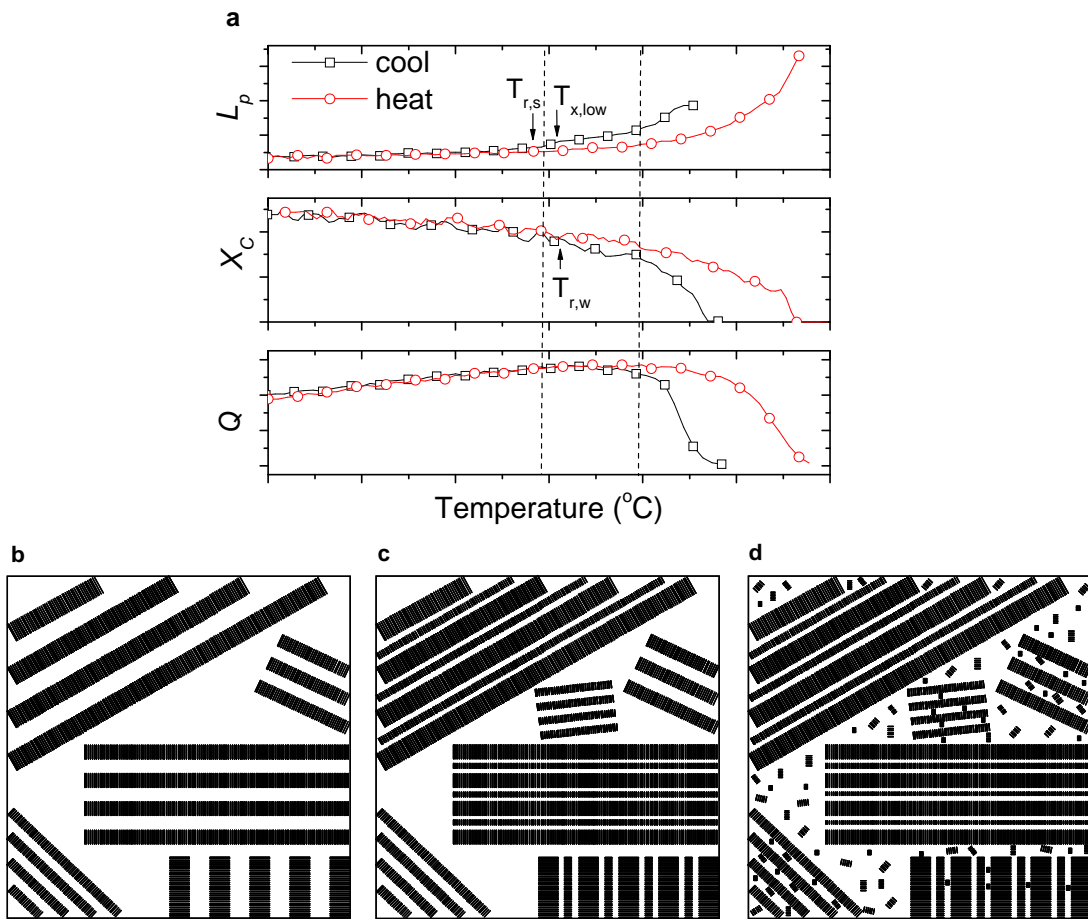


**Figure 3.16** a) General representation of SAXS long period ( $L_p$ ), WAXS crystallinity ( $X_c$ ), and SAXS integrated intensity ( $Q$ ) during cooling and subsequent heating ramps defining three crystallization regimes of random copolymers ( $T_{r,w}$ ,  $T_{r,s}$ , and  $T_{x,low}$  are marked for reference). Schematic representation of morphology in each regime: b) primary-irreversible at high-temperatures, c) secondary-irreversible, and d) reversible crystallization at low temperatures.

Due to the ESLD, the long period of random copolymers during irreversible crystallization is dictated by the size of the non-crystalline layers. Previous studies have demonstrated that the crystalline layer thickness is unaffected by temperature,<sup>48, 79, 88, 90</sup> and this observation is confirmed by estimates of crystalline and non-crystalline layer thicknesses provided in the Appendix. At the relatively high temperatures in the primary irreversible regime, only a small number of ethylene sequences will be of sufficient length to crystallize. However, due to the homogenous SCB distribution, these sequences have

equal probability of being found in all HPBD chains. Therefore, the incorporation of a small portion of almost all chains results in large non-crystalline layers between primary lamellae formed at the highest temperatures. At lower temperatures in the still high-temperature primary-irreversible regime, a greater number of ethylene sequences become capable of crystallization, resulting in a smaller part of the chain being left entirely out of the crystal corresponding to thinner non-crystalline layers. Therefore,  $L_p$  decreases with temperature.

#### **3.4.1.2 Secondary-Irreversible Crystallization**

During cooling through intermediate temperatures between the regime of rapid, irreversible crystallization/melting (primary-irreversible regime) and reversible crystallization/melting,  $X_c$  and  $L_p$  are less dependent on temperature compared with the primary-irreversible regime, consistent with decreased crystallization kinetics. We propose that this slowing of crystallization is a consequence of the depletion of the unconstrained melt (i.e., unpinned chains). Crystallization continues at a slower rate due to decreased chain mobility due to the majority of chains being pinned to already-formed crystals.<sup>45, 66</sup> This pinning severely hinders large conformational changes necessary for chain-folding. However, since crystals formed in this regime continue to exhibit hysteresis between cooling and subsequent heating, nucleation and growth is still expected to be the dominant means of crystallization. Hence, we propose that morphology evolution in this region continues by the growth of lamellae from shorter ethylene sequences that are capable of crystallization at the given temperature. These lamellae will have decreased lateral dimensions and include more defects than those formed during the primary-irreversible regime.<sup>80, 82</sup>

A small fraction of crystallization in this regime occurs in amorphous ‘lakes’ between primary lamellar stacks that were not able to sustain crystals at larger temperatures.<sup>91</sup> However, examination of the SAXS integrated intensity ( $Q$ ), which remains nearly constant at its maximum value in this regime, provides further insight about the predominant location of secondary lamellar growth. For an ideal two-phase system, the integrated intensity is proportional to the electron density difference between the two phases ( $\Delta\rho = \rho_c - \rho_a$ ) and the volume fraction of each phase ( $\varphi_1$  and  $\varphi_2 = 1 - \varphi_1$ ):

$$Q \propto (\Delta\rho)^2 \varphi_1 \varphi_2. \quad (3.2)$$

Therefore, for a constant electron density difference,  $Q$  will exhibit a maximum at 50% crystallinity. However, since crystallinity values in this temperature range are 25% to 35%, a maximum in integrated intensity can be accounted for by a decrease in the electron density contrast that counters the increase in crystallinity.<sup>67</sup> This can be realized via the formation of secondary lamellae between primary lamellae having the largest non-crystalline layers (Figure 3.16c). Consequently, the secondary-irreversible regime is not present in systems like HDPE that do not form large non-crystalline layers that can accommodate secondary lamellar ‘in-filling’.

The onset of the intermediate temperature region is marked by a well-defined lull in  $X_c$  at approximately 75 °C for L152 in Figure 3.7. Similar observations have been made in other studies, and left unexplained;<sup>66, 67</sup> however, these lulls are not abundant in the literature on copolymer crystallinity evolution. In S3, for example, this lull was almost entirely masked by the uncertainty in  $X_c$ , raising the question of whether or not this feature is real.

A possible explanation for these lulls is that they are artifacts of improper fitting

of the WAXS intensity curves. A number of previous studies have noted that fitting the amorphous halo with two peaks, rather than one as was done in this work, yields a better fit and more reasonable behavior of all peaks considered (position, width, etc.).<sup>33</sup><sup>92-96</sup> Sajkiewicz et al.<sup>92</sup> also observed a lull in the crystallinity evolution upon cooling of linear low density polyethylenes (LDPEs). These authors advocated the use of a three-phase model to account for the presence of a phase having intermediate properties to those of the crystalline and amorphous layers; although this resulted in a better fit and more reasonable behavior of the amorphous halo, the lull in the evolution of crystallinity remained. Hence, we conclude that the lull observed here is not an artifact of an improper fit to the WAXS features.

Based on their theory of the existence of an ‘intermediate phase’, Sajkiewicz et al. attributed the lull in crystallinity evolution to reorganization of the intermediate and crystalline phases.<sup>92</sup> Although this is a plausible explanation, arguments have been put forth that contribution to the scattering pattern from an intermediate region that is distributed between the crystalline and amorphous phases should be uniform and not limited to a particular angular region.<sup>33, 93</sup> This controversy is further examined in the following chapter using two-dimensional correlation analysis. Without concrete evidence for the existence of an intermediate phase, we attribute the lull to an induction period, which accounts for the temperature difference between the consumption of the unconstrained melt by propagating lamellae and the onset secondary crystallization can occur in constrained melt.

### 3.4.1.3 Reversible Crystallization at Low Temperatures

At lower temperatures,  $X_c$ ,  $L_p$ , and  $Q$  exhibit dynamic yet distinctly similar behavior upon cooling and subsequent heating. A small amount of reversible crystallization of

HDPE (15% of total) occurs at a constant long period and is accounted for by surface crystallization/melting.<sup>75, 77, 97</sup> In contrast, HPBD materials exhibit changes in crystallinity during the reversible step accounting for 20% to 30% of the total at  $T = 0$  °C with corresponding long period changes of 8% to 23%. For copolymers, reversible crystallization and melting can be attributed to very small crystals that form and melt at similar temperatures.<sup>76</sup> This lack of hysteresis suggests a crystallization mechanism dominated by clustering of neighboring ethylene sequences that are capable of crystallization at a given temperature.<sup>67</sup> These ethylene sequences are quite short and bundle into small, imperfect crystals, which are termed fringed micelles. To avoid ambiguity, in this work we define a fringed micelle as a bundle of non-folded chains with some crystallographic order and lateral dimensions that are on the same order of magnitude as the thickness ( $d \sim l$ ; Figure 3.17). These structures are distinct from lamellae, even poorly formed ones, which have thicknesses that are much smaller than their lateral dimensions ( $d \ll l$ ).

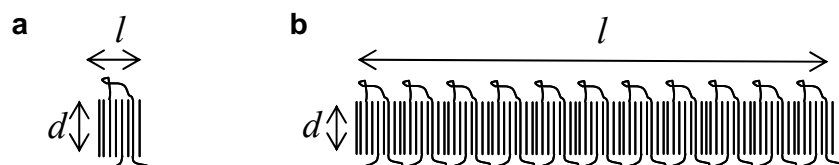


**Figure 3.17** Schematic representation of **a)** fringed micelle and **b)** lamellae.

This fringed micelle morphology is consistent with the observations of Alizadeh et al., who found DSC crystallinity to be independent of cooling rate in the reversible regime.<sup>45</sup> This result suggests that crystallization kinetics are not dependent upon the degree of subcooling and is in agreement with fringed micelle formation that is the result of local conformational fluctuations. These fringed micelles form between pre-existing lamellae as evidenced by decreasing SAXS intensity at all  $q$ -values during reversible crys-

tallization while crystallinity is below 50% (Figure 3.12).

### 3.4.1.4 Transition Temperatures

For the HPBD materials, the transition to reversible behavior of the SAXS integrated intensity,  $Q$ , occurs near its maximum value. At this temperature,  $Q$  becomes dominated by the electron density contrast in the system and not crystallinity, since crystallinity values are still below 50% (see eq 3.2). This temperature is also very close to the transition between the primary-irreversible and secondary-irreversible crystallization regimes, providing further evidence for ‘in-filling’ of primary lamellae via secondary lamellar growth occurring during secondary-irreversible crystallization.

Furthermore, the transition temperatures to reversible behavior of crystallinity and long period are separated by 4 – 8 °C. At an intermediate temperature,  $T_1$ , such that  $T_{r,s} < T_1 < T_{r,w}$ , the system exists with the same crystallinity during heating as during cooling. However, upon heating, the long period at  $T_1$  is smaller than during cooling. A possible explanation for this observation is if the crystals that melted upon reheating to  $T_1$  are located in different locations than those that formed during cooling below  $T_1$ . The implication then is that some crystals formed at lower temperatures turn out to be more stable than those formed at higher temperatures. These more stable crystals are located further away from pre-existing crystal structures, as deduced from their noticeable effect on long period, changes in which are believed to be dominated by changes in the amorphous layer thickness (see Appendix).<sup>80</sup> Upon heating, less stable crystals near crystal surfaces melt, suppressing the expected increase in the long period. This explanation is consistent with the observation that the smallest difference between  $T_{r,s}$  and  $T_{r,w}$  is exhib-

ited by the H4 polymer, which has a limited number of ethylene sequences of sufficient length to form crystals having increased stability during reversible crystallization.

### 3.4.2 DSC Double Melting

The evolution of morphology during temperature ramps described above can be reconciled with morphology formation during isothermal crystallization and account for the two DSC melting endotherms (Figure 3.5). We propose that the high-melting peak ( $T_{m,high}$ ) is due to primary lamellae that form from the longest ethylene sequences in unconstrained melt both during cooling to and at the isothermal temperature ( $T_c$ ). Evidence for crystallization during cooling is demonstrated by the appearance of a SAXS peak immediately upon reaching  $T_c$  (Figure 3.15). Additionally, the temperature of the high-melting peak ( $T_{m,high}$ ) following isothermal crystallization and the peak melting temperature ( $T_m$ ) following a cooling ramp are nearly identical, as previously observed.<sup>43</sup> Furthermore, our observation that  $T_{m,high}$  is nearly independent of  $T_c$  is supplemented by observations in prior literature showing that  $T_{m,high}$  is also independent of crystallization time ( $t_c$ ).<sup>45, 58, 70</sup> These observations indicate that the high melting fraction is primarily formed during cooling and thus is unaffected by isothermal treatment, as previously suggested by others.<sup>45, 70</sup>

On the other hand, monotonically increasing scattering intensity observed during the first two minutes of isothermal crystallization of L53 and S3 (Figure 3.15a-c) indicates a continuation of the crystallization occurring during cooling, resulting in a fraction of primary lamellar formation at  $T_c$ . These lamellae melt at temperatures dependent upon their formation temperature (i.e.,  $T_c$ ) and affect the dependence of  $T_{m,high}$  on  $T_c$  when

enough lamellae are present. In most cases, as evident from the nearly constant  $T_{m,high}$  with  $T_c$  (Figure 3.6 and Table 3.3), the portion of primary lamellae formed at  $T_c$  is low relative to the amount formed during cooling. However, some samples, like L53, exhibit homopolymer-like behavior manifested in a noticeable slope of  $T_{m,high}$  versus  $T_c$  (Figure 3.6 and Table 3.3).<sup>45</sup> For these materials, a significant fraction of primary lamellae within the system formed at  $T_c$  rather than during cooling. Molecules having lower molecular weight and SCB content are able to crystallize at higher temperatures, at which greater chain mobility and decreased nucleation rates result in less pinning of chains to crystal surfaces; consequently, more unconstrained melt is available for propagation of primary lamellae at the relatively high isothermal temperatures used for these materials. It follows that copolymer effects on thermal behavior are gradual, with greatest homopolymer-like behavior observed in systems with low SCB content and at high temperatures.<sup>45</sup>

The low melting peak ( $T_{m,low}$ ) is universally attributed to species formed at the isothermal crystallization temperature, as is evidenced by the lack of  $T_{m,low}$  after short times at  $T_c$ .<sup>56</sup> However, there is some speculation as to the morphology of these structures and, hence, the reason behind their decreased thermal stability. We attribute the low-melting peak ( $T_{m,low}$ ) to secondary lamellae that form isothermally from ethylene sequences whose lengths are dictated by  $T_c$ . It follows that the thickness of these crystals, and hence, their melting temperature, also depends on  $T_c$ . In agreement with Rabiej et al.,<sup>62</sup> but in contrast to other work,<sup>43, 45, 52, 55, 61</sup> we do not use the term fringed micelles to describe these structures since  $T_c = T_m - 16$  °C is in the primary-irreversible crystallization regime where fringed micelle formation is not expected. Secondary lamellar growth,

although unexpected, occurs because isothermal treatment provides sufficient time to overcome its sluggish kinetics.

The manifestation of these secondary lamellae is seen in Figure 3.15 as a decrease in scattering intensity at low  $q$  corresponding to the elimination of the largest long periods. This observation indicates that these secondary lamellae form between pre-existing primary lamellae having the largest non-crystalline regions.<sup>98, 99</sup> This ‘in-filling’ is most pronounced for L152 and S3 (Figure 3.15c and d). Based on DSC results (not shown), approximately 10% and 17% of total crystallinity at the end of 30 minutes at  $T_c = 87^\circ\text{C}$  is attributed to secondary lamellae for L152 and S3, respectively. This significant percentage of secondary crystal growth can be accommodated by the relatively large non-crystalline layers found between lamellae in random copolymers (see Appendix).<sup>48, 79, 80, 88, 90</sup>

Previous literature regarding the increase of  $T_{m,\text{low}}$  with increasing time at  $T_c$  (i.e., offset of the low melting peaks from  $T_m = T_c$  in Figure 3.6) has attributed the effect to crystal thickening,<sup>58, 100</sup> decreased conformational entropy of the amorphous phase due to secondary crystallization,<sup>45</sup> or an instrumental artifact.<sup>62</sup> Instead, we propose that sluggish secondary crystallization of short ethylene sequences can result in crystals having progressively greater stability when given more time for close-neighbor ethylene sequences to reorganize.

### 3.4.3 Effects of Molecular Characteristics

The four HPBD materials were selected in order to evaluate the effects of molecular topology: molecular weight, short-chain and long-chain branching. Comparisons

between L53 and L152 enable the isolation of molecular weight effects. Insight into long chain branching is gained by examining L152 and S3 and effects of short-chain branching can be inferred from L152, S3, and H4. It was found that SCB content and molecular weight has the greatest influence on morphology and crystallization kinetics.

### 3.4.3.1 Crystallinity

The transition temperature to reversible crystallization,  $T_{r,w}$ , upon cooling can be interpreted as the temperature at which the long ethylene sequences capable of nucleation and growth of primary and secondary lamellae have been consumed, and only shorter sequences capable of fringed micelle formation remain. Hence, the crystallinity at  $T_{r,w}$  decreases with the amount of long ethylene sequences in the molecule and, consequently, with increasing SCB content. In agreement, H4, having the highest SCB content, exhibits the lowest crystallinity at  $T_{r,w}$  out of the four HPBD materials examined.

The values for  $T_{r,w}$  vary from 32 to 43 °C below the peak melting point determined by DSC,  $T_m$ , and speak to the difficulty in defining similar apparent subcoolings ( $\Delta T = T_m - T_c$ ) for the different samples.  $T_{r,w}$  appears to be dependent primarily on molecular weight, which determines the amount of pinning of chains during crystallization. For example, at the same temperature, L152, which has three times the molecular weight of L53, contains three times as many crystallizable ethylene sequences, and hence three times as many pinning cites, resulting in greater constraint on the melt.

Two apparent inconsistencies with prior literature were observed in the current study. First, Alizadeh et al. observed a decrease in  $T_{r,w}$  with increasing SCB content,<sup>45</sup> hence similar values, differing by just 2 °C, for L152 and H4 would be unexpected (Figure 3.8). Second, reversible crystallinity has been observed to account for more of the

total  $X_c$  as SCB increases,<sup>45, 75, 79</sup> yet again L152 and H4 are unexpectedly similar (difference between circles and squares in Figure 3.8). However, Alizadeh et al. compared samples with a greater variation of SCB content. A difference of approximately 20 °C in  $T_{r,w}$  was observed between samples that differed in comonomer content by 9 mol % (Figure 5 of ref. 45). In contrast, L152 and H4 only differ by 1.4 mol % comonomer, for which we could estimate an expected difference in  $T_{r,w}$  of 2-3 °C and little change in the reversible fraction, consistent with our observations.

### 3.4.3.2 Long Period

The transition to reversible behavior of the long period occurs at similar values of  $L_p$  for the HPBD materials studied ( $15.5 \pm 1$  nm; filled squares in Figure 3.11). This observation suggests that  $T_{r,s}$  is dictated by the distribution of the lamellar crystals. The temperature at which each material develops this similar morphology that can only support fringed micelle formation ( $T_{r,s}$ ) depends on molecular weight and SCB content: materials with larger  $M_{w,tot}$  (S3 and L152 as compared to L53) and higher SCB content (H4 as compared to L152 and S3) require cooling to lower temperatures (Figure 3.11).

Although the long period at  $T_{r,s}$  is the same, the long period at  $T = 0$  °C differs among the HPBDs (filled circles in Figure 3.11), following a similar trend as the peak crystallization temperature. Since L53 begins crystallization at a higher temperature, it initially forms a larger long period which keeps the average long period higher than that of the other materials when compared at the same temperatures. For this thermal history (cooling at 10 °C/min), molecular characteristics are found to affect lamellar formation and hence influence the final long period. In contrast, previous studies have observed a long period of approximately 15 nm independent of molecular weight ( $M_w > 10$  kg/mol)

and SCB content (>20 SCB/1000 C) following quenching to room temperature.<sup>44,52</sup>

This discrepancy suggests the formation of different nanostructure, likely governed by different physics, for the two thermal treatments. The work of Voigt-Martin et al. confirms differences in structure formation; the authors observed that an HPBD with a molecular weight of 108 kg/mol was able to form medium-length, curved lamellae under slow-cooled conditions, but exhibited no lamellar character subsequent to quenching.<sup>101</sup> Additionally, Goderis et al. demonstrated that crystal thickness is greater in ethylene-co-octene samples that were slowly cooled compared to quenched.<sup>88</sup> During quenching, the majority of crystallization occurs from neighboring ethylene sequences having insufficient time to find most stable conformations. In contrast, crystallization during cooling ramps (even at 10 °C/min) provides adequate time for crystallization occurring from ethylene sequences of intermediate length, and hence, a greater effect of molecular characteristics is observed.

### 3.4.3.3 DSC Crystallization Kinetics

In the present study, the long-chain branched (LCB) molecules (S3 and H4) exhibited only slightly slower kinetics than linear samples; strong differences can be attributed to increased molecular weight (S3 vs. L53) and short-chain branching content (H4 vs. L152).<sup>29, 30, 33-37, 44</sup> The strong effect of long-chain branching on crystallization kinetics, expected based on prior literature, was *not* observed.<sup>4, 68, 69</sup> Although some qualitative agreement was seen with the work of Haigh et al.,<sup>68</sup> the conclusions reached here are quite different. In their work, Haigh et al. studied a short linear HPBD and a star HPBD similar to the ones examined here and observed the same relative behavior (i.e., the 3-arm star crystallized much slower than the linear polymer having molecular weight matching

one of the arms; see Figure 3.4). The authors argued that the crystallizing entities of the two polymers were the same (since the branch point cannot crystallize), and hence, the strong decrease in crystallization kinetics was attributed to long-chain branching. However, here, we were able to compare a star polymer to a linear HPBD of similar molecular weight and SCB content. The nearly identical thermal behavior of the two materials indicates that one long chain branch has negligible effect.

Similar crystallization kinetics between L152 and S3 indicate that melt dynamics do not dictate crystallization of random copolymers. L152 exhibits relaxation behavior that scales as a power law with its molecular weight.<sup>102</sup> In contrast, the star polymer relaxes by arm retraction and has relaxation times that scale exponentially with the molecular weight of the arms.<sup>103</sup> Therefore, despite the three-fold difference between  $M_{w,a}$  for the star and  $M_{w,tot}$  for the long linear polymer, the relaxation time of the star is significantly slower. The profound difference in melt dynamics yet nearly identical crystallization kinetics is another example of a principle difference between random copolymers and homopolymers. While crystallization kinetics of random copolymers are primarily dictated by molecular weight, this effect is not a consequence of melt dynamics, but rather because  $M_{w,tot}$  dictates the amount of chain pinning to crystal surfaces.

#### 3.4.4 Implications for Flow-Induced Crystallization

While a few long-chain branches have negligible effect on quiescent crystallization, their effect on the relaxation time of a molecule becomes important when exposed to a flow field. As relaxation time increases with LCB content,<sup>13, 14, 104</sup> molecules have a greater response to the flow field, allowing the for formation of oriented nuclei,<sup>11, 105</sup>

which enhance crystallization kinetics and result in oriented morphology.<sup>3, 4, 8, 105</sup>

Therefore, the ultimate material properties of processed semicrystalline polymers, which are directly related to morphology, are highly dependent upon the slow-relaxing molecules.<sup>12, 105, 106</sup> Model hydrogenated polybutadienes are thought to have opened the door for well-defined studies of the effects of melt dynamics on flow-induced crystallization (FIC).<sup>3</sup> The number and length of long-chain branches can be well-defined to systematically alter the relaxation times of these materials and can be used to control the morphology formation subsequent to flow.<sup>107, 108</sup>

We conducted preliminary studies to probe the effects of melt dynamics on flow-induced crystallization (FIC) by examining a bimodal system containing a small concentration of a slow-relaxing species in the form of a model comb polymer blended with fast-relaxing matrix (short, linear copolymer). The bimodal components were selected to have matching SCB content in order to specifically isolate the effect of long-chain branches. Details of the experiment are provided in Thesis Appendix B. Contrary to our expectations, neither increased crystallization kinetics nor preferred orientation was observed. This surprising result suggests that even under flow, short-chain branching significantly hinders crystallization. The effect of short-chain branching on FIC is explored in Chapter 5.

### 3.5 CONCLUSION

The study of model hydrogenated polybutadienes (HPBDs) of complex architecture revealed that the interplay between long-chain and short-chain branches is dominated by the ethylene sequence length distribution (ESLD). Differences in thermal and morpho-

logical behavior observed between (1) a short, linear chain, (2) a long, linear chain, (3) a star-polymer, and (4) an H-polymer are primarily explained by differences in SCB content and molecular weight. This is also the case for crystallization kinetics, which have previously been reported to be strongly dependent on long-chain branching.<sup>68</sup> Nearly identical crystallization kinetics observed between materials having significant differences in melt dynamics, highlights the importance of ESLD in the crystallization of random copolymers. Even in the presence of a flow field, oriented crystallization in the presence of a slow-relaxing comb polymer was suppressed, indicating the dominance of SCB content.

The evolution of morphology in SCB systems was examined both during temperature ramps and under isothermal conditions. During temperature ramps, three temperature regions defined by specific morphology development were identified:

- (1) The ‘primary-irreversible’ regime is characterized by rapid, irreversible crystallization at relatively high temperatures via the propagation of primary lamellae in an unconstrained melt.
- (2) The ‘secondary-irreversible’ regime is characterized by slower, irreversible crystallization at intermediate temperatures via the formation of secondary lamellae in constrained melt between previously-formed lamellae having the largest non-crystalline regions.
- (3) The ‘reversible’ crystallization regime is characterized by slow, reversible crystallization at low temperatures via the formation of fringed micelles between pre-existing crystals.

In light of these regimes, double melting behavior observed by DSC subsequent

to isothermal crystallization is explained by the melting of primary and secondary lamellae. The high-melting peak ( $T_{m,high}$ ) is attributed to the same rapidly-crystallizing, primary lamellae that form at the highest temperature during cooling ramps (primary-irreversible regime). These primary lamellae form both during cooling to and at the isothermal crystallization temperature ( $T_c$ ). Given that the isothermal temperature used in these, as well as in many other studies,<sup>44, 45, 55, 62, 109</sup> is in the irreversible regime, the low-melting peak ( $T_{m,low}$ ) is attributed to the melting of secondary lamellae—and not fringed micelles—that form from ethylene sequences whose length, and hence thermal stability, is dictated by  $T_c$ .

The effect of the heterogeneous morphology in copolymers is manifested as dynamic SAXS and WAXS data obtained during crystallization. This data is well suited for a prevalent technique in the field of vibrational spectroscopy to examine changes in spectra as a function of a perturbation variable, such as temperature or time. Two-dimensional correlation analysis is used in the following chapter in order to further examine morphology development and explore questions regarding the presence of an intermediate phase and the onset of crystallization.

### 3.6 APPENDIX—Crystalline and Amorphous Layer Thickness

For an ideal, two-phase system, it is possible to estimate the crystalline and amorphous layer thicknesses ( $L_c$  and  $L_a$ , respectively) from the long period ( $L_p$ ) and volume fraction crystallinity ( $\varphi_1$ ). Volume fraction crystallinity for each material was estimated from  $X_c$  by taking the density of purely crystalline PE to be 1.0 g/cm<sup>3</sup> and that of amorphous PE to be 0.855 g/cm<sup>3</sup>.<sup>110, 111</sup> Hence,

$$L_c = L_p \varphi_1, \quad (3.3)$$

and

$$L_a = L_p (1 - \varphi_1). \quad (3.4)$$

We acknowledge that this analysis is not rigorous due to both the assumption of a two-phase model<sup>112</sup> and the fact that SAXS and WAXS are sensitive to different morphological features: WAXS identifies crystalline unit cells, and SAXS arises as the result of electron density contrast.<sup>67, 113-115</sup> However, a number of qualitative observations from this analysis are useful for elucidating the morphology.

This analysis indicates that the decrease in the long period during cooling is the result of a strong decrease in the apparent thickness of the amorphous layer (Figure 3.18). The crystalline layer thickness remains relatively constant with decreasing temperature, in agreement with past literature.<sup>48, 79, 88, 90</sup> From Figure 3.18, it is apparent that the temperature of the transition to reversible behavior is dominated by the amorphous layer. Below this transition temperature (shaded region in Figure 3.18), estimated  $L_a$  and  $L_c$  values are invalid, since we do not expect formation of lamellae in this region. Additionally, the crystalline layer exhibited reversible behavior with little change at temperatures below

the primary crystallization temperature, as determined by DSC ( $T_{x,high}$ ). For all HPBD materials, the amorphous layer was thicker than the crystalline layer at all temperature examined and dominated  $L_p$  behavior.

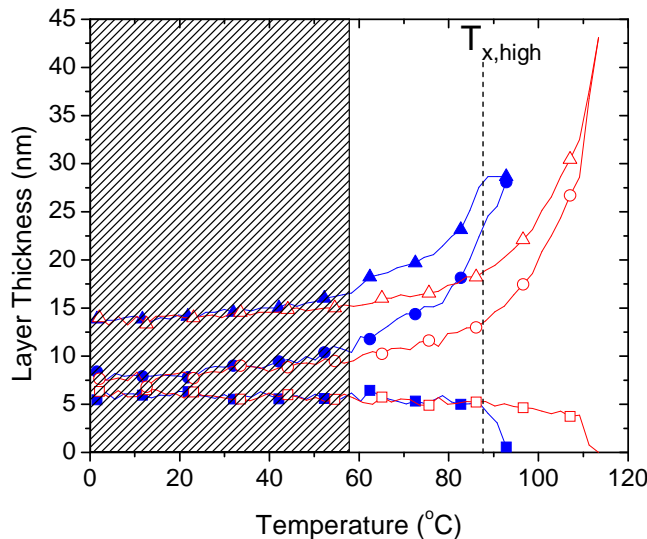


**Figure 3.18** Long period ( $L_p$ , triangles), crystalline ( $L_c$ , squares) and amorphous ( $L_a$ , circles) layer thicknesses of L152 during cooling (solid symbols) and subsequent heating (open symbols) at 10 °C/min.

### 3.7 ACKNOWLEDGEMENTS

This work would not have been possible without ExxonMobil Research and Engineering Company (Clinton, NJ), particularly Dr. David Lohse, Dr. Cynthia Mitchell, Dr. Manika Varma-Nair, Dr. Lisa Baugh and the rest of the team, who provided financial support, experimental assistance, and fruitful discussions. The materials examined here were graciously synthesized by Prof. Nikos Hadjichristidis (University of Athens, Athens, Greece) and made available through collaboration with ExxonMobil. Additionally, we would like to thank Dr. Soo-Young Park (Kyunpook National University, Daegu, South Korea) and Robert Panepinto (ExxonMobil) for conducting DSC studies. We must thank the beamline staff at beamline X27C at NSLS BNL (Dr. Lixia Rong and Jie Zhu) and at

beamline 7.3.3 at ALS LBL (Dr. Alexander Hexemer and Eliot Gann). X-ray data was collected with the assistance of Zuleikha Kurji (Caltech). Finally, we would like to thank Prof. Rufina Alamo and Madhavi Vadlama (Florida State University) for fruitful discussions and their aid in the visualization of polymer morphology. Part of this work was funded by the National Science Foundation (DMR-0505393 and GOALI-0523083). Manuscript preparation was assisted by Prof. Julia Kornfield (Caltech), Oliver W. Buccicone (Tanner Research, Monrovia, CA), Havaala O.T. Pye (Caltech), and Mary Louie (Caltech).

### 3.8 REFERENCES

1. Gahleitner, M., Melt rheology of polyolefins. *Progress in Polymer Science* **2001**, 26, (6), 895-944.
2. Wood-Adams, P. M.; Dealy, J. M.; deGroot, A. W.; Redwine, O. D., Effect of molecular structure on the linear viscoelastic behavior of polyethylene. *Macromolecules* **2000**, 33, (20), 7489-7499.
3. Heeley, E. L.; Fernyhough, C. M.; Graham, R. S.; Olmsted, P. D.; Inkson, N. J.; Embrey, J.; Groves, D. J.; McLeish, T. C. B.; Morgovan, A. C.; Meneau, F.; Bras, W.; Ryan, A. J., Shear-induced crystallization in blends of model linear and long-chain branched hydrogenated polybutadienes. *Macromolecules* **2006**, 39, 5058-5071.
4. Bustos, F.; Cassagnau, P.; Fulchiron, R., Effect of molecular architecture on quiescent and shear-induced crystallization of polyethylene. *Journal of Polymer Science Part B - Polymer Physics* **2006**, 44, (11), 1597-1607.
5. Agarwal, P. K.; Somani, R. H.; Weng, W.; Mehta, A.; Yang, L.; Ran, S.; Liu, L.; Hsiao, B. S., Shear-Induced Crystallization in Novel Long Chain Branched Polypropylenes by in Situ Rheo-SAXS and -WAXD. *Macromolecules* **2003**, 36, 5226-5235.
6. Nogales, A.; Hsiao, B. S.; Somani, R. H.; Srinivas, S.; Tsou, A. H.; Balta-Calleja, F. J.; Ezquerra, T. A., Shear-induced crystallization of isotactic polypropylene with different molecular weight distributions: in situ small- and wide-angle X-ray scattering studies. *Polymer* **2001**, 42, (12), 5247-5256.
7. Fernandez-Ballester, L. Formation of oriented precursors in flow-induced polymer crystallization: experimental methods and model materials. California Institute of Technology, Pasadena, CA, 2007.
8. Kumaraswamy, G.; Kornfield, J. A.; Yeh, F.; Hsiao, B. S., Shear-Enhanced Crystallization in Isotactic Polypropylene. 3. Evidence for a Kinetic Pathway to Nucleation.

*Macromolecules* **2002**, 35, 1762-1769.

9. Bond, E. B.; Spruiell, J. E., Melt spinning of metallocene catalyzed polypropylenes. I. On-line measurements and their interpretation. *Journal of Applied Polymer Science* **2001**, 82, (13), 3223-3236.
10. Liedauer, S.; Eder, G.; Janeschitz-Kriegl, H.; Jerschow, P.; Geymayer, W.; Ingolic, E., On the kinetics of shear-induced crystallization in polypropylene. *International Polymer Processing* **1993**, 8, (3), 236-244.
11. Kumaraswamy, G., Crystallization of Polymers from Stressed Melts. *Journal of Macromolecular Science, Part C: Polymer Reviews* **2005**, 45, 375-397.
12. Somani, R. H.; Yang, L.; Zhu, L.; Hsiao, B. S., Flow-induced shish-kebab precursor structures in entangled polymer melts *Polymer* **2005**, 46, 8587-8623.
13. McLeish, T. C. B., Hierarchical-relaxation in tube models of branched polymers. *Europhysics Letters* **1988**, 6, (6), 511-516.
14. Kapnistos, M.; Vlassopoulos, D.; Roovers, J.; Leal, L. G., Linear Rheology of Architecturally Complex Macromolecules: Comb Polymers with Linear Backbones. *Macromolecules* **2005**, 38, 7852-7862.
15. Malmberg, A.; Kokko, E.; Lehmus, P.; Lofgren, B.; Seppala, J. V., Long-chain branched polyethylene polymerized by metallocene catalysts Et[Ind](2)ZrCl<sub>2</sub>/MAO and Et[IndH(4)](2)ZrCl<sub>2</sub>/MAO. *Macromolecules* **1998**, 31, (24), 8448-8454.
16. Shiono, T.; Azad, S. M.; Ikeda, T., Copolymerization of atactic polypropene macro-monomer with propene by an isospecific metallocene catalyst. *Macromolecules* **1999**, 32, (18), 5723-5727.
17. Mehdiabadi, S.; Soares, J. B. P.; Dekmezian, A. H., Production of Long-Chain Branched Polyolefins with Two Single-Site Catalysts: Comparing CSTR and Semi-Batch Performance. *Macromolecular Reaction Engineering* **2008**, 2, (6), 529-550.

18. Schwerdtfeger, E. D.; Irwin, L. J.; Miller, S. A., Highly branched polyethylene from ethylene alone via a single zirconium-based catalyst. *Macromolecules* **2008**, 41, (4), 1080-1085.
19. Lofgren, B.; Kokko, E.; Seppala, J., Specific structures enabled by metallocene catalysis in polyethenes. In *Long-Term Properties of Polyolefins*, Springer-Verlag Berlin: Berlin, 2004; Vol. 169, pp 1-12.
20. Wood-Adams, P. M.; Dealy, J. M., Using rheological data to determine the branching level in metallocene polyethylenes. *Macromolecules* **2000**, 33, (20), 7481-7488.
21. Alamo, R. G.; Mandelkern, L., The crystallization behavior of random copolymers of ethylene. *Thermochimica Acta* **1994**, 238, 155-201.
22. Hadjichristidis, N.; Xenidou, M.; Iatrou, H.; Pitsikalis, M.; Poulos, Y.; Avgeropoulos, A.; Sioula, S.; Paraskeva, S.; Velis, G.; Lohse, D. J.; Schulz, D. N.; Fetters, L. J.; Wright, P. J.; Mendelson, R. A.; Garcia-Franco, C. A.; Sun, T.; Ruff, C. J., Well-defined, model long chain branched polyethylene. 1. Synthesis and characterization. *Macromolecules* **2000**, 33, (7), 2424-2436.
23. Bender, J. T.; Knauss, D. M., Synthesis of Low Polydispersity Polybutadiene and Polyethylene Stars by Convergent Living Anionic Polymerization. *Journal of Polymer Science: Part A: Polymer Chemistry* **2006**, 44, 828-836.
24. Driva, P.; Iatrou, H.; Lohse, D. J.; Hadjichristidis, N., Anionic Homo-and Copolymerization of Double-Tailed Macromonomers: A Route to Novel Macromolecular Architectures. *Journal of Polymer Science: Part A: Polymer Chemistry* **2005**, 43, 4070-4078.
25. Koutalas, G.; Iatrou, H.; Lohse, D. J.; Hadjichristidis, N., Well-Defined Comb, Star-Comb, and Comb-on-Comb Polybutadienes by Anionic Polymerization and the Macromer Strategy. *Macromolecules* **2005**, 38, 4996-5001.
26. Vazaios, A.; Lohse, D. J.; Hadjichristidis, N., Linear and Star Block Copolymers of

Styrenic Macromoners by Anionis Polymerization. *Macromolecules* **2005**, 38, 5468-5474.

27. Rachapudy, H.; Smith, G. G.; Raju, V. R.; Graessley, W. W., Properties of Amorphous and Crystallizable Hydrocarbon Polymers .3. Studies of the Hydrogenation of Polybutadiene. *Journal of Polymer Science Part B-Polymer Physics* **1979**, 17, (7), 1211-1222.

28. Krigas, T. M.; Carella, J. M.; Struglinski, M. J.; Crist, B.; Graessley, W. W.; Schilling, F. C., Model Copolymers of Ethylene with Butene-1 Made by Hydrogenation of Polybutadiene - Chemical Composition and Selected Physical Properties. *Journal of Polymer Science: Part B: Polymer Physics* **1985**, 23, (3), 509-520.

29. Cerrada, M. L.; Benavente, R.; Perez, E., Influence of thermal history on morphology and viscoelastic behavior of ethylene-1-octene copolymers synthesized with metallocene catalysts. *Journal of Materials Research* **2001**, 16, (4), 1103-1111.

30. Peeters, M.; Goderis, B.; Vonk, C.; Reynaers, H.; Mathot, V., Morphology of Homogeneous Copolymers of Ethene and 1-Octene. I. Influence of Thermal History on Morphology. *Journal of Polymer Science: Part B: Polymer Physics* **1997**, 35, 2689-2713.

31. Krishnaswamy, R. K.; Yang, Q.; Fernandez-Ballester, L.; Kornfield, J. A., Effect of the distribution of short-chain branches on crystallization kinetics and mechanical properties of high-density polyethylene. *Macromolecules* **2008**, 41, (5), 1693-1704.

32. Bensason, S.; Minick, J.; Moet, A.; Chum, S.; Hiltner, A.; Baer, E., Classification of Homogeneous Ethylene-Octene Copolymers Based on Comonomer Content. *Journal of Polymer Science: Part B: Polymer Physics* **1996**, 34, 1301-1315.

33. Simanke, A. G.; Alamo, R. G.; Galland, G. B.; Mawler, R. S., Wide-angle X-ray scattering of random metallocene-ethylene copolymers with different types and concentration of comonomer. *Macromolecules* **2001**, 34, (20), 6959-6971.

34. Alamo, R.; Domszy, R.; Mandelkern, L., Thermodynamic and Structural-Properties of Copolymers of Ethylene. *Journal of Physical Chemistry* **1984**, 88, (26), 6587-6595.

35. Alamo, R. G.; Mandelkern, L., Crystallization Kinetics of Random Ethylene Co-polymers. *Macromolecules* **1991**, 24, 6480-6493.

36. Stadler, F. J.; Takahashi, T.; Yonetake, K., Crystallite dimensions - characterization of ethene-/alpha-olefin Copolymers with various comonomers and comonomer Ccontents measured by small- and wide angle X-ray scattering. *E-Polymers* **2009**, 19.

37. Mathot, V. B. F.; Scherrenberg, R. L.; Pijpers, T. F. J. In *Metastability and order in linear, branched and copolymerized polyethylenes*, 1998; Elsevier Sci Ltd: 1998; pp 4541-4559.

38. Mandelkern, L.; Glotin, M.; Benson, R. A., Supermolecular Structure and Thermodynamic Properties of Linear and Branched Polyethylene under Rapid Crystallization Conditions. *Macromolecules* **1981**, 14, 22-34.

39. Alamo, R. G.; Viers, B. D.; Mandelkern, L., Phase-Structure of Random Ethylene Copolymers - a Study of Coint Content and Molecular-Weight as Independent Variables. *Macromolecules* **1993**, 26, (21), 5740-5747.

40. Shirayam.K; Watabe, H.; Kita, S., Effects of Branching on Some Properties of Ethylene Alpha-Olefin Copolymers. *Makromolekulare Chemie* **1972**, 151, (JAN20), 97-&.

41. Richardson, M. J.; Flory, P. J.; Jackson, J. B., Crystallization and Melting of Co-polymers of Polymethylene. *Polymer* **1963**, 4, (2), 221-236.

42. Laupretre, F.; Monnerie, L.; Barthelemy, L.; Vairon, J. P.; Sauzeau, A.; Roussel, D., Influence of Crystallization Conditions on the Location of Side-Chain Branches in Ethylene Copolymers as Studied by High-Resolution Solid-State C-13 Nmr. *Polymer Bulletin* **1986**, 15, (2), 159-164.

43. Crist, B.; Williams, D. N., Crystallization and melting of model ethylene-butene ran-

dom copolymers: Thermal studies. *Journal of Macromolecular Science-Physics* **2000**, B39, (1), 1-13.

44. Alamo, R. G.; Chan, E. K. M.; Mandelkern, L.; Voigt-Martin, I. G., Influence of Molecular Weight on the Melting and Phase Structure of Random Copolymers of Ethylene. *Macromolecules* **1992**, 25, (24), 6381-6394.

45. Alizadeh, A.; Richardson, L.; Xu, J.; McCartney, S.; Marand, H.; Cheung, Y. W.; Chum, S., Influence of Structural and Topological Constraints on the Crystallization and Melting Behavior of Polymers. 1. Ethylene/1-Octene Copolymers. *Macromolecules* **1999**, 32, 6221-6235.

46. Alamo, R. G.; Mandelkern, L., Thermodynamic and Structural-Properties of Ethylene Copolymers. *Macromolecules* **1989**, 22, (3), 1273-1277.

47. Liu, W. D.; Yang, H. L.; Hsiao, B. S.; Stein, R. S.; Liu, S. S.; Huang, B. T. In *Real-time crystallization and melting study at ethylene-based copolymers by SAXS, WAXD, and DSC techniques*, 2000; Cebe, P.; Hsiao, B. S.; Lohse, D. J., Eds. Amer Chemical Soc: 2000; pp 187-200.

48. Vanden Eynde, S.; Mathot, V.; Koch, M. H. J.; Reynaers, H., Thermal behaviour and morphology of homogeneous ethylene-propylene and ethylene-1-butene copolymers with high comonomer contents. *Polymer* **2000**, 41, (9), 3437-3453.

49. Howard, P. R.; Crist, B., Unit-Cell Dimensions in Model Ethylene Butene-1 Copolymers. *Journal of Polymer Science Part B-Polymer Physics* **1989**, 27, (11), 2269-2282.

50. Mathot, V. B. F.; Pijpers, M. F. J., Molecular-Structure, Melting Behavior, and Crystallinity of 1-Octene-Based Very Low-Density Polyethylenes (Vldpes) as Studied by Fractionation and Heat-Capacity Measurements with Dsc. *Journal of Applied Polymer Science* **1990**, 39, (4), 979-994.

51. Flory, P. J., Theory of Crystallization in Copolymers. *Transactions of the Faraday Society*

*Society* **1955**, 51, (6), 848-857.

52. Crist, B.; Howard, P. R., Crystallization and Melting of Model Ethylene-Butene Copolymers. *Macromolecules* **1999**, 32, 3057-3067.

53. Kolesov, I. S.; Androsch, R.; Radusch, H. J. In *Non-isothermal crystallization of polyethylenes as function of cooling rate and concentration of short chain branches*, 2004; Kluwer Academic Publ: 2004; pp 885-895.

54. Wunderlich, B., *Macromolecular Physics*. Academic Press: New York, 1999; Vol. 3.

55. Crist, B.; Claudio, E. S., Isothermal crystallization of random ethylene-butene copolymers: Bimodal kinetics. *Macromolecules* **1999**, 32, (26), 8945-8951.

56. Rabiej, S.; Goderis, B.; Janicki, J.; Mathot, V. B. F.; Koch, M.; Reynaers, H.; Włochowicz, A. In *Influence of thermal treatment on the supermolecular structure of homogeneous polyethylene-1-octene copolymers*, 2003; Inst Chemical Fibres: 2003; pp 28-31.

57. Minick, J.; Moet, A.; Hiltner, A.; Baer, E.; Chan, S. P., Crystallization of Very-Low-Density Copolymers of Ethylene With Alpha-Olefins. *Journal of Applied Polymer Science* **1995**, 58, (8), 1371-1384.

58. Wang, C.; Chu, M. C.; Lin, T. L.; Lai, S. M.; Shih, H. H.; Yang, J. C., Microstructures of a highly short-chain branched polyethylene. *Polymer* **2001**, 42, (4), 1733-1741.

59. Okui, N.; Kawai, T., Crystallization of Ethylene/Vinylacetate Random Copolymers. *Makromolekulare Chemie* **1972**, 154, (NAPR), 161-&.

60. Qiu, J.; Xu, D.; Zhao, J.; Niu, Y.; Wang, Z., New Insights into the Multiple Melting Behaviors of the Semicrystalline Ethylene-Hexene Copolymer: Origins of Quintuple Melting Peaks. *Journal of Polymer Science: Part B: Polymer Physics* **2008**, 46, 2100-2115.

61. Zhang, F. J.; Liu, J. P.; Xie, F. C.; Fu, Q.; He, T. B., Polydispersity of ethylene se-

quence length in metallocene ethylene/alpha-olefin copolymers. II. Influence on crystallization and melting behavior. *Journal of Polymer Science Part B-Polymer Physics* **2002**, 40, (9), 822-830.

62. Rabiej, S.; Goderis, B.; Janicki, J.; Mathot, V. B. F.; Koch, M. H. J.; Groeninckx, G.; Reynaers, H.; Gelan, J.; Wlochowicz, A., Characterization of the dual crystal population in an isothermally crystallized homogeneous ethylene-1-octene copolymer. *Polymer* **2004**, 45, 8761-8778.

63. The author would like to thank Lixia Rong and Jie Zhu with beamline assistance.

64. The author would like to thank Eliot Gann and Alexander Hexemer with beamline assistance, as well as Zuleikha Kurji for aid in conducting experiments.

65. Cser, F., About the Lorentz correction used in the interpretation of small angle X-ray scattering data of semicrystalline polymers. *Journal of Applied Polymer Science* **2001**, 80, (12), 2300-2308.

66. Goderis, B.; Reynaers, H.; Koch, M. J., Primary and Secondary Crystallization in a Homogeneous Ethylene-1-Octene Copolymer: Crystallinity Heterogeneity Studied by SAXS. *Macromolecules* **2002**, 25, 5840-5853.

67. Mathot, V. B. F.; Scherrenberg, R. L.; Pijpers, M. F. J.; Bras, W., Dynamic DSC, SAXS and WAXS on homogeneous ethylene-propylene and ethylene-octene copolymers with high comonomer contents. *Journal of Thermal Analysis* **1996**, 46, (3-4), 681-718.

68. Haigh, J. A.; Nguyen, C.; Alamo, R. G.; Mandelkern, L., CRYSTALLIZATION AND MELTING OF MODEL POLYETHYLENES WITH DIFFERENT CHAIN STRUCTURES. *Journal of Thermal Analysis and Calorimetry* **2000**, 59, 435-440.

69. Isasi, J. R.; Haigh, J. A.; Graham, J. T.; Mandelkern, L.; Alamo, R. G. In *Some aspects of the crystallization of ethylene copolymers*, 2000; Elsevier Sci Ltd: 2000; pp 8813-8823.

70. Peng, Y.; Fu, Q.; Chiu, F.-C., Crystallization and morphology of metallocene polyethylenes with well-controlled molecular weight and branching content. *Polymer International* **2003**, 52, 164-171.

71. Hoffman, J. D.; Weeks, J. J., Melting Process and Equilibrium Melting Temperature of Polychlorotrifluoroethylene. *Journal of Research of the National Bureau of Standards Section a-Physics and Chemistry* **1962**, 66, (JAN-F), 13-&.

72. Mandelkern, L., The Dependence of the Melting Temperature of Bulk Homopolymers on the Crystallization Temperature. *Journal of Polymer Science* **1960**, 47, (0149), 494-496.

73. Kim, M. H.; Phillips, P. J.; Lin, J. S., The equilibrium melting points of random ethylene-octene copolymers: A test of the Flory and Sanchez-Eby theories. *Journal of Polymer Science Part B-Polymer Physics* **2000**, 38, (1), 154-170.

74. Lorenzo, A. T.; Arnal, M. L.; Muller, A. J.; de Fierro, A. B.; Abetz, V., High speed SSA thermal fractionation and limitations to the determination of lamellar sizes and their distributions. *Macromolecular Chemistry and Physics* **2006**, 207, (1), 39-49.

75. Androsch, R.; Wunderlich, B., Specific reversible melting of polyethylene. *Journal of Polymer Science Part B-Polymer Physics* **2003**, 41, (18), 2157-2173.

76. Nam, J. Y.; Kadomatsu, S.; Saito, H.; Inoue, T., Thermal reversibility in crystalline morphology of LLDPE crystallites. *Polymer* **2002**, 43, (7), 2101-2107.

77. Schultz, J. M.; Fischer, E. W.; Schaumburg, O.; Zachmann, H. A., Small-Angle X-Ray-Scattering Studies of Melting. *Journal of Polymer Science Part B-Polymer Physics* **1980**, 18, (2), 239-245.

78. Androsch, R.; Wunderlich, B., Analysis of the degree of reversibility of crystallization and melting in poly(ethylene-co-1-octene). *Macromolecules* **2000**, 33, (24), 9076-9089.

79. Joubert, D. J.; Goderis, B.; Reynaers, H.; Mathot, V. B. F., Spatially inhomogeneous

crystallinity in heterogeneous ethylene-alpha-olefin copolymers. *Journal of Polymer Science Part B-Polymer Physics* **2005**, 43, (21), 3000-3018.

80. Strobl, G. R.; Schneider, M. J.; Voigtmartin, I. G., Model of Partial Crystallization and Melting Derived from Small-Angle X-Ray-Scattering and Electron-Microscopic Studies on Low-Density Polyethylene. *Journal of Polymer Science Part B-Polymer Physics* **1980**, 18, (6), 1361-1381.

81. Li, Y.; Akpalu, Y. A., Probing the Melting Behavior of a Homogeneous Ethylene/1-Hexene Copolymer by Small-Angle Light Scattering. *Macromolecules* **2004**, 27, 7265-7277.

82. Schouterden, P.; Vandermarliere, M.; Riekel, C.; Koch, M. H. J.; Groeninckx, G.; Reynaers, H., Characterization of the Morphological-Changes in Linear Low-Density Polyethylene During the Melting Process Using Synchrotron Radiation. *Macromolecules* **1989**, 22, (1), 237-244.

83. Vonk, C. G.; Koga, Y., An X-Ray-Diffraction Study of Nonlinear Polyethylene .2. Small-Angle Scattering Observations near the Melting-Point. *Journal of Polymer Science Part B-Polymer Physics* **1985**, 23, (12), 2539-2548.

84. Akpalu, Y. A.; Amis, E. J., Evolution of density fluctuations to lamellar crystals in linear polyethylene. *Journal of Chemical Physics* **1999**, 111, (18), 8686-8695.

85. Bark, M.; Zachmann, H. G.; Alamo, R.; Mandelkern, L., Investigations of the Crystallization of Polyethylene by Means of Simultaneous Small-Angle and Wide-Angle X-Ray-Scattering. *Makromolekulare Chemie-Macromolecular Chemistry and Physics* **1992**, 193, (9), 2363-2377.

86. Chiu, F. C.; Wang, Q.; Fu, Q.; Honigfort, P.; Cheng, S. Z. D.; Hsiao, B. S.; Yeh, F. J.; Keating, M. Y.; Hsieh, E. T.; Tso, C. C., Structural and morphological inhomogeneity of short-chain branched polyethylenes in multiple-step crystallization. *Journal of Macromolecular Science-Physics* **2000**, B39, (3), 317-331.

87. Xu, J. T.; Li, B. T.; Fan, Z. Q.; Ryan, A. J., Simultaneous SAXS/WAXS/DSC studies on microstructure of conventional and metallocene-based ethylene-butene copolymers. *Chinese Journal of Polymer Science* **2004**, 22, (3), 279-287.

88. Goderis, B. In *Thermal behaviour and real-time morphology of polyolefin systems*, 2003; Inst Chemical Fibres: 2003; pp 14-19.

89. Rabiej, S., On the origin of the multiple melting observed after isothermal crystallization of homogeneous ethylene/1-octene copolymers. *Polimery* **2004**, 49, (6), 414-423.

90. Janicki, J. In *SAXS and WAXD real time studies on nanostructure of selected polymer materials*, 2004; Elsevier Science Sa: 2004; pp 61-67.

91. Wang, Z.; Wang, H.; Shimizu, K.; Dong, K.-Y.; Hsiao, B. S.; Han, C. C., Structural and morphological development in poly(ethylene-co-hexene) and poly(ethylene-co-butylene) blends due to the competition between liquid-liquid phase separation and crystallization. *Polymer* **2005**, 46, 2675-2684.

92. Sajkiewicz, P.; Hashimoto, T.; Saijo, K.; Gradys, A., 'Intermediate phase' in poly(ethylene) as elucidated by the WAXS. Analysis of crystallization kinetics. *Polymer* **2005**, 46, (2), 513-521.

93. Baker, A. M. E.; Windle, A. H., Evidence for a partially ordered component in polyethylene from wide-angle X-ray diffraction. *Polymer* **2001**, 42, (2), 667-680.

94. McFaddin, D. C.; Russell, K. E.; Wu, G.; Heyding, R. D., Characterization of Polyethylenes by X-Ray-Diffraction and C-13-Nmr - Temperature Studies and the Nature of the Amorphous Halo. *Journal of Polymer Science Part B-Polymer Physics* **1993**, 31, (2), 175-183.

95. Monar, K.; Habenschuss, A. In *Modeling the principal amorphous halo in quiescent melts of polyethylene and ethylene copolymers using wide-angle X-ray scattering and its implications*, 1999; John Wiley & Sons Inc: 1999; pp 3401-3410.

96. Russell, K. E.; Hunter, B. K.; Heyding, R. D., Polyethylenes Revisited - WAXS and

the Phase-Structure. *European Polymer Journal* **1993**, 29, (2-3), 211-217.

97. Wunderlich, B., Reversible crystallization and the rigid-amorphous phase in semicrystalline macromolecules. *Progress in Polymer Science* **2003**, 28, (3), 383-450.

98. Janimak, J. J.; Stevens, G. C., Comparative crystallisation and exploratory micro-structure studies of novel polyethylenes with tailored molecular characteristics. *Polymer* **2000**, 41, (11), 4233-4248.

99. Akpalu, Y.; Kielhorn, L.; Hsiao, B. S.; Stein, R. S.; Russell, T. P.; Egmond, J. v.; Muthukumar, M., Structure Development during Crystallization of Homogeneous Copolymers of Ethene and 1-Octene: Time-Resolved Synchrotron X-ray and SALS Measurements. *Macromolecules* **1999**, 32, 765-770.

100. Mirabella, F. M., Crystallization and melting of narrow composition distribution polyethylenes: Investigation and implications of crystal thickening. *Journal of Polymer Science Part B-Polymer Physics* **2003**, 41, (3), 235-246.

101. Voigt-Martin, I. G.; Alamo, R.; Mandelkern, L., A Quantitative Electron-Microscopic Study of the Crystalline-Structure of Ethylene Copolymers. *Journal of Polymer Science Part B-Polymer Physics* **1986**, 24, (6), 1283-1302.

102. Doi, M.; Edwards, S. F., *The Theory of Polymer Dynamics*. Oxford University Press: Oxford, 1986.

103. Milner, S. T.; McLeish, T. C. B., Parameter-Free Theory for Stress Relaxation in Star Polymer Melts. *Macromolecules* **1997**, 30, 2159-2166.

104. Ferry, J. D., *Viscoelastic Properties of Polymers*. 2 ed.; Wiley: New York, 1970.

105. Seki, M.; Thurman, D. W.; Oberhauser, J. P.; Kornfield, J. A., Shear-mediated crystallization of isotactic polypropylene: The role of long chain -- long chain overlap. *Macromolecules* **2002**, 35, 2583-2594.

106. Yang, L.; Soman, R. H.; Sics, I.; Hsiao, B. S.; Kolb, R.; Lohse, D., The role of high molecular weight chains in flow-induced crystallization precursor structures.

*Journal of Physics: Condensed Matter* **2006**, 18, S2421-S2436.

107. Daniels, D. R.; McLeish, T. C. B.; Kant, R.; Crosby, B. J.; Young, R. N.; Pryke, A.; Allgaier, J.; Groves, D. J.; Hawkins, R. J., Linear rheology of diluted linear, star and model long chain branched polymer melts. *Rheologica Acta* **2001**, 40, (5), 403-415.

108. Inkson, N. J.; Graham, R. S.; McLeish, T. C. B.; Groves, D. J.; Fernyhough, C. M., Viscoelasticity of monodisperse comb polymer melts. *Macromolecules* **2006**, 39, (12), 4217-4227.

109. Glotin, M.; Mandelkern, L., Crystalline Morphology of Isothermally Crystallized Branched Polyethylene. *Macromolecules* **1981**, 14, (5), 1394-1404.

110. Swan, P. R., Polyethylene Unit Cell Variations with Branching. *Journal of Polymer Science* **1962**, 56, (164), 409-&.

111. Allen, G.; Gee, G.; Wilson, G. J., Intermolecular Forces and Chain Flexibilities in Polymers .1. Internal Pressures and Cohesive Energy Densities of Simple Liquids. *Polymer* **1960**, 1, (4), 456-466.

112. Wang, Z. G.; Hsiao, B. S.; Fu, B. X.; Liu, L.; Yeh, F.; Sauer, B. B.; Chang, H.; Schultz, J. M., Correct determination of crystal lamellar thickness in semicrystalline poly(ethylene terephthalate) by small-angle X-ray scattering. *Polymer* **2000**, 41, (5), 1791-1797.

113. Peeters, M.; Goderis, B.; Reynaers, H.; Mathot, V., Morphology of Homogeneous Copolymers of Ethylene and 1-Octene. II. Structural Changes on Annealing. *Journal of Polymer Science: Part B: Polymer Physics* **1999**, 37, (1), 83-100.

114. Vonk, C. G.; Pijpers, A. P., An X-Ray-Diffraction Study of Nonlinear Polyethylene .1. Room-Temperature Observations. *Journal of Polymer Science Part B: Polymer Physics* **1985**, 23, (12), 2517-2537.

115. Stribeck, N.; Alamo, R. G.; Mandelkern, L.; Zachmann, H. G., Study of the

Phase-Structure of Linear Polyethylene by Means of Small-Angle X-Ray-  
Scattering and Raman-Spectroscopy. *Macromolecules* **1995**, 28, (14), 5029-5036.

## Chapter 4

### Morphology Development in Model Polyethylenes via Two-Dimensional Correlation Analysis

<b>4.1</b>	<b>INTRODUCTION.....</b>	<b>IV-2</b>
<b>4.2</b>	<b>EXPERIMENTAL METHODS .....</b>	<b>IV-6</b>
4.2.1	Materials .....	IV-6
4.2.2	X-ray Scattering.....	IV-6
4.2.3	Computation.....	IV-7
4.2.3.1	Conventional 2D Correlation Analysis .....	IV-7
4.2.3.2	Two-Dimensional Moving Window Analysis .....	IV-8
4.2.3.3	Heterospectral Correlation Analysis .....	IV-9
<b>4.3</b>	<b>RESULTS AND DISCUSSION .....</b>	<b>IV-11</b>
4.3.1	WAXS .....	IV-12
4.3.1.1	Polyethylene WAXS Features .....	IV-12
4.3.1.2	Crystallization of Homopolymers.....	IV-14
4.3.1.3	Crystallization of Random Copolymers.....	IV-19
4.3.1.4	Searching for a Semi-Ordered Phase .....	IV-28
4.3.2	SAXS .....	IV-30
4.3.2.1	Crystallization of Random Copolymers.....	IV-30
4.3.3	SAXS/WAXS Heterospectral Correlation Analysis .....	IV-38
4.3.3.1	Crystallization of Random Copolymers.....	IV-38
4.3.3.2	Scattering at the Onset of Crystallization .....	IV-43
4.3.4	Material Comparisons .....	IV-45
<b>4.4</b>	<b>CONCLUSION .....</b>	<b>IV-45</b>
<b>4.5</b>	<b>ACKNOWLEDGEMENTS .....</b>	<b>IV-49</b>
<b>4.6</b>	<b>REFERENCES.....</b>	<b>IV-50</b>

## 4.1 INTRODUCTION

The physical properties of semicrystalline polymeric materials are ultimately dictated by their morphology in the solid state. This morphology is a complex function of molecular characteristics (molecular weight, architecture, etc.), thermal history (cooling rate, etc.), and processing (shear stress, extensional flow rate, etc.). The large number of variables that affect the morphology, and hence material properties, has led to extensive studies that try to discern morphological development using techniques such as wide angle and small angle x-ray scattering (WAXS and SAXS, respectively).<sup>1-15</sup> Information relevant to the sample morphology is often discerned from many conventional x-ray data analysis techniques that involve the calculation of morphological parameters such as crystallinity ( $X_c$ ), long period ( $L_p$ ), and the SAXS integrated intensity ( $Q$ ).

The application of such conventional techniques on SAXS and WAXS data obtained during crystallization of hydrogenated polybutadiene (HPBD) materials in Chapter 3 revealed that morphology development of these short-chain branched (SCB) materials during cooling can be separated into three crystallization regimes (Figure 3.15 in Chapter 3). ‘Primary-irreversible’ crystallization occurs at the highest temperatures and is marked by large changes in the morphological parameters ( $X_c$ ,  $L_p$ , and  $Q$ ) as primary lamellae propagate rapidly through unconstrained melt. Once the majority of unconstrained melt is consumed, secondary lamellar growth in the largest non-crystalline regions between primary lamellae marks slower ‘secondary-irreversible’ crystallization that occurs at intermediate temperatures. This temperature region is marked by slower changes in  $X_c$  and  $L_p$  and a nearly constant  $Q$  near its maximum value. The secondary-irreversible regime is not evident in homopolymers, such as HDPE, due to the relatively uniform and narrow

non-crystalline layer thickness in the primary lamellar stacks under the conditions examined. Both irreversible regimes obtain their names from the hysteresis that is observed between the morphological parameters during cooling and subsequent heating as a consequence of supercooling requirements for nucleation and growth of entangled polymers. At low temperatures, the values of the morphological parameters are equal during cooling and subsequent heating marking the slow formation of fringed micelles that occurs in the ‘reversible’ crystallization regime. Unlike homopolymers, reversible crystallization of random copolymers exhibits significant changes in  $X_c$  and  $L_p$ , which has important implications for physical aging of these materials.<sup>16</sup> Additionally, a decrease in  $Q$  observed when while  $X_c$  was below 50% is consistent with a decrease in electron density contrast during reversible crystallization of HPBDs. These three crystallization regimes exhibit unique and complex behavior, the understanding of which can aid in the control of material properties.

The complex evolution of morphology during crystallization of polymers can be better understood by examining x-ray scattering curves as a whole, rather than particular characteristics, such as peak location or area. Such an examination can be conducted using two-dimensional (2D) correlation analysis whose application is abundant in the field of vibrational spectroscopy.<sup>17-20</sup> This powerful technique allows for the examination of sometimes subtle changes in spectral intensities in response to a perturbation variable, such as temperature. This versatile analysis has been frequently applied to protein,<sup>21-23</sup> liquid crystal,<sup>24, 25</sup> and polymer<sup>26-31</sup> systems when studied by Raman or infrared spectroscopy. However, although the generalization of the 2D correlation analysis by Noda has allowed it to be easily applied to most three-dimensional datasets,<sup>17-19</sup> its application to

experimental data obtained using other probes, such as x-rays, has been surprisingly limited.<sup>31, 32</sup>

The application of 2D correlation analysis provides distinct advantages that can be utilized to extract information about morphology from x-ray scattering data during crystallization or melting. These advantages include the simplification of complex scattering curves through the de-convolution of overlapping features, the determination of sequential order of intensity changes, and the enhancement of spectral resolution by spreading data over a second dimension. Additionally, 2D moving window analysis (MW2D) allows for the examination of correlated intensity changes as a function of (versus a general response to) the perturbation variable.<sup>17, 18, 31</sup> Furthermore, heterospectral correlation analysis,<sup>18</sup> an extension of the conventional 2D method, allows one to directly visualize changes in SAXS and WAXS that are the result of the same physical processes.

This analysis can provide new insight into important aspects of polymer crystallization. For example, there has been significant debate behind the reasons for poor results when WAXS curves of ethylene copolymers are fitted for the purposes of crystallinity calculations using a two-phase model: one peak for the amorphous halo and one peak for each of the crystalline reflections.<sup>4, 5, 7, 33-37</sup> Some of these studies have noted that fitting the amorphous halo with two peaks yields a better fit and more reasonable behavior of all peaks considered (position, width, etc.).<sup>4, 5, 7, 33, 34, 37</sup> The physical justification of this additional peak is controversial. Observation of a hexagonal mesophase reported in some studies<sup>38-40</sup> was not corroborated in others.<sup>33, 34, 41-43</sup> Alternatively, one or more peaks have been proposed to account for a ‘semi-ordered,’ ‘transition,’ or ‘intermediate’ phase/region. Simanke et al. reject this possibility based on the idea that scattering from

such a phase would not be limited to any particular angular region in the WAXS patterns due to conformationally diffuse interfacial region between ordered and disordered phases.<sup>33</sup> Nonetheless, some groups maintain the existence of a semi-ordered phase that contributes one or two relatively narrow reflections. Sajkiewicz et al.<sup>5</sup> proposed the presence of a phase having intermediate properties to those of the crystalline and amorphous layers. As such, this intermediate phase was believed to contribute a hidden, relatively narrow peak to the WAXS intensity located between the amorphous halo and the (110) reflection. As would be expected, this peak was found to broaden and shift in angular position towards the amorphous halo with increasing SCB content and molecular weight (based on the fitting algorithm used). When two peaks have been used to account for the semi-ordered region, they have closely resembled the (110) and (200) orthorhombic reflections, but had lesser intensity and were shifted to lower  $q$ -values.<sup>7, 34, 35, 37</sup> These are referred to as '(110)' and '(200)', respectively, by Rabiej et al.<sup>35</sup> As an alternative explanation for the poor fit provided by the two-phase model, some authors suggest that a possible transition region between the crystalline and non-crystalline layers contributes to density heterogeneity in the amorphous halo which can be captured by an additional amorphous-halo-like scattering in a large angular range.<sup>4, 36</sup> The sensitivity of 2D correlation analysis to overlapping features makes it a well-suited technique to gain further insight into the possibility of a semi-ordered phase.

In the following, we examine the evolution of morphology during the crystallization of random copolymers (HPBDs) using conventional and heterospectral 2D correlation analysis. WAXS behavior of a homopolymer (HDPE) was also examined for comparison. Unique features corresponding to the development of different morphologies

(primary and secondary lamellae, fringed micelles) and the occurrence of physical processes (crystal growth, thermal contraction, etc.) are identified. The application of heterospectral analysis in the earliest stages of crystallization is used to comment on the dominant physical processes during the onset of crystallization.

## 4.2 EXPERIMENTAL METHODS

### 4.2.1 Materials

The materials used for the present study are the same hydrogenated polybutadienes (HPBDs) as described in the previous chapter (Section 3.2.1). Table 3.1 is reproduced for convenience as Table 4.1.

**Table 4.1 Molecular characteristics of polyethylene materials examined. All values provided by ExxonMobil.**

Polymer	Type	$M_{w,tot}$ (kg/mol)	PDI	$M_{w,b}$ (kg/mol)	$M_{w,a}$ (kg/mol)	Branches/ 1000 C <sup>a</sup>
L53	Linear	53	<1.05	53		19.2
L152	Linear	152	<1.05	152		19.5
S3	3-arm star	141	<1.05		47	18.9
H4	H- polymer	156	<1.05	112	11	26.3
HDPE	Linear	529	3.0	529		0.2

<sup>a</sup> obtained via  $^{13}\text{C}$  NMR

### 4.2.2 X-ray Scattering

Morphology development during heating and cooling ramps (10 °C/min from 180 to 0 °C) was followed using wide and small angle x-ray scattering (WAXS and SAXS, respectively) as described in the previous chapter with scattering patterns collected every 2 °C (Section 3.2.2 of Chapter 3).

### 4.2.3 Computation

#### 4.2.3.1 Conventional 2D Correlation Analysis

Two-dimensional (2D) correlation analysis of the x-ray scattering data was conducted using Noda's generalized method<sup>19, 20</sup> as described in Section 2.2.4 of Chapter 2. Discrete 'spectra' consisted of the Lorentz corrected SAXS and WAXS intensities,  $J(q) = I(q)q^2$ , as a function of the scattering vector,  $q$ . An exception was made in an examination of the onset of crystallization; here, the Lorentz correction does not apply because of the lack of a well-resolved scattering peak at the highest temperatures hence non-Lorentz corrected curves,  $I(q)$ , were analyzed.<sup>44</sup> The perturbation variable was temperature, as in Chapter 2. Correlation analysis was applied separately to scattering curves corresponding to primary-irreversible, secondary-irreversible, and reversible crystallization regimes (see previous chapter). Additionally, modified mean normalization was applied SAXS data as it has been observed to help discriminate overlapped peaks.<sup>45</sup> In this case, prior to calculation of the 2D correlation plots, individual scattering curves ( $I_i(q) = I(q, T_i)$  for  $i = 1, 2, 3, \dots, m$ ) were normalized for average intensity,  $I_{i,mean}$ , and maximum intensity,  $I_{i,max}$ :

$$I_{i,norm} = \frac{I_i}{I_{i,mean}^2 / I_{i,max}}, \quad (4.1)$$

where

$$I_{i,mean} = \frac{1}{q_{\max} - q_{\min}} \int_{q_{\min}}^{q_{\max}} I_i(q) dq. \quad (4.2)$$

This pre-treatment accounts for differences in peak area and half width by approximating bands as Lorentzian peaks in order to minimize effects of strong intensity changes.<sup>45</sup> The

resulting scattering curves were examined to ensure no artificial peaks resulted from the normalization.<sup>46-48</sup>

#### 4.2.3.2 Two-Dimensional Moving Window Analysis

While conventional 2D correlation analysis allows for the identification of overall trends in response to a perturbation, sometimes this results in omission of subtle aspects that are limited to a specific range of the perturbation variable. For example, minor intensity changes at high temperature may not be apparent if significant changes dominate at low temperatures. In this case, intensity changes as a function of the perturbation variable,  $T$ , of a large dataset ( $I_i(q) = I(q, T_i)$  for  $i = 1, 2, 3, \dots, m$ , represented schematically in Figure 4.1a) can be examined by the implementation of moving window 2D correlation (MW2D) analysis.<sup>25, 49, 50</sup> The synchronous 2D correlation spectrum is calculated for a subset or smaller ‘window’ of spectra ( $I_i(q)$ ,  $i = M, \dots, M + \Delta M$ , where  $1 < M < M + \Delta M < m$ ) that is shifted sequentially by one spectrum through the full data set (Figure 4.1a,b). Here, subsets examined corresponded to 10 °C. For each window, a 1D spectrum is selected to be characteristic of the 2D spectrum (Figure 4.1c). The autocorrelation intensity (diagonal of the synchronous spectrum) is used in conventional MW2D, as it depicts the overall changes in intensity occurring simultaneously. When MW2D is used in conjunction with heterospectral analysis (see below), the autocorrelation intensity has little meaning, hence a specifically selected slice spectrum that represents the behavior of interest is used instead. The set of 1D spectra obtained from the window as it is shifted sequentially through the data set is plotted as a function of the perturbation variable, or in this case, temperature (Figure 4.1d).

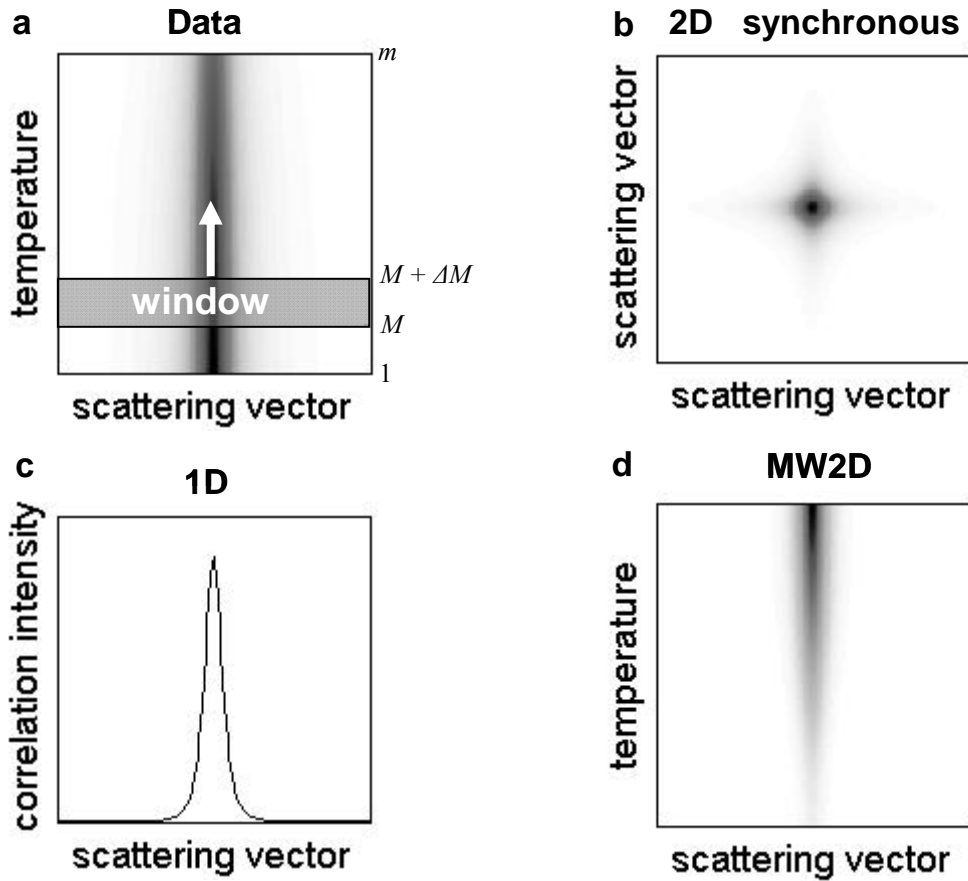


**Figure 4.1** A schematic representation of 2D moving window analysis. **a)** A ‘window’ from the full dataset is selected and shifted sequentially through the set. **b)** For each window, a 2D synchronous spectrum is calculated. **c)** A 1D spectrum is selected to represent the 2D spectrum in **b**. **d)** These 1D spectra for each window plotted as a function of the perturbation variable (i.e., temperature).

#### 4.2.3.3 Heterospectral Correlation Analysis

Simultaneous changes in SAXS and WAXS occurring as a consequence of the same physical processes are revealed by 2D heterospectral correlation analysis. Heterospectral correlation analysis identifies simultaneous changes in the system observed by two different probes under the same perturbation: Lorentz corrected SAXS ( $J_{SAXS,i}(q) = J_{SAXS}(q, T_i)$ ,  $i = 1, 2, 3, \dots, m$ ) and WAXS ( $J_{WAXS,i}(q) = J_{WAXS}(q, T_i)$ ,  $i = 1, 2, 3, \dots, m$ ) curves collected during temperature ramps. Dynamic scattering curves for both SAXS and

WAXS intensities,  $\tilde{J}_i(q)$ , are calculated with respect to the temperature-averaged spectrum:

$$\tilde{J}_i(q) = J_i(q) - \bar{J}(q), \quad (4.3)$$

where

$$\bar{J}(q) = \frac{1}{m} \sum_{i=1}^m J(q, T_i). \quad (4.4)$$

The synchronous 2D heterospectral correlation spectrum is calculated as

$$\Phi(q_1, q_2) = \frac{1}{m-1} \sum_{i=1}^m \tilde{J}_{SAXS,i}(q_1) \cdot \tilde{J}_{WAXS,i}(q_2). \quad (4.5)$$

The asynchronous spectrum was not considered because it lacks well-established interpretation.<sup>17, 18, 31</sup>

Additionally, the onset of crystallization was examined using a combination of 2D heterospectral correlation analysis in conjunction with MW2D. In this case, forgoing the Lorentz correction allowed us to include SAXS curves that lack a well-defined peak.<sup>44</sup> Two-dimensional hetero-spectra were calculated for data ‘windows’ corresponding to approximately 10 °C, as described above, in order to gauge simultaneous changes in SAXS and WAXS intensities early in the crystallization process. For the 1D representation of the 2D hetero-spectra, the correlation intensity corresponding to the (110) WAXS reflection was examined as a function of temperature.

For image presentation, contour levels were adjusted to exclude the bottom 5% of intensity values. Additionally, contour plots reveal relative intensities; therefore different figures have different contour levels in order to highlight the relevant features in each case. Unless otherwise stated, intensity values between different figures cannot be compared by the apparent relative intensity of features.

### 4.3 RESULTS AND DISCUSSION

In Chapter 3, we showed that morphology evolution during quiescent cooling and heating ramps can be characterized by two well-defined regimes: irreversible and reversible crystallization/melting.<sup>3, 51-54</sup> The irreversible crystallization regime occurs at higher temperatures relative to the reversible one and is marked by relatively large changes with temperature in morphological parameters (long period,  $L_p$ , crystallinity,  $X_c$ , and SAXS integrated intensity,  $Q$ ), which exhibit a hysteresis upon cooling and heating (Figure 3.16 in Chapter 3). Irreversible crystallization of model random copolymers can be further divided into two regimes according to the degree of change of the morphological parameters: the ‘primary-irreversible’ regime, which exhibits the fastest changes in morphological parameters (Figure 3.16a,b in Chapter 3) and, at lower temperatures, ‘secondary-irreversible’ crystallization regime, which is characterized by slower changes in  $X_c$  and  $L_p$  and a broad maximum in  $Q$  (Figure 3.16a,c in Chapter 3). Reversible crystallization occurs at the lowest temperatures where morphological parameters during heating and cooling overlap and change mildly with temperature relative to the irreversible regimes (Figure 3.16a in Chapter 3). The WAXS and SAXS results for these regimes are well-suited for the application of 2D correlation analysis, with goals to both to elucidate features corresponding to specific morphology changes that are difficult to discern via traditional analysis and to establish characteristic 2D signatures of the three regimes, which correspond to the evolution of different morphology (primary and secondary lamellae, as well as fringed micelles).

### 4.3.1 WAXS

#### 4.3.1.1 Polyethylene WAXS Features

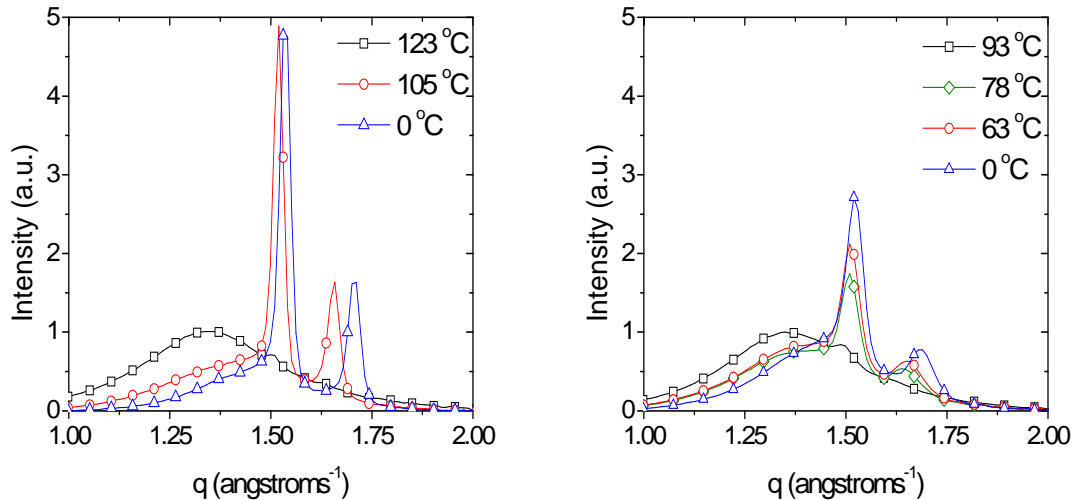


**Figure 4.2** WAXS intensity during cooling at 10 °C/min at temperatures marking the bounds of different crystallization regimes for **a**) HDPE and **b**) L152 while cooling at 10 °C/min.

Examination of the WAXS crystallinity evolution through the analysis of two-dimensional correlation plots focuses on three salient WAXS features of polyethylene materials: the broad amorphous halo (centered at approximately  $1.35 \text{ \AA}^{-1}$ ) and the two most prominent crystalline reflections of the orthorhombic unit cell, which are due to the (110)-planes (near  $1.5 \text{ \AA}^{-1}$ ) and the (200)-planes (near  $1.65 \text{ \AA}^{-1}$ ) (Figure 4.2).

Figure 4.2 compares 1D WAXS curves at temperatures corresponding to the transitions between different crystallization regimes for HDPE and L152. HDPE develops almost all of its crystallinity via irreversible crystallization in the range between 123 and 105 °C as evidenced by large changes in intensity of the crystalline reflections (Figure 4.2a). Little change in the intensity of the crystalline peaks was observed between 105 and 0 °C, consistent with minimal crystallization occurring in the reversible regime

(Figure 4.2a). However, crystalline reflections are shifted to higher values of  $q$  at the end of the reversible regime ( $T = 0$  °C) compared to at its beginning ( $T = 105$  °C) as a consequence of thermal contraction.<sup>55, 56</sup>

Behavior of L152 is more complex and is characterized by 4 temperatures of interest that define its three crystallization regimes: primary-irreversible (93 to 78 °C), secondary-irreversible (78 to 63 °C), and reversible (below 63 °C). Appreciable crystallinity develops during all three regimes marked by the increase in magnitude of the crystal reflections. An increase in width of the crystal reflections is also observed and is a consequence of SCB content. At lower temperatures, crystallization of shorter ethylene sequences leads to more chain defects (i.e., short-chain branches) encountered by the crystal growth front. The result is a decrease in coherence of unit cells manifested as a broadening of the crystal reflections.

Similar to HDPE, L152 crystal reflections shift to higher  $q$ -values with decreasing temperature as the result of thermal contraction but their intensities change as well. Moreover, L152 (Figure 4.2b) exhibits crystalline reflections that are shifted to slightly lower  $q$ -values relative to HDPE; for example, the (200) reflection at 0 °C is located at 1.68 Å<sup>-1</sup> for L152 versus 1.70 Å<sup>-1</sup> for HDPE. This is a result of SCB-induced expansion of the orthorhombic unit cell—a phenomenon frequently observed in prior literature on ethylene copolymers.<sup>4, 5, 33, 57-63</sup> Although the reason for this effect is obvious in the case of methyl groups that are incorporated into the crystal lattice,<sup>64</sup> ethyl, butyl, and hexyl branches also have a small but noticeable effect attributed to the strain they induce by crowding at the interface of thin crystals.<sup>57, 62</sup>

A final important feature is the increase in scattering intensity in a small  $q$ -range near  $1.45 \text{ \AA}^{-1}$  during secondary-irreversible crystallization (compare 78 with  $63^\circ\text{C}$  in Figure 4.2) and reversible crystallization (compare 0 with  $63^\circ\text{C}$  in Figure 4.2). In contrast to HDPE, L152 does not exhibit a monotonic decrease in amorphous halo scattering with decreasing temperature, but rather a pronounced change in shape. Some authors attribute this shape change to the presence of a third phase having intermediate properties between crystalline and amorphous phases.<sup>5</sup> In light of this and other theories, scattering in this region is further explored using 2D correlation analysis.

#### 4.3.1.2 Crystallization of Homopolymers

Since HDPE has only two crystallization regimes: (1) irreversible crystallization that occurs in the range of  $123$  to  $105^\circ\text{C}$  and accounts for approximately  $85\%$  of crystallinity developed during cooling to  $0^\circ\text{C}$  (Figure 3.7 in Chapter 3) and (2) reversible crystallization in the range of  $105$  to  $0^\circ\text{C}$ , two-dimensional correlation analysis was applied to WAXS spectra in these two temperature ranges. As mentioned previously, a secondary-irreversible regime was not present.

##### *Irreversible Crystallization*

Irreversible crystallization of HDPE is characterized by a strong increase in the amount of crystalline material, which is manifested as an increase in diffracted intensity of the (110) and (200) crystalline reflections. Consequently, the 2D synchronous pattern is dominated by two strong autopeaks (located along the diagonal) at approximately  $1.5$  and  $1.65 \text{ \AA}^{-1}$  associated with monotonic changes in the (110) and (200) reflections

(Figure 4.3a). In addition, since the intensities of both peaks increase as the result of the same physical process—the formation of orthorhombic unit cells—the cross peaks at  $(1.52 \text{ \AA}^{-1}, 1.66 \text{ \AA}^{-1})$  and  $(1.66 \text{ \AA}^{-1}, 1.52 \text{ \AA}^{-1})$ , which measure the extent to which changes in both peaks occur simultaneously are also strong. The sign of these cross peaks is positive, consistent with the intensity change of (110) and (200) peaks occurring in the same direction (i.e., both increasing during crystallization).

Formation of crystallites inherently consumes the subcooled melt, both by organizing polyethylene strands into crystals and by altering the non-crystalline material that is trapped between lamellae. The corresponding amorphous halo is very broad, so its change in peak intensity is much weaker than that of the crystalline reflections (approximately 11% as large as the change in the intensity of the (110) reflection). Consequently, the autocorrelation peak associated with the amorphous halo is extremely weak compared to crystalline peaks and is below the contour threshold of the synchronous pattern in Figure 4.3a. Indeed, compared to the (110) peak, the halo autocorrelation intensity is only  $(11\%)^2 \approx 1\%$ , due to the quadratic nature of 2D correlation, and is practically invisible. Correlation peaks between the amorphous halo and the crystalline reflections, on the other hand, are readily visible on this scale as negative cross peaks: their magnitude scales as the product of the amount of the change in the amorphous halo (weak) and the change in the respective crystalline peak (strong). The shape of these features is elongated due to the breadth of the amorphous halo and the sharpness of the diffraction peaks. Their negative sign indicates that crystalline peaks change in the opposite direction from the amorphous halo consistent with the growth of crystals occurring at the expense of non-crystalline material, in accord with physical interpretation of crystallization.

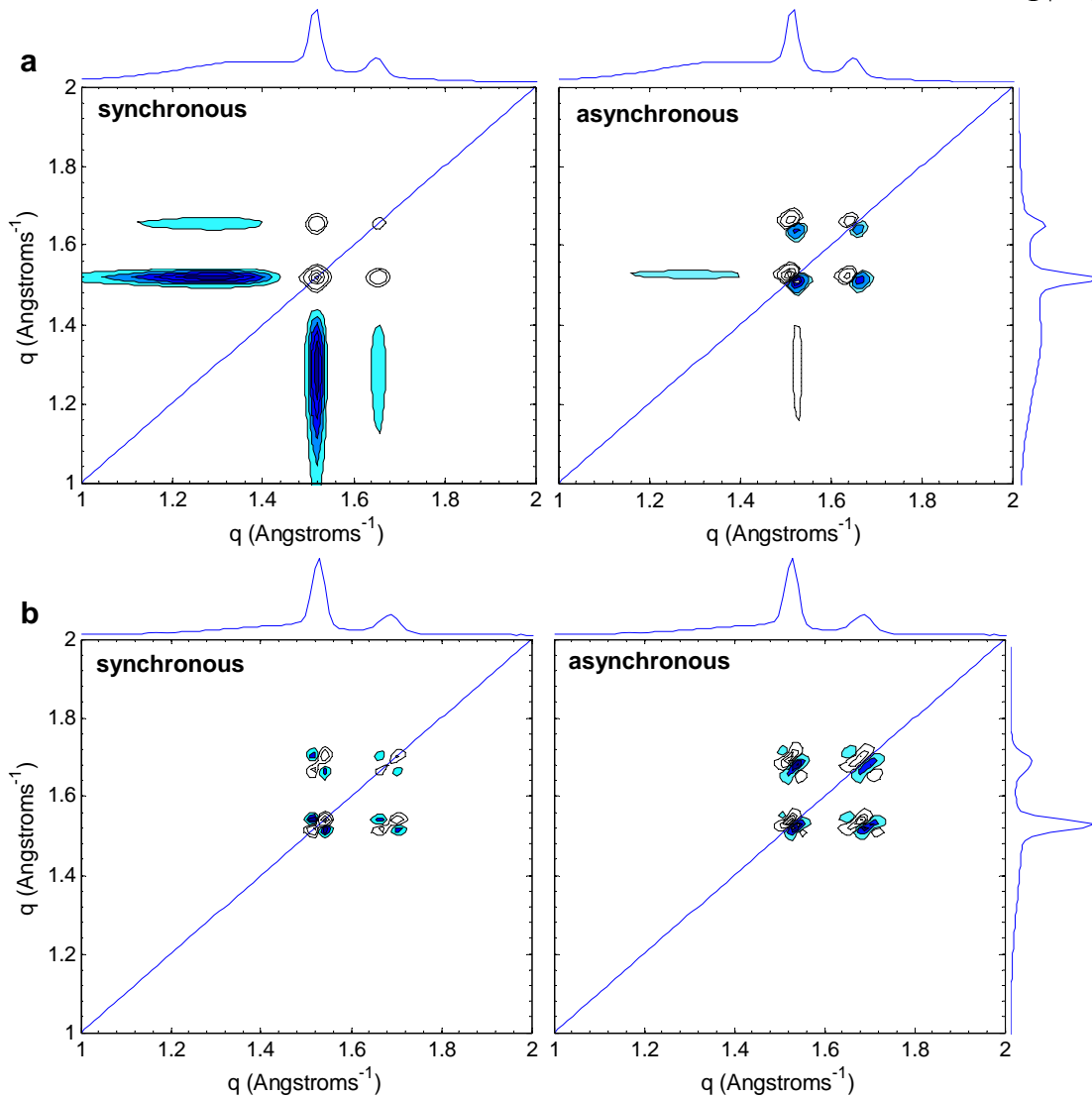


**Figure 4.3** 2D synchronous (left) and asynchronous (right) correlation plots derived from Lorentz corrected WAXS curves collected during **a**) irreversible ( $105\text{ }^{\circ}\text{C} < T < 123\text{ }^{\circ}\text{C}$ ) and **b**) reversible ( $0\text{ }^{\circ}\text{C} < T < 105\text{ }^{\circ}\text{C}$ ) crystallization of HDPE occurring during cooling at  $10\text{ }^{\circ}\text{C}/\text{min}$ . Positive and negative contours are shown as open and filled, respectively. Averaged 1D scattering profiles are shown on the sides.

The asynchronous plot reveals that crystallization is not the only physical process that occurs during cooling. Different physical processes can be identified by intensity changes that are temporally separated, the extent of which can be observed in the corresponding asynchronous plots. In the case of HDPE undergoing irreversible crystallization ( $105\text{ }^{\circ}\text{C} < T < 123\text{ }^{\circ}\text{C}$ ), the asynchronous plot displays tightly-packed pairs of cross peaks

located at the vertices of the correlation square defined by the crystalline reflections:  $(1.52 \text{ \AA}^{-1}, 1.52 \text{ \AA}^{-1})$ ,  $(1.66 \text{ \AA}^{-1}, 1.66 \text{ \AA}^{-1})$ ,  $(1.52 \text{ \AA}^{-1}, 1.66 \text{ \AA}^{-1})$ , and  $(1.66 \text{ \AA}^{-1}, 1.52 \text{ \AA}^{-1})$ . A doublet corresponding to a crystalline reflection can arise either from overlapping peaks changing at different rates (e.g., different crystal morphs) or from a shift in the position of a single peak. Given that the orthorhombic crystal morph is the only one expected under these conditions,<sup>65</sup> the doublets here are attributed to mild changes in peak position,<sup>66, 67</sup> which is a consequence of thermal contraction. The position of the doublet attributed to the (200) reflection at  $(1.64 \text{ \AA}^{-1}, 1.66 \text{ \AA}^{-1})$  can be interpreted as a shift in position of this reflection from approximately  $1.64 \text{ \AA}^{-1}$  to  $1.66 \text{ \AA}^{-1}$ ; the corresponding  $0.09 \text{ \AA}$  change in the unit cell parameter,  $a$ , is consistent with thermal contraction of the  $a$ -axis of the polyethylene crystal in the temperature range associated with irreversible crystallization.<sup>55</sup> The doublets appearing at the cross positions near  $(1.52 \text{ \AA}^{-1}, 1.66 \text{ \AA}^{-1})$  are a consequence of the shape of the features along the diagonal. The intensities of these doublets are an order of magnitude lower than corresponding synchronous peaks indicating that peak shifting is a secondary process to crystal formation.

Weak cross peaks can also be observed between the amorphous halo ( $1.2\text{--}1.4 \text{ \AA}^{-1}$ ) and the (110) reflection ( $1.52 \text{ \AA}^{-1}$ ). The corresponding cross peak between the amorphous halo and the (200) reflection ( $1.2\text{--}1.4 \text{ \AA}^{-1}$  and  $1.66 \text{ \AA}^{-1}$ ) is too weak and is not observed in Figure 4.3 due to the contour threshold. These cross peaks are consistent with the change in the amorphous halo exhibiting slight temporal separation from the growth of crystalline peaks. Following Noda's rules for the determination of sequential order of intensity changes,<sup>68</sup> it can be determined that change in the amorphous halo precedes the growth of

crystalline reflections. This observation can be explained by thermal contraction of the polyethylene melt prior to significant crystal formation.<sup>4</sup>

### *Reversible Crystallization*

While crystallinity development is the dominant physical process during irreversible crystallization, only approximately 15% of total crystallinity develops in the range from 105 to 0 °C corresponding to the reversible regime. This difference is apparent in the 2D correlation patterns which exhibit clusters of peaks corresponding to the crystalline reflections of HDPE, which exhibit characteristic features of a shift in peak position (Figure 4.3b). The “clover-leaf” patterns observed in the synchronous spectrum (positive autopeaks with negative cross peaks) indicate that both the (110) and (200) reflections undergo simultaneous decrease and increase in intensity on either side of the peak. While this could suggest the presence of overlapping peaks, the corresponding “butterfly” patterns in the asynchronous plot (Figure 4.3b, right) are characteristic of well-defined peak shifts of both of these crystalline reflections.<sup>18, 66, 69, 70</sup> These well-defined patterns indicating position shifts are evident because they are not convoluted by strong changes in intensity like during irreversible crystallization (see Figure 4.2a). When such patterns are present, the two autopeaks of the clover-leaf pattern corresponding to a single reflection indicate the starting and ending peak positions; for the (200) reflection, these positions are 1.66 and 1.70 Å<sup>-1</sup>, respectively, which is confirmed by the 1D WAXS curves (Figure 4.2). The sign of the ‘wing’ below the diagonal in the asynchronous butterfly patterns indicates that the positions of crystalline reflections shift in the direction from smaller to larger  $q$ -values, in agreement with thermal contraction.<sup>18</sup> The peak shift of the (200) reflection corresponds to a contraction in  $a$  of approximately 0.36 Å, which

is again consistent with thermal effects expected across the 105 °C range of reversible crystallization.<sup>55, 71, 72</sup> It is reassuring to note that the positions of the crystalline reflections, as determined by 2D correlation analysis, are continuous through the transition between the two crystallization regimes. The symmetry of the clover patterns is consistent with only minor changes in peak intensity during the shift, indicating that thermal contraction of the crystal phase is the dominant physical process in this regime.

#### **4.3.1.3 Crystallization of Random Copolymers**

The crystallization of L152 and the other HPBD materials investigated can be separated into three regimes: (1) primary-irreversible crystallization (93 to 78 °C), which accounts for 63% of the total crystallinity at 0 °C, (2) secondary-irreversible crystallization (78 to 63 °C), which accounts for 13% of total crystallinity at 0 °C, and (3) reversible crystallization (63 to 0 °C), which accounts for 24% of total crystallinity developed during cooling to 0 °C (Figure 3.7 in Chapter 3).

##### *Primary-Irreversible Crystallization*

The synchronous spectrum of L152 during primary-irreversible crystallization occurring between 93 and 78 °C (Figure 4.4a, left) displays similar features to that of HDPE (Figure 4.3a, left) with the exception of an additional autopeak corresponding to the amorphous halo near 1.3 Å<sup>-1</sup>. The latter should be not interpreted as a greater change in the amorphous halo in L152 compared with HDPE; rather, it is a consequence of the much weaker (110) and (200) diffraction peaks of L152 relative to HDPE (Figure 4.2). The crystalline reflections in this regime are located at almost the same peak position as

HDPE ((1.51  $\text{\AA}^{-1}$ , 1.51  $\text{\AA}^{-1}$ ) for the (110) reflection and (1.66  $\text{\AA}^{-1}$ , 1.66  $\text{\AA}^{-1}$ ) for the (200) reflection) despite the difference in temperature ( $\sim 30$   $^{\circ}\text{C}$ ) at which primary-irreversible crystallization occurs (78 to 93  $^{\circ}\text{C}$  for L152 versus 105 to 123  $^{\circ}\text{C}$  for HDPE). This is explained by the thermal contraction of the unit cell being offset by the effect of SCB, which is known to cause expansion of the unit cell.<sup>4, 5, 33, 57-63</sup>

Similar to HDPE, the asynchronous features of L152 are over an order of magnitude smaller than synchronous ones (Figure 4.4a, right). However, L152 and HDPE asynchronous plots exhibit marked differences that are the result of an increased relative contribution of the amorphous halo in the case of L152. Correlation between the amorphous halo and the (110) reflection reveals a pattern resembling an asymmetric, highly elongated doublet near (1.49  $\text{\AA}^{-1}$ , 1.15  $\text{\AA}^{-1}$ ) and (1.52  $\text{\AA}^{-1}$ , 1.35  $\text{\AA}^{-1}$ ) consistent with temporal separation between changes in the non-crystalline and crystalline phases. The fluctuating outlines of the features corresponding to the amorphous halo indicate that it is barely above the noise, hence the temporal separation between changes in the crystalline and non-crystalline phases is mild.

The crystalline reflections can again be recognized in the asynchronous plot by the appearance of doublets. The doublet corresponding to the (110) reflection at (1.52  $\text{\AA}^{-1}$ , 1.49  $\text{\AA}^{-1}$ ) is tightly spaced, similar to the case of HDPE, indicating minor changes in the (110) peak position consistent with thermal contraction. In contrast, the feature corresponding to the (200) reflection is further offset from the diagonal at (1.66  $\text{\AA}^{-1}$ , 1.62  $\text{\AA}^{-1}$ ). This feature cannot be fully explained by thermal contraction because a 0.04  $\text{\AA}^{-1}$  shift in the peak position corresponds to too large a difference in unit cell dimensions (almost 0.18  $\text{\AA}$  difference in  $a$ ) in this 15  $^{\circ}\text{C}$  range.<sup>73, 74</sup>

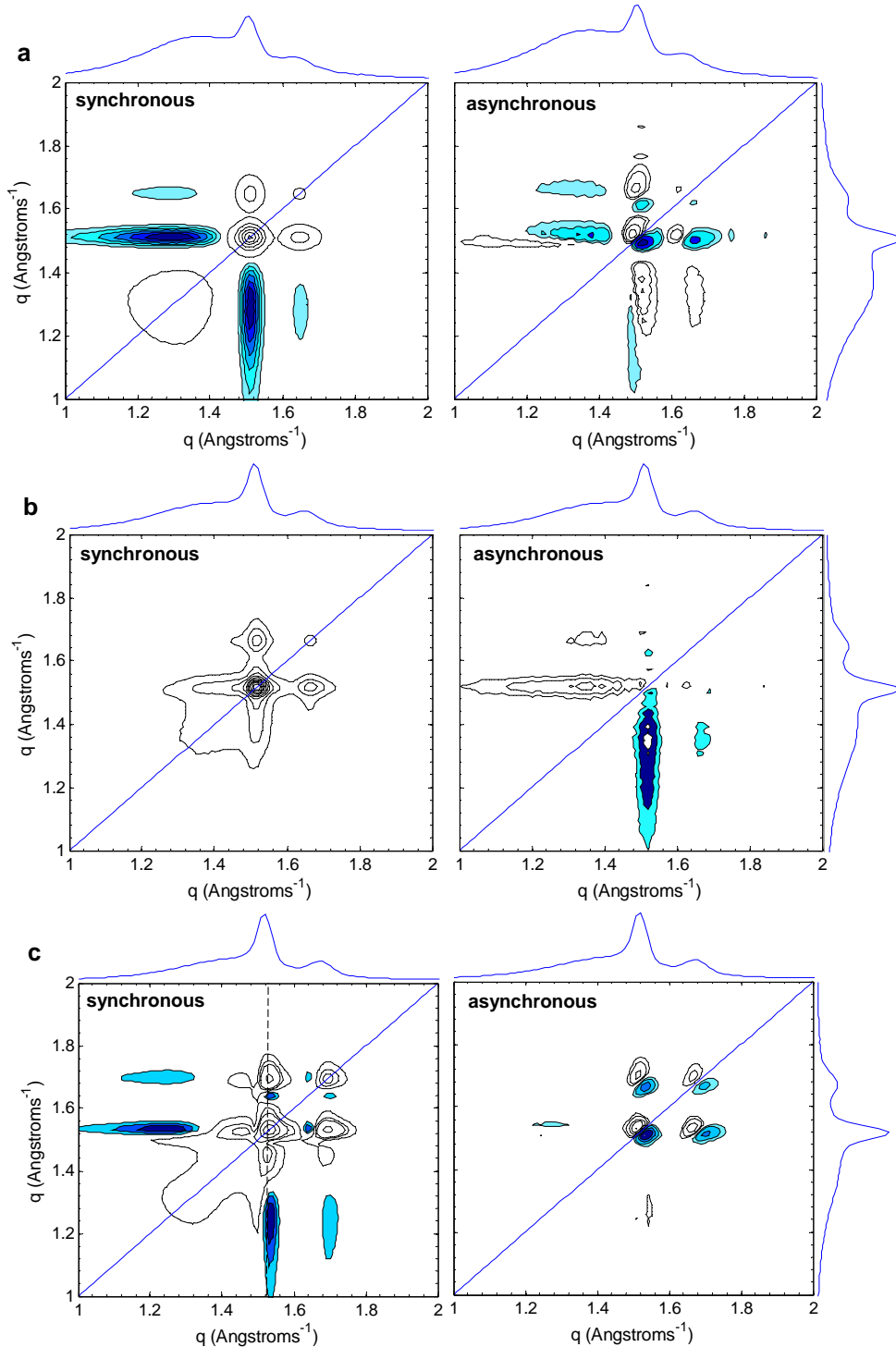


**Figure 4.4** 2D synchronous (left) and asynchronous (right) correlation plots derived from Lorentz corrected WAXS curves collected during cooling at  $10\text{ }^{\circ}\text{C/min}$  in the **a**) primary-irreversible ( $78\text{ }^{\circ}\text{C} < T < 93\text{ }^{\circ}\text{C}$ ) **b**) secondary-irreversible ( $63\text{ }^{\circ}\text{C} < T < 78\text{ }^{\circ}\text{C}$ ) and **c**) reversible ( $0\text{ }^{\circ}\text{C} < T < 63\text{ }^{\circ}\text{C}$ ) regimes of L152. Positive and negative contours are shown as open and filled, respectively. Averaged 1D scattering profiles are shown on the sides.

Alternatively, one may argue that the feature corresponding to the (200) reflection reflect temporally separated changes at 1.62 and 1.66 Å<sup>-1</sup> and are therefore the result of two scattering populations. One may assign the two overlapped peaks as the crystalline (200) reflection centered at 1.66 Å<sup>-1</sup> and the '(200)' semi-ordered phase reflection centered at 1.62 Å<sup>-1</sup>.<sup>35</sup> In this scenario, the tightly-spaced (110) doublet would also be attributed to changes in the (110) crystalline reflection and the '(110)' reflection of the semi-ordered phase, which are closer spaced at 1.52 and 1.49 Å<sup>-1</sup>, respectively.

On the other hand, the unusual magnitude and position of the (200) reflection may be attributed to a convolution of its behavior with changes in the broad amorphous halo having comparable magnitude. In addition to thermal contraction of the non-crystalline material (shifting the halo to large  $q$ ), during crystallization of HPBDs, the amorphous halo changes shape due to the enrichment of butyl branches in the non-crystalline regions as they are rejected from the crystals. This shape change results in comparable changes in magnitude between the amorphous halo and the (200) reflection. Hence, the decrease in the amorphous halo during crystallization convoluted with the change in position of the (200) reflection results in an altered 2D feature.

#### *Secondary-Irreversible Crystallization*

Crystallization in the secondary-irreversible regime is characterized by an overall increase in intensity occurring both in the crystalline reflections and the amorphous halo immediately adjacent to the (110) peak (Figure 4.4b, left). In addition to the familiar autopeaks and cross peaks associated with the (110) and (200) crystalline reflections at 1.52 and 1.67 Å<sup>-1</sup>, analogous to those in Figure 4.3a and Figure 4.4a, a change in shape of the amorphous halo combined with a minimal change in crystallinity (13% in this re-

gime) resulted in a qualitatively different 2D pattern. In contrast to the primary-irreversible regime, negative features corresponding to the decrease in the amorphous halo as a consequence of the development of crystallinity were not observed. Instead, the magnitude of the amorphous halo increased in the  $q$ -region adjacent to the (110) reflection near  $1.35\text{--}1.46\text{ \AA}^{-1}$ . A scattering peak in this region was suggested to correspond to an ‘intermediate’ phase by Sajkiewicz et al.<sup>5</sup> On the other hand, this observation is also consistent with increased packing density of a fraction of the non-crystalline regions resulting in a heterogeneous density distribution.<sup>4, 36</sup>

The asynchronous plot is dominated by features corresponding to the amorphous region below  $1.46\text{ \AA}^{-1}$  and the crystalline reflections (Figure 4.4b, right). Although the temperature range corresponding to secondary-irreversible crystallization is the same as for primary-irreversible crystallization ( $15\text{ }^\circ\text{C}$ ), the asynchronous spectrum here lacks elongated doublets corresponding to thermal contraction of the crystalline phase (compare with Figure 4.4a, right). Instead, a (200) feature is too weak to see and the (110) doublet (which is not resolved from the amorphous feature) is barely above the noise. These observations highlight the different physical processes that dominate these crystallization regimes. We speculate that the secondary lamella forming in this lower-temperature regime suffer more interfacial stress due to the accumulation of SCB at their crystal faces leading to formation of expanded unit cells.<sup>4, 5, 33, 57-63</sup> This effect counters the decrease in the unit cell due to thermal contraction resulting in little change in position of the diffraction peaks, which is confirmed by the 1D WAXS curves (Figure 4.2b). Ultimately, the relative intensity of the asynchronous compared to the synchronous fea-

tures is even weaker in the secondary-irreversible than in the primary-irreversible regime (i.e., the changes in  $I(q)$  occur very nearly simultaneously).

If one accepts that a semi-ordered phase develops during primary-irreversible crystallization, then it can account for the growth of scattering intensity in the region of  $1.35\text{--}1.46\text{ \AA}^{-1}$  during crystallization. However, the jump of this reflection to lower  $q$ -values (from  $1.49\text{ \AA}^{-1}$  during primary-irreversible crystallization) is unlikely. The positive cross peaks between the two crystalline reflections at  $(1.61\text{ \AA}^{-1}, 1.52\text{ \AA}^{-1})$  can be attributed to growth in the '(200)' semi-ordered phase reflection, which is located at the same position as in the primary-irreversible regime. Alternatively, an increase in scattering of the amorphous halo may be a consequence of the increase in density of non-crystalline regions with decreasing temperature.<sup>37</sup> This increase scattering is unevenly distributed (greatest near  $1.35\text{--}1.46\text{ \AA}^{-1}$ ) due to heterogeneities arising within the non-crystalline regions as a result of its enrichment with butyl groups immediately adjacent to the crystal surface and consequent crowding of pinned chains that are incapable of crystallization. These alternative scenarios are further discussed in Section 4.3.1.4.

#### *Reversible Crystallization*

The significant increase in crystallinity that is unique to reversible crystallization of L152, and the other HPBDs examined, is apparent in the synchronous plot in the familiar autopeaks corresponding to the (110) and (200) crystalline reflections at  $(1.53\text{ \AA}^{-1}, 1.53\text{ \AA}^{-1})$  and  $(1.70\text{ \AA}^{-1}, 1.70\text{ \AA}^{-1})$ . These peaks are shifted to larger  $q$ -values relative to crystallization in the irreversible regimes as a consequence of thermal contraction (Figure 4.4c, left). Thermal contraction continues in the range below  $63\text{ }^{\circ}\text{C}$  corresponding to reversible crystallization resulting in the elongated doublets in the asynchronous plot

(Figure 4.4c, right). These features are similar to those observed during irreversible crystallization of HDPE (Figure 4.3a, right) and are consistent with peak shifting occurring simultaneously with more pronounced changes in intensity.

As discussed previously, all diffraction features shift to higher values of  $q$  through a decrease of intensity at low  $q$ -values and increase of intensity at high  $q$ -values, which can be seen from 1D WAXS curves at two different temperature in this regime in Figure 4.2b (at the beginning at  $T = 63$  °C and at  $T = 0$  °C). The autopeaks in the synchronous plot corresponding to the diffraction peaks resemble triangles as a consequence of the increasing breadth of the crystalline reflections, which is the result of crystallization of random copolymers at low temperatures (Figure 4.2b). Increased width of the diffraction peaks results from incoherent growth of unit cells as more chain defects are encountered during crystallization at low temperatures. This effect is manifested as increasing intensity on the right side (high- $q$  side) of the crystalline reflections and corresponding triangular shape of 2D synchronous features. This shape is mirrored by the corresponding cross peaks since both crystalline reflections change simultaneously.

To further appreciate the richness of the 2D synchronous plot in the reversible regime, it is instructive to consider selected section through the plot. In particular, a section of  $I(q_1, q_2)$  holding  $q_1$  files at the (110) diffraction peak, such that  $q_1 = q_{(110)}$ , is indicated by the dashed line in Figure 4.4c. Moving along the dashed line from high  $q$  to low  $q$  (Figure 4.5c) there is a strong positive peak, a shallow negative interval, a shoulder leading up to the strong (110) autopeak, a resolved positive peak, and a broad negative feature. These features are compared with the temperature-averaged intensity in this regime

$(\bar{I}(q))$ , analogous to eq 4.4; Figure 4.5a) and the intensity pattern along the diagonal of the 2D synchronous plot referred to as the autocorrelation intensity (Figure 4.5b).

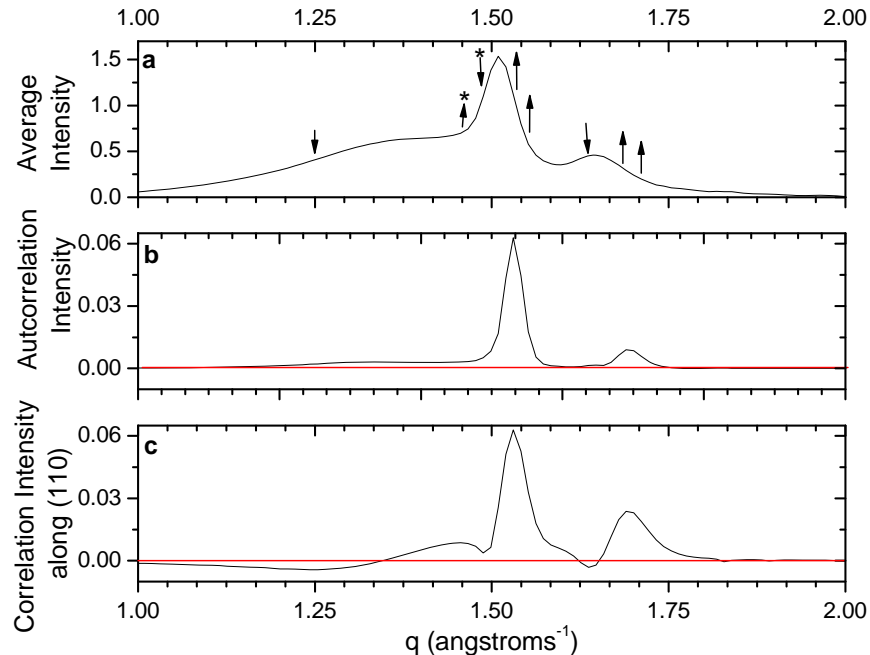


**Figure 4.5** WAXS data for reversible crystallization of L152: **a**) average curve with arrows indicating direction of intensity change, **b**) intensity along the diagonal of the synchronous plot, and **c**) synchronous correlation intensity along the (110) reflection marked by dashed line in Figure 4.4c, left.

The strongest feature in Figure 4.5c is attributed to the (110) autopeak (where the dashed line crossed the diagonal in Figure 4.4c), which is confirmed by its correspondence in position with the peak in the autocorrelation spectrum (Figure 4.5b). This peak is offset to high- $q$  relative to the (110) peak in the average intensity (Figure 4.5a), since it reflects the *increase* of intensity during cooling from 63 to 0 °C. This increase occurs mainly on the high- $q$  side of the diffraction peaks (indicated by upward arrows on the

high- $q$  side of both diffraction peaks in Figure 4.5a) due to the simultaneous thermal contraction of previously formed crystallites and the formation of new ones.

The second strongest feature in the correlation intensity along  $q_{(110)}$  occurs at 1.70  $\text{\AA}^{-1}$  and is readily assigned to the positive correlation between growth of intensity on the high- $q$  side of both the (110) and (200) peaks; it is a section through the (110)/(200) cross peak above the diagonal in Figure 4.4c where the dashed line passes through it.

There is a third positive peak in the correlation intensity along  $q_{(110)}$  at 1.46  $\text{\AA}^{-1}$  in Figure 4.5c. Like the (110)/(200) cross peak, the positive sign of this peak indicates an increase of intensity at 1.46  $\text{\AA}^{-1}$  that coincides with the increase in intensity on the high- $q$  side of the (110) peak. Due to both its position and breadth, this feature is attributed to the non-crystalline material.

There are also two negative intervals in the correlation intensity with the (110) diffraction peak: a broad one at  $q < 1.34 \text{\AA}^{-1}$  and a narrow one at 1.64  $\text{\AA}^{-1}$ . The former is assigned to the decrease in intensity in the amorphous halo at  $q < 1.34 \text{\AA}^{-1}$  (compare 63 to 0 °C in Figure 4.2b and observe where the dashed line in Figure 4.4c cuts through the elongated native feature in the synchronous plot). The latter is attributed to the substantial shift of the (200) reflection to higher  $q$ -values as a consequence of thermal contraction, resulting in a decrease of intensity on the low- $q$  side of the (200) peak (see downward arrow in Figure 4.5c at 1.64  $\text{\AA}^{-1}$ ). A similar negative feature is expected on the low- $q$  side of the (110) peak also. Instead, the decrease of the diffracted intensity at 1.49  $\text{\AA}^{-1}$  due to thermal contraction (manifested by the local minimum in Figure 4.5c) is offset by the increase of scattered intensity in the broad range around 1.46  $\text{\AA}^{-1}$  (see arrows marked with asterisks in Figure 4.5a).

The simultaneous occurrence of the change in non-crystalline scattering

as crystallites form suggests that the formation of crystals alters the structure in adjacent non-crystalline material. The effect has negligible time lag (very weak signatures in the asynchronous plot in Figure 4.4c, right), suggesting that the effect is local; as reversible crystal form, they perturb the non-crystalline structure in their immediate vicinity. This is consistent with the physical interpretation of crystallization at low temperatures, which results in excessive crowding of butyl groups at the crystal surface resulting in greater constraint of the non-crystalline regions compared to higher temperatures.

#### 4.3.1.4 Searching for a Semi-Ordered Phase

The existence of a semi-ordered phase that contributes relatively narrow reflections to WAXS has been suggested in prior literature in an attempt to improve the calculation of crystallinity from 1D spectra.<sup>5, 7, 34, 35, 37</sup> However, evidence in the form of a resolved feature of such a phase has never been observed in 1D scattering curves. The enhancement of spectral features possible through 2D correlation analysis makes it a useful technique to determine the existence of a semi-ordered phase.

All three crystallization regimes (primary-irreversible, secondary-irreversible, and reversible) exhibited features that could be construed as evidence of a semi-ordered phase. Cross correlation features in different regimes indicated changes in WAXS near 1.61–1.64 Å<sup>-1</sup> (at the low-*q* side of the (200) reflection) and changes in the region near 1.46 and 1.49 Å<sup>-1</sup> (adjacent to the (110) reflection), which one might assign to the '(200)' and '(110)' semi-ordered reflections, respectively.<sup>35</sup>

However, our analysis of the 2D correlation spectra forces us to reject this hypothesis of a semi-ordered phase resembling the crystalline phase. First of all, even employing the normalization schemes that are known to enhance spectral features (see Table 2.1 of Section 2.2.4) failed to resolve any autopeaks near  $1.46\text{--}1.49\text{ \AA}^{-1}$  and  $1.61\text{--}1.64\text{ \AA}^{-1}$ .<sup>45, 75-77</sup>

Second, an effort was made to reconcile the changes in the WAXS in the three crystallization regimes. The three crystallization regimes exhibit (1) increases near  $1.49$  and  $1.61\text{ \AA}^{-1}$  during primary-irreversible crystallization, (2) increases near  $1.46$  and  $1.61\text{ \AA}^{-1}$  during secondary-irreversible crystallization, and (3) an increase at  $1.46\text{ \AA}^{-1}$  but a decrease at  $1.64\text{ \AA}^{-1}$  during reversible crystallization. The shift of the presumed '(110)' peak to lower  $q$  between the primary- and secondary- irreversible regimes ( $1.49$  versus  $1.46\text{ \AA}^{-1}$ , respectively) without a corresponding shift in '(200)' as well as opposite changes in intensity of the two features during reversible crystallization defies a unified explanation in terms of a distinct, semi-ordered phase. Thus, the observed changes in the non-crystalline regions of WAXS do not support this hypothesis.

Alternatively, the changes in the non-crystalline regions of WAXS patterns may be explained by such well-established physical phenomena as thermal contraction, the loss of coherence in unit cell growth of copolymers at low temperatures, and crystallization-induced heterogeneity in the density distribution of the amorphous halo. The latter phenomenon is a consequence of the crystallization of HPBDs, which results in the enrichment of the non-crystalline regions closest to crystal faces with the rejected butyl groups and the shortest ethylene sequences. In contrast to HDPE, which crystallizes by chain folding with frequent nearby re-entry of the chain into the crystal (Figure 4.6a),

crystallization of HPBDs incorporates ‘crystalline stems’ that are usually delimited by butene units, resulting in strongly reduced probability of nearby re-entry (Figure 4.6b). The result is extreme crowding of chains at the crystal surface, which in addition to localized butene concentration and thermal contraction of these non-crystalline regions, can explain the change in the shape and position of the amorphous halo.<sup>33, 36</sup> Therefore, we favor the interpretation of McFaddin et al.<sup>4</sup> that attributes observed changes in the non-crystalline WAXS during crystallization to density heterogeneities rather than a semi-ordered phase.

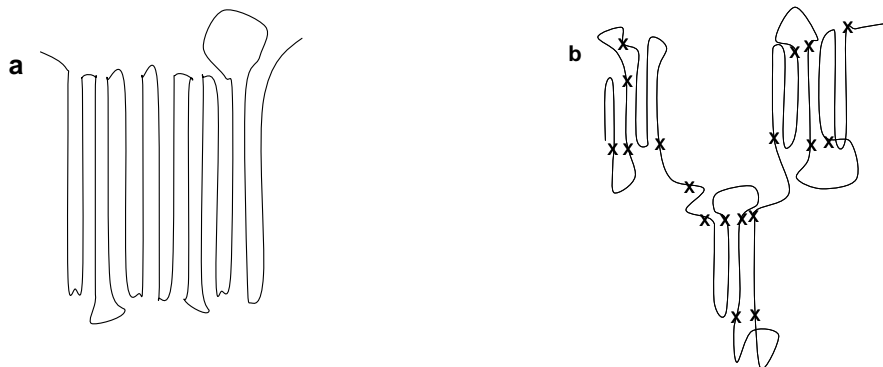


**Figure 4.6** Schematic representation of crystallization of **a**) homopolymers and **b**) random copolymers.

### 4.3.2 SAXS

#### 4.3.2.1 Crystallization of Random Copolymers

Two-dimensional correlation analysis provides an opportunity to examine the complex SAXS behavior of polyethylenes containing short-chain branches, which exhibit significant variation with temperature (Figure 3.9 in Chapter 3).<sup>6, 43, 78-80</sup> The three regimes of crystallization exhibited by HPBD materials are apparent in the evolution of Lorentz-corrected SAXS curves during cooling of L152 (Figure 4.7). Irreversible crystallization at high temperatures (primary-irreversible regime, dashed lines in Figure 4.7) is

characterized by an overall increase in the scattering power and a shift in the peak position to larger values of  $q$ . At intermediate temperatures (secondary-irreversible regime, solid lines in Figure 4.7), overall scattering power stays relatively constant while the peak position continues its shift. In the reversible regime at lower temperatures (dotted lines in Figure 4.7), the overall scattering power decreases while the peak position shifts further and broadens. It is important to note that in each regime, the change in the peak position and shape (magnitude and width) is monotonic, enabling the application of Noda's rules for sequential order determination based on asynchronous spectra.<sup>68</sup> Each regime is marked by unique signatures in the 2D correlation plots corresponding to the changes in the nanoscale structure during crystallization.

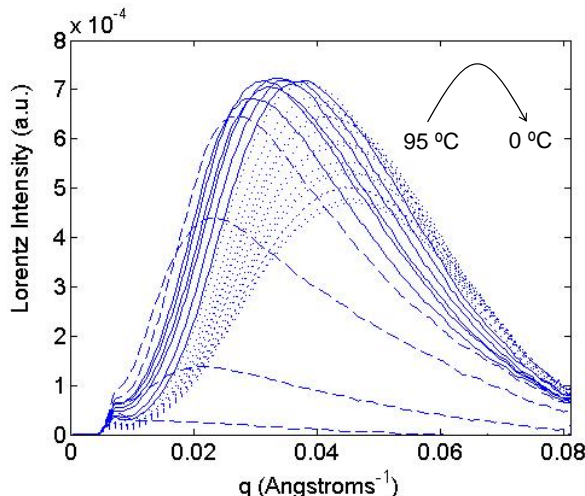


**Figure 4.7** Lorentz-corrected SAXS of L152 during cooling at 10 °C/min exhibiting primary-irreversible (dashed lines), secondary-irreversible (solid lines), and reversible (dotted lines) regimes.

#### *Primary-Irreversible Crystallization*

The change in scattering power dominates both the synchronous and asynchronous plots during primary-irreversible crystallization of L152 (Figure 4.8a). The triangular shape of the solitary autopeak, whose center coincides with the peak of the average

scattering curves in this regime (above and beside Figure 4.8a), is consistent with an overall increase in scattering across a broad  $q$ -range. This synchronous feature can be interpreted as the formation of lamellae with a broad distribution of long periods centered near 22 nm. The asynchronous plot contains an elongated feature, the sign of which below the diagonal is consistent with growth of intensity at large  $q$ -values ( $q > 0.02 \text{ \AA}^{-1}$ ) lagging that at low  $q$ -values ( $q \sim 0.017 \text{ \AA}^{-1}$ ). This pattern—negative peak centered at  $(0.017 \text{ \AA}^{-1}, 0.031 \text{ \AA}^{-1})$ —indicates that the broad distribution of long periods arises through the initial formation of lamellae with an average long period of approximately 37 nm followed by the formation of a distribution of lamellae centered around 20 nm. The latter population has a distribution approximately twice as broad as the former population as indicated by the shape of the asynchronous cross peak.

A strictly positive change in scattering intensity at all  $q$ -values is consistent with the formation of primary lamellae propagating into unconstrained melt, as suggested in Chapter 3. The formation of lamellae with different characteristic length scales is a consequence of the ethylene sequence length distribution (ESLD). Initially, at the highest temperatures of this regime, only the longest ethylene sequences can crystallize. Due to the homogenous SCB distribution, although the number of these long sequences is small, they can be found in almost every chain. The crystallization of these sequences results in the majority of chains being pinned to crystal surfaces (even at low crystallinity), limiting their crystallization at elevated temperatures and resulting in large non-crystalline regions. As temperature decreases, progressively shorter-ethylene sequences can participate involving a larger percentage of each polymer chain. Hence, the non-crystalline layers decrease, resulting in a smaller long period.

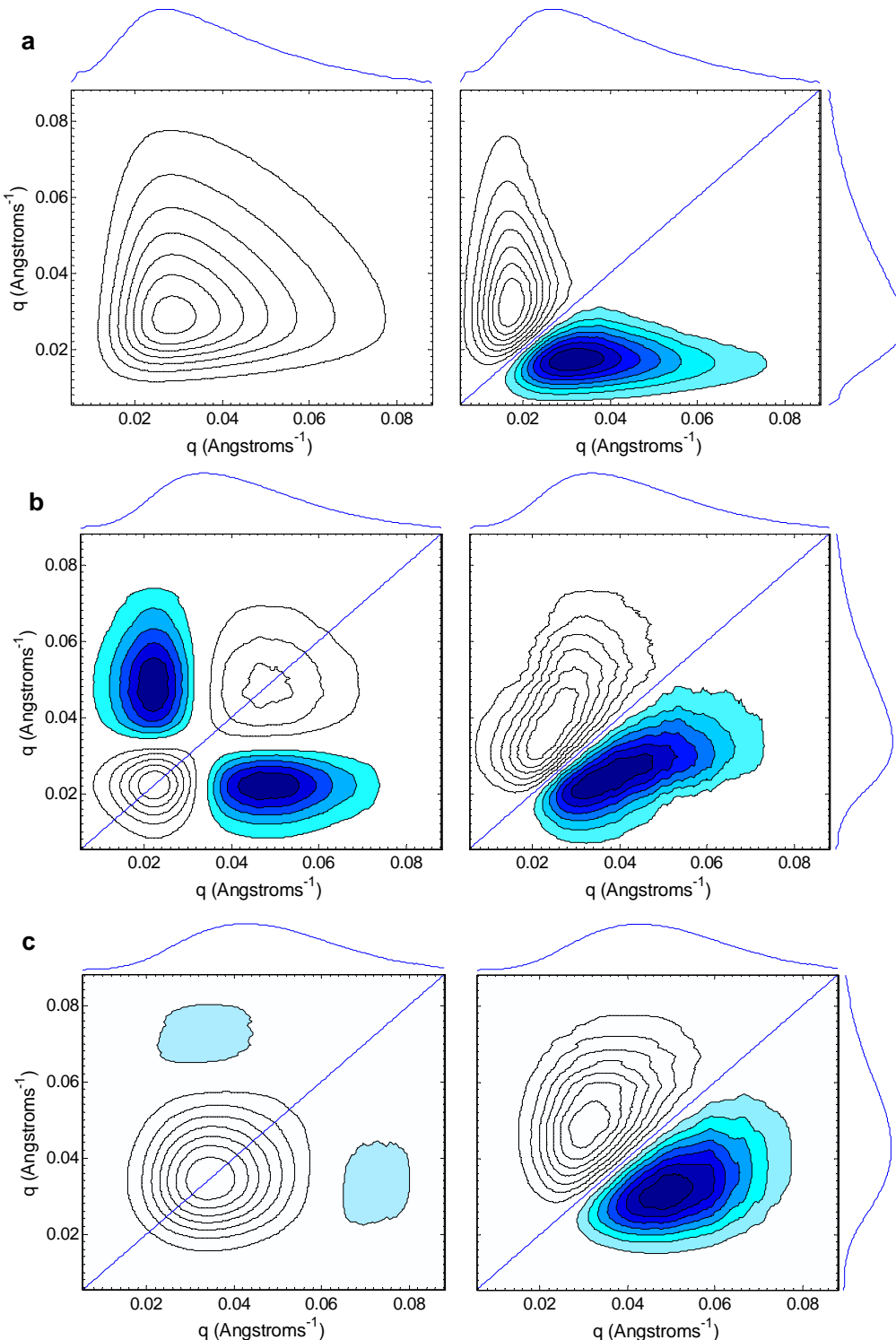


**Figure 4.8** 2D synchronous (left) and asynchronous (right) correlation plots computed from Lorentz-corrected SAXS curves collected in **a**) primary-irreversible (78 °C < T < 93 °C), **b**) secondary-irreversible (63 °C < T < 78 °C), and **c**) reversible (0 °C < T < 63 °C) crystallization regimes of L152. Positive and negative contours are shown as open and filled, respectively. Averaged 1D scattering profiles are shown on the sides.

*Secondary-Irreversible Crystallization*

Consistent with the pattern observed in the 1D scattering curves in the secondary-irreversible crystallization regime (Figure 4.7, solid lines), the 2D plots exhibit features characteristic of a well-defined peak shift (Figure 4.8b). The synchronous plot displays an ‘angel’ pattern containing two autopeaks at  $0.022$  and  $0.048 \text{ \AA}^{-1}$  that indicate the start and end of the shift. The angel pattern is analogous to the clover-leaf pattern observed in 2D analysis of WAXS but modified by intensity changes that occur concurrently with the shift resulting in asymmetry between the two autopeaks. Corresponding negative cross peaks are consistent with an overall decrease in one peak coinciding with an overall increase in the other. The asynchronous plot exhibits a butterfly pattern, consistent with a shift in peak position (rather than two stationary peaks simultaneously changing intensities in opposite directions that are also consistent with an angel pattern). The negative sign of the ‘wing’ below the diagonal indicates that the direction of the shift is to larger  $q$ -values.<sup>18</sup>

During secondary-irreversible crystallization, the average long period decreases from 28 to 13 nm. This type of peak shift can be interpreted physically as the formation of secondary lamellae within the non-crystalline regions of previously-formed lamellae, particularly in the least constrained (thickest) non-crystalline layers. This lamellar insertion explains the decrease of scattering corresponding to the largest long periods (low  $q$ ) and increased scattering corresponding to long periods that are approximately half in size (higher  $q$ ).

*Reversible Crystallization*

The synchronous 2D plot is indicative of a loss in overall intensity in a broad range of  $q$  ( $<0.06 \text{ \AA}^{-1}$ ) and a mild increase at  $q \sim 0.07 \text{ \AA}^{-1}$ . The decrease in intensity is evident as a broad, prominent autopeak centered at  $0.035 \text{ \AA}^{-1}$  (Figure 4.8c). Just as the single prominent autopeak in Figure 4.7a reflected the increase of intensity as primary lamellae formed, here the autopeak reflects the loss of intensity as reversible crystallites (fringed micelles) form in the non-crystalline layers of lamellar stacks causing a decrease in the electron density contrast.<sup>3</sup> Weak negative cross peaks at  $(0.070 \text{ \AA}^{-1}, 0.035 \text{ \AA}^{-1})$  indicate that as intensity decreases near  $0.035 \text{ \AA}^{-1}$ , it simultaneously increases near  $0.070 \text{ \AA}^{-1}$ . The corresponding autopeak (not shown) is hardly above the baseline, speaking to the small change in its intensity. The asynchronous plot again contains a single feature that is elongated along the diagonal suggesting a *mild* shift in peak position.<sup>66</sup> Based on the sign of the feature below the diagonal, this shift is toward larger values of  $q$  (i.e., smaller characteristic length scales).<sup>18</sup> Concurrently with decreasing scattering intensity that is apparent from 1D scattering curves, this slight shift in peak position is consistent with the formation of reversible crystals in the largest non-crystalline regions (corresponding to the largest  $L_p$ ) first, followed by gradual growth in smaller regions. Additionally, the subtle autopeak at  $0.070 \text{ \AA}^{-1}$  suggests that the reversible crystals have a structural length scale of approximately 9.0 nm.

*Normalization*

Prior to the examination of heterospectral correlation analysis of SAXS and WAXS, this section closes with additional tools that are used when changes in both peak intensity and position are significant. In this case, 2D correlation plots, especially asyn-

chronous, can be difficult to interpret.<sup>66</sup> This is apparent from Figure 4.8a, in which development of intensity at the onset of crystallization, masks the shift in peak position and the expected butterfly pattern in the asynchronous plot. In addition to the change in shape of the 2D features, it has been previously reported in the context of spectroscopy that the relationship between the position of features in the 2D correlation spectra and the positions of relevant changes in the 1D spectra become less reliable as intensity changes increase.<sup>66</sup> To minimize effects of intensity changes, normalization of each 1D scattering curve by its overall intensity effectively re-scales all the spectra to the same intensity range, enhancing subtle features like peak shifting or broadening.

The application of Modified Mean Normalization (MMN; eqs 4.1 and 4.2)<sup>45</sup> has the greatest effect on the 2D correlation plots in the primary-irreversible regime (compare Figure 4.8a and Figure 4.9a). After normalization, the synchronous plot reveals an angel pattern with two autopeaks at  $(0.015 \text{ \AA}^{-1}, 0.015 \text{ \AA}^{-1})$  and  $(0.037 \text{ \AA}^{-1}, 0.037 \text{ \AA}^{-1})$ , corresponding to long periods of 42 and 17 nm, respectively. It is of note that these values are close but not identical to the characteristic length scales obtained from the asynchronous pattern without normalization (37 and 20 nm). The latter are skewed to the intermediate values corresponding to conditions when maximum of scattering was observed (see Figure 4.9). The asynchronous plot depicts a distorted butterfly pattern that indicates a peak shift from  $0.015$  to  $0.037 \text{ \AA}^{-1}$ . Hence, primary-irreversible crystallization is characterized by the steady decrease in the average long period due to the formation of crystal-line structures with reduced characteristic length scales.

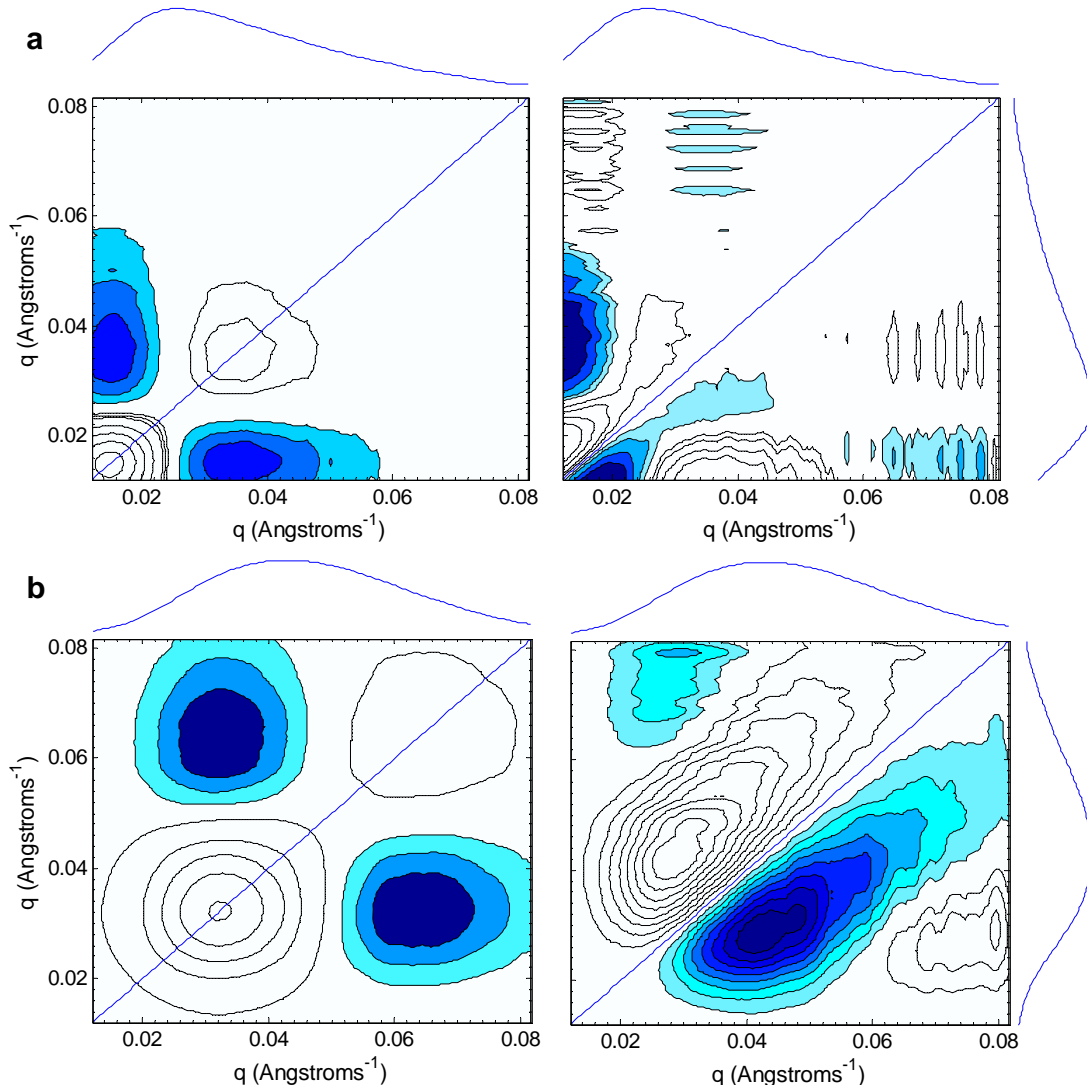


**Figure 4.9** 2D synchronous (left) and asynchronous (right) correlation plots computed from SAXS curves that were Lorentz-corrected and Modified Mean Normalized in **a**) primary-irreversible and **b**) reversible crystallization regimes of L152. Positive and negative contours are shown as open and filled, respectively. Averaged 1D scattering profiles are shown on the sides.

The features at high  $q$  in the asynchronous plot are the result of noise that is rescaled by the normalization, suggesting that the application of normalization schemes requires care. Normalized 1D curves should be checked to ensure that artificial behavior is not introduced by the normalization.<sup>48</sup>

Since the overall intensity exhibits only weak changes in the secondary-irreversible regime, normalization has little effect here. MMN application in the reversible crystallization regime allows for the direct visualization of the previously-invisible feature at high  $q$  (compare Figure 4.9b with Figure 4.8c) indicative of structures with a characteristic length scale of approximately 9.7 nm. The angel—with autopeaks at 0.032 and  $0.065 \text{ \AA}^{-1}$ —and distorted butterfly pattern in the synchronous and asynchronous plots, respectively, are consistent with gradual ‘in-filling’ of the largest non-crystalline layers. The distribution of long periods corresponding to lamellae undergoing ‘in-filling’ is centered at approximately 20 nm, with the smallest long periods exceeding 12 nm. The crystal in-filling, which results in an increase in the formation of structures with a reduced characteristic length-scale, is consistent with fringed micelle formation.

### 4.3.3 SAXS/WAXS Heterospectral Correlation Analysis

#### 4.3.3.1 Crystallization of Random Copolymers

Heterospectral correlation analysis allows for direct examination of the coincident relationships between SAXS and WAXS in the three crystallization regimes of HPBD materials, and consequently the relationship between the development of crystals evident in WAXS and nanoscale structures (e.g., lamellae) probed by SAXS, specifically for L152.

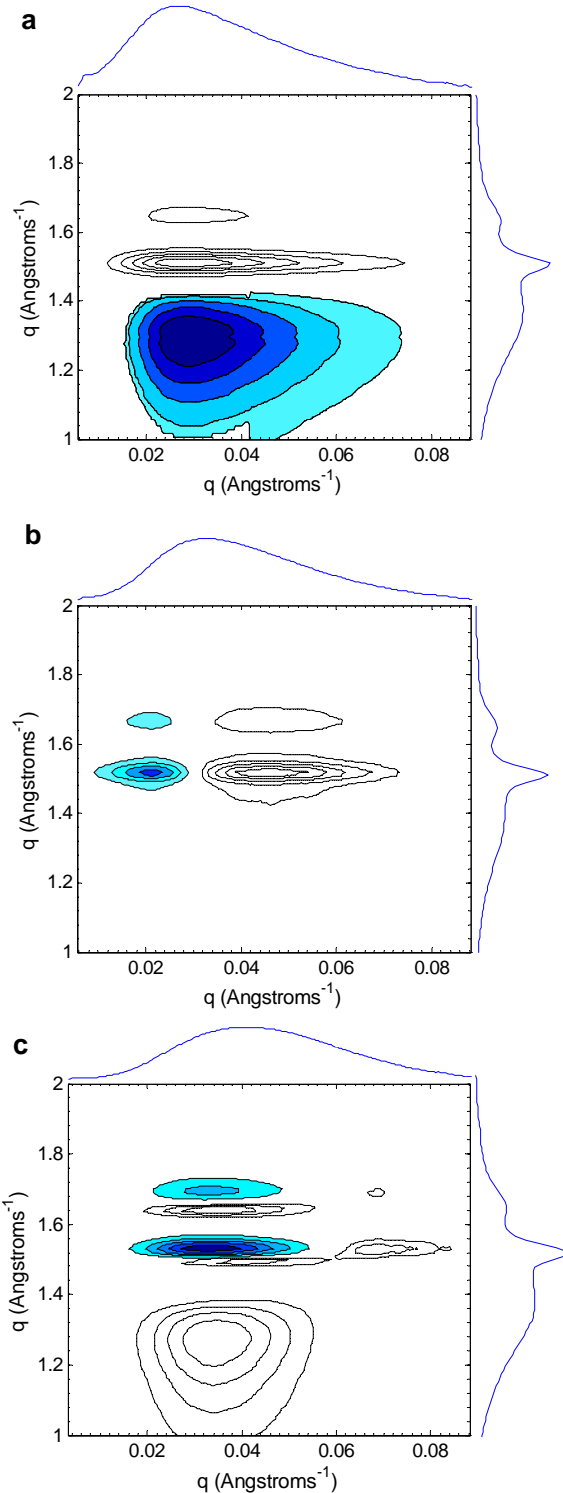


**Figure 4.10** 2D heterospectral correlation plots computed from Lorentz-corrected SAXS and WAXS (horizontal and vertical axes, respectively) in **a**) primary-irreversible **b**) secondary-irreversible and **c**) reversible crystallization regimes of L152. Positive and negative contours are shown as open and filled, respectively. Averaged 1D scattering profiles are shown on the sides.

### *Primary-Irreversible Crystallization*

The strong increase in overall SAXS intensity (Figure 4.8a) and development of crystalline reflections in WAXS at the expense of the amorphous halo (Figure 4.4a) give rise to three characteristic features in the heterospectral plot for the primary-irreversible regime (Figure 4.10a); each of the WAXS features (amorphous halo and 2 crystalline reflections) is correlated with the SAXS peak that is centered at approximately  $0.03 \text{ \AA}^{-1}$ . The crystalline reflections are positively correlated, while the amorphous halo is negatively correlated. These observations are consistent with polymer crystals organizing into lamellae with an average long period of approximately 21 nm. Hence, this heterospectral pattern, which is characteristic of rapid propagation of primary lamellae in an unconstrained melt, exhibits a change in sign of the correlation intensity along the WAXS  $q$ -axis (vertical direction in Figure 4.10a).

### *Secondary-Irreversible Crystallization*

The secondary-irreversible crystallization regime is characterized by a shift in the SAXS peak at nearly constant intensity (Figure 4.8b) as well as a growth of both the WAXS crystalline reflections and the portion of the amorphous halo immediately adjacent to the (110) reflection ( $1.4\text{--}1.46 \text{ \AA}^{-1}$  in Figure 4.4b). The shift in the SAXS peak position causes the WAXS crystalline reflections to be correlated both positively (for  $q > 0.03 \text{ \AA}^{-1}$ , where SAXS intensity increases) and negatively (for  $q < 0.03 \text{ \AA}^{-1}$ , where SAXS intensity decreases) with the SAXS intensity (Figure 4.10b). Changes in the amorphous halo are too weak to be observed. Negative peaks are apparent centered at  $(0.022 \text{ \AA}^{-1}, 1.5 \text{ \AA}^{-1})$  and  $(0.022 \text{ \AA}^{-1}, 1.65 \text{ \AA}^{-1})$  corresponding to the simultaneous increase in intensity of the crystalline reflections and the decrease of intensity in the low- $q$  side of the SAXS

peak. These features indicate that crystallites form in the non-crystalline layers of the lamellar stacks having the largest long periods. Positive features centered at (0.048 Å<sup>-1</sup>, 1.5 Å<sup>-1</sup>) and (0.048 Å<sup>-1</sup>, 1.65 Å<sup>-1</sup>) show that these new crystallites increase scattering corresponding to structures having a smaller long period. Hence, the development of crystallinity in the secondary-irreversible crystallization regime is attributed to secondary lamellae that form between already-formed lamellae having the largest long period essentially cutting the original long period in half. The heterospectral pattern characteristic of this physical process exhibits a change in sign of the correlation intensity along the SAXS *q*-axis (horizontal direction in Figure 4.10b).

#### *Reversible Crystallization*

Heterospectral analysis in the reversible regime reveals scattering behavior that was not immediately apparent from the conventional 2D correlation analysis of SAXS and WAXS alone. The conventional 2D SAXS correlation plots exhibited implicit evidence for the formation of crystals that have a characteristic length scale of approximately 9.0 nm, but a direct peak was not observed without normalization (Figure 4.8c). In contrast, the heterospectral plot exhibits two positive features centered at (0.068 Å<sup>-1</sup>, 1.53 Å<sup>-1</sup>) and (0.068 Å<sup>-1</sup>, 1.70 Å<sup>-1</sup>) that unambiguously correlate increases at the two crystal-line reflections with SAXS scattering at large *q*.

Conventional 2D correlation analysis of WAXS in the reversible regime revealed complex behavior, including direct evidence of a shift in position of the amorphous halo and the (200) reflection coinciding with an increase in their intensities (Figure 4.4c). A shift in the (110) reflection was implied from the resolved feature at 1.46 Å<sup>-1</sup> (Figure 4.5). This conclusion is confirmed by the heterospectral plot, which reveals similar behavior

between the two crystalline reflections in the form of pairs of positive/negative peaks (Figure 4.10c, see negative peaks at  $(0.033 \text{ \AA}^{-1}, 1.53 \text{ \AA}^{-1})$  and  $(0.033 \text{ \AA}^{-1}, 1.70 \text{ \AA}^{-1})$ ). These features indicate that crystallinity development in the reversible regime is marked by an increase in WAXS scattering at  $1.53$  and  $1.70 \text{ \AA}^{-1}$ , which corresponds to unit cell parameters  $a = 7.39 \text{ \AA}$  and  $b = 4.94 \text{ \AA}$ , consistent with dimensions of PE crystals near room temperature.<sup>55, 81</sup> Simultaneously, a decrease in SAXS scattering is observed at  $0.033 \text{ \AA}^{-1}$ , corresponding to a long period of  $19 \text{ nm}$ . This suggests that reversible crystallites preferentially form in non-crystalline layers that were too small to permit growth of secondary lamellae. The corresponding positive features are centered at  $(0.039 \text{ \AA}^{-1}, 1.50 \text{ \AA}^{-1})$  and  $(0.034 \text{ \AA}^{-1}, 1.64 \text{ \AA}^{-1})$  indicating that growth in crystallinity with decreasing temperature coincides with a decrease in WAXS scattering from crystals with unit cell dimensions of  $a = 7.66 \text{ \AA}$  and  $b = 5.00 \text{ \AA}$ . Although these dimensions are greater than the average expected below  $60 \text{ }^{\circ}\text{C}$ ,<sup>73, 74</sup> they can be attributed to the high-tail end of the unit cell size distribution. This heterospectral pattern, which is characteristic of fringed micelle formation in fully constrained melt, exhibits changes in sign of the correlation intensity along both the SAXS and WAXS  $q$ -axis (horizontal and vertical direction in Figure 4.10c, respectively).

No correlation was observed between SAXS intensity changes and the feature at  $1.46 \text{ \AA}^{-1}$  apparent in the WAXS synchronous plot in this regime. Therefore, changes in WAXS are again accounted for by variations in position and shape of only the amorphous halo and the crystalline reflections; there is no apparent need to invoke a semi-ordered phase in the spectra.

#### 4.3.3.2 Scattering at the Onset of Crystallization

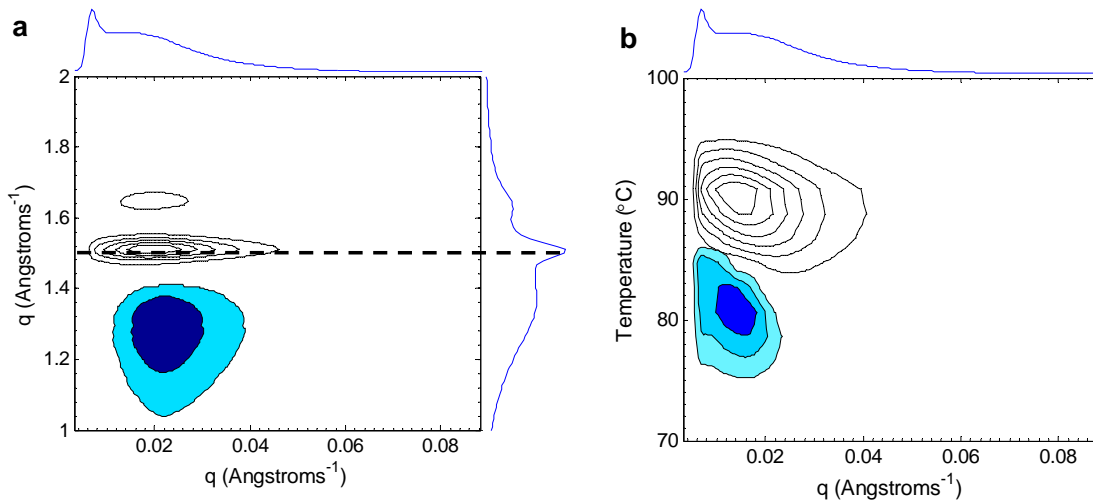


**Figure 4.11** a) 2D heterospectral correlation plot computed for SAXS and WAXS curves ( $I(q)$ , horizontal and vertical axes, respectively) for L152 during a cooling ramp at 10 °C/min through the primary-irreversible regime. b) Corresponding moving window analysis on heterospectral data using a 10 °C window plotting the correlation along the (110) WAXS (dotted line in a) as a function of the average temperature. Positive and negative contours are shown as open and filled, respectively. Averaged 1D scattering profiles are shown on the sides in a.

Two-dimensional correlation analysis offers a unique approach to examine the debate about the onset of crystallization in HPBDs. Crystallization is revealed in WAXS by the appearance of the (110) and (200) reflections of the orthorhombic PE crystal. On the other hand, the appearance of a resolved peak in the SAXS curve, corresponding to a well-defined long period, occurs at lower temperatures during cooling. Instead, initial changes in SAXS scattering occur at zero scattering angle, below the beamstop. Previously, an observed lag between the increase in SAXS scattering at low  $q$  and the appearance of WAXS peaks has led some authors to invoke the interpretation of spinodal decomposition as a precursor to crystal formation.<sup>82-85</sup> The relationship between this initial scattering and the onset of crystallization can be examined through the application of heterospectral correlation analysis to SAXS and WAXS data.

A heterospectral correlation plot of non-Lorentz corrected SAXS and WAXS scattering curves ( $I(q)$ ) collected during primary-irreversible crystallization ( $78 \text{ }^{\circ}\text{C} < T < 95 \text{ }^{\circ}\text{C}$ ) of L152 is depicted in Figure 4.11a. This figure contains the same features as the heterospectral correlation plot for Lorentz corrected data in the same regime (Figure 4.10a): positive peaks are observed, corresponding to the primary SAXS peak and the (110) and (200) WAXS reflections and a negative peak is apparent corresponding to the primary SAXS peak and the WAXS amorphous halo. These observations are consistent with the primary-irreversible crystallization regime being dominated by the formation of orthorhombic unit cells (leading to an increase in WAXS crystalline reflections and a decrease in amorphous halo scattering) that simultaneously organize into nanoscale structures with a well-defined long period (resulting in the development of a well-defined SAXS peak).

The WAXS (110) reflection is also positively correlated with SAXS intensity at low  $q$  ( $<0.005 \text{ \AA}^{-1}$ ), indicating that generally, the crystallization in the primary-irreversible regime coincides with an increase in zero angle scattering in SAXS. As stated previously, this growth occurs in the earliest stages of crystallization. As such, it may be examined by evaluating heterospectral correlation plots corresponding to small temperature windows near the start of primary-irreversible crystallization. To gauge the relationship between zero-angle scattering and crystal formation, the heterospectral correlation intensity along the WAXS (110) reflection (dashed line in Figure 4.11a) was calculated for  $10 \text{ }^{\circ}\text{C}$  subsets of the SAXS/WAXS data that are shifted sequentially through high temperatures. These intensities were then used to obtain the contour plot depicting the correlation of SAXS scattering at low  $q$  with the WAXS (110) reflection as a function of

temperature in Figure 4.11b. At the earliest stages of crystallization (95 to 85 °C), the positive contour indicates that an increase in SAXS scattering at low  $q$ -values occurs simultaneously with growth of the (110) crystal reflection. This observation is consistent with the initial increase in SAXS intensity being due to isolated crystals in the melt, and not spinodal decomposition, in agreement with previous findings.<sup>1, 86-89</sup> The same conclusions were reached for all materials examined. Therefore, the dominant physical process at the early stages of crystallization of HPBD materials during cooling is the formation of isolated crystals in the melt that are engulfed by the crystalline network that propagates at lower temperatures.

#### 4.3.4 Material Comparisons

Two-dimensional correlation analysis did not reveal differences in the evolution of morphology between the four HPBD materials examined (short linear, long linear, 3-arm star and H-polymer). All four exhibited the same characteristic length scales in the secondary-irreversible and reversible regimes. In the former, the system evolved gradually from having an average long period of  $26 \pm 2$  nm to  $13 \pm 1$  nm through the insertion of secondary lamellae within the greatest-spaced primary lamellae. In the following reversible regime, the system primarily lost crystal structure with a long period of  $18 \pm 2$  nm and gained crystals with characteristic length scale of  $9 \pm 1$  nm.

### 4.4 CONCLUSION

Two-dimensional correlation analysis, which is well-established in the field of vibrational spectroscopy,<sup>17-20</sup> proved useful in analyzing x-ray scattering data and elucidating a number of phenomena associated with quiescent crystallization of random ethylene-

copolymers. Morphology evolution in the three crystallization regimes of random copolymers—primary-irreversible, secondary-irreversible, and reversible—resulted in unique signatures in conventional 2D correlation plots of WAXS and SAXS, as well as 2D heterospectral correlation patterns, which are summarized in Table 4.2.

**Table 4.2 Summary of crystallization behavior of HPBD materials.**

Crystallization Regimes			
	Primary- irreversible	Secondary- irreversible	Reversible
<b>Morphological parameters</b>	$X_c$ , $L_p$ , and $Q$ change rapidly with hysteresis between cool and heat	$X_c$ and $L_p$ change slowly and $Q$ is near maximum with hysteresis between cool and heat	$X_c$ , $L_p$ , and $Q$ change rapidly with <i>no</i> hysteresis between cool and heat
<b>SAXS</b>	Peak intensity grows	Constant peak intensity Peak position moves to higher $q$	Peak intensity decreases
<b>WAXS</b>	Decrease in intensity of amorphous halo	Change in shape and position of amorphous halo Crystalline peak intensities grow, broaden, and move to higher $q$	Strong change in shape and position of amorphous halo
<b>2D Hetero SAXS/WAXS</b>	Intensity redistribution in WAXS	Intensity redistribution in SAXS	Intensity redistribution in SAXS and WAXS
<b>Physical interpretation</b>	Primary lamellar growth in unconstrained melt	Secondary lamellar growth in constrained melt within the largest non-crystalline regions between primary lamellae	Fringed micelle formation in severely constrained melt within largest non-crystalline layers

Two-dimensional correlation analysis SAXS was used to infer the nanoscopic superstructure development during crystallization. The morphology evolution dominating each crystallization regime resulted in 2D correlation features that are associated with primary lamellar propagation, secondary lamellar insertion, and fringed micelle ‘infilling.’ Additionally, it was demonstrated that when structure evolution is dominated by

strong intensity changes, further insight may be gained by minimizing this effect through normalization schemes.

Heterospectral analysis provided insight about the direct relationship between unit cell growth (as given by WAXS) and simultaneous their organization into superstructures (as given by SAXS). Each crystallization regime exhibited unique 2D heterospectral patterns emphasizing the different physics that govern crystallization in the three crystallization regimes of random copolymers. Propagation of primary lamellae through an unconstrained melt during primary-irreversible crystallization is characterized by correlation features that are negative at low WAXS wavevectors and positive at high WAXS wavevectors (Figure 4.10a). Growth of secondary lamellae within the largest non-crystalline layers between primary lamellae during secondary-irreversible crystallization is characterized by correlation features that are negative and positive at low and high SAXS wavevectors, respectively. Fringed-micelle formation in severely constrained non-crystalline regions is characterized by changes in sign of the correlation intensity along both the SAXS and WAXS wavevectors. These heterospectral patterns can be used to fingerprint the corresponding physical processes in other polymer systems.

Additionally, heterospectral analysis corresponding to the onset of crystallization revealed that the initial increase in scattering at low  $q$  during cooling is the result of isolated lamellae in the melt, and not spinodal decomposition, consistent with conclusions from previous studies.<sup>1, 86-89</sup>

WAXS data in the three crystallization regimes of random copolymers revealed no evidence for the formation of a semi-ordered phase that has been proposed in previous studies.<sup>5, 7, 34, 35, 37</sup> Those features that could be attributed to the reflections of a crystal-

like semi-ordered phase, lead to inconsistent behavior of this supposed ‘phase.’

We offer an alternative explanation in which these features are ascribed to thermal contraction of the crystalline phase, loss of coherent unit cell growth at low temperatures, and a change in shape and position of the amorphous halo. The latter observation is explained by thermal contraction of the non-crystalline material and its enrichment with butyl branches nearest to the crystal surface that are excluded as crystallization proceeds. The rejection of chain defects also causes increased crowding at the crystal interface resulting in heterogeneity in the non-crystalline phase. This heterogeneity is evident at lower temperatures associated with the formation of secondary lamellae and fringed micelles in a constrained melt. Further insight into the development of this heterogeneity can be achieved through the examination of materials with varying SCB content. One would expect that the amount of non-crystalline heterogeneity would increase with crystal defects.<sup>37,57</sup> Hence, the application of 2D correlation analysis may provide further insight into this phenomenon if applied to highly-branched systems.

Two-dimensional correlation analysis of WAXS data proved to be highly sensitive to spectral changes, revealing, for example, subtle, yet complex behavior associated with fringed micelle formation and very mild shifting of the crystalline reflections due to thermal contraction. This sensitivity of 2D correlation analysis makes it a powerful tool to study materials with different crystal morphs that are difficult to resolve from 1D curves, such as may be the case with some block copolymers.<sup>90</sup>

## 4.5 ACKNOWLEDGEMENTS

This work would not have been possible without ExxonMobil Research and Engineering Company (Clinton, NJ), particularly Dr. David Lohse and his team, who provided materials and financial support. We must thank the beamline staff at beamline X27C at NSLS BNL (Dr. Lixia Rong and Jie Zhu) and beamline 7.3.3 at ALS LBL (Dr. Alexander Hexemer and Eliot Gann). X-ray data was collected with the assistance of Zuleikha Kurji (Caltech). Part of this work was also funded by the National Science Foundation (DMR-0505393 and GOALI-0523083). Manuscript preparation was assisted by Prof. Julia Kornfield (Caltech).

## 4.6 REFERENCES

1. Akpalu, Y. A.; Amis, E. J., Evolution of density fluctuations to lamellar crystals in linear polyethylene. *Journal of Chemical Physics* **1999**, 111, (18), 8686-8695.
2. Goderis, B.; Peeters, M.; Mathot, V. B. F.; Koch, M. H. J.; Bras, W.; Ryan, A. J.; Reynaers, H., Morphology of homogeneous copolymers of ethylene and 1-octene. III. Structural changes during heating as revealed by time-resolved SAXS and WAXD. *Journal of Polymer Science Part B-Polymer Physics* **2000**, 38, (15), 1975-1991.
3. Mathot, V. B. F.; Scherrenberg, R. L.; Pijpers, M. F. J.; Bras, W., Dynamic DSC, SAXS and WAXS on homogeneous ethylene-propylene and ethylene-octene copolymers with high comonomer contents. *Journal of Thermal Analysis* **1996**, 46, (3-4), 681-718.
4. McFaddin, D. C.; Russell, K. E.; Wu, G.; Heyding, R. D., Characterization of Polyethylenes by X-Ray-Diffraction and C-13-Nmr - Temperature Studies and the Nature of the Amorphous Halo. *Journal of Polymer Science Part B-Polymer Physics* **1993**, 31, (2), 175-183.
5. Sajkiewicz, P.; Hashimoto, T.; Saijo, K.; Gradys, A., 'Intermediate phase' in poly(ethylene) as elucidated by the WAXS. Analysis of crystallization kinetics. *Polymer* **2005**, 46, (2), 513-521.
6. Strobl, G. R.; Schneider, M. J.; Voigtmartin, I. G., Model of Partial Crystallization and Melting Derived from Small-Angle X-Ray-Scattering and Electron-Microscopic Studies on Low-Density Polyethylene. *Journal of Polymer Science Part B-Polymer Physics* **1980**, 18, (6), 1361-1381.

7. Russell, K. E.; Hunter, B. K.; Heyding, R. D., Polyethylenes Revisited - WAXS and the Phase-Structure. *European Polymer Journal* **1993**, 29, (2-3), 211-217.
8. Rabiej, S.; Goderis, B.; Janicki, J.; Mathot, V. B. F.; Koch, M.; Reynaers, H.; Włochowicz, A. In *Influence of thermal treatment on the supermolecular structure of homogeneous polyethylene-1-octene copolymers*, 2003; Inst Chemical Fibres: 2003; pp 28-31.
9. Fernandez-Ballester, L.; Gough, T.; Meneau, F.; Bras, W.; Ania, F.; Balta-Calleja, F. J.; Kornfield, J. A., Simultaneous birefringence, small- and wide-angle X-ray scattering to detect precursors and characterize morphology development during flow-induced crystallization of polymers. *Journal of Synchrotron Radiation* **2008**, 15, (2), 185-190.
10. Vanden Eynde, S.; Mathot, V.; Koch, M. H. J.; Reynaers, H., Thermal behaviour and morphology of homogeneous ethylene-propylene and ethylene-1-butene copolymers with high comonomer contents. *Polymer* **2000**, 41, (9), 3437-3453.
11. Wang, Z.; Wang, H.; Shimizu, K.; Dong, K.-Y.; Hsiao, B. S.; Han, C. C., Structural and morphological development in poly(ethylene-co-hexene) and poly(ethylene-co-butylene) blends due to the competition between liquid-liquid phase separation and crystallization. *Polymer* **2005**, 46, 2675-2684.
12. Nogales, A.; Hsiao, B. S.; Somani, R. H.; Srinivas, S.; Tsou, A. H.; Balta-Calleja, F. J.; Ezquerra, T. A., Shear-induced crystallization of isotactic polypropylene with different molecular weight distributions: in situ small- and wide-angle X-ray scattering studies. *Polymer* **2001**, 42, (12), 5247-5256.

13. Liang, S.; Wang, K.; Tang, C. Y.; Zhang, Q.; Du, R. N.; Fua, Q., Unexpected molecular weight dependence of shish-kebab structure in the oriented linear low density polyethylene/high density polyethylene blends. *Journal of Chemical Physics* **2008**, 128, (17), 9.
14. Peeters, M.; Goderis, B.; Reynaers, H.; Mathot, V., Morphology of Homogeneous Copolymers of Ethylene and 1-Octene. II. Structural Changes on Annealing. *Journal of Polymer Science: Part B: Polymer Physics* **1999**, 37, (1), 83-100.
15. Heeley, E. L.; Gough, T.; Bras, W.; Gleeson, A. J.; Coates, P. D.; Ryan, A. J., Polymer processing: Using synchrotron radiation to follow structure development in commercial and novel polymer materials. *Nuclear Instruments & Methods in Physics Research Section B - Beam interactions with materials and atoms* **2005**, 238, (1-4), 21-27.
16. Struik, L. C. E., The Mechanical and Physical Aging of Semicrystalline Polymers .1. *Polymer* **1987**, 28, (9), 1521-1533.
17. Noda, I. In *Recent advancement in the field of two-dimensional correlation spectroscopy*, 2008; Elsevier Science Bv: 2008; pp 2-26.
18. Noda, I.; Ozaki, Y., *Two-Dimensional Correlation Spectroscopy*. John Wiley & Sons Ltd.: West Sussex 2004.
19. Noda, I., Generalized Two-Dimensional Correlation Method Applicable to Infrared, Raman, and Other Types of Spectroscopy. *Applied Spectroscopy* **1993**, 47, (9), 1329-1336.
20. Noda, I., Determination of Two-Dimensional Correlation Spectra Using the Hilbert Transform. *Applied Spectroscopy* **2000**, 54, (7), 994-999.

21. Ashton, L.; Boguslawa, C. M. B.; Blanch, E. W. In *Application of two-dimensional correlation analysis to Raman optical activity*, 2006; Elsevier Science Bv: 2006; pp 61-71.

22. Goormaghtigh, E.; Ruysschaert, J. M.; Raussens, V., Evaluation of the information content in infrared spectra for protein secondary structure determination. *Biophysical Journal* **2006**, 90, (8), 2946-2957.

23. Murayama, K.; Czarnik-Matusewicz, B.; Wu, Y.; Tsenkova, R.; Ozaki, Y., Comparison between Conventional Spectral Analysis Methods, Chemometrics, and Two-Dimensional Correlation Spectroscopy in the Analysis of Near-Infrared Spectra of Protein. *Applied Spectroscopy* **2000**, 54, (7), 978-985.

24. Huang, J. Y.; Shih, W. T. In *Probing field-induced submolecular motions in a ferroelectric liquid crystal mixture with time-resolved two-dimensional infrared spectroscopy*, 2006; Iop Publishing Ltd: 2006; pp 7593-7603.

25. Thomas, M.; Richardson, H. H., Two-dimensional FT-IR correlation analysis of the phase transitions in a liquid crystal, 4 '-n-octyl-4-cyanobiphenyl (8CB). *Vibrational Spectroscopy* **2000**, 24, (1), 137-146.

26. Watanabe, S.; Noda, I.; Ozaki, Y., Thermally induced conformational and structural disordering in polyethylene crystal studied by near-infrared spectroscopy. *Polymer* **2008**, 49, (3), 774-784.

27. Gregoriou, V. G.; Noda, I.; Dowrey, A. E.; Marcott, C.; Chao, J. L.; Palmer, R. A., Dynamic Rheooptical Characterization of a Low-Density Polyethylene Perdeuterated High-Density Polyethylene Blend by 2-Dimensional Step-Scan Ftir Spectroscopy. *Journal of Polymer Science Part B-Polymer Physics* **1993**, 31, (12), 1769-1777.

28. Jung, Y. M.; Shin, H. S.; Kim, S. B.; Noda, I., Two-dimensional gradient mapping technique useful for detailed spectral analysis of polymer transition temperatures. *Journal of Physical Chemistry B* **2008**, 112, (12), 3611-3616.

29. Sasic, S.; Zhang, J. M.; Ozaki, Y., Detailed interpretation of the results of two-dimensional correlation analysis of infrared spectra obtained during isothermal crystallization of isotactic polystyrene and poly(3-hydroxybutyrate). *Vibrational Spectroscopy* **2007**, 44, (1), 50-55.

30. Zhang, J. M.; Duan, Y. X.; Sato, H.; Men, D. Y.; Yan, S. K.; Noda, I.; Ozaki, Y., Initial crystallization mechanism of isotactic polystyrene from different states. *Journal of Physical Chemistry B* **2005**, 109, (12), 5586-5591.

31. Kim, H. J.; Bin Kim, S.; Kim, J. K.; Jung, Y. M., Two-dimensional heterospectral correlation analysis of wide-angle X-ray scattering and infrared spectroscopy for specific chemical interactions in weakly interacting block copolymers. *Journal of Physical Chemistry B* **2006**, 110, (46), 23123-23129.

32. Noda, I. Dynamic Infrared Dichroism and Two-Dimensional Correlation Spectroscopy. Univeristy of Tokyo, 1997.

33. Simanke, A. G.; Alamo, R. G.; Galland, G. B.; Mawler, R. S., Wide-angle X-ray scattering of random metallocene-ethylene copolymers with different types and concentration of comonomer. *Macromolecules* **2001**, 34, (20), 6959-6971.

34. Baker, A. M. E.; Windle, A. H., Evidence for a partially ordered component in polyethylene from wide-angle X-ray diffraction. *Polymer* **2001**, 42, (2), 667-680.

35. Rabiej, S.; Bnias, W.; Binias, D., The Transition Phase in Polyethylenes - WAXS and Raman Investigations. *Fibres & Textiles in Eastern Europe* **2008**, 16, (6), 57-62.

36. Rabiej, S. In *WAXS investigations of the amorphous phase structure in linear polyethylene and ethylene-1-octene homogeneous copolymers*, 2005; Inst Chemical Fibres: 2005; pp 30-34.

37. Monar, K.; Habenschuss, A. In *Modeling the principal amorphous halo in quiescent melts of polyethylene and ethylene copolymers using wide-angle X-ray scattering and its implications*, 1999; John Wiley & Sons Inc: 1999; pp 3401-3410.

38. Androsch, R.; Blackwell, J.; Chvalun, S. N.; Wunderlich, B., Wide- and small-angle X-ray analysis of poly(ethylene-co-octene). *Macromolecules* **1999**, *32*, (11), 3735-3740.

39. Kolesov, I. S.; Androsch, R.; Radusch, H. J. In *Non-isothermal crystallization of polyethylenes as function of cooling rate and concentration of short chain branches*, 2004; Kluwer Academic Publ: 2004; pp 885-895.

40. Androsch, R.; Wunderlich, B., Analysis of the degree of reversibility of crystallization and melting in poly(ethylene-co-1-octene). *Macromolecules* **2000**, *33*, (24), 9076-9089.

41. Hu, W. G.; Srinivas, S.; Sirota, E. B., Crystalline structure and properties of EP and EB copolymers by solid-state NMR, DSC, and WAXS. *Macromolecules* **2002**, *35*, (13), 5013-5024.

42. Azzurri, F.; Gomez, M. A.; Alfonso, G. C.; Ellis, G.; Marco, C. In *Time-resolved SAXS/WAXS studies of the polymorphic transformation of 1-butene/ethylene copolymers*, 2004; Marcel Dekker Inc: 2004; pp 177-189.

43. Goderis, B.; Reynaers, H.; Koch, M. J., Primary and Secondary Crystallization in a Homogeneous Ethylene-1-Octene Copolymer: Crystallinity Heterogeneity Studied by SAXS. *Macromolecules* **2002**, *25*, 5840-5853.

44. Cser, F., About the Lorentz correction used in the interpretation of small angle X-ray scattering data of semicrystalline polymers. *Journal of Applied Polymer Science* **2001**, *80*, (12), 2300-2308.

45. Wang, Y. W.; Gao, W. Y.; Noda, I.; Yu, Z. W. In *A modified mean normalization method to reduce the effect of peak overlap in two-dimensional correlation spectroscopy*, 2006; Elsevier Science Bv: 2006; pp 128-133.

46. Noda, I.; Ozaki, Y., Response to "some comments on the application of two-dimensional correlation spectroscopy and normalization of the dynamic spectra" by Miroslaw A. Czarnecki. *Applied Spectroscopy* **2003**, *57*, (1), 110-112.

47. Czarnecki, M. A., Some comments on the application of two-dimensional correlation spectroscopy and normalization of the dynamic spectra. *Applied Spectroscopy* **2003**, *57*, (1), 107-109.

48. Diewok, J.; Ayora-Canada, M. J.; Lendl, B., 2D correlation spectroscopy and multivariate curve resolution in analyzing pH-dependent evolving systems monitored by FT-IR spectroscopy, a comparative study. *Analytical Chemistry* **2002**, *74*, (19), 4944-4954.

49. Morita, S.; Shinzawa, H.; Tsenkova, R.; Noda, I.; Ozaki, Y. In *Computational simulations and a practical application of moving-window two-dimensional correlation spectroscopy*, 2006; Elsevier Science Bv: 2006; pp 111-120.

50. Shinzawa, H.; Morita, S.; Noda, I.; Ozaki, Y. In *Effect of the window size in moving-window two-dimensional correlation analysis*, 2006; Elsevier Science Bv: 2006; pp 28-33.

51. Alizadeh, A.; Richardson, L.; Xu, J.; McCartney, S.; Marand, H.; Cheung, Y. W.; Chum, S., Influence of Structural and Topological Constraints on the Crystallization and Melting Behavior of Polymers. 1. Ethylene/1-Octene Copolymers. *Macromolecules* **1999**, 32, 6221-6235.

52. Rabiej, S.; Goderis, B.; Janicki, J.; Mathot, V. B. F.; Koch, M. H. J.; Groeninckx, G.; Reynaers, H.; Gelan, J.; Wlochowicz, A., Characterization of the dual crystal population in an isothermally crystallized homogeneous ethylene-1-octene copolymer. *Polymer* **2004**, 45, 8761-8778.

53. Androsch, R.; Wunderlich, B., Specific reversible melting of polyethylene. *Journal of Polymer Science Part B-Polymer Physics* **2003**, 41, (18), 2157-2173.

54. Nam, J. Y.; Kadomatsu, S.; Saito, H.; Inoue, T., Thermal reversibility in crystalline morphology of LLDPE crystallites. *Polymer* **2002**, 43, (7), 2101-2107.

55. Swan, P. R., Polyethylene Unit Cell Variations with Temperature. *Journal of Polymer Science* **1962**, 56, (164), 403-&.

56. Basiura, M.; Gearba, R. I.; Ivanov, D. A.; Janicki, J.; Reynaers, H.; Groeninckx, G.; Bras, W.; Goderis, B., Rapidly cooled polyethylenes: On the thermal stability of the semicrystalline morphology. *Macromolecules* **2006**, 39, (24), 8399-8411.

57. Alamo, R.; Domszy, R.; Mandelkern, L., Thermodynamic and Structural-Properties of Copolymers of Ethylene. *Journal of Physical Chemistry* **1984**, 88, (26), 6587-6595.

58. Shirayama, K.; Watabe, H.; Kita, S., Effects of Branching on Some Properties of Ethylene Alpha-Olefin Copolymers. *Makromolekulare Chemie* **1972**, 151, (JAN20), 97-&.

59. Swan, P. R., Polyethylene Unit Cell Variations with Branching. *Journal of Polymer Science* **1962**, 56, (164), 409-&.

60. Perez, E.; Benavente, R.; Quijada, R.; Narvaez, A.; Galland, G. B., Structure characterization of copolymers of ethylene and 1-octadecene. *Journal of Polymer Science Part B-Polymer Physics* **2000**, 38, (11), 1440-1448.

61. Peeters, M.; Goderis, B.; Vonk, C.; Reynaers, H.; Mathot, V., Morphology of Homogeneous Copolymers of Ethene and 1-Octene. I. Influence of Thermal History on Morphology. *Journal of Polymer Science: Part B: Polymer Physics* **1997**, 35, 2689-2713.

62. Howard, P. R.; Crist, B., Unit-Cell Dimensions in Model Ethylene Butene-1 Copolymers. *Journal of Polymer Science Part B-Polymer Physics* **1989**, 27, (11), 2269-2282.

63. Qiu, J.; Xu, D.; Zhao, J.; Niu, Y.; Wang, Z., New Insights into the Multiple Melting Behaviors of the Semicrystalline Ethylene-Hexene Copolymer: Origins of Quintuple Melting Peaks. *Journal of Polymer Science: Part B: Polymer Physics* **2008**, 46, 2100-2115.

64. Quinn, F. A.; Mandelkern, L., Thermodynamics of Crystallization in High Polymers - Poly-(Ethylene). *Journal of the American Chemical Society* **1958**, 80, (13), 3178-3182.

65. Bunn, C. W., The crystal structure of long-chain normal paraffin hydrocarbons. The "shape" of the > CH<sub>2</sub> group. *Transactions of the Faraday Society* **1939**, 35, (1), 0482-0490.

66. Czarnecki, M. A., Interpretation of two-dimensional correlation spectra: Science or art? *Applied Spectroscopy* **1998**, 52, (12), 1583-1590.

67. Morita, S.; Miura, Y. F.; Sugi, M.; Ozaki, Y., New correlation indices invariant to band shifts in generalized two-dimensional correlation infrared spectroscopy. *Chemical Physics Letters* **2005**, 402, (1-3), 251-257.

68. Noda, I., 2-Dimensional Infrared (2d Ir) Spectroscopy - Theory and Applications. *Applied Spectroscopy* **1990**, 44, (4), 550-561.

69. Gericke, A.; Gadaleta, S. J.; Brauner, J. W.; Mendelsohn, R., Characterization of biological samples by two-dimensional infrared spectroscopy: Simulation of frequency, bandwidth, and intensity changes. *Biospectroscopy* **1996**, 2, (6), 341-351.

70. Nabet, A.; Auger, M.; Pezolet, M., Investigation of the temperature behavior of the bands due to the methylene stretching vibrations of phospholipid acyl chains by two-dimensional infrared correlation spectroscopy. *Applied Spectroscopy* **2000**, 54, (7), 948-955.

71. Davis, G. T.; Eby, R. K.; Colson, J. P., Thermal Expansion of Polyethylene Unit Cell-Effect of Crystal Size. *Bulletin of the American Physical Society* **1970**, 15, (3), 330-&.

72. Davis, G. T.; Eby, R. K.; Colson, J. P., Thermal Expansion of Polyethylene Unit Cell - Effect of Lamella Thickness. *Journal of Applied Physics* **1970**, 41, (11), 4316-&.

73. Watanabe, S.; Sano, N.; Noda, I.; Ozaki, Y., Surface Melting and Lamella Rearrangement Process in Linear Low Density Polyethylene. *Journal of Physical Chemistry B* **2009**, 113, (11), 3385-3394.

74. Knudsen, K. D.; Hemmingsen, P. V.; We, F., Temperature-induced structural changes in some random ethylene/1-hexene copolymers. *Polymer* **2007**, 48, (11), 3148-3161.

75. Sasic, S.; Muszynski, A.; Ozaki, Y., A new possibility of the generalized two-dimensional correlation spectroscopy. 1. Sample-sample correlation spectroscopy. *Journal of Physical Chemistry A* **2000**, 104, (27), 6380-6387.

76. Sasic, S.; Ozaki, Y., Comparison of principal component analysis and generalized two-dimensional correlation spectroscopy: Spectral analysis of synthetic model system and near-infrared spectra of milk. *Applied Spectroscopy* **2001**, 55, (1), 29-38.

77. Wang, Y. W.; Gao, W. Y.; Wang, X. G.; Yu, Z. W. In *A novel normalization method based on principal component analysis to reduce the effect of peak overlaps in two-dimensional correlation spectroscopy*, 2008; Elsevier Science Bv: 2008; pp 66-72.

78. Li, Y.; Akpalu, Y. A., Probing the Melting Behavior of a Homogeneous Ethylene/1-Hexene Copolymer by Small-Angle Light Scattering. *Macromolecules* **2004**, 27, 7265-7277.

79. Schouterden, P.; Vandermarliere, M.; Riekel, C.; Koch, M. H. J.; Groeninckx, G.; Reynaers, H., Characterization of the Morphological-Changes in Linear Low-Density Polyethylene During the Melting Process Using Synchrotron Radiation. *Macromolecules* **1989**, 22, (1), 237-244.

80. Vonk, C. G.; Koga, Y., An X-Ray-Diffraction Study of Nonlinear Polyethylene .2. Small-Angle Scattering Observations near the Melting-Point. *Journal of Polymer Science Part B-Polymer Physics* **1985**, 23, (12), 2539-2548.

81. Wiley Database of Polymer Properties. In John Wiley & Sons, Inc.: 1999-2009.

82. Cahn, J. W.; Hilliard, J. E., Free Energy of a Nonuniform System .1. Interfacial Free Energy. *Journal of Chemical Physics* **1958**, 28, (2), 258-267.

83. Cahn, J. W., Phase Separation by Spinodal Decomposition in Isotropic Systems. *Journal of Chemical Physics* **1965**, 42, (1), 93-&.

84. Cook, H. E., Brownian Motion in Spinodal Decomposition. *Acta Metallurgica* **1970**, 18, (3), 297-&.

85. Stribeck, N.; Nochel, U.; Funari, S. S., Melting and Crystallization of Differently Oriented Sets of Crystallites in Hard-Elastic Polypropylene. *Macromolecules* **2009**, 42, (6), 2093-2101.

86. Panine, P.; Urban, V.; Boesecke, P.; Narayanan, T. In *Combined small- and wide-angle X-ray scattering study of early stages of polymer crystallization*, 2003; Blackwell Munksgaard: 2003; pp 991-994.

87. Akpalu, Y.; Kielhorn, L.; Hsiao, B. S.; Stein, R. S.; Russell, T. P.; Egmond, J. v.; Muthukumar, M., Structure Development during Crystallization of Homogeneous Copolymers of Ethene and 1-Octene: Time-Resolved Synchrotron X-ray and SALS Measurements. *Macromolecules* **1999**, 32, 765-770.

88. Wang, H., SANS study of the early stages of crystallization in polyethylene solutions. *Polymer* **2006**, 47, (14), 4897-4900.

89. Panine, P.; Di Cola, E.; Sztucki, M.; Narayanan, T., Early stages of polymer melt crystallization. *Polymer* **2008**, *49*, (3), 676-680.

90. Hamley, I. W.; Parras, P.; Castelletto, V.; Castillo, R. V.; Muller, A. J.; Pollet, E.; Dubois, P.; Martin, C. M., Melt structure and its transformation by sequential crystallization of the two blocks within poly(L-lactide)-block-poly(epsilon-caprolactone) double crystalline diblock copolymers. *Macromolecular Chemistry and Physics* **2006**, *207*, (11), 941-953.

## Chapter 5

### Morphology Development in HDPE/Copolymer Blends: Quiescent and Flow-Induced Crystallization

<b>5.1</b>	<b>INTRODUCTION.....</b>	<b>V-2</b>
<b>5.2</b>	<b>EXPERIMENTAL METHODS .....</b>	<b>V-4</b>
5.2.1	Materials .....	V-4
5.2.2	Differential Scanning Calorimetry.....	V-5
5.2.3	Flow-Induced Crystallization .....	V-6
5.2.4	Optical Characterization.....	V-8
5.2.5	X-ray Scattering.....	V-9
5.2.6	Scanning Transmission Electron Microscopy.....	V-11
<b>5.3</b>	<b>RESULTS .....</b>	<b>V-12</b>
5.3.1	Quiescent Crystallization .....	V-12
5.3.1.1	DSC Nucleation Studies .....	V-12
5.3.1.2	Optical Characterization .....	V-13
5.3.1.3	X-ray Characterization .....	V-19
5.3.1.4	STEM Images .....	V-21
5.3.2	Flow-Induced Crystallization .....	V-22
5.3.2.1	Optical Characterization .....	V-22
5.3.2.2	X-ray Characterization .....	V-25
<b>5.4</b>	<b>DISCUSSION .....</b>	<b>V-26</b>
5.4.1	Quiescent Crystallization .....	V-26
5.4.1.1	Nucleation Effects.....	V-26
5.4.1.2	Morphology Evolution.....	V-28
5.4.2	Flow-Induced Crystallization .....	V-32
<b>5.5</b>	<b>CONCLUSION .....</b>	<b>V-38</b>
<b>5.6</b>	<b>ACKNOWLEDGEMENTS .....</b>	<b>V-40</b>
<b>5.7</b>	<b>REFERENCES.....</b>	<b>V-41</b>

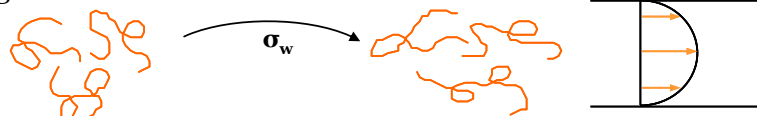
## 5.1 INTRODUCTION

Due to their flexibility and toughness, materials containing short-chain branches (SCB) have found a significant niche in the plastics industry to make products, such as films having high tensile strength, impact and puncture resistance. The most common material used for these applications is linear low density polyethylene (LLDPE), which is typically either a heterogeneous or homogeneous ethylene copolymer depending on the catalyst used for its synthesis (Ziegler-Natta or metallocene, respectively).<sup>1,2</sup>

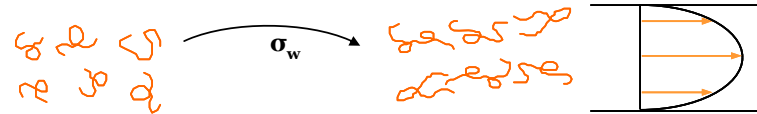
The development of single-site metallocene catalyst has allowed for large-scale production of relatively well-defined ethylene/α-olefin copolymers with narrow molecular weight distributions and uniform SCB distribution.<sup>3-8</sup> Therefore, a great deal of effort has been put forth to understand crystallization behavior of these systems (e.g., studies in Chapter 3 on model SCB-containing materials) and achieve control over their physical properties.<sup>9-19</sup> Short-chain-branched systems exhibit strong changes in morphology compared to un-branched samples due to the exclusion of the short-chain branches from the crystalline phase.<sup>19-24</sup> The resulting decreased crystallinity leads to increased toughness and flexibility of the final material, prompting a number of studies of copolymer blends.<sup>18,25-27</sup> Additionally, the presence of these chain defects results in a significant decrease in the response of the materials to flow without enhancement of crystallization kinetics or oriented morphology (see thesis Appendix B). This observation can be explained by either (1) the material's inability to form oriented nuclei that lead to an increased nucleation density and template oriented growth or (2) the material's inability to effectively propagate growth from an oriented nuclei.

To further examine these possibilities, we examine flow-induced crystallization (FIC) of a metallocene ethylene copolymer spiked with small amounts of high density polyethylene (HDPE) in order to promote oriented nuclei formation. The low concentration of a high-molecular-weight (slow-relaxing) HDPE ensures that the blend exhibits melt dynamics that are dominated by the fast-relaxing matrix, such that the few HDPE chains present are oriented by flow and form thread-like nuclei (Figure 5.1). In this way, we can evaluate the copolymer's ability to propagate an oriented morphology.

**a. Long Chains – Narrow Distribution**



**b. Short Chains – Narrow Distribution**



**c. Bimodal Distribution**

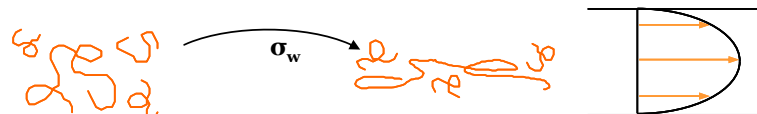


**Figure 5.1** Schematic representation of the orientation of molecules by shear. **a)** Blends containing only long (slow-relaxing) chains undergo a small strain. **b)** Blends containing only short (fast-relaxing) chains undergo a large strain, but does not exhibit increased orientation compared to **a**. **c)** Blends containing a small amount of long chains in a predominately short-chain matrix exhibit melt dynamics dictated by the matrix (large strain) such that the slow-relaxing species is oriented by flow.

Recent studies of similar systems have observed the nucleation of polyethylenes having lower density or molecular weight by higher density or molecular weight polyethylene.<sup>28-30</sup> Increased crystallization kinetics and sample clarity were observed. These effects are further examined here both under quiescent conditions and subsequent to flow.

## 5.2 EXPERIMENTAL METHODS

### 5.2.1 Materials

Bimodal blends examined here consisted of a minor component of high density polyethylene (HDPE) having high molecular weight ( $M_w$ ) and polydispersity (PDI =  $M_w/M_n$ ) of 3.0. The major component was a fast-relaxing—but still entangled ( $M_e \sim 1000$  g/mol)<sup>31</sup>—random ethylene copolymer (EH50) with a melt index (MI) of 16.5 g/10 min. This metallocene-catalyzed copolymer having approximately 5 mol % hexene was selected to mimic the SCB content of the series of hydrogenated polybutadienes (HPBDs) outlined in Chapter 3. One of these HPBDs, L53, is included for comparison in Table 5.1, which outlines the molecular characteristics of the bimodal blend components. EH50 was graciously provided and characterized by Dr. David Lohse and his team (ExxonMobil, Clinton, NJ) and the HDPE sample by Chevron Phillips.

**Table 5.1 Molecular characteristics of polyethylene materials.**

Polymer	Type	$M_w$ (kg/mol)	PDI	SCB/ 1000 back- bone C <sup>a</sup>	$T_m$ (°C) <sup>d</sup>
EH50 <sup>b</sup>	Linear	50	2.9	25.7	96
HDPE <sup>c</sup>	Linear	529	3.0	0.2	136
L53 <sup>b*</sup>	Linear	53	<1.05	19.2	110

<sup>a</sup> obtained via  $^{13}\text{C}$  NMR

<sup>b</sup> corresponding values provided by ExxonMobil

<sup>c</sup> corresponding values provided by Chevron Phillips

<sup>d</sup> peak temperature as determined by DSC during ramps at 10 °C/min

\* not examined in current studies

Blends containing a small concentration of HDPE in EH50 were made via solution blending. This blending procedure results in homogeneous mixtures and avoids problems encountered in melt extrusion blending,<sup>32</sup> such as long-chain degradation and incomplete mixing due to viscosity differences between the two components. Both poly-

mers were dissolved in 1,2,4-trimethylbenzene at 130 °C along with approximately 30 mg of antioxidant, butylated hydroxytoluene (BHT). The solutions were precipitated in an excess (8:1) of cold methanol, and the resulting precipitates were filtered and dried in a vacuum oven for one week at 60 °C. Low HDPE concentrations were selected in order to minimize crystallization-induced phase separation. Concentrations on either side of the HDPE overlap concentration,  $c^*$ , were selected. The overlap concentration is defined as the concentration at which the corresponding chains just pervade all volume (see Figure B.1) and thus depends upon the radius of gyration ( $R_g$ ) and molecular weight ( $M_w$ ) of chains:

$$c^* = \frac{3M_w}{4\pi R_g^3 \rho N_a}, \quad (5.1)$$

where  $N_a$  is Avogadro's number ( $6.022 \times 10^{23}$ ) and  $\rho$  is density.<sup>33, 34</sup> From small-angle neutron scattering measurements,  $R_g$  (Å) of melt-crystallized linear polyethylene was found to depend on  $M_w$  (g/mol) as<sup>35, 36</sup>

$$R_g = (0.45 \pm 0.01)M_w^{1/2}. \quad (5.2)$$

Using a density of 0.95 g/cm<sup>3</sup>, eqs 5.1 and 5.2 yield  $c^* \approx 0.6\%$ . Hence, blends containing 0%, 0.25%, 0.5%, 0.75%, 1% and 5% HDPE by weight were examined.

### 5.2.2 Differential Scanning Calorimetry

Differential Scanning Calorimetry (DSC) experiments were conducted by Dr. Soo-Young Park (Kyunpook National University, Daegu, South Korea) to study nucleation in HDPE blends (5-10 mg samples) using a Perkin Elmer 7 DSC system calibrated with an indium standard. Both temperature ramps and isothermal studies were conducted

under a nitrogen atmosphere. Temperature ramps were conducted at 10 °C/min from 160 °C to 40 °C to obtain peak melting and crystallization temperatures ( $T_m$  and  $T_x$ , respectively).

Nucleation studies examined the effect of hold-time ( $t_{hold}$ ) at elevated temperatures on subsequent crystallization rates at lower temperature; at the elevated temperature negligible crystallization of EH50 (major component) occurs while HDPE (minor component) is highly supercooled. Samples containing 0, 0.5, and 1 wt % HDPE were first heated to 160 °C and left for 5 minutes in order to erase thermal history. Samples were then cooled to the hold temperature ( $T_{hold}$ ) of 100 °C or 105 °C at 40 °C/min where they were left for  $0 \leq t_{hold} \leq 5$  min. Subsequently, samples were cooled to an isothermal crystallization temperature ( $T_c$ ) of 90 °C at 40 °C/min and left to crystallize for 1 hour during which period heat flow was recorded as a function of time. Position of the peak in heat flow,  $t_{max}$ , was used as a measure of crystallization rate.

### 5.2.3 Flow-Induced Crystallization

Flow-induced crystallization (FIC) studies were conducted using a shear-stress-controlled instrument previously built and described by Kumaraswamy et al.<sup>37</sup> Briefly, a pneumatic actuator drove molten polymer into a rigid flow cell equipped with windows for in-situ monitoring of morphology development. For optical characterization, the quartz windows of the flow cell were replaced with low-birefringence BK7 windows (Foctek Photonics, Inc.). For x-ray characterization, diamond or beryllium windows were used. The flow channel is a rectangular slit with an aspect ratio greater than 10 in order to approximate a two-dimensional flow profile (width = 6.35mm, height = 0.5 mm, length =

63.5 mm). Assuming parallel-plate flow, the shear imposed on the sample varies linearly from its value at the wall ( $\sigma_w$ ) to 0 at the center of the channel in the direction of the velocity gradient ( $\nabla v$ ). Minor alterations to the instrument included the use of compressed air and a re-circulating oil bath set to 0 °C in order to enable rapid cooling of the sample to the lower temperatures that are necessary for polyethylene (PE) compared to polypropylene, for which the instrument was initially designed.

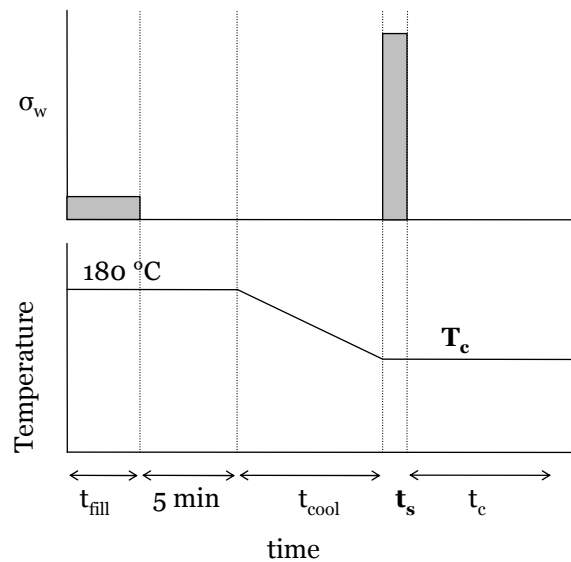


**Figure 5.2** Experimental short-term shearing protocol.

Isothermal crystallization was examined following a short shear pulse based on a protocol developed by Janeschitz-Kriegl and co-workers (Figure 5.2).<sup>38</sup> Initially, the cell was filled with sample at 180 °C and low wall shear stress ( $t_{\text{fill}} = 25$  s,  $\sigma_w \sim 0.02$  MPa). The sample was maintained at this high temperature, which is above the equilibrium melting point of polyethylene (~ 145 °C)<sup>39</sup> for 5 min to ensure full erasure of the flow history. The cell was then cooled to the crystallization temperature,  $T_c$ , as quickly as possible; cooling times ( $t_{\text{cool}}$ ) ranged between 8 and 15 min, with the large thermal mass of the instrument being the limiting factor in cooling rate. Isothermal crystallization was ex-

amined at  $T_c = 92, 95$ , and  $98^\circ\text{C}$ . Once at  $T_c$ , the system temperature was maintained with the aid of a second re-circulating oil bath set to  $T_c + 6^\circ\text{C}$ . For FIC studies, upon reaching  $T_c$ , a pressure drop between 60 and 100 psi was applied across the flow cell (corresponding to  $0.07 \text{ MPa} \leq \sigma_w \leq 0.14 \text{ MPa}$ ) for shearing times ( $t_s$ ) ranging between 6 and 15 seconds. The amount of polymer extruded was limited to 110 mg to ensure that all material reaching the analysis window of the flow cell had the same flow and thermal histories.

#### 5.2.4 Optical Characterization

Isothermal crystallization was followed *in situ* using optical and x-ray probes in the velocity gradient direction (Figure 5.3). A 632.8 nm He-Ne laser was employed for transmittance, apparent birefringence, and  $H_v$  (cross-polarized) small angle light scattering (SALS) measurements both during and following the shear pulse. Sample transmittance ( $I/I_0$ ) is given by total intensity,  $I$ , normalized by the pre-shear total intensity,  $I_0$ , and can be used to monitor overall crystallization kinetics. Optical anisotropy of the sample is manifested in what we term the ‘apparent’ birefringence:  $I_{perp}/I = I_{perp}/(I_{para} + I_{perp})$ , where  $I_{perp}$  and  $I_{para}$  are the light intensity transmitted through crossed and parallel polarizers, respectively. This value is related to the birefringence by

$$\frac{I_{perp}}{I} = \sin^2\left(\frac{\pi d \Delta n}{\lambda}\right) = \sin^2\left(\frac{\delta}{2}\right), \quad (5.3)$$

where  $d$  is the sample thickness along the direction of light with wavelength  $\lambda = 632.8 \text{ nm}$ ,  $\Delta n$  is the birefringence averaged over the path length of the laser, and  $\delta$  is the sample retardance.<sup>40</sup> SALS patterns in  $H_v$  polarization mode were recorded using a polarizer and

analyzer oriented at  $+45^\circ$  and  $-45^\circ$  to vertical. These patterns were collected simultaneously with the other optical measurements by the use of a hole at the center of the analyzer that allows un-scattered light to pass through. SALS provides additional information regarding morphological superstructures developed during crystallization.

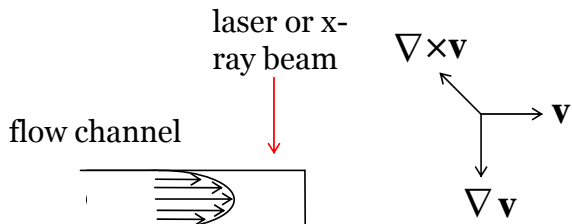


**Figure 5.3** Schematic representation depicting coordinate axes relevant to flow experiment.

### 5.2.5 X-ray Scattering

Morphology development during quiescent crystallization and crystallization subsequent to flow was followed using wide and small angle x-ray scattering (WAXS and SAXS, respectively). WAXS was conducted at beamline X27C of the National Synchrotron Light Source (Brookhaven National Lab, Upton, NY).<sup>41</sup> A MARCCD detector with 158  $\mu\text{m}$  pixel size was used to record two-dimensional scattering patterns generated with x-rays of wavelength,  $\lambda$ , of 1.371  $\text{\AA}$ . The camera length was calibrated using aluminum oxide ( $\text{Al}_2\text{O}_3$ ). Thermal and flow history were controlled by the apparatus described above.

SAXS experiments were conducted at the DUBBLE beamline (BM26) at the European Synchrotron Radiation Facility (ESRF, Grenoble, France).<sup>42</sup> A multi-wire gas-filled detector with 260  $\mu\text{m}$  pixel size was used to record two-dimensional scattering patterns generated with x-rays of wavelength,  $\lambda$ , of 1.03  $\text{\AA}$ . The sample-to-detector distance was calibrated using dry rattail collagen. Shear experiments were conducted using the

apparatus described above. Additionally, quiescent crystallization was conducted at 95 and 98 °C using a Linkam Shear cell equipped with Kapton windows. The gap width was set to 500 μm to match the light path length in the flow apparatus described above.

X-ray data pre-treatment included the subtraction of a background and adjustment for incident flux and acquisition time. The azimuthally-averaged intensity,  $I(q)$ , was extracted as a function of scattering vector,  $q = 4\pi\sin(\theta)/\lambda$ , where  $\theta$  is the scattering angle. For isotropic samples, a Lorentz correction was applied by multiplying the scattering intensity,  $I(q)$ , by the square of the scattering vector,  $q$ :  $J(q) = I(q)q^2$ .<sup>43</sup>

The area under the Lorentz-corrected SAXS intensity curve (for isotropic samples) for the full range of  $q$  ( $0 < q < \infty$ ) defines the invariant, which is a measure of the total scattering power of the sample. Given the experimental constraints, we approximate the invariant by the integrated intensity,  $Q$ , in the range available ( $q_{min} < q < q_{max}$ ):

$$Q = \int_{q_{min}}^{q_{max}} q^2 I(q) dq . \quad (5.4)$$

The evolution of this invariant can be used to examine relative crystallization kinetics and relative crystallinity in systems with similar electron density differences.

Wide angle x-ray scattering data proved difficult to analyze by conventional methods (peak fitting of amorphous halo and crystalline reflections)<sup>44</sup> due to the low crystallinity levels of the blends. Instead, the azimuthally-averaged intensity of the (110) reflection is used as an estimate of relative crystallinity. Crystallization rates could be compared by the autocorrelation intensity,  $A$ , of the (110) crystalline reflection during crystallization:

$$A(q_{110}) = \frac{1}{m-1} \sum_{i=1}^m \tilde{I}(q_{110}, t_i) \cdot \tilde{I}(q_{110}, t_i), \quad (5.5)$$

where  $m$  is the total number of intensity curves,  $t_i$  corresponds to the time point of acquisition, and  $\tilde{I}(q, t_i)$  is the dynamic intensity defined as

$$\tilde{I}(q, t_i) = I(q, t_i) - \frac{1}{m} \sum_{i=1}^m I(q, t_i). \quad (5.6)$$

Alternatively, relative crystallinity and degree of orientation were examined using a differential analysis developed by Hajimorad et al.<sup>45</sup> In this analysis, the relative degree of crystallinity was measured by the peak intensity of the (110) reflection. A quantitative comparison of the degree of orientation was made using the normalized harmonic of the Fourier transform capturing the azimuthal dependence of the intensity (in our case, the second harmonic). These measurements were made for both overall scattering intensities and differential intensities. The latter were calculated by examining 2D scattering patterns relative to previous points in time. For example, data presented at  $t = 615$  s were collected from a 2D image that was obtained by subtracting the 2D scattering pattern at the previous time point of  $t = 195$  s from the 2D scattering image at  $t = 615$  s after both were normalized to account for the incident beam flux and acquisition time.<sup>45</sup>

### 5.2.6 Scanning Transmission Electron Microscopy

Scanning transmission electron microscopy (STEM) images for EH50 and its blends containing 0.5, 0.75, and 5 wt % HDPE were obtained by Dr. John Stuyver and Dr. Anton-Jan Bons (ExxonMobil, Machelen, Belgium). These samples were isothermally crystallized at 98 °C for 30 minutes and subsequently cooled to room temperature at

40 °C/min in a Perkin Elmer 7 DSC system under nitrogen atmosphere. Images were obtained in high-angle annular dark field (HAADF) mode following staining with ruthenium tetroxide ( $\text{RuO}_4$ ) and cryo-microtoming. Image contrast was inverted in order to be comparable with conventional transmission electron microscopy (TEM) bright field images.

## 5.3 RESULTS

### 5.3.1 Quiescent Crystallization

#### 5.3.1.1 DSC Nucleation Studies

The addition of HDPE to EH50 resulted in a pronounced enhancement of crystallization kinetics (Figure 5.4). In these studies, we examined the peak crystallization time ( $t_{\max}$ ) for isothermal crystallization at 90 °C following a hold for a specified time,  $t_{\text{hold}}$ , at  $T_{\text{hold}} = 100$  or 105 °C. The addition of even a small amount of HDPE (0.5 wt %) led to nearly a 5-fold increase in crystallization rate. At short hold times of 0 or 1 min, doubling the HDPE concentration from 0.5 to 1 wt % doubled the crystallization rate. Longer hold times led to greater enhancement of crystallization kinetics for the 1 wt % HDPE blend. When the samples were cooled stepwise with a 3-minute hold at 100 °C, the 1 wt % blend exhibited crystallization kinetics that were approximately 25 times faster compared to the 0.5 wt % blend. In contrast, the crystallization kinetics of the 0 and 0.5 wt % blends were not significantly affected by hold times of up to 5 minutes at elevated temperatures (i.e., similar  $t_{\max}$  at different  $t_{\text{hold}}$ ).

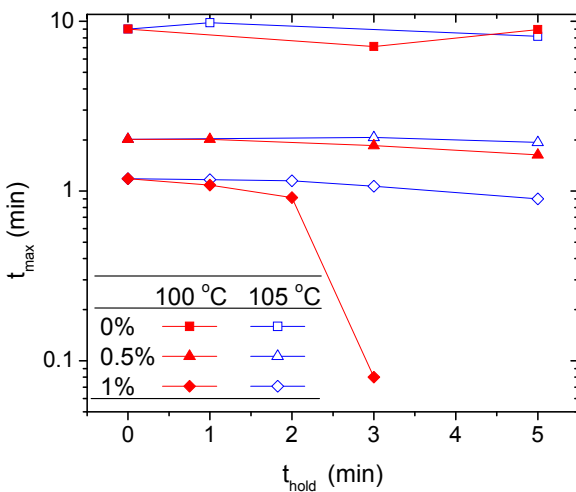


**Figure 5.4** Time of peak crystallization ( $t_{\max}$ ) during 60 min at 90 °C as a function of hold time ( $t_{\text{hold}}$ ) at 100 and 105 °C for 0, 0.5 and 1 wt % blends of HDPE in EH50.

### 5.3.1.2 Optical Characterization

Blends containing HDPE in EH50, even at the lowest concentration examined of 0.25 wt %, exhibited transmittance behavior that was qualitatively different from the ethylene-co-hexene base resin (Figure 5.5). Quiescent crystallization of EH50 containing 0 wt % HDPE exhibited a monotonic decrease in transmittance during crystallization at 98 °C following an induction period of approximately 10<sup>3</sup> s. In contrast, the three blends exhibited minima in transmittance evolution and subsequently maintained transmittance values above 50% on the same timescale. In previous studies, this minimum has been attributed to the half-filling of space by crystalline structures (i.e., when the size of the morphological features is on the order of the space between them).<sup>46-50</sup> The depth of the minima and their position in time followed a monotonic trend with HDPE concentration. Greater clarity both at the minimum in transmittance and during subsequent crystallization was observed with increasing HDPE content in the range examined; the 1 wt %

HDPE blend recovered to 96% transmittance. Additionally, the increase of turbidity (decrease of transmittance) with time and hence, crystallinity, reduced with increasing HPDE content. The nucleating effect of HDPE is apparent in the onset of the growth of turbidity which occurs at approximately 90 s for the 0.25% HDPE blend, 40 s for the 0.5% blend, and 10 s for the 1% blend.

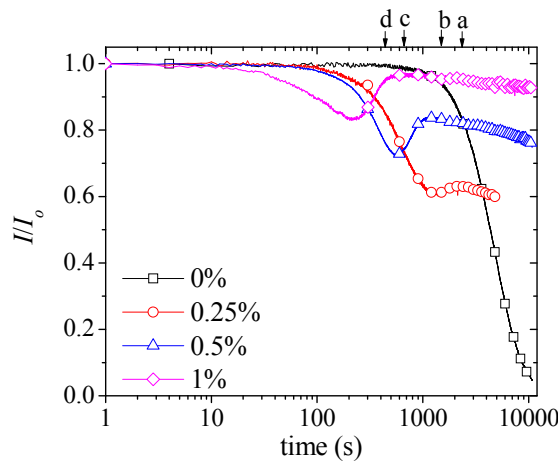


**Figure 5.5** Transmittance ( $I/I_0$ ) of HPDE blends crystallized quiescently at 98 °C. a, b, c, and d denote the times at which  $H_v$  SALS patterns (Figure 5.6) were collected for the 0, 0.25, 0.5 and 1 wt % blends, respectively.

The difference in optical behavior between EH50 and HDPE/EH50 blends is also apparent in 2D  $H_v$  SALS patterns (Figure 5.6). EH50 exhibited isotropic  $H_v$  SALS patterns corresponding to depolarization of light by randomly oriented scattering entities (Figure 5.6a). In contrast, HDPE/EH50 blends exhibited  $H_v$  SALS patterns with an azimuthal dependence that mimics 4-lobe patterns, which are usually associated with spherulite formation (Figure 5.6b-d).<sup>51, 52</sup> Even at the lowest concentration examined of 0.25 wt % HDPE, a faint 4-lobe pattern was observed (Figure 5.6b). The distorted 4-lobe SALS patterns apparent for 0.5 and 1 wt % HDPE blends (Figure 5.6c and d, respectively) are typically attributed to very poorly formed spherulites categorized as ‘type-c’

spherulites.<sup>53</sup>

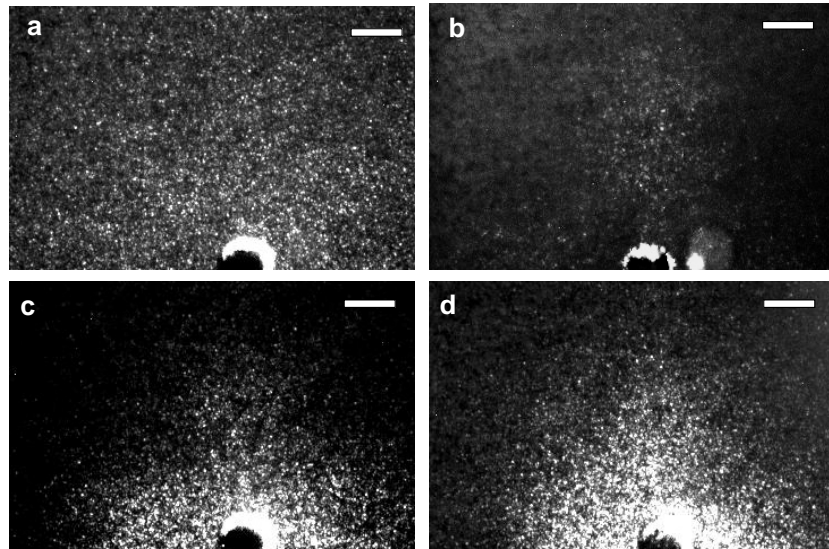


**Figure 5.6**  $H_v$  SALS patterns of **a)** 0 wt %, **b)** 0.25 wt %, **c)** 0.5 wt %, and **d)** 1 wt % HDPE blends collected at time points indicated in Figure 5.5 during quiescent crystallization at 98 °C. Scale bar corresponds to  $2\theta = 2^\circ$ .

Intensity and shape of  $H_v$  SALS patterns of HDPE/EH50 blends vary with position along the non-monotonic transmittance curve (Figure 5.7–5.9). With the apparatus used here, no scattering pattern could be recorded prior to the minimum in light transmittance (SALS images 1-3 in Figure 5.8 and half-filled symbols in Figure 5.9). Even the 0.25 wt % HDPE blend (not shown), whose minimum corresponded to 60% transmittance, exhibited only minor increases in overall  $H_v$  scattering power prior to the minimum (similar to Figure 5.9). Near the minimum in transmittance, a strong increase in  $H_v$  SALS intensity was observed (point 4 in Figure 5.7–5.9). The  $H_v$  SALS pattern (image 4 Figure 5.8) exhibited some azimuthal dependence (Figure 5.9), which became more pronounced as transmittance values increased (points 5-6 in Figure 5.7). A 4-lobe pattern was easily recognized in the range where transmittance resumed decreasing (points 7 and 8 in Figure 5.7–5.9). Furthermore, azimuthal dependence at long times ( $>10^4$  s) revealed increased

scattering both within and between the ‘lobes’ of the  $H_v$  SALS pattern (curve 8 in Figure 5.9). These observations are in agreement with prior studies of polyethylene crystallization.<sup>49, 54</sup>

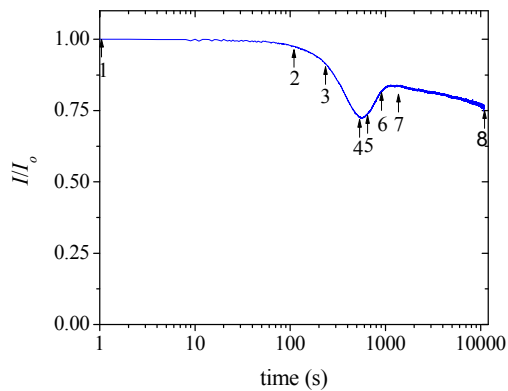


**Figure 5.7** Transmittance of 0.5 wt % HPDE blend crystallized quiescently at 98 °C. Numbers mark time at which  $H_v$  SALS images (Figure 5.8) were collected.

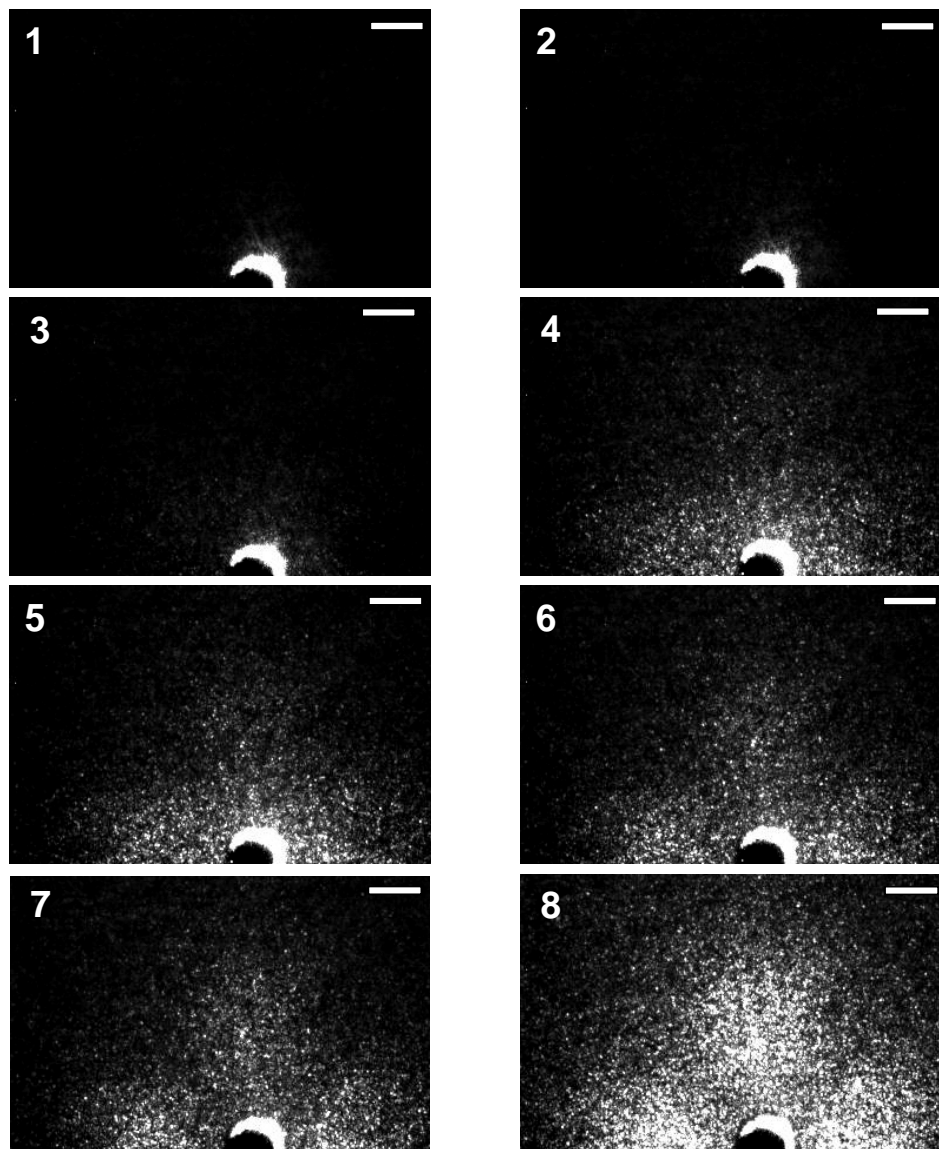


**Figure 5.8**  $H_v$  SALS images of 0.5 wt % HPDE blend undergoing quiescent crystallization at 98 °C corresponding to points marked in transmittance curve (Figure 5.7). Scale bar corresponds to  $2\theta = 2^\circ$ .

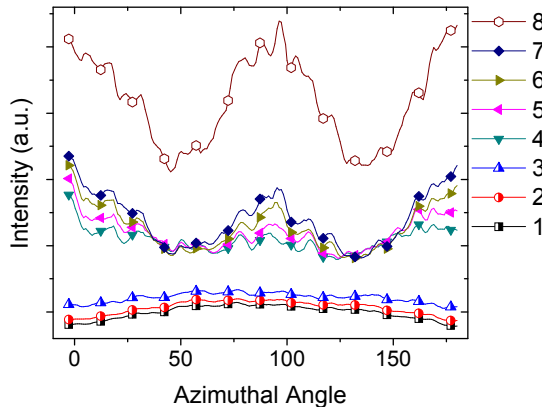


**Figure 5.9** Azimuthal dependence of  $H_v$  SALS intensity in Figure 5.8 for 0.5 wt % HDPE blend quiescently crystallized at 98 °C at time points marked in Figure 5.7.

While there are similarities between these optical behaviors and those in previous studies,<sup>49, 54</sup> a very important distinction exists. Although 4-lobe  $H_v$  SALS images are predominately associated with spherulitic growth, polarized optical microscopy (POM) images indicated that hardly any spherulites form for the 0, 0.5, and 0.75 wt % blends (Figure 5.10).

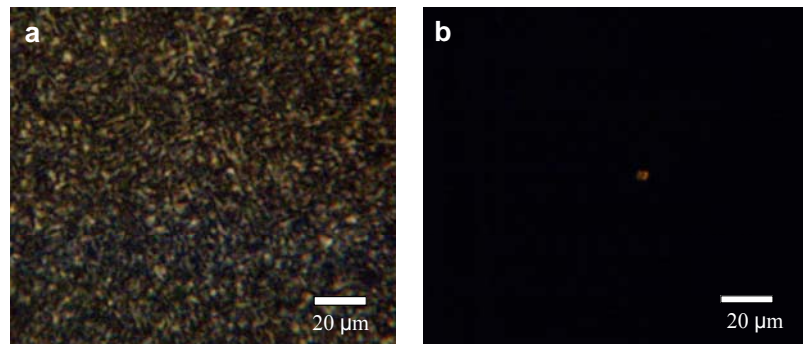


**Figure 5.10** POM images of a) HDPE and b) 0.5 wt% HDPE/EH50 blend.

The nucleation effect of HDPE is also apparent in  $H_v$  scattering patterns at short crystallization times. In contrast to the 0.5 wt % HDPE blend, for which an induction period for the development of  $H_v$  scattering was observed, the 1 wt % HDPE blend exhibited an isotropic scattering pattern upon reaching the isothermal crystallization tempera-

ture of 98 °C (Figure 5.11; compare with image 1 in Figure 5.8), indicating crystallization of the blend during cooling. Analogous to the  $H_v$  pattern of the 5 wt % blend, that of the 1 wt % blend remained relatively unchanged up until the minimum in transmittance (Figure 5.5), at which point the scattering pattern developed azimuthal dependence. At long times ( $t \sim 10^4$  s), a 4-lobe pattern emerged.

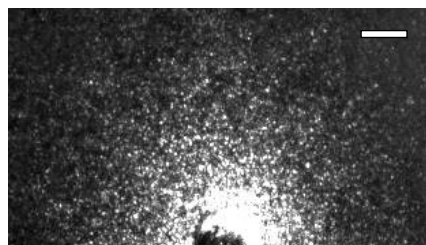


**Figure 5.11**  $H_v$  SALS image of 1 wt % HDPE blend at the onset of isothermal crystallization at 98 °C ( $t = 0$  s). Scale bar corresponds to  $2\theta = 2^\circ$ .

### 5.3.1.3 X-ray Characterization

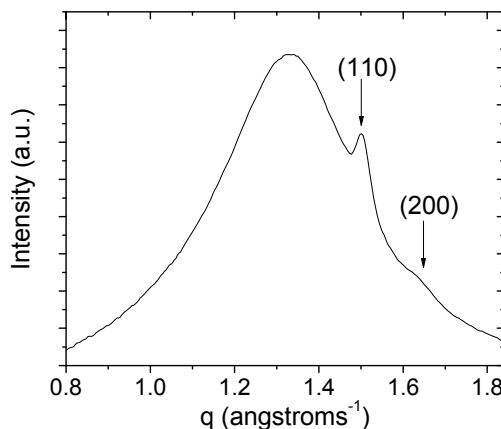


**Figure 5.12** WAXS intensity of 1 wt % HDPE/EH50 blend after isothermal crystallization at 98 °C for 30 minutes with crystalline reflections as indicated.

Extremely low crystallinity levels at the elevated isothermal temperatures examined here present significant challenges to WAXS data processing. The (110) orthorhombic reflection consistently displayed lower intensity than the amorphous halo and the

(200) crystalline reflection was never resolved (Figure 5.12; compare with Figure 4.2 in Chapter 4). Peak fitting of the amorphous halo and the crystalline reflections was not successful, and hence, a crystallinity index could not be evaluated. Alternatively, the peak intensity of the (110) crystalline reflection was used to gauge the relative amount of crystallinity. Relative crystallization rates could be compared via the autocorrelation intensity,  $A(q_{110})$ , of the (110) crystalline reflection (eqs 5.5 and 5.6), which is a measure of the overall rate of change of intensity at a given  $q$ -value, and hence the rate of crystallization. Crystallization rates were observed to increase with HDPE concentration (Table 5.2), and furthermore, the significant difference between the rates of change of the 0.75 and 1 wt % blends suggests that the overlap concentration for HDPE lies between these two concentrations ( $0.75 < c^* < 1$ ).

**Table 5.2 Autocorrelation intensities of (110) reflections during isothermal crystallization of HDPE/EH50 blends.**

% HDPE	$T_c = 95^\circ\text{C}$ ( $\times 10^{-4}$ )	$T_c = 98^\circ\text{C}$ ( $\times 10^{-4}$ )
0.25%		2
0.5%	1	5
0.75%	4	7
1%	30	

Small angle x-ray scattering of the 0, 0.5 and 0.75 wt % blends during isothermal crystallization at  $98^\circ\text{C}$  (and  $95^\circ\text{C}$ , not shown) revealed an overall increase in scattering power of the blends (Figure 5.13a). This behavior is similar to that of a hydrogenated polybutadiene undergoing isothermal crystallization at a high temperature that was observed in Chapter 3 (Figure 3.15a); a decrease of scattering intensity at low  $q$  was not observed, indicating that morphology development was dominated by growth of primary lamellae. The SAXS integrated intensity revealed increased crystallinity and confirmed

increased crystallization rate with greater HDPE content (Figure 5.13b).

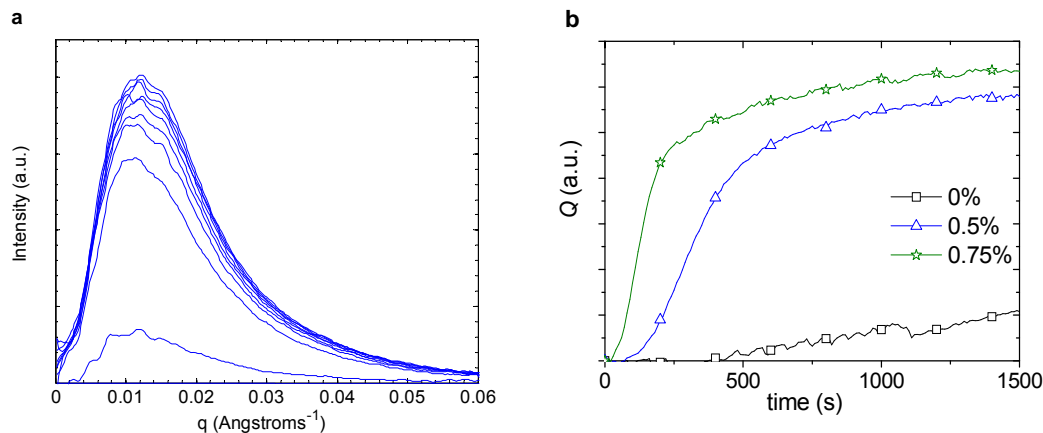


**Figure 5.13** a) Evolution of SAXS intensity,  $I(q)$ , for 0.75 wt % HDPE blend during quiescent crystallization at 98 °C. b) Relative SAXS integrated intensity ( $Q$ ) for different HDPE/EH50 blends during quiescent, isothermal crystallization at 98 °C.

#### 5.3.1.4 STEM Images

STEM images obtained for samples crystallized at 98 °C for 30 minutes and subsequently cooled to room temperature at 40 °C/min underscore the pronounced effect of HDPE on the morphology of copolymer systems (Figure 5.14). EH50 alone was found to consist of short, randomly oriented lamellae (Figure 5.14a). On the other hand, an addition of HDPE at concentrations even below its overlap concentration ( $c = 0.5$  wt %  $< c^*$ ) resulted in a significant increase in length and local orientation of the lamellae (Figure 5.14b). The 5 wt % HDPE blend ( $c \sim 10 \times c^*$ ) exhibited evidence of phase separation (Figure 5.14c), showing thicker lamellae compared with 0.5 wt % HDPE blend embedded in the fine-grained, randomly oriented morphology characteristic of pure EH50 (Figure 5.14a). No evidence of spherulitic growth was observed.

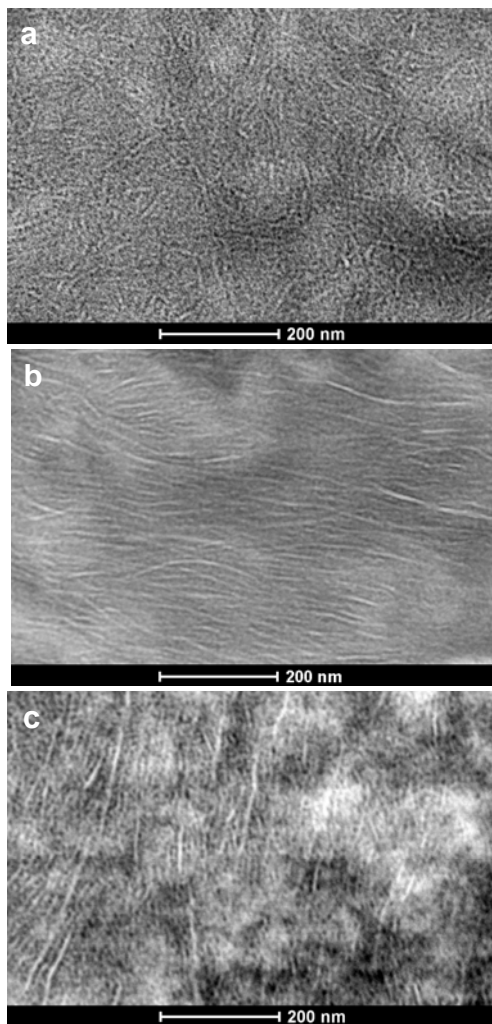


**Figure 5.14** STEM images of a) EH50, b) 0.5 wt % HDPE blend, and c) 5 wt % HDPE blend subsequent to crystallization at 98 °C for 30 min and cooling to room temperature.

### 5.3.2 Flow-Induced Crystallization

#### 5.3.2.1 Optical Characterization

The clarifying effect observed under quiescent conditions was also observed following the imposition of shear (Figure 5.15a). Similar to the quiescent case, transmittance for both the 0 and 0.5 wt % blends subsequent to shear decreased to a local minimum; however, relative to the quiescent case, these minima were shallower and, for the 1

wt % blend, occur at earlier time (no significant difference for 0.5 wt % blend).

In contrast to quiescent conditions (Figure 5.5), both 0.5 and 1 wt % HDPE blends produced equally transparent microstructures (Figure 5.15a,  $t > 500$  s). Relative to the quiescent case, short-term shearing improved the transmittance of the 0.5 wt % blend and decreased the transmittance of the 1 wt % blend. These opposite trends may be related to the increase in transmittance and oriented structure formation of the 1 wt % blend.

The 1 wt % HDPE blend exhibited an increase in transmittance during shear above its initial value at the start of the experiment ( $t = 0$  s when  $T = 98$  °C). This value,  $I/I_0(t = 0)$  was below 1.0 because crystallization during cooling ( $t_{cool}$  region in Figure 5.15a) resulted in the formation of scattering entities. Upon shear ( $t_s$  region in Figure 5.15a), sample transmittance was almost fully restored.

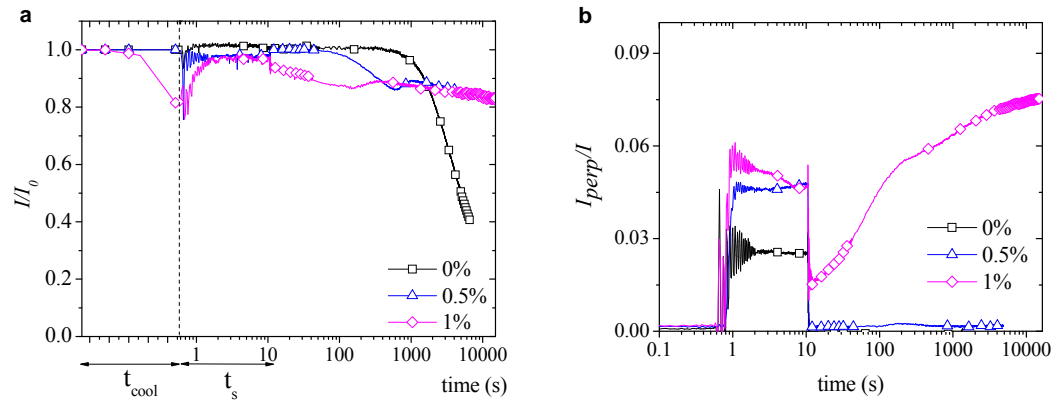


**Figure 5.15 a)** Transmittance and **b)** corresponding apparent birefringence of HDPE/EH50 blends during and subsequent to shear at 98 °C,  $\sigma_w = 0.14$  MPa for  $t_s = 10$ s. **a** includes transmittance during cooling ( $t_{cool}$ ) on a linear timescale occurring over 9 min.

Apparent birefringence ( $I_{perp}/I$ ) revealed no orientation for blends having HDPE concentration below overlap ( $c < c^*$ ) and surprisingly little orientation for the 1 wt % HDPE ( $c > c^*$ ; Figure 5.15b). The non-zero value of  $I_{perp}/I$  at the cessation of shear ( $t =$

10 s) exhibited by the 1 wt % HDPE blend indicates the presence of oriented structures. The largest apparent birefringence values reached at long times subsequent to shear were not much greater than melt birefringence during flow. This represents a stark contrast to prior literature on bimodal blends with a small concentration of long chains in a matrix of chain that have similar very low chain defect content (i.e., stereo-errors in isotactic polypropylene, iPP, or comonomer in PE) has shown that the creation of oriented structures during flow templates highly oriented growth after cessation of flow.<sup>38, 46, 55-57</sup> In these previous systems, the birefringence often increases much more than ten times relative to the birefringence that remains after cessation of shear. Additionally, the shape of the birefringence curve at long time is dissimilar to highly crystalline systems undergoing FIC (e.g., Figure B.3 in thesis Appendix B). Highly oriented growth is generally characterized by rapidly increasing  $I_{perp}/I$  subsequent to shear with a rate of change that increases with time as oriented structures propagate; the slope,  $dI_{perp}/dt$ , only decreases when the sample retardance,  $\delta$ , approaches  $\pi/2$  due to its sinusoidal dependence.<sup>56</sup> In contrast, at approximately 200 s, the apparent birefringence of the 1 wt % HDPE shows a distinct decrease in slope even though  $\delta \ll 1$ ; this decrease in slope was apparent for all samples displaying non-zero birefringence following shear.

$H_v$  SALS images confirmed mild oriented growth in both blends. Similar to quiescent crystallization, the 0.5 wt % blend did not exhibit  $H_v$  scattering until after an induction period of approximately 420 s. At this point, a very light streak normal to the shear direction could be observed corresponding to long, slender scattering objects aligned parallel to the flow direction.<sup>52, 58, 59</sup> This streak persisted for a short time (less than 480 s) after which a very light 4-lobe pattern could be observed. The 1 wt % blend

exhibited both a streak and isotropic scattering immediately following shear. As time progressed, this streak became dominated by isotropic scattering.

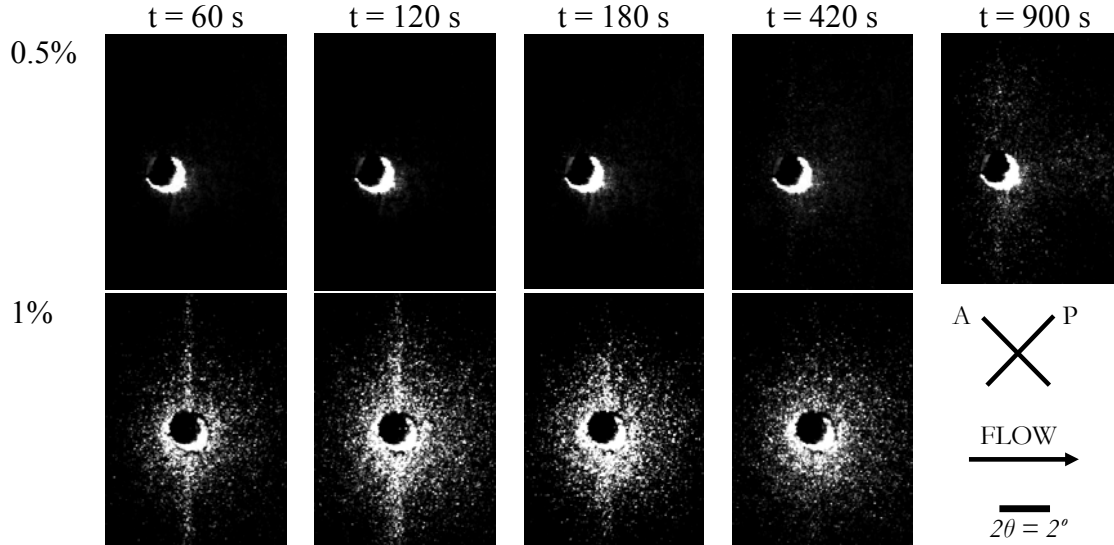


**Figure 5.16**  $H_v$  SALS images collected subsequent to shear at  $98^\circ\text{C}$ ,  $\sigma_w = 0.14 \text{ MPa}$  for  $t_s = 10 \text{ s}$ .

### 5.3.2.2 X-ray Characterization

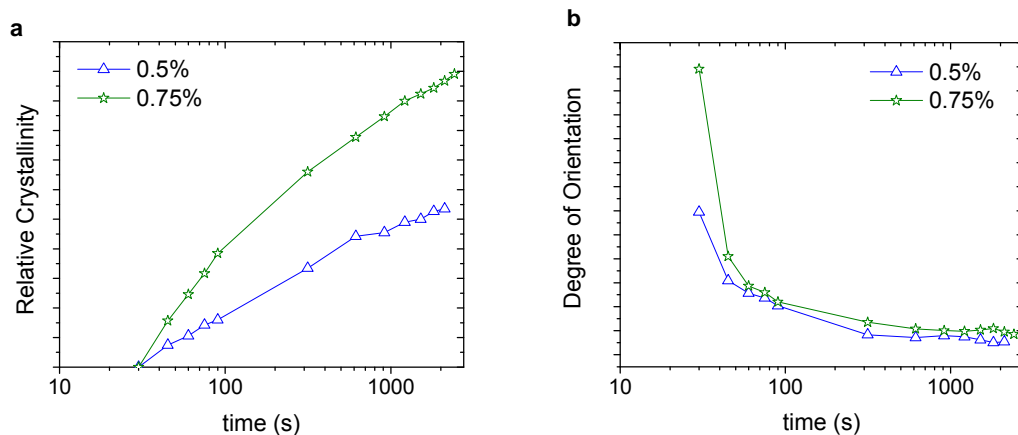


**Figure 5.17** **a)** Relative crystallinity (measured as (110) peak intensity) and **b)** degree of orientation (measured as the second harmonic of Fourier transform of intensity versus azimuthal angle) for crystallization of HDPE subsequent to shear at  $95^\circ\text{C}$ ,  $\sigma_w = 0.09 \text{ MPa}$ ,  $t_s = 15 \text{ s}$ .

The surprisingly low levels of oriented crystallization of these materials despite evidence that oriented precursors were formed during shear was apparent in x-ray scatter-

ing results. SAXS patterns did not exhibit significant anisotropy, in contrast to the oriented lobes in the SAXS patterns typically observed in highly crystalline systems following flow (not shown).<sup>4, 39, 60-62</sup> WAXS intensity also exhibited very little azimuthal dependence. Furthermore, the degree of orientation quickly decreased during the first minute of crystallization while crystallinity continued to increase (Figure 5.17).

## 5.4 DISCUSSION

### 5.4.1 Quiescent Crystallization

#### 5.4.1.1 Nucleation Effects

High density polyethylene (HDPE) was found to serve as a nucleating agent in the ethylene-co-hexene (EH50) matrix, as has been similarly observed in other polyethylene systems.<sup>28, 63</sup> Enhanced crystallization kinetics were observed by DSC (Figure 5.4), optical transmittance (Figure 5.5), and x-ray scattering (Figure 5.13). At the concentrations examined ( $c < 1$  wt % HDPE), an increase in HDPE concentration resulted in an increase in crystallization kinetics.<sup>28, 64</sup> Furthermore, this nucleation effect was insensitive to thermal history when the HDPE concentration was below overlap ( $c < c^* \approx 0.6$  wt %), but was dependent on thermal history for blends having a concentration of HDPE that is above its overlap concentration ( $c > c^*$ ).

In DSC nucleation studies, the 0.5 wt % blend ( $c < c^* \approx 0.6$  wt %) exhibited little change in response to hold times of up to 5 min at both 105 and 100 °C. On the other hand, crystallization kinetics of the 1 wt % blend exhibited much stronger dependence on hold time at elevated temperatures. An order of magnitude decrease in peak crystalliza-

tion time was observed following a hold of 3 min at 100 °C compared to  $t_{\text{hold}} = 0$  min. At these intermediate temperatures, HDPE is highly supercooled (31 °C and 36 °C below the peak melting point of neat HDPE). On the other hand, neat EH50 is incapable of crystallization on short time scales (peak melting temperature 96 °C), and hence, crystal nuclei are predominantly composed of HPDE chains.

When the amount of HDPE is below the overlap concentration, crystallization of HPDE at intermediate temperatures of 100 and 105 °C is limited by the diffusion of HDPE chains to the growth front. This results in HDPE nucleating structures that are sparse, compact, and isolated; one can envision nucleated HDPE structures that are surrounded by region depleted of HDPE chains. On the other hand, at concentrations above overlap, HDPE crystals can readily propagate through the melt forming a network of nucleating structures. Overlap concentration of a slow-relaxing species is known to be important in bimodal systems undergoing flow-induced crystallization (FIC).<sup>39, 65-68</sup> In FIC, concentration of slow-relaxing species in a bimodal blend is important due to differences in melt dynamics, which dictate the response of the system to flow. However, to the best of our knowledge, this is the first time a non-linear concentration dependence of crystallization kinetics on a slow-relaxing species has been observed for quiescent crystallization; in fact, in contrast to observations here, iPP blends (which consist of components that are equally subcooled) exhibit nearly identical turbidity traces during isothermal crystallization, independent of whether high-molecular weight chains (slow-relaxing species) are above overlap or completely absent.<sup>61</sup> The difference in behavior observed here arises from the different degrees of subcooling for the two components examined here; under quiescent conditions, crystallization of the HDPE/EH50 blends is dictated by both the

difference between the melting temperature of the two species and the diffusivity of the crystallizable chains. Therefore, systems utilizing a semicrystalline polymer as a nucleating agent are expected to exhibit a complex dependence on nucleant concentration, relative comonomer content, relative relaxation time, and thermal and flow histories.

#### 5.4.1.2 Morphology Evolution

Neat EH50 was found to be incapable of multi-lamellar structure formation under the conditions examined. At 98 °C, it crystallized slowly (only after approximately 30 min), forming short, randomly oriented lamellae (Figure 5.14a). The lack of multi-lamellar structure was apparent from the isotropic  $H_v$  SALS patterns (Figure 5.6a).

The minima in optical transmittance curves (Figure 5.7) and the 4-lobe patterns in  $H_v$  SALS images exhibited by HDPE/EH50 blends (Figure 5.8) have previously been attributed to spherulite formation when observed during isothermal crystallization of polyethylene.<sup>49, 50, 54</sup> In past studies, the 4-lobe pattern in  $H_v$  scattering arose from the optical anisotropy of a polyethylene spherulite (resulting from different indices of refraction along the axes of the orthorhombic unit cell<sup>69</sup>).<sup>52</sup> The difference between the onset of the decrease in light transmittance and the onset of significant  $H_v$  scattering has been explained by a low level of anisotropy in the initial crystal structures, either as a consequence of low crystallinity or low orientation correlation among crystals.<sup>49</sup> The minimum in transmittance has been interpreted as the point at which spherulites fill 50% of the available volume as a consequence of the dependence of light scattering on the difference in the index of refraction and the amount of the scattering entities (spherulites) and the surrounding medium (melt).<sup>49, 50, 54</sup> Following this point, the transmittance increases due to the increasing size of the spherulites; an increase in size of scattering objects results in

the contraction of the scattering pattern leading to more scattering at lower angles near 0°, and hence, more light entering the photodetector.<sup>50</sup> A difference in optical behavior between these previous studies and the present study is the transmittance following spherulite impingement. Here the transmittance values decline, whereas in the previous studies, transmittance stabilized at a constant value that corresponded to the orientation correlations (anisotropy) within the spherulite.<sup>50</sup> However, present materials are distinguished by the conspicuous absence of spherulitic structure when examined using either polarized light optical microscopy (POM), which would detect spherulites on lengths scales greater than a micron, or using electron microscopy, which would detect submicron-sized spherulites in these HDPE/EH50 blends (Figure 5.10b and Figure 5.14b).

Three-dimensional spherulites are not able to propagate at 95 or 98 °C due to the limited amount of crystallizable material (i.e., small concentrations of HDPE and limited number of ethylene sequences of sufficient length in EH50). Instead, we envision two-dimensional growth, or discs (Figure 5.18), which, when randomly oriented, also give a 4-lobe  $H_v$  scattering pattern.<sup>70-72</sup> The difference in the time between the onset of the drop in transmittance and the onset of  $H_v$  scattering can again be explained by low anisotropy of the initial scattering particles (Figure 5.18a). Likewise, the minimum in transmittance and the accompanying appearance of the 4-lobe pattern can be attributed to half-space-filling of the anisotropic, randomly-oriented, stacks of discs (Figure 5.18b). As the number of discs in a stack increases, the anisotropy of the system increases, resulting in an increase in  $H_v$  scattering.

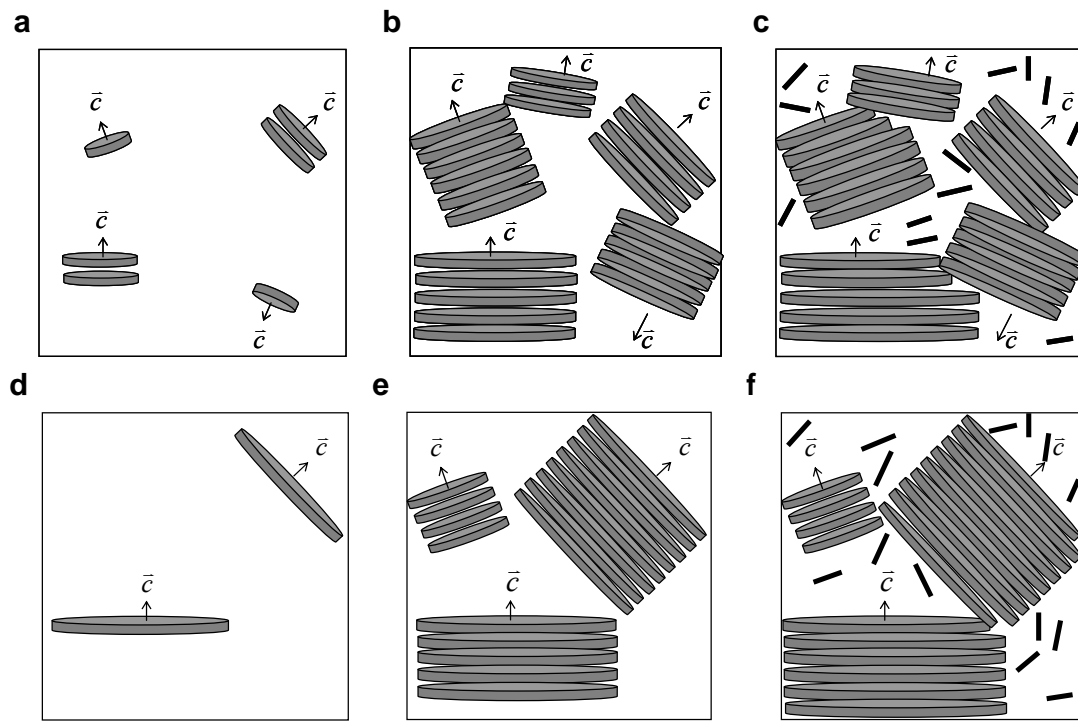


**Figure 5.18** Schematic representation of isothermal crystallization of 0.5 and 1 wt % HDPE blends before the minimum in transmittance (a and d, respectively), after minimum in transmittance (b and e, respectively), and at long times when transmittance decreases (c and f, respectively). Vector  $c$  indicates direction of chain axis.

The presence of stacks, as indicated by high degree of local orientation in STEM micrographs (Figure 5.14b), is likely the consequence of HDPE templating, which has been previously observed under shear.<sup>46, 68</sup> In this scenario, the initial discs that form dictate the surrounding orientation distribution since only the crystal structures oriented roughly parallel to the initial discs can propagate. Similar to the case of spherulitic morphology, scattering at zero angle increases as the stacks of discs grow in size, resulting in an increase in transmittance. A constant value of transmittance is not reached at long times because total impingement of crystal structures is not achieved. Instead, transmittance decreases as  $H_v$  scattering increases both at and between the ‘lobes,’ consistent with the growth of randomly oriented lamellae that occur in neat EH50 (Figure 5.18c).

The HDPE/EH50 blend containing HDPE concentration above overlap ( $c = 1 \text{ wt \%} > c^* \approx 0.6 \text{ wt \%}$ ) follows a similar evolution of a 4-lobe pattern as the 0.5 wt % blend ( $c < c^*$ ) but starting from isotropic  $H_v$  scattering upon reaching  $T_c = 98 \text{ }^\circ\text{C}$ , which indicates crystallization of the blend during cooling. The fact that the initial scattering pattern is isotropic rather than 4-lobe means that the initial scattering entities are large but not arranged in stacks of discs. Instead, one can envision isolated, unilamellar discs, approximately 15 nm thick (from SAXS) and 1  $\mu\text{m}$  in diameter, composed primarily of HDPE (Figure 5.18d). Since HDPE concentration is above overlap and chain diffusion limitations are reduced, HDPE chains can rapidly form nuclei and the growth front can advance more rapidly compared to the 0.5 wt % blend, resulting in crystallization during cooling ( $\sim 8 \text{ }^\circ\text{C/min}$ ). Hence, crystallization of the 1 wt % blend occurs at higher temperatures, leading to increased amounts of crystallization-induced phase separation. Although STEM images for the 1 wt % blend were not available, one can envision them to be intermediate between Figure 5.14b and Figure 5.14c, corresponding to the 0.5 and 5 wt % HDPE blends, respectively. Similar to the latter, the 1 wt % HDPE blend likely contains some large lamellae that do not template the surrounding crystallites; hence, they contribute to isotropic  $H_v$  scattering. However, the appearance of a 4-lobe  $H_v$  SALS pattern indicates that the 1 wt % HDPE blend still contains templated regions in which stacks of lamellar discs can be found (Figure 5.18 e and f).

Blends containing HDPE exhibited increased clarity with increasing HDPE content at long times during isothermal crystallization. Since the sample is contained between two windows, surface effects are negligible and the clarity is only a function of bulk optical transmittance. The clarifying effect of nucleating agents has been observed

previously in spherulitic iPP systems, in which the clarifying effect was attributed to a decrease in spherulite size and a decrease in their scattering effectiveness with increasing nucleation density.<sup>64</sup> Highly crystalline systems, such as iPP and HPDE, are turbid due to large, closely-packed spherulites. EH50 has higher clarity than such highly crystalline systems because it does not organize into multi-lamellar structures. However, an intermediate amount of order, such as that in HDPE/EH50 blends, results in a further increase of sample clarity, which is important for the production of plastic films.<sup>29</sup>

#### 5.4.2 Flow-Induced Crystallization

The interplay between defect-free HDPE chains and a defect-ridden copolymer matrix results in morphology evolution that is not commonly encountered in FIC of semicrystalline systems. Blends containing 0.5 and 1 wt % HDPE exhibited several unusual optical behaviors subsequent to flow (Figure 5.15a): (1) the transmittance of the 1 wt % HDPE blend increased during the shear pulse, (2) the transmittance at long times of the 1 wt % blend was lower for the sheared case than the quiescent case, while (3) the transmittance of the 0.5 wt % blend was higher compared with the quiescent case.

Initial crystal structures in both blends nucleate/template crystal growth at longer times. Flow can both alter the orientation distribution of structures formed during cooling and induce the formation of additional precursors. The orientation distribution of structures within the system at the cessation of flow will affect the orientation distribution of crystallites that propagate from the initial structures at later times. As mentioned previously, crystallization of the 1 wt % blend during cooling resulted in the formation of large crystals that were capable of scattering light (Figure 5.18d). Hence, the orientation of

these large, platelet-like crystals by flow resulted in a strong increase in transmittance (the increase in transmittance was not the result of crystal destruction, as confirmed by WAXS—not shown). This behavior is reminiscent of increased transmittance following the elongation of polymer films.<sup>50</sup> In the present case, this increase in transmittance can be explained by the specific orientation of the platelet-shaped crystals by shear flow. In previous studies, platelet-like particles have been observed to be oriented such that their surface normal ( $\bar{c}$  in Figure 5.19 corresponding to the chain axis) is nearly parallel to the velocity gradient direction ( $\nabla \mathbf{v}$ ),<sup>73-76</sup> which in the current system corresponds to the direction of light through the sample (Figure 5.19). Prior to shear, the random orientation of discs results in scattering arising from the difference between refractive indices along the three unit cell axes ( $a$ ,  $b$ , and  $c$  with refractive indices of 1.514, 1.519, and 1.575, respectively)<sup>69</sup> and the polyethylene melt (refractive index of approximately 1.49).<sup>77</sup> Subsequent to shear, the  $c$ -axis is aligned along the light path (Figure 5.19); hence, the contrast in refractive indices that is probed is reduced to 1.514 and 1.519 for the crystallites—quite close to that of the melt (1.49) so the transmittance increases.

Although an increase in transmittance is not observed during shear of the 0.5 wt % HDPE blend, DSC nucleation studies indicate that some structure formation in this blend is expected during cooling. However, at short crystallization times, these structures are too small to scatter light (Figure 5.18a). Evidence for their orientation is not apparent until long times when they have increased in size, resulting in increased transmittance of the sheared 0.5 wt % blend compared with the quiescent case.

In addition to orientation of pre-existing crystals, application of shear to the 1 wt % blend results in oriented nuclei formation (evident from apparent birefringence in

Figure 5.15b and streak in the  $H_v$  SALS pattern in Figure 5.16). Scattering from these cylindrical objects results in a large increase in turbidity of the sample due to the fact that their  $c$ -axis is oriented parallel to the direction of flow. This effect offsets the increase in transmittance from the orientation of pre-existing platelet-like crystals resulting in a decrease in transmittance relative to the quiescent case of the 1 wt % HDPE blend.

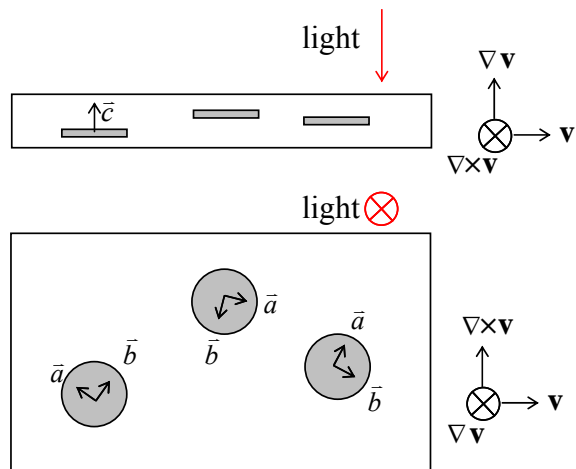


**Figure 5.19** Schematic representation of orientation of lamellar discs by flow.

HDPE/EH50 blends did not exhibit the strong response to flow-induced crystallization (FIC) typical of more crystalline systems.<sup>4, 39, 46, 60-62, 67, 78, 79</sup> While this is expected at HDPE concentrations below overlap ( $c < c^*$ ) where slow-relaxing species (here, HPDE chains) are not effective at triggering oriented nuclei formation,<sup>65, 66, 80</sup> it was surprising that 0.75 wt % and 1 wt % blends ( $c > c^*$ ) also did not exhibit evidence of a dominant oriented morphology. Instead, the behavior of the latter blends suggests two crystallization regimes: (1) oriented structure propagation at short times following shear and (2) isotropic crystal growth at longer times.

At short times ( $t < 200$  s), HDPE/EH50 blends exhibited evidence of oriented growth in the form of a rapidly increasing apparent birefringence trace that began from a

non-zero value following shear (Figure 5.15b), a streak in the  $H_v$  scattering pattern (Figure 5.16), and an elevated degree of orientation in the WAXS images (Figure 5.17). Following 200 s, however, oriented growth appeared to have stopped. In contrast to more crystalline systems (see, for example, Figure B.3), the slope in  $I_{perp}/I$  dropped to a smaller, almost constant value. This change coincided with the poorly-defined minimum in the corresponding transmittance curve. A small increase in transmittance following the minimum is consistent with a lack of significant increase in the size of oriented structures. Further evidence that the growth front from the oriented precursors halts its advance is the absence of a contraction of the scattering patterns.<sup>50, 81</sup> Additionally, following the break in the rate of oriented growth,  $H_v$  SALS patterns developed significant isotropic scattering and the WAXS degree of orientation drastically decreased due to an increase in isotropic scattering.

The transition to isotropic scattering is a consequence of the copolymer base matrix. As oriented structures propagate, the longest ethylene sequences of EH50 are incorporated into the crystal. However, along with these crystallizable sequences, defects in the form of short-chain branches are also encountered. As more and more defects are crowded at the growth front, the crystal structures cease to grow and crystallization can only continue from newly-formed point-like nuclei in the melt. Therefore, the incorporation of the copolymer matrix into the oriented crystals pollutes the growth front, limiting the size of the oriented structures. This reasoning is similar to the explanation for the deterioration of morphology observed with increased SCB content of copolymers during quiescent crystallization.<sup>19</sup> Consequently, one could conjecture that the lateral dimensions of crystal structures can be manipulated by controlling the length of ethylene sequences

consumed by the growth front (i.e., number of short-chain branches encountered), which, in turn, can be achieved by changing the temperature of crystallization (Figure 5.20).

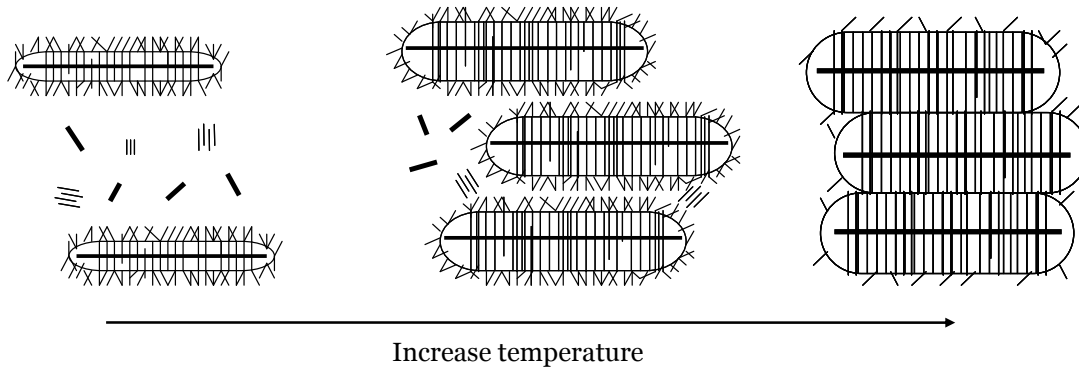


**Figure 5.20** Schematic representation of the varying extent of oriented growth as a consequence of comonomer incorporation as dictated by temperature.

In agreement with this theory is the study by Hsiao et al. on bimodal blends composed of a linear ultrahigh molecular weight polyethylene (UHMWPE) at a low concentration ( $c = 2 \text{ wt \%} > c^*$ ) in a short-chain-branched matrix.<sup>82</sup> This previous study revealed the propagation of large oriented shish-kebab structures following shear at elevated temperatures, at which the major, short-chain branched component could not crystallize.

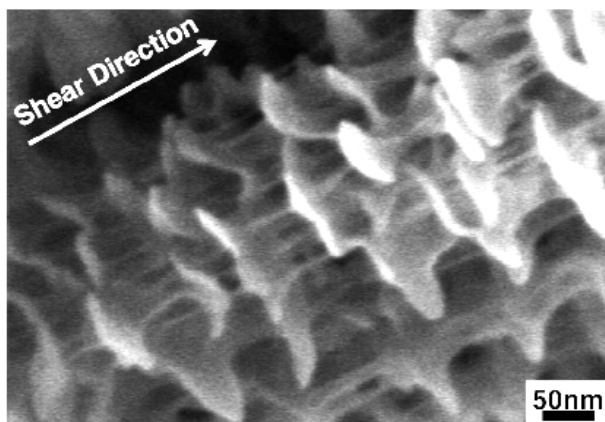


**Figure 5.21** Shish-kebab structure observed subsequent to flow of a blend containing 2 wt % UHMWPE in a non-crystallizable PE. (Reprinted Fig. 3 with permission from Hsiao, B.S., et al. Phys. Rev. Lett. Vol. 94, 117802, 2005. Copyright (2005) by the American Physical Society).

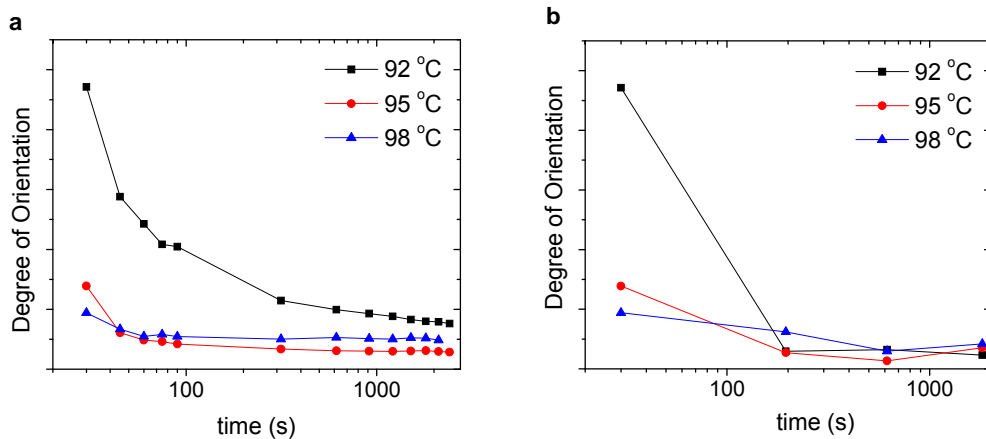


**Figure 5.22** Evolution of degree of orientation of 0.75 wt % HDPE blend subsequent to shear at  $\sigma_w = 0.09$  MPa for  $t_s = 15$  s at different temperatures for **a**) full scattering patterns and **b**) differential scattering patterns.

Our theory was further confirmed by examining the degree of orientation of the 0.75 wt % blend at three different temperatures: 92, 95, and 98 °C (Figure 5.22a). The lowest temperature exhibited the greatest degree of orientation as more EH50 material could crystallize due the decrease in the required ethylene sequence length; only a small amount of orientation was evident at the highest crystallization temperature. For all three temperatures, a rapid decrease in WAXS anisotropy was observed. Further investigation into this evolution of WAXS anisotropy was conducted using the differential analysis developed by Hajimorad et al.<sup>45</sup> The relative degree of orientation was calculated for WAXS patterns that developed between the four time points of interest: (1)  $0 < t_c < 30$  s, (2)  $30 < t_c < 195$  s, (3)  $195 < t_c < 615$  s, and (4)  $615 < t_c < 1815$  s. Crystallization occurring within 30 s of shear was characterized by the greatest degree of orientation (Figure 5.22b). At the two lower temperatures, 92 and 95 °C, anisotropy of subsequent crystallization (immediately following  $t = 30$  s) was substantially diminished. In contrast, the an-

sotropy of crystallization at 98 °C was nearly constant from 0 to 195 s consistent with less pollution of the oriented growth front at the elevated temperature.

Not surprisingly, temperature affects more than simply the amount of EH50 that can crystallize. The large difference between the melting points of ethylene copolymers and branch-free PE chains, which are necessary to ensure formation of oriented nuclei, leads to a significant amount of material that is already crystalline upon reaching  $T_c$  in this system resulting in poor control of initial system morphology. In future work, a potential means to circumvent difficulties regarding oriented nuclei formation is to utilize a system with embedded oriented fibers that can serve as well controlled (size and amount) oriented nuclei. This will allow one to utilize instruments having better temperature control which are not limited by large thermal mass. Rapid cooling in addition to examination of materials having slightly less comonomer content may decrease crystallization-induced phase separation and allow for proper control of the initial morphology.

## 5.5 CONCLUSION

Crystallization of an ethylene-copolymer (EH50) was examined in the presence of small concentrations ( $c < 5$  wt %) of a high density polyethylene (HDPE) both under quiescent conditions and subsequent to flow at temperatures where both blend components could crystallize. These multimodal systems may be encountered in industry both by specific blending and through specific synthetic routes to metallocene copolymers. Due to the difference in melting point between the two materials as a consequence of short-chain branching, HDPE proved to be an effective nucleating agent. Furthermore, due to its semicrystalline nature and its ability to organize into super molecular structures, the ef-

fectiveness of HDPE as a nucleant was found to be sensitive to thermal history above its overlap concentration ( $c > c^*$ ).

HDPE also proved to be an effective clarifying agent. Small concentrations ( $c < 1$  wt %) of HDPE resulted in high clarity samples at long crystallization times. This was a consequence of a change in morphology from randomly distributed lamellae (without HDPE) to stacks of lamellae having local orientation (with small amounts of HDPE). The clarifying effect was evident both under isothermal conditions and subsequent to shear.

HDPE/EH50 blends containing 1 wt % HDPE or less exhibited surprisingly little response to shear in contrast to more crystalline isotactic polypropylene (iPP) and HDPE systems. Evidence of a dominant oriented morphology was not observed. Instead, the samples exhibited two crystallization regimes: (1) oriented growth at short times following shear and (2) isotropic growth at long times following shear. The transition between the two regimes appears to be a consequence of the incorporation of ethylene sequences into the oriented structures which results in a build up of short-chain branches (i.e., defects) and a pollution of the growth front. At later times, the oriented growth front is extinguished by the tethered copolymer. Subsequent growth requires new nuclei to form; since the remaining melt is fully relaxed at these long times, point-like nuclei form and the subsequent growth is isotropic.

We propose that this behavior can be exploited to control the lateral dimensions of the oriented structures by controlling the incorporation of ethylene sequences, which, in turn, is dictated by temperature. The ability to precisely control the size of morphological features in semicrystalline systems would enable more accurate tuning of the ultimate physical properties.

## 5.6 ACKNOWLEDGEMENTS

This work would not have been possible without ExxonMobil Research and Engineering Company, particularly Dr. David Lohse, Dr. Manika Varma-Nair, Dr. Andrew Tsou and the rest of the team, who provided materials, financial support, experimental assistance, and fruitful discussions. Additionally, we thank Dr. John Stuyver and Dr. Anton-Jan Bons (ExxonMobil, Machelen, Belgium) for providing STEM images. We would like to thank Dr. Soo-Young Park (Kyunpook National University, Daegu, South Korea) for conducting DSC studies. We must thank the beamline staff at beamline X27C at NSLS BNL (Dr. Lixia Rong and Jie Zhu) and BM26 DUBBLE at ESRF (Dr. Wim Bras, Dr. Kristina Kvanshnina, Dr. Giuseppe Portale, and Dirk Detollenaere). X-ray scattering experiments were conducted with the help of Dr. Lucia Fernandez Ballester (ESRF, DUBBLE, Grenoble, France), Dr. Timothy Gough (University of Bradford, UK), Dr. Fernando Ania, and Dr. Araceli Flores (Instituto de Estructura de la Materia, Madrid, Spain). Part of this work was also funded by the National Science Foundation (DMR-0505393 and GOALI-0523083). Manuscript preparation was aided by Prof. Julia Kornfield and Mary Louie (Caltech).

## 5.7 REFERENCES

1. Mirabella, F. M., Correlation of the melting behavior and copolymer composition distribution of Ziegler-Natta-catalyst and single-site-catalyst polyethylene copolymers. *Journal of Polymer Science Part B-Polymer Physics* **2001**, 39, (22), 2800-2818.
2. Galante, M. J.; Mandelkern, L.; Alamo, R. G.; Lehtinen, A.; Paukkeri, R., Crystallization kinetics of metallocene type polypropylenes - Influence of molecular weight and comparison with Ziegler-Natta type systems. *Journal of Thermal Analysis* **1996**, 47, (4), 913-929.
3. Malmberg, A.; Kokko, E.; Lehmus, P.; Lofgren, B.; Seppala, J. V., Long-chain branched polyethylene polymerized by metallocene catalysts  $\text{Et}[\text{Ind}](2)\text{ZrCl}_2/\text{MAO}$  and  $\text{Et}[\text{IndH}(4)](2)\text{ZrCl}_2/\text{MAO}$ . *Macromolecules* **1998**, 31, (24), 8448-8454.
4. Agarwal, P. K.; Soman, R. H.; Weng, W.; Mehta, A.; Yang, L.; Ran, S.; Liu, L.; Hsiao, B. S., Shear-Induced Crystallization in Novel Long Chain Branched Polypropylenes by in Sity Rheo-SAXS and -WAXD. *Macromolecules* **2003**, 36, 5226-5235.
5. Shiono, T.; Azad, S. M.; Ikeda, T., Copolymerization of atactic polypropene macro-monomer with propene by an isospecific metallocene catalyst. *Macromolecules* **1999**, 32, (18), 5723-5727.
6. Mehdiabadi, S.; Soares, J. B. P.; Dekmezian, A. H., Production of Long-Chain Branched Polyolefins with Two Single-Site Catalysts: Comparing CSTR and Semi-Batch Performance. *Macromolecular Reaction Engineering* **2008**, 2, (6), 529-550.
7. Schwerdtfeger, E. D.; Irwin, L. J.; Miller, S. A., Highly branched polyethylene from ethylene alone via a single zirconium-based catalyst. *Macromolecules* **2008**, 41, (4), 1080-1085.
8. Lofgren, B.; Kokko, E.; Seppala, J., Specific structures enabled by metallocene catalysis in polyethenes. In *Long-Term Properties of Polyolefins*, Springer-Verlag Ber-

lin: Berlin, 2004; Vol. 169, pp 1-12.

9. Wang, C.; Chu, M. C.; Lin, T. L.; Lai, S. M.; Shih, H. H.; Yang, J. C., Microstructures of a highly short-chain branched polyethylene. *Polymer* **2001**, 42, (4), 1733-1741.
10. Chiu, F. C.; Wang, Q.; Fu, Q.; Honigfort, P.; Cheng, S. Z. D.; Hsiao, B. S.; Yeh, F. J.; Keating, M. Y.; Hsieh, E. T.; Tso, C. C., Structural and morphological inhomogeneity of short-chain branched polyethylenes in multiple-step crystallization. *Journal of Macromolecular Science-Physics* **2000**, B39, (3), 317-331.
11. Zhang, F. J.; Liu, J. P.; Xie, F. C.; Fu, Q.; He, T. B., Polydispersity of ethylene sequence length in metallocene ethylene/alpha-olefin copolymers. II. Influence on crystallization and melting behavior. *Journal of Polymer Science Part B-Polymer Physics* **2002**, 40, (9), 822-830.
12. Xu, J. T.; Li, B. T.; Fan, Z. Q.; Ryan, A. J., Simultaneous SAXS/WAXS/DSC studies on microstructure of conventional and metallocene-based ethylene-butene copolymers. *Chinese Journal of Polymer Science* **2004**, 22, (3), 279-287.
13. Perez, E.; Benavente, R.; Quijada, R.; Narvaez, A.; Galland, G. B., Structure characterization of copolymers of ethylene and 1-octadecene. *Journal of Polymer Science Part B-Polymer Physics* **2000**, 38, (11), 1440-1448.
14. Stadler, F. J.; Takahashi, T.; Yonetake, K., Crystallite dimensions - characterization of ethene-/alpha-olefin Copolymers with various comonomers and comonomer Ccontents measured by small- and wide angle X-ray scattering. *E-Polymers* **2009**, 19.
15. Bubeck, R. A., Structure-property relationships in metallocene polyethylenes. *Materials Science and Engineering R* **2002**, 39, 1-28.
16. Cerrada, M. L.; Benavente, R.; Perez, E., Influence of thermal history on morphology and viscoelastic behavior of ethylene-1-octene copolymers synthesized with metallocene catalysts. *Journal of Materials Research* **2001**, 16, (4), 1103-1111.

17. Peeters, M.; Goderis, B.; Vonk, C.; Reynaers, H.; Mathot, V., Morphology of Homogeneous Copolymers of Ethene and 1-Octene. I. Influence of Thermal History on Morphology. *Journal of Polymer Science: Part B: Polymer Physics* **1997**, 35, 2689-2713.
18. Krishnaswamy, R. K.; Yang, Q.; Fernandez-Ballester, L.; Kornfield, J. A., Effect of the distribution of short-chain branches on crystallization kinetics and mechanical properties of high-density polyethylene. *Macromolecules* **2008**, 41, (5), 1693-1704.
19. Bensason, S.; Minick, J.; Moet, A.; Chum, S.; Hiltner, A.; Baer, E., Classification of Homogeneous Ethylene-Octene Copolymers Based on Comonomer Content. *Journal of Polymer Science: Part B: Polymer Physics* **1996**, 34, 1301-1315.
20. Alamo, R.; Domszy, R.; Mandelkern, L., Thermodynamic and Structural-Properties of Copolymers of Ethylene. *Journal of Physical Chemistry* **1984**, 88, (26), 6587-6595.
21. Alamo, R. G.; Viers, B. D.; Mandelkern, L., Phase-Structure of Random Ethylene Copolymers - a Study of Coint Content and Molecular-Weight as Independent Variables. *Macromolecules* **1993**, 26, (21), 5740-5747.
22. Alizadeh, A.; Richardson, L.; Xu, J.; McCartney, S.; Marand, H.; Cheung, Y. W.; Chum, S., Influence of Structural and Topological Constraints on the Crystallization and Melting Behavior of Polymers. 1. Ethylene/1-Octene Copolymers. *Macromolecules* **1999**, 32, 6221-6235.
23. Richardson, M. J.; Flory, P. J.; Jackson, J. B., Crystallization and Melting of Copolymers of Polymethylene. *Polymer* **1963**, 4, (2), 221-236.
24. Alamo, R. G.; Mandelkern, L., Thermodynamic and Structural-Properties of Ethylene Copolymers. *Macromolecules* **1989**, 22, (3), 1273-1277.
25. Adhikari, R.; Godehardt, R.; Lebek, W.; Frangov, S.; Michler, G. H.; Radusch, H.; Calleja, F. J. B. In *Morphology and micromechanical properties of ethylene/1-octene copolymers and their blends with high density polyethylene*, 2005; John Wiley &

Sons Ltd: 2005; pp 156-166.

26. Adhikari, R.; Godehardt, R.; Lebek, W.; Michler, G. H., Blends of High Density Polyethylene and Ethylene/1-Octene Copolymers: Structure and Properties. *Journal of Applied Polymer Science* **2007**, 103, 1887-1893.
27. Bensason, S.; Nazarenko, S.; Chum, S.; Hiltner, A.; Baer, E., Blends of homogeneous ethylene-octene copolymers. *Polymer* **1997**, 38, (14), 3513-3520.
28. Song, S. J.; Wu, P. Y.; Ye, M. X.; Feng, J. C.; Yang, Y. L., Effect of small amount of ultra high molecular weight component on the crystallization behaviors of bimodal high density polyethylene. *Polymer* **2008**, 49, (12), 2964-2973.
29. Ommundsen, E.; Skar, M.; Nord-Varhaug, K. Nucleating Agent. 2007.
30. Andreassen, E.; Larsen, A.; Nord-Varhaug, K.; Skar, M.; Oysaed, H., Haze of Polyethylene Films -- Effects of Material Parameters and Clafifying Agents. *Polymer Engineering and Science* **2002**, 42, (5), 1082-1097.
31. Rubinstein, M.; Colby, R. H., *Polymer Physics*. Oxford University Press: New York, 2003.
32. Nogales, A.; Hsiao, B. S.; Soman, R. H.; Srinivas, S.; Tsou, A. H.; Balta-Calleja, F. J.; Ezquerra, T. A., Shear-induced crystallization of isotactic polypropylene with different molecular weight distributions: in situ small- and wide-angle X-ray scattering studies. *Polymer* **2001**, 42, (12), 5247-5256.
33. deGennes, P.-G., *Scaling Concepts in Polymer Physics*. Cornell University Press: Ithica, NY, 1979.
34. Takahashi, Y.; Isono, Y.; Noda, I.; Nagasawa, M., Zero-Shear Viscosity of Linear Polymer Solutions over a Wide Range of Concentration. *Macromolecules* **1985**, 18, (5), 1002-1008.
35. Schelten, J.; Ballard, D. G. H.; Wignall, G. D.; Longman, G.; Schmatz, W., Small-Angle Neutron-Scattering Studies of Molten and Crystalline Polyethylene. *Polymer*

1976, 17, (9), 751-757.

36. Lieser, G.; Fischer, E. W.; Ibel, K., Conformation of Polyethylene Molecules in Melt as Revealed by Small-Angle Neutron-Scattering. *Journal of Polymer Science Part C-Polymer Letters* **1975**, 13, (1), 39-43.

37. Kumaraswamy, G.; Verma, R. K.; Kornfield, J. A., Novel flow apparatus for investigating shear-enhanced crystallization and structure development in semicrystalline polymers. *Review of Scientific Instruments* **1999**, 70, (4), 2097-2104.

38. Liedauer, S.; Eder, G.; Janeschitz-Kriegl, H.; Jerschow, P.; Geymayer, W.; Ingolic, E., On the kinetics of shear-induced crystallization in polypropylene. *International Polymer Processing* **1993**, 8, (3), 236-244.

39. Keum, J. K.; Zuo, F.; Hsiao, B. S., Probing the flow-induced shish-kebab structure in entangled polyethylene melts by synchrotron X-ray scattering. *Journal of Applied Crystallography* **2007**, 40, (Supplement), s48-s51.

40. Macosko, C. W., *Rheology: Principles, Measurements, and Applications*. VCH: New York, 1994.

41. The author would like to thank Dr. Lixia Rong and Jie Zhu with beamline assistance. Additionally, the author thanks Dr. Lucia Fernandez Ballester and Dr. Timothy Gough for experimental assistance.

42. The author would like to thank beamline staff Dr. Wim Bras, Dr. Kristina Kvanshnina, Dr. Giuseppe Portale, and Dirk Detollenaere among others for their support. Additional experimental assistance was provided by Dr. Lucia Fernandez Ballester, Dr. Timothy Gough, Dr. Fernando Ania, and Dr. Araceli Flores.

43. Cser, F., About the Lorentz correction used in the interpretation of small angle X-ray scattering data of semicrystalline polymers. *Journal of Applied Polymer Science* **2001**, 80, (12), 2300-2308.

44. Aggarwal, S. L.; Tilley, G. P., Determination of Crystallinity in Polyethylene by X-

Ray Diffractometer. *Journal of Polymer Science* **1955**, 18, (87), 17-26.

45. Hajimorad, M.; Smirnova, D.; Kornfield, J., *Manuscript in preparation*. **2009**.

46. Langouche, F., Orientation deveopment during shear flow-induced crystallization of i-PP. *Macromolecules* **2006**, 39, 2568-2573.

47. Baert, J.; Van Puyvelde, P.; Langouche, F., Flow-induced crystallization of PB-1: From the low shear rate region up to processing rates. *Macromolecules* **2006**, 39, (26), 9215-9222.

48. Ding, Z. M.; Spruiell, J. E., An experimental method for studying nonisothermal crystallization of polymers at very high cooling rates. *Journal of Polymer Science Part B-Polymer Physics* **1996**, 34, (16), 2783-2804.

49. Akpalu, Y.; Kielhorn, L.; Hsiao, B. S.; Stein, R. S.; Russell, T. P.; Egmond, J. v.; Muthukumar, M., Structure Development during Crystallization of Homogeneous Copolymers of Ethene and 1-Octene: Time-Resolved Synchrotron X-ray and SALS Measurements. *Macromolecules* **1999**, 32, 765-770.

50. Clough, S.; Rhodes, M. B.; Stein, R. S., Transmission of Light by Films of Crystalline Polymers. *Journal of Polymer Science Part C-Polymer Symposium* **1967**, (18PC), 1-&.

51. Haudin, J. M., *Optical Properties of Polymers*. Elsevier Applied Science Publishers: New York, 1986.

52. Stein, R. S.; Rhodes, M. B., Photographic Light Scattering by Polyethylene Films. *Journal of Applied Physics* **1960**, 31, (11), 1873-1884.

53. Mandelkern, L.; Glotin, M.; Benson, R. A., Supermolecular Structure and Thermodynamic Properties of Linear and Branched Polyethylene under Rapid Crystallization Conditions. *Macromolecules* **1981**, 14, 22-34.

54. Xiao, Z. C.; Akpalu, Y. A., New insights into the characteristics of early stage crystallization of a polyethylene. *Polymer* **2007**, 48, (18), 5388-5397.

55. Kumaraswamy, G.; Kornfield, J. A.; Yeh, F.; Hsiao, B. S., Shear-Enhanced Crystallization in Isotactic Polypropylene. 3. Evidence for a Kinetic Pathway to Nucleation. *Macromolecules* **2002**, 35, 1762-1769.

56. Kumaraswamy, G.; Issaian, A. M.; Kornfield, J. A., Shear-Enhanced Crystallization in Isotactic Polypropylene. 1. Correspondence between in Situ Rheo-Optics and ex Situ Structure Determination. *Macromolecules* **1999**, 32, (22), 7537-7547.

57. Jerschow, P.; Janeschitz-Kriegl, H., The role of long molecules and nucleating agents in shear induced crystallization of isotactic polypropylenes. *Internation Polymer Processing* **1997**, 12, (1), 72-77.

58. Pogodina, N. V.; Lavrenko, V. P.; Srinivas, S.; Winter, H. H., Rheology and structure of isotactic polypropylene near the gel point: quiescent and shear-induced crystallization. *Polymer* **2001**, 42, (21), 9031-9043.

59. Ogino, Y.; Fukushima, H.; Takahashi, N.; Matsuba, G.; Nishida, K.; Kanaya, T., Crystallization of Isotactic Polypropylene under Shear Flow Observed in a Wide Spatial Scale. *Macromolecules* **2006**, 39, 7617-7625.

60. Kumaraswamy, G.; Verma, R. K.; Kornfield, J. A.; Yeh, F.; Hsiao, B. S., Shear-enhanced crystallization in isotactic polypropylene. In-situ synchrotron SAXS and WAXD. *Macromolecules* **2004**, 37, 9005-9017.

61. Fernandez-Ballester, L. Formation of oriented precursors in flow-induced polymer crystallization: experimental methods and model materials. California Institute of Technology, Pasadena, CA, 2007.

62. Somani, R. H.; Hsiao, B. S.; Nogales, A.; Srinivas, S.; Tsou, A. H.; Sics, I.; Balta-Calleja, F. J.; Ezquerra, T. A., Structure Development during Shear Flow-Induced Crystallization of i-PP: In-Situ Small-Angle X-ray Scattering Study. *Macromolecules* **2000**, 33, 9385-9394.

63. Wendt, U., Nucleation of Low-Density Polyethylene by High-Density Polyethylene.

*Journal of Materials Science Letters* **1988**, 7, (6), 643-645.

64. Kristiansen, M.; Werner, M.; Tervoort, T.; Smith, P.; Blomenhofer, M.; Schmidt, H. W., The binary system isotactic polypropylene/bis(3,4-dimethylbenzylidene)sorbitol: Phase behavior, nucleation, and optical properties. *Macromolecules* **2003**, 36, (14), 5150-5156.

65. Seki, M.; Thurman, D. W.; Oberhauser, J. P.; Kornfield, J. A., Shear-mediated crystallization of isotactic polypropylene: The role of long chain -- long chain overlap. *Macromolecules* **2002**, 35, 2583-2594.

66. Heeley, E. L.; Fernyhough, C. M.; Graham, R. S.; Olmsted, P. D.; Inkson, N. J.; Embrey, J.; Groves, D. J.; McLeish, T. C. B.; Morgovan, A. C.; Meneau, F.; Bras, W.; Ryan, A. J., Shear-induced crystallization in blends of model linear and long-chain branched hydrogenated polybutadienes. *Macromolecules* **2006**, 39, 5058-5071.

67. Ogino, Y.; Fukushima, H.; Matsuba, G.; Takahashi, N.; Nishida, K.; Kanaya, T., Effects of high molecular weight component on crystallization of polyethylene under shear flow. *Polymer* **2006**, 47, 5669-5677.

68. Yang, L.; Somani, R. H.; Sics, I.; Hsiao, B. S.; Kolb, R.; Fruitwala, H.; Ong, C., Shear-induced crystallization precursor studies in model polyethylene blends by in-situ rheo-SAXS and rheo-WAXD. *Macromolecules* **2004**, 37, 4845-4859.

69. Bunn, C. W.; Daubeny, R. D., The Polarizabilities of Carbon Carbon Bonds. *Transactions of the Faraday Society* **1954**, 50, (11), 1173-1177.

70. Chu, W.; Stein, R. S., Effect of Birefringence on Low-Angle Light-Scattering Patterns from Oriented Polymer Films .2. *Journal of Polymer Science Part a-2-Polymer Physics* **1970**, 8, (4), 489-&.

71. Clough, S.; Vanaarts.J; Stein, R. S., Scattering of Light by 2-Dimensional Spherulites. *Journal of Applied Physics* **1965**, 36, (10), 3072-&.

72. Finkelst.Rs; Sarko, A., Light-Scattering by Anisotropic Elliptical Objects. *Journal of*

*Polymer Science Part a-2-Polymer Physics* **1972**, 10, (7), 1193-&.

73. Stefanescu, E. A.; Dundigalla, A.; Ferreiro, V.; Loizou, E.; Porcar, L.; Negulescu, I.; Garno, J.; Schmidt, G., Supramolecular structures in nanocomposite multilayered films. *Physical Chemistry Chemical Physics* **2006**, 8, (14), 1739-1746.

74. Bafna, A.; Beauchage, G.; Mirabella, F.; Mehta, S., 3D Hierarchical orientation in polymer-clay nanocomposite films. *Polymer* **2003**, 44, (4), 1103-1115.

75. Galgali, G.; Agarwal, S.; Lele, A., Effect of clay orientation on the tensile modulus of polypropylene-nanoclay composites. *Polymer* **2004**, 45, (17), 6059-6069.

76. Medellin-Rodriguez, F. J.; Burger, C.; Hsiao, B. S.; Chu, B.; Vaia, R.; Phillips, S., Time-resolved shear behavior of end-tethered Nylon 6-clay nanocomposites followed by non-isothermal crystallization. *Polymer* **2001**, 42, (21), 9015-9023.

77. Wiley Database of Polymer Properties. In John Wiley & Sons, Inc.: 1999-2009.

78. Yang, L.; Somani, R. H.; Sics, I.; Hsiao, B. S.; Kolb, R.; Lohse, D., The role of high molecular weight chains in flow-induced crystallization precursor structures. *Journal of Physics: Condensed Matter* **2006**, 18, S2421-S2436.

79. Pople, J. A.; Mitchell, G. R.; Sutton, S. J.; Vaughan, A. S.; Chai, C. K., The development of organized structures in polyethylene crystallized from a sheared melt, analyzed by WAXS and TEM. *Polymer* **1999**, 40, (10), 2769-2777.

80. Kumaraswamy, G., Crystallization of Polymers from Stressed Melts. *Journal of Macromolecular Science, Part C: Polymer Reviews* **2005**, 45, 375-397.

81. Ashizawa, H.; Spruiell, J. E.; White, J. L., An Investigation of Optical Clarity and Crystalline Orientation in Polyethylene Tubular Film. *Polymer Engineering and Science* **1984**, 24, (13), 1035-1042.

82. Hsiao, B. S.; Yang, L.; Somani, R. H.; Avila-Orta, C. A.; Zhu, L., Unexpected Shish-Kebab Structure in a Sheared Polyethylene Melt. *Physical Review Letters* **2005**, 94, (11).

## Appendix A

### MATLAB Code for X-ray Data and 2D Correlation Analysis

<b>A.1</b>	<b>Save Experimental Parameters.....</b>	<b>A-2</b>
<b>A.2</b>	<b>Open Image Files.....</b>	<b>A-2</b>
<b>A.3</b>	<b>Extract <math>I(q)</math> vs. <math>q</math>.....</b>	<b>A-4</b>
<b>A.4</b>	<b>Lorentz Correction .....</b>	<b>A-5</b>
<b>A.5</b>	<b>Long Period .....</b>	<b>A-6</b>
<b>A.6</b>	<b>SAXS Integrated Intensity .....</b>	<b>A-7</b>
<b>A.7</b>	<b>Conventional 2D Correlation Analysis .....</b>	<b>A-8</b>
<b>A.8</b>	<b>Hilbert-Noda Matrix.....</b>	<b>A-12</b>
<b>A.9</b>	<b>2D Hetero-Spectral Analysis .....</b>	<b>A-12</b>
<b>A.10</b>	<b>2D Moving Window Analysis.....</b>	<b>A-14</b>
<b>A.11</b>	<b>ACKNOWLEDGEMENTS.....</b>	<b>A-15</b>
<b>A.12</b>	<b>REFERENCES.....</b>	<b>A-16</b>

Due to the acquisition of x-ray data in many file formats, MATLAB code was written in order to facilitate data processing. After determination of beam center and sample-to-detector distance using FIT2D software,<sup>1</sup> the following algorithms were employed.

General code is also provided for conventional and hetero-spectral two-dimensional (2D) correlation analysis, as well as 2D moving window analysis.

## A.1 Save Experimental Parameters

This function asks for necessary experimental parameters: beam center ('x0','y0'), sample to detector distance ('L'), detector pixel size ('pixsize'), and x-ray wavelength ('lamda') and saves them in Matlab matrix 'BNLsaxsApr2009.mat'.

```
function getparameters
x0=input('Enter x coordinate of center:');
y0=input('Enter y coordinate of center:');
L=input('Enter sample-to-detector distance in mm:');
pixsize=input('Enter pixel size in microns:');
lamda=input('Enter wavelength in angstroms:');
lamda=lamda*10^-10;
pixsize=pixsize*10^-6;
L=L*10^-3;
x0=x0*pixsize;
y0=y0*pixsize;
save('BNLsaxsApr2009.mat'); % save parameter matrix
end
```

## A.2 Open Image Files

This function looks for x-ray images (.tif) in directory 'dname' and creates a movie of  $I(q)$  versus  $q$  and saves the corresponding 3D matrix. 'TempA' and 'TempB' are the slope and y-intercept of the ramp temperature profile, respectively. Variables 'timeA' and 'timeB' are the slope and y-intercept of the time dependence on the frame number. 'IC1A' and 'IC1B' are the slope and y-intercept of the IC1 value (prior to sample) dependence on the frame number. It load background matrices 'B' which should be double-format and corrected for IC1 and any difference for acquisition time. This function calls radialintegrationBNL.

```
function waxsdataBNL(dname,TempA,TempB,timeA,timeB,IC1A,IC1B,f)
%% prepare for analysis
```

```

%load background matrices (only IC1 normalized)
%load('Bsaxs1s.mat');
%load('Bwaxs1s.mat');
load('Bsaxs7s.mat');
%load('PEL161sri871.mat');

disp(['File selected for analysis: ', dname]);

% create new directories
if isequal(exist(strcat(dname, '\movies')),0)
    mkdir(dname, 'movies');
end
if isequal(exist(strcat(dname, '\IvsQ')),0)
    mkdir(dname, 'IvsQ');
end

waxsfolder=dname;
waxsfiles=dir(waxsfolder);
wsize=size(waxsfiles);
numfiles=wsize(1);

%get movie name
sfile=waxsfiles(10).name;
index=strfind(sfile, 'i'); % 'r' before for ramps
newdname=sfile(1:index);
moviefile=strcat(waxsfolder, '\movies', newdname, '_IvsQ');
mov=avifile(moviefile, 'compression', 'none', 'fps', 2);

%find start of files
track=1;
while waxsfiles(track).isdir~=0
    track=track+1;
end
intensity=zeros(250,3,numfiles-4);
ii=1;
for count=track:numfiles-2;
    if waxsfiles(count).isdir==0
        filename=waxsfiles(count).name;
        wholepathwaxs=strcat(waxsfolder, '\', filename);
        imagemat=imread(wholepathwaxs, 'tiff');
        imagemat=double(imagemat)+1;
        n=strfind(filename, 'i');
        frame=str2double(filename(n+1:n+4));
        time=timeA*frame+timeB;
        Temp=TempA*time+TempB;
    end
end

```

```

IC1=IC1A*frame+IC1B;
imagemat=imagemat/IC1-f*B;
IvsQ=radialintegrationBNL(imagemat);
intensity(:,1,ii)=Temp;
intensity(:,2,ii)=IvsQ(:,1);
intensity(:,3,ii)=IvsQ(:,2);
ii=ii+1;
plot(IvsQ(:,1),IvsQ(:,2));
%axis([0 1.94 0 1]); %for WAXS
axis([0 0.12 0 3]); %for SAXS
set(gca,'YGrid','on');
time2=strcat('Temp=',num2str(Temp),'\circC');
text(0.07,.75,time2);
F=getframe(gcf);
mov=addframe(mov,F);
end
end
mov=close(mov);
intname=strcat(waxsfolder,'IvsQ',newdname,'_intmat');
save(intname,'intensity');
end

```

### A.3 Extract I(q) vs. q

This function requires the input of a 2D matrix containing intensity values (double) corresponding to the x-ray scattering image ('imagemat'). It returns I(q) vs. q in matrix 'IvsQ'. It loads the experimental parameters saved in A.1. Start and end pixel counts can be adjusted as needed. It is important to resize matrices 'allpixels' and 'sortedpix' accordingly.

```

function [IvsQ]=radialintegrationBNL(imagemat)

%load('BNLwaxsApr2009.mat');
load('BNLsaxsApr2009.mat');
%%
allpixels=zeros(160801,2); %WAXS: 463761; SAXS: 160801
pixelnum=1;

for xcount=312:712 %WAXS: 168:848; SAXS: 312:712
    for ycount=311:711 %WAXS: 173:853; SAXS: 311:711
        r=((0.5*pixsize*(2*xcount-1)-x0)^2+(0.5*pixsize*(2*ycount-1)-y0)^2)^0.5;
        q=4*10^-10*pi*sin(0.5*atan(r/L))/lamda;
        allpixels(pixelnum,1)=q;
        allpixels(pixelnum,2)=imagemat(ycount,xcount);
        pixelnum=pixelnum+1;
    end
end

```

```

end
%%
sortedpix=zeros(160801,2); %WAXS: 463761; SAXS: 160801
[temp,IX]=sort(allpixels);
for count=1:160801 %WAXS: 463761; SAXS: 160801
    sortedpix(count,1)=temp(count,1);
    sortedpix(count,2)=allpixels(IX(count,1),2);
end

[n,xout]=hist(sortedpix(:,1),250); %can change bin as desired
sizen=size(n);
bin=sizen(2);
Ivsq=zeros(bin,2);
mark=1;
for count=1:bin
    Ivsq(count,1)=xout(count); %set binned q
    ave=0;
    for ii=mark:mark+n(count)-1
        ave=ave+sortedpix(ii,2)/n(count);
    end
    Ivsq(count,2)=ave;
    mark=mark+n(count);
end

%no dezinger
IvsQ=Ivsq;

end

```

#### A.4 Lorentz Correction

This function creates and saves the Lorentz-corrected intensity matrix calculated from the intensity matrix created in A.2. It also saves each frame as a separate ascii file for crystallinity evaluation in Origin or other software.

```

function lorentz

[filename,pathname]=uigetfile('*.mat','Select matrix for ascii extraction');
disp(['File selected: ', filename])
A=load(strcat(pathname,filename));
mat=A.intensity;

[m,n,k]=size(mat);
lformat=mat;
temp=zeros(189,2); %don't include Temperature values
for count=1:k

```

```

for q=1:m
    lormat(q,3,count)=lormat(q,2,count)^2*lormat(q,3,count);
end
temp(:,1)=lormat(1:189,2,count); % 1st column is Temp values
temp(:,2)=lormat(1:189,3,count)+0.5;
if count<10
    name=strcat('L52cw','00',num2str(count));
elseif (count>9) && (count<100)
    name=strcat('L52cw','0',num2str(count));
else
    name=strcat('L52cw',num2str(count));
end
save(strcat(pathname,name),'temp','-ascii');
end
len=length(filename);
name=filename(1:len-11);
save(strcat(pathname,name,'_lormat'),'lormat');
end

```

## A.5 Long Period

This function approximates the long period from the peak of the scattering curve on the frame range from ‘start’ to ‘finish’. Note: not valid for noisy data.

```

function [Lp]=getLp(start,finish)

%% load lorentzian corrected matrix
[filename,pathname]=uigetfile('Select Lorentzian corrected matrix');
A=load(strcat(pathname,filename));
%intensity=A.intensity;
intensity=A.lormat;
%intensity=A.intmat;
%% adjust matrix size
[m1,n,k]=size(intensity);
intensity(130:m1,:,:)=[]; % was 205 for BNL materials
[m2,n,k]=size(intensity);
intensity(1:10,:,:)=[]; % 22 for PEL52, PEL161, and MS3 at BNL; 37 for EH4 for
BNL; 10 for LBL materials
[m,n,k]=size(intensity);
%%
Lp=zeros(finish-start+1,2);
track=1;
for count=start:finish
    Lp(track,1)=intensity(1,1,count);
    [c,i]=max(smooth(intensity(:,3,count)));
    Lp(track,2)=0.2*pi/intensity(i,2,count);

```

```

track=track+1;
end

figure(1);
plot(Lp(:,1),Lp(:,2));
xlabel('Temperature (°C)');
ylabel('Long period (nm)');
plottitle=input('Enter plot title: ','s');
title(plottitle);

len=length(filename);
name=filename(1:len-4);
save(strcat(pathname,name,'_Lpmat'),Lp');
save(strcat(pathname,name,'_Lpmat'),Lp','-ascii');
nameplot=strcat(pathname,name,'_Lpgraph');
saveas(gcf,nameplot,'fig');
saveas(gcf,nameplot,'jpg');
end

```

## A.6 SAXS Integrated Intensity

This function calculates the SAXS integrated intensity on a frame interval from ‘start’ to ‘finish’.

```

function [Area]=getArea(start,finish)

%% load lorentzian corrected matrix
[filename,pathname]=uigetfile('Select Lorentzian corrected matrix');
A=load(strcat(pathname,filename));
intensity=A.lormat;
%intensity=A.intmat;
%% adjust matrix size
[m1,n,k]=size(intensity);
intensity(205:m1,:,:)=[];
%[m2,n,k]=size(intensity);
%intensity(1:37,:,:)=[]; %22 for all paper materials; 37 for EH4
[m,n,k]=size(intensity);
%%%
Lp=zeros(finish-start+1,2);
track=1;
for count=start:finish
    Area(track,1)=intensity(1,1,count);
    A=0;
    for q=2:m
        A=A+(intensity(q,3,count)+intensity(q-1,3,count))*(intensity(q,2,count)-
intensity(q-1,2,count))/2;
    end
    track=track+1;
end

```

```

end
Area(track,2)=A;
track=track+1;
end

figure(1);
plot(Area(:,1),Area(:,2));
xlabel('Temperature (°C)');
ylabel('Invariant');
plottitle=input('Enter plot title: ','s');
title(plottitle);

len=length(filename);
name=filename(1:len-4);
save(strcat(pathname,name,'_Areamat'),'Area');
save(strcat(pathname,name,'_Areamat'),'Area','-ascii');
nameplot=strcat(pathname,name,'_Areagraph');
saveas(gcf,nameplot,'fig');
saveas(gcf,nameplot,'jpg');
end

```

## A.7 Conventional 2D Correlation Analysis

```

function cormat
%% Conventional 2D correlation analysis on a ax2xm matrix containing
%% intensity values at equally spaced points along a perturbation

%% load matrix
[filename,pathname]=uigetfile('Select mutli-spectra matrix for analysis');
disp(['File selected: ', filename])
A=load(strcat(pathname,filename));
sepmat=A.sepmat; %adjust if matrix name is not sepmat (ex:
sepmat=A.matrix_name;

%% 
[a,b,m]=size(sepmat);
range=a;

figure(1);
hold on;
for speccount=1:m
    plot(sepmat(:,1,speccount),sepmat(:,2,speccount)); %plot all spectra
    y(speccount,:)=sepmat(:,2,speccount);
end
xlabel('Raman Shift (cm^{-1})'); %set axis
ylabel('Intensity'); %set axis

```

```

plottitle=input('Enter plot title:','s');
title(plottitle);
hold off;

len=length(filename);
name=filename(1:len-8);
nameall=strcat(pathname,name);
saveas(gcf,nameall,'fig');
saveas(gcf,nameall,'jpg');

%% calculate differential matrix and plot (not necessary)
diffmat=zeros(range,2,m-1);
figure(5);
hold on;
for count=1:m-1
    diffmat(:,1,count)=sepmat(:,1,count);
    diffmat(:,2,count)=sepmat(:,2,count+1)-sepmat(:,2,count);
    plot(diffmat(:,1,count),diffmat(:,2,count));
end
xlabel('Raman Shift (cm^{-1})'); % set axis
ylabel('Difference in Intensity'); % set axis
title({plottitle;'Change in Spectra'});
hold off;
namediff=strcat(pathname,name,'_diff');
saveas(gcf,namediff,'fig');
saveas(gcf,namediff,'jpg');

depvar=sepmat(:,1,1); % spectral variables
dim=length(depvar);

%% calculate perturbation-averaged spectrum
yave=zeros(1,dim);
for count=1:m
    yave=yave+y(count,:);
end
yave=yave/m;

%% plot perturbation-averaged spectrum
figure(2);
plot(depvar,yave);
xlabel('Raman Shift (cm^{-1})'); % set axis
ylabel('Intensity'); % set axis
title({plottitle;'Averaged Spectra'});
nameave=strcat(pathname,name,'_ave');
saveas(gcf,nameave,'fig');

```

```

saveas(gcf,nameave,'jpg');

%% save average spectrum
avemat(:,1)=depvar;
avemat(:,2)=yave;
nameavemat= strcat(pathname,name,'_avemat');
save(nameavemat,'avemat');

%% calculate dynamic spectrum
for count=1:m
    ys(count,:)=y(count,:)-yave;
end

%% calculate synchronous spectrum
Phi=(1/(m-1))*ys'*ys;

%% if want to set noise threshold to 5%
%[a,a]=size(Phi);
%maxPhi=max(max(Phi));
%for count1=1:a
%    for count2=1:a
%        if abs(Phi(count1,count2))<0.05*maxPhi
%            Phi(count1,count2)=0;
%        end
%    end
%end

%% plot and save synchronous spectrum
figure(3);
contour(depvar',depvar',Phi);
%imagesc(depvar',depvar',Phi); %if contour is too noisy
hold on;
plot(depvar,depvar);
xlabel('Raman Shift (cm^{-1})');
ylabel('Raman Shift (cm^{-1})');
title({'Synchronous 2D Correlation Spectra:';plottitle});
axis xy;
hold off;
namePhi=strcat(pathname,name,'_Phi');
saveas(gcf,namePhi,'fig');
saveas(gcf,namePhi,'jpg');
namePhimat=strcat(pathname,name,'_Phimat');
save(namePhimat,'Phi');

%% calculate asynchronous spectrum

```

```

N=makeN(m); % calculate Hilbert-Noda matrix (see A.8)
Psi=(1/(m-1))*ys*N*ys;

%% if want to set noise threshold to 5%
%[b,b]=size(Psi);
%maxPsi=max(max(Psi));
%for count1=1:b
%  for count2=1:b
%    if abs(Psi(count1,count2))<0.05*maxPsi
%      Psi(count1,count2)=0;
%    end
%  end
%end

%% plot and save asynchronous spectrum
figure(4);
contour(depvar',depvar',Psi');
%imagesc(depvar',depvar',Psi'); %if countour is too noisy
hold on;
plot(depvar,depvar);
xlabel('Raman Shift (cm^{-1})');
ylabel('Raman Shift (cm^{-1})');
title({'Asynchronous 2D Correlation Spectra';plottitle});
axis xy;
hold off;
namePsi= strcat(pathname,name,'_Psi');
saveas(gcf,namePsi,'fig');
saveas(gcf,namePsi,'jpg');
namePsimat= strcat(pathname,name,'_Psimat');
save(namePsimat,'Psi');

%% calculate, plot, and save autocorrelation intensity
v=diag(Phi);
figure(6);
plot(depvar',v);
xlabel('Raman Shift (cm^{-1})');
ylabel('Autocorrelation Intensity');
title({'Autocorrelation Spectrum';plottitle});
nameapow= strcat(pathname,name,'_pow');
saveas(gcf,nameapow,'fig');
saveas(gcf,nameapow,'jpg');
apowmat(:,1)=depvar;
apowmat(:,2)=v;
nameapowmat= strcat(pathname,name,'_apowmat');
save(nameapowmat,'apowmat');

```

```
%%
end
```

## A.8 Hilbert-Noda Matrix

```
function [N]=makeN(m)
%% calculate Hilbert-Noda matrix
N=zeros(m);
for j=1:m
    for k=1:m
        if j==k
            N(j,k)=0;
        else
            N(j,k)=1/(pi*(k-j));
        end
    end
end
end
```

## A.9 2D Hetero-Spectral Analysis

```
function heterocorr
%% Conduct 2D hetero-spectral correlation analysis on two matrices (here
%% SAXS and WAXS data) that contain the same number of points along the
%% perturbation. This is written for ax3xm matrices where there are a
%% spectral variables (which are located in column 2) and m points along
%% the perturbation. Column 3 contains the intensity values. Column 1
%% contains temperatures (not used here).

%% load matrices
[filename1,pathname1]=uigetfile('Select SAXS matrix');
disp(['File selected: ', filename1])
A=load(strcat(pathname1,filename1));
sepmat1=A.intensity; %for matrix named intensity or change to
    %sepmat1=A.matrix_name;
[filename2,pathname2]=uigetfile('Select WAXS matrix');
disp(['File selected: ', filename2])
A=load(strcat(pathname2,filename2));
sepmat2=A.intensity; %for matrix named intensity or change to
    %sepmat2=A.matrix_name;

%% establish matrix size -- note: it is required that m1=m2
[a1,b1,m1]=size(sepmat1);
[a2,b2,m2]=size(sepmat2);
%%
for speccount=1:m1
```

```

y1(speccount,:)=sepmat1(:,3,speccount); %change if only 2 column
matrix
end
for speccount=1:m2
    y2(speccount,:)=sepmat2(:,3,speccount); %change if only 2 column matrix
end
len=length(filename1);
name=filename1(1:len-4);
nameall=strcat(pathname1,name);

depvar1=sepmat1(:,2,1); % spectral variables set 1
depvar2=sepmat2(:,2,1); % spectral variables set 2
dim1=length(depvar1);
dim2=length(depvar2);

%% calculate average spectra for each dataset
yave1=zeros(1,dim1);
yave2=zeros(1,dim2);
for count=1:m1
    yave1=yave1+y1(count,:);
end
yave1=yave1/m1;
for count=1:m2
    yave2=yave2+y2(count,:);
end
yave2=yave2/m2;

%% plot average spectra for each dataset
figure(1);
plot(depvar1,yave1);
xlabel('q (A^{-1})');
ylabel('Intensity');
title('Averaged Spectra');
nameave=strcat(pathname1,name,'_ave1');
saveas(gcf,nameave,'fig');
saveas(gcf,nameave,'jpg');
namedep1=strcat(pathname1,name,'_depvar1');
save(namedep1,'depvar1');
figure(2);
plot(depvar2,yave2);
xlabel('q (A^{-1})');
ylabel('Intensity');
title('Averaged Spectra');
nameave=strcat(pathname1,name,'_ave2');
saveas(gcf,nameave,'fig');

```

```

saveas(gcf,nameave,'jpg');
namedep2=strcat(pathname1,name,'_depvar2');
save(namedep2,'depvar2');

%% calculate dynamic spectra for each dataset
for count=1:m1
    ys1(count,:)=y1(count,:)-yave1;
end
for count=1:m2
    ys2(count,:)=y2(count,:)-yave2;
end

%% calculate synchronous spectra
Phi=(1/(m1-1))*ys1'*ys2;
[a,a]=size(Phi);
maxPhi=max(max(Phi));
for count1=1:a
    for count2=1:a
        if abs(Phi(count1,count2))<0.05*maxPhi
            Phi(count1,count2)=0;
        end
    end
end

%% plot synchronous spectrum
figure(3);
contour(depvar2',depvar1',Phi);
%imagesc(depvar',depvar',Phi); %if contours are too noisy
xlabel('q (A^{-1})'); %set axis
ylabel('q (A^{-1})'); %set axis
title('Synchronous 2D Correlation Spectra:'); %set title
axis xy;

%% save synchronous spectrum
namePhi=strcat(pathname1,name,'_Phi');
saveas(gcf,namePhi,'fig');
saveas(gcf,namePhi,'jpg');
namePhimat=strcat(pathname1,name,'_Phimat');
save(namePhimat,'Phi');
end

```

## A.10 2D Moving Window Analysis

```
function [movwin]=MW2D(intensity,win)
```

```

%% conduct moving window 2D analysis on matrix 'intensity' of window
of size 'win'
[m,n,k]=size(intensity);
%% load desired spectra into y (general spectra)
for count=1:k
    y(count,:)=intensity(:,2,count); %for 2 column matrix
end
%% now conduct analysis on smaller windows
depvar=intensity(:,1,1); %spectral variable
movwin=zeros(k-win+1,m); %2D moving window plot
ycord=zeros(k-win+1,1); %perturbation coordinate
for start=1:(k-win+1)
    for count=1:win
        ywin(count,:)=y(count+start-1,:);
    end
    yave=zeros(1,m);
    %calculate average spectrum
    for count=1:win
        yave=yave+ywin(count,:);
    end
    yave=yave/win;
    %calculate dynamic spectra
    for count=1:win
        ys(count,:)=ywin(count,:)-yave;
    end
    Phi=(1/(win-1))*ys'*ys; %calculate synchronous spectrum
    movwin(start,:)=diag(Phi); %take autocorrelation intensity
    frame=start+floor(win/2); % take representative value of frame (or perturbation)
    % for 'window'
    time=10*frame; %set time dependence on frame (or each perturbation point)
    ycord(start)=time;
end

%% plot 2D moving window plot
contour(depvar,ycord,movwin,10); %set to 10 contours
xlabel('q (Angstroms^{-1})'); %set axis
ylabel('Temperature'); %set axis
end

```

## A.11 ACKNOWLEDGEMENTS

Motivation for this work came from Dr. Eleni Pavlopoulou (University of Athens, Greece) and Dr. Luigi Balzano (Technical University of Eindhoven, Netherlands). Understanding of x-ray data analysis was facilitated by Dr. Lucia Fernandez Ballester

(DUBBLE, ESRF, Grenoble, France), Dr. Timothy Gough (University of Bradford, UK), Dr. Giuseppe Portale (DUBBLE, ESRF, Grenoble, France), and Dr. Wim Bras (DUBBLE, ESRF, Grenoble, France). Code development was assisted by Eliot Gann (ALS, Lawrence Berkeley National Lab), Andrew Metcalf (Caltech) and Meisam Hajimorad (Caltech). This work was greatly assisted by the National Science Foundation (NSF) International Research and Education in Engineering (IREE) initiative.

## A.12 REFERENCES

1. Hammersley, A. FIT2D. <http://www.esrf.eu/computing/scientific/FIT2D/>

## Appendix B

### Flow-Induced Crystallization of Model Systems

<b>B.1 INTRODUCTION.....</b>	<b>B-2</b>
<b>B.2 EXPERIMENTAL METHODS.....</b>	<b>B-4</b>
<b>B.2.1 Materials .....</b>	<b>B-4</b>
B.2.1.2 Overlap Concentration .....	B-5
<b>B.2.2 Shear-Induced Crystallization .....</b>	<b>B-6</b>
<b>B.3 RESULTS.....</b>	<b>B-6</b>
<b>B.4 DISCUSSION .....</b>	<b>B-7</b>
<b>B.5 CONCLUSION.....</b>	<b>B-10</b>
<b>B.6 ACKNOWLEDGEMENTS.....</b>	<b>B-10</b>
<b>B.7 REFERENCES .....</b>	<b>B-12</b>

## B.1 INTRODUCTION

The physical properties of semicrystalline materials are ultimately dictated by their morphology in the solid state, which is a strong function of the response of the polymer melt to processing conditions. Under certain conditions, the formation of oriented nuclei under flow produces an oriented morphology,<sup>1</sup> which results in increased crystallization kinetics and enhancement of physical properties.<sup>2-6</sup> The formation of oriented nuclei in part depends on the perturbation of crystallizable chains from their equilibrium configurations in the melt. The degree of chain orientation is dictated by their relaxation dynamics relative to an applied flow field.<sup>3</sup> Highly branched materials relax through a hierarchy of motions,<sup>7</sup> hence, materials with well-defined architectures, such as hydrogenated polybutadienes (HPBDs),<sup>8-12</sup> are ideal systems with which to probe the effects of melt dynamics on flow-induced crystallization (FIC) of semicrystalline polymers.<sup>13</sup>

The effect of the slow-relaxing species (i.e., the model HPBD) can be examined through the implementation of bimodal blends which contain a small concentration of the slow-relaxing species in a fast-relaxing matrix. These model bimodal systems are common in FIC studies, in which they are usually composed of two species with substantially different molecular weights (e.g., Chapter 5).<sup>14-19</sup> The concentration of the slow relaxing species has a non-linear effect on FIC behavior; greatly enhanced crystallization kinetics and development of oriented morphology are observed near its overlap concentration,  $c^*$ , at which chains just pervade all sample volume (Figure B.1).<sup>13-</sup><sup>15</sup> Hence, although it is important to keep the concentration of the slow-relaxing species

low in order to minimize its effects on the viscosity of the blend (and to not introduce a new experimental variable), the concentrations need to be at least as high as  $c^*$  to observe pronounced FIC effects.

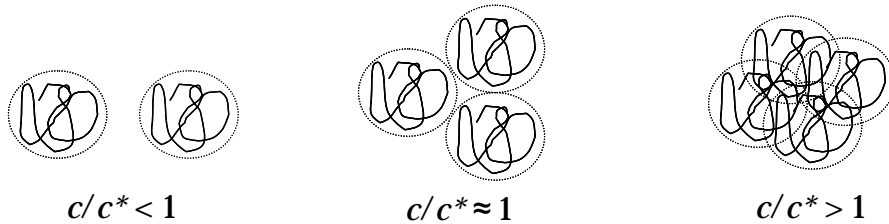


**Figure B.1** Schematic representation of overlap concentration,  $c^*$ .

The major component of the bimodal blend must meet particular requirements with regard to the study of HPBD materials. Due to the nature of anionic polymerization, which is used to synthesize model HPBDs, the resulting materials contain short-chain branches (SCB) and are analogous to random ethylene-co-butenes with a minimum of 4 mol % butene.<sup>20, 21</sup> In order to deconvolute the effects of relaxation dynamics from short-chain branching, it is necessary to select a base resin containing comparable amounts of SCB.

In the following section, we present preliminary FIC studies on a bimodal blend containing an HPBD comb polymer in an ethylene-co-hexene matrix with comparable SCB content. This comb polymer, which exhibits two relaxation processes—that of the arms followed by that of the backbone<sup>22</sup>—was anticipated to have a profound effect on oriented morphology following shear.

## B.2 EXPERIMENTAL METHODS

### B.2.1 Materials

Molecular characteristics of the bimodal blend components are provided in Figure B.2 and Table B.1. The minor component in the bimodal blends was a hydrogenated polybutadiene (HPBD) comb polymer (C4) synthesized via anionic polymerization, followed by hydrogenation, in conjunction with hydrosillation.<sup>8, 20</sup> This molecule contained an average of 4 teeth per backbone. The polydispersity (PDI =  $M_w/M_n$ ) of the comb backbone and teeth components was below 1.05, but since the number of teeth per backbone is an average, the combs themselves could not be considered monodisperse. Similar to the H4 polymer in Chapter 3, C4 exhibited intrachain heterogeneity in the SCB distribution due to the synthetic route to the telechelic backbone; the teeth contained approximately 19 SCB per 1000 backbone carbon atoms while the backbone contained higher SCB content (approximately 40 SCB/1000 backbone C). C4 was graciously provided by Professor Nikos Hadjichristidis (University of Athens, Athens, Greece) and characterized by Dr. David Lohse and his team (ExxonMobil, Clinton, NJ).

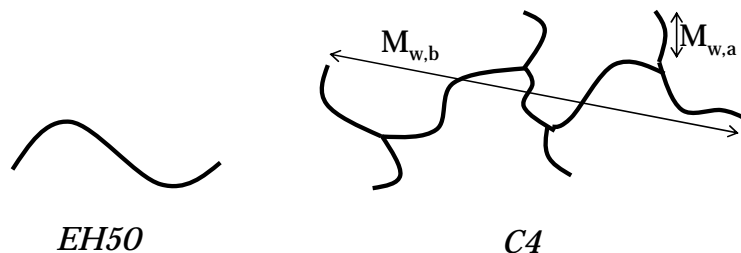


**Figure B.2** Schematic representation of bimodal blend components.

**Table B.1 Molecular characteristics of blend components studied under flow. All values provided by ExxonMobil.**

Polymer	Type	M <sub>w,tot</sub> (kg/mol)	PDI	M <sub>w,b</sub> (kg/mol)	M <sub>w,a</sub> (kg/mol)	SCB/ 1000 backbone C <sup>a</sup>
EH50	linear	50	2.0	50		23.2
C4 <sup>b</sup>	comb	232		100	33	24.4

<sup>a</sup> obtained via <sup>13</sup>C NMR

The major component in the bimodal blends was metallocene-catalyzed random ethylene copolymer with approximately 5 mol % hexene. Given the strong dependence of crystallization behavior on SCB content, EH50 was selected due to its similar SCB content in an attempt to isolate the effects of LCB and SCB. EH50 was graciously provided and characterized by Dr. David Lohse and his team (ExxonMobil, Clinton, NJ).

Blends containing 1, 1.5 and 5 wt % C4 in EH50 were created as described in Chapter 5. Comb concentrations in the blends were selected to be above and below their overlap concentration,  $c^* \approx 0.012$ , which is the concentration at which chains just pervade all sample volume resulting in a non-linear response to the flow field.<sup>13-15</sup> An estimate of  $c^*$  was made based on the comb backbone length, M<sub>w,b</sub>, as done by Heeley et al.<sup>13</sup>

### B.2.1.2 Overlap Concentration

If we assume that the backbone is the only part of the comb oriented by flow, it is possible to estimate the overlap concentration,  $c^*$ , for comb-comb contact as that of a linear chain having comparable molecular weight to the backbone (M<sub>w,b</sub>), as done by Heeley et al.<sup>13</sup> Hence,

$$c^* = \frac{3M_{w,b}}{4\pi(R_g^2)^{3/2} \rho N_a}, \quad (B.1)$$

where  $N_a$  is Avogadro's number,  $\rho$  is density, and  $R_g$  is the radius of gyration.<sup>23</sup>

<sup>24</sup> From small-angle neutron scattering measurements,  $R_g$ (Å) for linear hydrogenated polybutadienes was found to depend on  $M_{w,tot}$  (g/mol) as<sup>25</sup>

$$R_g = 0.5 (M_{w,tot})^{1/2}. \quad (B.2)$$

Using eqs B.1 and B.2, we find that  $c^* \approx 0.012$ . As this is a rough approximation, blends of 1, 1.5 and 5 wt % comb in EH50 were made.

### B.2.2 Shear-Induced Crystallization

Isothermal crystallization of comb blends following a short shear pulse was studied using the same instrument and protocol as described in Section 5.2.3 of Chapter 5. The isothermal crystallization temperature used was  $T_c = 98$  °C. Wall shear stresses ( $\sigma_w$ ) imposed were 0.11 MPa for a shearing time ( $t_s$ ) of 10 s and 0.14 MPa for  $t_s = 15$  s. The total sample mass extruded, and hence the total strain, was kept relatively constant just below 100 mg. Morphology development was followed in situ via optical transmittance ( $I/I_0$ ) and apparent birefringence ( $I_{perp}/I$ ) measurements.

## B.3 RESULTS

Shear was found to have no effect on the crystallization of 1 or 1.5 wt % comb blends. Apparent birefringence revealed no orientation and crystallization kinetics (as given by transmittance) were unchanged from the quiescent case (not shown). The 5 wt % blend exhibited turbidity traces that were difficult to interpret with regard to crystallization kinetics (Figure B.3a). At first glance, sheared samples appeared to crystallize slower, reaching 80% transmittance multiple decades later than samples crystallizing quiescently. However, this lag is the result of the development of a local

minimum that resembles that of HDPE blends in Chapter 5 (Figure 5.5).

Apparent birefringence traces of all sheared samples exhibit increased values during shear as a consequence of flow birefringence (Figure B.3b). However, the immediate drop in  $I_{perp}/I$  following cessation of shear indicates that no anisotropic structures were formed.<sup>3, 26</sup>

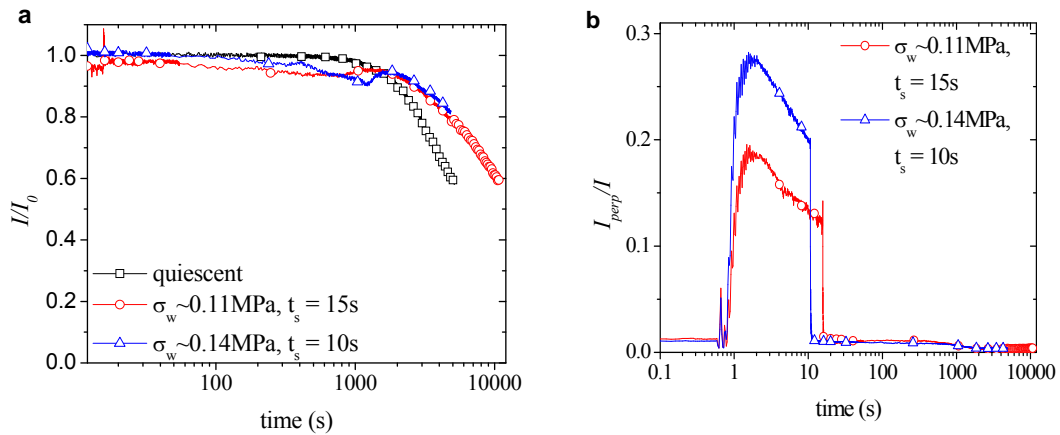


**Figure B.3** a) Transmittance ( $I/I_0$ ) and b) apparent birefringence ( $I_{perp}/I$ ) for 5 wt % comb blend sheared at 98 °C.

## B.4 DISCUSSION

Comb blends did not exhibit the expected behavior in response to shear. For reference, the evolution of transmittance and apparent birefringence is provided in Figure B.4 for an isotactic polypropylene (iPP) sample. In response to shear, this sample exhibited the expected enhancement of crystallization kinetics (evidenced by the shorter time to reach 50% transmittance in Figure B.4a) and oriented crystal growth (evidenced by growth in birefringence after cessation of shear in Figure B.4b). For iPP, the monotonic trend in the transmittance allows us to relate increased turbidity of the sample to its crystallinity development, contrary to blends of the HPBD (above) and HDPE

(Chapter 5). In highly oriented samples, apparent birefringence exhibits sinusoidal behavior (see eq 5.3 in Chapter 5).<sup>19,27</sup> A comparison between Figure B.3b and Figure B.4b quickly reveals a complete lack of oriented growth.

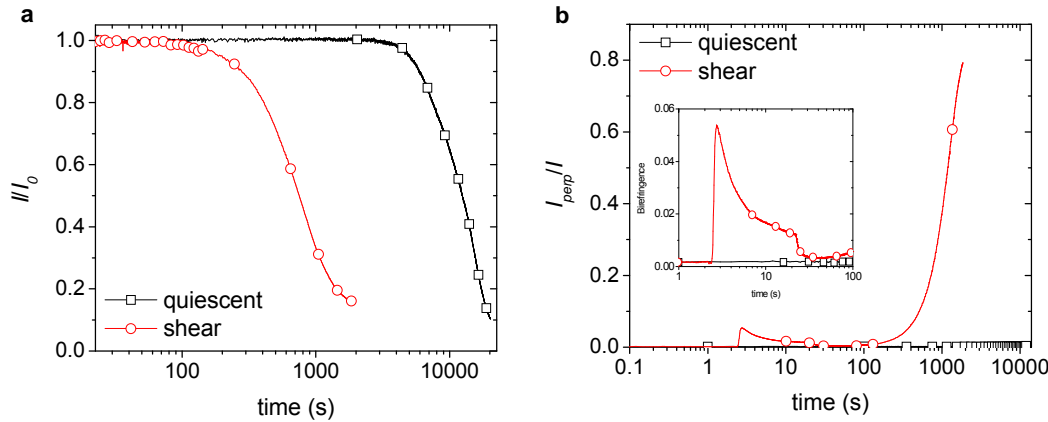


**Figure B.4** a) Transmittance and b) apparent birefringence comparisons for sheared and quiescently crystallized iPP presented for comparison.

This surprising result is not a consequence of a lack of comb chain orientation in response to the flow field. The degree of orientation expected for comb chains can be inferred from the Wiessenberg number (Wi),<sup>28-31</sup> which is a ratio of the relaxation time of the chains to the time scale for the shear process. The orientation of chains by flow is expected for  $Wi > 1$ . For the current shear process,

$$Wi = \dot{\gamma} \tau_{r,comb}, \quad (B.3)$$

where  $\tau_{r,comb}$  is the characteristic relaxation time of the comb chains. The shear rate,  $\dot{\gamma}$ , can be estimated from

$$\dot{\gamma} \sim \sigma_w / \mu, \quad (B.4)$$

where  $\mu$  is the viscosity of the blend. The viscosity is related to the relaxation modulus,  $G$ , as

$$\mu = \int_0^{\infty} G(t) dt \sim G_N^0 \tau_r . \quad (B.5)$$

The approximation of  $\mu$  as the product of the plateau modulus,  $G_N^0$ , and terminal relaxation time,  $\tau_r$ , is valid for monodisperse, entangled, linear melts. Given that the current sample only meets the entangled criterion, we acknowledge that this is not a rigorous calculation but, rather, an order of magnitude estimate. Using  $G_N^0 \sim 1$  MPa for polyethylene,<sup>32</sup>  $\sigma_w \sim 0.1$  MPa, and the terminal relaxation time of the melt,  $\tau_r \approx 0.005$  s,<sup>33</sup> the shear rate for these experiments determined to be approximately  $20$  s<sup>-1</sup>. The comb polymer has a terminal relaxation time of  $7.5$  s,<sup>34</sup> resulting in  $Wi \sim 100$ . Hence, we expect the comb chains to be strongly oriented by flow.

The unusual transmittance curves (Figure B.3a) further support the deformation of chains from their equilibrium configurations during shear. When combs are above their overlap concentrations (i.e., 5 wt % blend), sample transmittance decreases to a minimum following the cessation of shear, recovers slightly, and resumes a monotonic decrease at a slower rate than in the quiescent case. This behavior is most pronounced at highest shear stress suggesting that it is a consequence of chain response to the flow field.

Since we expect the orientation of comb chains by the flow field, the lack of subsequent oriented growth must be the result of the inability of the system to effectively propagate oriented crystals from these chains. Given the strong effect of SCB content on quiescent crystallization (see Chapter 3 and references within), we anticipate that these chain defects are to blame for the lack of oriented growth.

## B.5 CONCLUSION

Application of a flow field to bimodal blends containing well-defined HPBD combs at concentrations above their overlap concentration did not result in typical flow-induced crystallization behavior. Although comb chains were oriented by the application of a shear pulse ( $Wi \gg 1$ ), subsequent oriented growth was not observed. This lack of oriented morphology can be accounted for by either (1) a lack of oriented nuclei formation from the oriented chains, or (2) if oriented nuclei did form, the inability of the melt to effectively propagate oriented growth from the nuclei. We hypothesize that either scenario can be a consequence of the relatively high short-chain branching content of both the base resin (EH50 having 23.2 SCB/1000 backbone C) and the slow-relaxing comb polymer (C4 having 24.4 SCB/1000 backbone C).

To further examine this theory, we propose FIC studies on the same high-SCB-content base resin (EH50) but blended with small amounts of a high- $M_w$  (i.e., slow-relaxing) high-density polyethylene (HDPE). The latter molecule is well-known to form oriented nuclei,<sup>35-38</sup> hence, the effect of SCB content on the propagation of an oriented morphology can be examined. These studies (described in Chapter 5) can provide further insight into the crystallization of industrially relevant linear-low density polyethylenes (LLDPE).

## B.6 ACKNOWLEDGEMENTS

This work would not have been possible without ExxonMobil Research and Engineering Company, particularly Dr. David Lohse, Dr. Cynthia Mitchell, Dr. Jung Hun Lee and the rest of the team, who provided materials, financial support, experimental

assistance, and fruitful discussions. Additionally, the model materials examined here were graciously provided by Prof. Nikos Hadjichristidis (University of Athens, Athens, Greece) and made available through collaboration with ExxonMobil. Experimental assistance was also provided by Dr. Lucia Fernandez Ballester. Additional funding was provided by the National Science Foundation (DMR-0505393 and GOALI-0523083). Manuscript preparation was assisted by Mary Louie (Caltech).

## B.7 REFERENCES

1. Liedauer, S.; Eder, G.; Janeschitz-Kriegl, H.; Jerschow, P.; Geymayer, W.; Ingolic, E., On the kinetics of shear-induced crystallization in polypropylene. *International Polymer Processing* **1993**, 8, (3), 236-244.
2. Bond, E. B.; Spruiell, J. E., Melt spinning of metallocene catalyzed polypropylenes. I. On-line measurements and their interpretation. *Journal of Applied Polymer Science* **2001**, 82, (13), 3223-3236.
3. Kumaraswamy, G.; Kornfield, J. A.; Yeh, F.; Hsiao, B. S., Shear-Enhanced Crystallization in Isotactic Polypropylene. 3. Evidence for a Kinetic Pathway to Nucleation. *Macromolecules* **2002**, 35, 1762-1769.
4. Haas, T. W.; Maxwell, B., Effects of Shear Stress on Crystallization of Linear Polyethylene and Polybutene-1. *Polymer Engineering and Science* **1969**, 9, (4), 225-&.
5. Andersen, P. G.; Carr, S. H., Crystal Nucleation in Sheared Polymer Melts. *Polymer Engineering and Science* **1978**, 18, (3), 215-221.
6. Kantz, M. R.; Stigale, F. H.; Newman, H. D., Skin-Core Morphology and Structure-Property Relationships in Injection-Molded Polypropylene. *Journal of Applied Polymer Science* **1972**, 16, (5), 1249-&.
7. McLeish, T. C. B., Hierarchical-relaxation in tube models of branched polymers. *Europhysics Letters* **1988**, 6, (6), 511-516.
8. Hadjichristidis, N.; Xenidou, M.; Iatrou, H.; Pitsikalis, M.; Poulos, Y.; Avgeropoulos, A.; Sioula, S.; Paraskeva, S.; Velis, G.; Lohse, D. J.; Schulz, D. N.; Fetters, L. J.; Wright, P. J.; Mendelson, R. A.; Garcia-Franco, C. A.; Sun, T.; Ruff, C. J.; Well-

defined, model long chain branched polyethylene. 1. Synthesis and characterization. *Macromolecules* **2000**, 33, (7), 2424-2436.

9. Bender, J. T.; Knauss, D. M., Synthesis of Low Polydispersity Polybutadiene and Polyethylene Stars by Convergent Living Anionic Polymerization. *Journal of Polymer Science: Part A: Polymer Chemistry* **2006**, 44, 828-836.

10. Driva, P.; Iatrou, H.; Lohse, D. J.; Hadjichristidis, N., Anionic Homo-and Copolymerization of Double-Tailed Macromonomers: A Route to Novel Macromolecular Architectures. *Journal of Polymer Science: Part A: Polymer Chemistry* **2005**, 43, 4070-4078.

11. Koutalas, G.; Iatrou, H.; Lohse, D. J.; Hadjichristidis, N., Well-Defined Comb, Star-Comb, and Comb-on-Comb Polybutadienes by Anionic Polymerization and the Macromer Strategy. *Macromolecules* **2005**, 38, 4996-5001.

12. Vazaios, A.; Lohse, D. J.; Hadjichristidis, N., Linear and Star Block Copolymers of Styrenic Macromonomers by Anionis Polymerization. *Macromolecules* **2005**, 38, 5468-5474.

13. Heeley, E. L.; Fernyhough, C. M.; Graham, R. S.; Olmsted, P. D.; Inkson, N. J.; Embrey, J.; Groves, D. J.; McLeish, T. C. B.; Morgovan, A. C.; Meneau, F.; Bras, W.; Ryan, A. J., Shear-induced crystallization in blends of model linear and long-chain branched hydrogenated polybutadienes. *Macromolecules* **2006**, 39, 5058-5071.

14. Kumaraswamy, G., Crystallization of Polymers from Stressed Melts. *Journal of Macromolecular Science, Part C: Polymer Reviews* **2005**, 45, 375-397.

15. Seki, M.; Thurman, D. W.; Oberhauser, J. P.; Kornfield, J. A., Shear-mediated crystallization of isotactic polypropylene: The role of long chain -- long chain overlap. *Macromolecules* **2002**, *35*, 2583-2594.
16. Hsiao, B. S.; Yang, L.; Somani, R. H.; Avila-Orta, C. A.; Zhu, L., Unexpected Shish-Kebab Structure in a Sheared Polyethylene Melt. *Physical Review Letters* **2005**, *94*, (11).
17. Yang, L.; Somani, R. H.; Sics, I.; Hsiao, B. S.; Kolb, R.; Lohse, D., The role of high molecular weight chains in flow-induced crystallization precursor structures. *Journal of Physics: Condensed Matter* **2006**, *18*, S2421-S2436.
18. Zuo, F.; Keum, J. K.; Yang, L.; Somani, R. H.; Hsiao, B. S., Thermal Stability of Shear-Induced Shish-Kebab Precursor Structure from High Molecular Weight Polyethylene Chains. *Macromolecules* **2006**, *39*, 2209-2218.
19. Fernandez-Ballester, L.; Gough, T.; Meneau, F.; Bras, W.; Ania, F.; Balta-Calleja, F. J.; Kornfield, J. A., Simultaneous birefringence, small- and wide-angle X-ray scattering to detect precursors and characterize morphology development during flow-induced crystallization of polymers. *Journal of Synchrotron Radiation* **2008**, *15*, (2), 185-190.
20. Rachapudy, H.; Smith, G. G.; Raju, V. R.; Graessley, W. W., Properties of Amorphous and Crystallizable Hydrocarbon Polymers .3. Studies of the Hydrogenation of Polybutadiene. *Journal of Polymer Science Part B-Polymer Physics* **1979**, *17*, (7), 1211-1222.
21. Krigas, T. M.; Carella, J. M.; Struglinski, M. J.; Crist, B.; Graessley, W. W.; Schilling, F. C., Model Copolymers of Ethylene with Butene-1 Made by

Hydrogenation of Polybutadiene - Chemical Composition and Selected Physical Properties. *Journal of Polymer Science: Part B: Polymer Physics* **1985**, 23, (3), 509-520.

22. Kapnistos, M.; Vlassopoulos, D.; Roovers, J.; Leal, L. G., Linear Rheology of Architecturally Complex Macromolecules: Comb Polymers with Linear Backbones. *Macromolecules* **2005**, 38, 7852-7862.

23. deGennes, P.-G., *Scaling Concepts in Polymer Physics*. Cornell University Press: Ithica, NY, 1979.

24. Takahashi, Y.; Isono, Y.; Noda, I.; Nagasawa, M., Zero-Shear Viscosity of Linear Polymer Solutions over a Wide Range of Concentration. *Macromolecules* **1985**, 18, (5), 1002-1008.

25. Crist, B.; Tanzer, J. D.; Graessley, W. W., Small-Angle Neutron-Scattering of a Model Crystallizable Polymer - Crystallization and Size-Mismatch Effects. *Journal of Polymer Science Part B - Polymer Physics* **1987**, 25, (3), 545-556.

26. Kumaraswamy, G.; Verma, R. K.; Kornfield, J. A., Novel flow apparatus for investigating shear-enhanced crystallization and structure development in semicrystalline polymers. *Review of Scientific Instruments* **1999**, 70, (4), 2097-2104.

27. Kumaraswamy, G.; Issaian, A. M.; Kornfield, J. A., Shear-Enhanced Crystallization in Isotactic Polypropylene. 1. Correspondence between in Situ Rheo-Optics and ex Situ Structure Determination. *Macromolecules* **1999**, 32, (22), 7537-7547.

28. Beek, M. H. E. V. d.; Peters, G. W. M.; Meijer, H. E. H., Classifying the Combined Influence of Shear Rate, Temperature, and Pressure on Crystalline Morphology and Specific Volume of Isotactic (Poly)propylene. *Macromolecules* **2006**, 39, 9278-9284.

29. Acierno, S.; Palomba, B.; Winter, H. H.; Grizzuti, N., Effect of molecular weight on the flow-induced crystallization of isotactic poly(1-butene). *Rheologica Acta* **2003**, 42, (3), 243-250.

30. Elmoumni, A.; Winter, H. H.; Waddon, A. J.; Fruitwala, H., Correlation of material and processing time scales with structure development in isotactic polypropylene crystallization. *Macromolecules* **2003**, 36, (17), 6453-6461.

31. Bustos, F.; Cassagnau, P.; Fulchiron, R., Effect of molecular architecture on quiescent and shear-induced crystallization of polyethylene. *Journal of Polymer Science Part B - Polymer Physics* **2006**, 44, (11), 1597-1607.

32. Rubinstein, M.; Colby, R. H., *Polymer Physics*. Oxford University Press: New York, 2003.

33. Rheology studies were graciously conducted by Dr. Juhn Hun Lee at ExxonMobil (Clinton, NJ).

34. Rheology studies were graciously conducted by Dr. Juhn Hun Lee at ExxonMobil (Clinton, NJ).

35. Langouche, F., Orientation deveopment during shear flow-induced crystallization of i-PP. *Macromolecules* **2006**, 39, 2568-2573.

36. Pople, J. A.; Mitchell, G. R.; Sutton, S. J.; Vaughan, A. S.; Chai, C. K., The development of organized structures in polyethylene crystallized from a sheared melt, analyzed by WAXS and TEM. *Polymer* **1999**, 40, (10), 2769-2777.

37. Liang, S.; Wang, K.; Tang, C. Y.; Zhang, Q.; Du, R. N.; Fua, Q., Unexpected molecular weight dependence of shish-kebab structure in the oriented linear low

density polyethylene/high density polyethylene blends. *Journal of Chemical Physics* **2008**, 128, (17), 9.

38. Somani, R. H.; Yang, L.; Zhu, L.; Hsiao, B. S., Flow-induced shish-kebab precursor structures in entangled polymer melts  
*Polymer* **2005**, 46, 8587-8623.